UNIVERSITAT POLITÈCNICA
DE CATALUNYA
BARCELONATECH

PhD program in Geotechnical Engineering

Imaging and discrete modelling of sand shape

Doctoral thesis by:
Riccardo Rorato

Thesis advisors:
Prof. Marcos Arroyo Álvarez de Toledo
Prof. Antonio Gens Solé
Prof. Edward Carlo Giorgio Andò

This dissertation is submitted in fulfillment of the requirements for the degree of Doctor of Philosophy from Universitat Politècnica de Catalunya

Department of Geotechnical Engineering and Geosciences – UPC
Barcelona, Spain
November 2019

To *my family*

Acknowledgments

This thesis has received support by the Spanish Ministry of Economy through grants BIA2014-59467-R and BIA2017-84752-R and by EU through 645665 - GEO-RAMP - MSCA-RISE, which are gratefully acknowledged.

From the personal side, the support of many people must be acknowledged for the achievement of this thesis. First of all, I want to express my gratitude to my PhD advisors, Professors Marcos Arroyo, Antonio Gens and Edward Andò, for their support all over these years and for the infinite knowledge they shared with me. Further, thank you Marcos for your patience and willingness to answer my daily questions and continuous doubts. Your assistance, ideas and encouragement have been the guiding light during all this time. Thank you Antonio for your targeted inputs that improved the quality of this thesis. Thank you Eddy for putting me in the conditions to start my PhD since the very first months. Your passion, energy and continuous support really motivated me. This work would have not been possible without your help and brilliant ideas.
Beside my thesis supervisors, I want to thank Prof. Cino Viggiani for having introduced me to the world of research. I would have never started a PhD without the conversations with him.

I also would like to acknowledge the people and research groups that hosted me during the visiting periods spent abroad. In chronological order: thanks to Fabian Dedecker, Sacha Emam and all the Itasca team based in Lyon for introducing me to PFC5; thanks to Prof. Mingjing Jiang and co-workers for your warm welcome in Shanghai and Tianjin;

thank you Francesco Calvetti for the great conversations we had in Lecco about geotechnics, DEM and sports; thank you Matteo Ciantia for your constant support and for hosting me in Dundee.

Special thanks are addressed to all the amazing friends and colleagues I met in Barcelona and Grenoble. I cannot list all of your names but your daily support was very important for me. A big THANKS to Gaia, without whom this experience would have been completely different.

Last but not least, thanks to my family. Thank you for always being there.

Abstract

The shape of particles is known to play an important role in soil behaviour, with significant effects of engineering responses. Investigating how the shape of particles can be measured and quantified is therefore considered increasingly important in modern soil mechanics. This is propelled by the advent of computer based image-analyses and discrete modelling algorithms, which have opened new ways to tackle this problem. This work demonstrates how these two techniques can be made to work together.

Image analyses are performed on x-rays micro-tomographs (µ-CT) of triaxial sand specimens, focusing on the characterisation and quantification of particle shapes. Two very different particle shape sands are studied in details: Caicos ooids (rounded) and Hostun sand (angular). A discrete *Digital Volume Correlation* (DVC) algorithm is then used to track the kinematics of individual grains (around 50000 for each sand specimen) during the triaxial test and measure, with good precision, their cumulated displacements and rotations. Joint analysis of the shape and kinematic databases acquired is performed to find how particle shape descriptors are related to observed kinematics at the microscale level. It appears that true sphericity is a good predictor of upper bound rotational restraint.

Modelling is based on the Discrete Element Method (DEM). Models that introduce rolling resistance at the contact are widely employed in DEM simulations, these approaches offer substantial computational benefits at the price of increased calibration complexity. In this work, the values of true sphericity obtained by image analysis of the grains, either directly by 3D acquisition or by correlation with simpler to obtain 2D shape measures, are used to establish mechanically equivalent rotational restrictions. An empirical relation between a contact parameter (*rolling friction*) and a 3D grain shape descriptor (*true sphericity* is first calibrated - using both specimen-scale and grain scale results from two triaxial tests in Hostun sand and Caicos ooids. It is then validated by simulating other triaxial tests (1) with the same sands, but in different conditions (2) with Ottawa sand, for which 3D grain images were also available for examination, and (3) with Ticino sand, for which only 2D grain images were available.

Finally, results of large-scale DEM simulations on the Cone Penetration Test (CPT) - exploiting the new proposed contact model - are presented. Experimental data on the CPT performed in a Calibration Chamber (CC) comprised of Ticino sand are successfully fitted by the numerical penetration curves at different confining pressures and conditions. A parametric study about the influence of particle shape and particle shape variability put in evidence the strong-coupled effects of rolling and frictional resistances at the particles contacts. The work described in this thesis will ease the use of DEM for large-scale simulations of geotechnical engineering problems.

Keywords

CPT test; DEM; Granular materials; Large strains; Particle-scale behaviour; Particle shape; Rolling resistance; Shear strength; Statistical analysis; X-rays microtomography.

Resumen

Se sabe que la forma de las partículas juega un papel importante en el comportamiento del suelo, con efectos significativos de las respuestas mecánicas relevantes en ingeniería geotécnica. Por lo tanto, investigar cómo se puede medir y cuantificar la forma de las partículas se considera cada vez más importante en la mecánica del suelo moderna. Esto se acrecienta debido a las técnicas de análisis computacionales de imágenes y algoritmos de modelado discreto (DEM), que han abierto nuevas formas de abordar este problema. Este trabajo demuestra cómo se pueden hacer que estas dos técnicas funcionen juntas.

Los análisis de imagen se realizan sobre micro-tomografías de rayos X (μ-CT) de muestras de arena en celdas triaxiales, centrándose en la caracterización y cuantificación de la forma de las partículas. Se estudian en detalle dos arenas con la forma de sus partículas muy diferentes: Caicos ooids (redondeados) y Hostun sand (angular). Luego se utiliza un algoritmo discreto de correlación de volumen digital (DVC) para rastrear la cinemática de granos individuales (alrededor de 50000 por cada muestra de arena) durante la prueba triaxial y medir, con buena precisión, sus desplazamientos y rotaciones acumulados. El análisis conjunto de la forma y las bases de datos cinemáticas adquiridas se realiza para encontrar cómo los descriptores de forma de partículas se relacionan con la cinemática observada a nivel de micro-escala. Resulta que la esfericidad verdadera predice bien el límite superior de rotación de una partícula.

La modelización numérica se basa en el Método de Elementos Discretos (DEM). Los modelos que introducen resistencia a la rotación en el contacto se emplean ampliamente en simulaciones DEM, estos enfoques ofrecen beneficios computacionales sustanciales a costa de una mayor complejidad de calibración. En este trabajo, los valores de esfericidad verdadera (i.e., true sphericity) obtenidos mediante análisis de imagen de los granos, ya sea directamente por adquisición 3D o por correlación con medidas de forma 2D más simples, se utilizan para establecer restricciones de rotación mecánicamente equivalentes. Una relación empírica entre un parámetro de contacto (rolling friction) y un descriptor de forma de grano 3D (la esfericidad verdadera) se calibra primero, utilizando los resultados de la escala de muestras y de la escala de granos de dos pruebas triaxiales en las arenas de Hostun y de Caicos. Luego se valida simulando otras pruebas triaxiales (1) con las mismas arenas, pero en diferentes condiciones (2) con arena de Ottawa, para la que también estaban disponibles imágenes 3D de granos para su examen, y (3) con arena de Ticino, para la cual solo estaban disponibles imágenes 2D de los granos.

Finalmente, se presentan resultados de simulaciones DEM a gran escala de la prueba de penetración de cono (CPT), aprovechando el nuevo modelo de contacto propuesto. Los datos experimentales del CPT realizado en una cámara de calibración (CC) sobre arena de Ticino se ajustan con éxito por las curvas de penetración numérica a diferentes presiones y condiciones de confinamiento. Un estudio paramétrico sobre la influencia de la forma de las partículas y la variabilidad de las formas de las partículas puso de manifiesto los efectos fuertemente acoplados de las resistencias rotacional y friccional en los contactos entre partículas. El trabajo descrito en esta tesis facilitará el uso de DEM para simulaciones a gran escala en problemas de ingeniería geotécnica.

Palabras clave:

CPT test; DEM; Materiales granulares; Grandes deformaciones; Comportamiento a la escala de las partículas; Forma de las partículas; Resistencia rotacional; Resistencia al corte; Análisis estadística; Microtomografía Rayos-X.

Declaration

I hereby declare that this thesis has been composed by myself and that the work has not been submitted for any other degree or professional qualification. I confirm that the work submitted is my own, except where work which has formed part of jointly authored publications has been included. My contribution and those of the other authors to this work have been explicitly indicated below. Further, I have acknowledged all sources used and have cited these in the references sections.
This doctoral work produced the following publications (published-accepted-submitted) wherein some ideas and figures may have appeared previously.

- Rorato, R., Arroyo, M., Gens, A., Andò, E., Viggiani G. (2019), 'Image-based calibration of rolling resistance in discrete element models of sand', Computers & Geotechnics (submitted).
- Rorato, R., Arroyo, M., Gens, A., Andò, E., Viggiani G. (2019), 'Particle shape and rotation during triaxial shearing', Géotechnique (submitted).
- Rorato, R., Arroyo, M., Gens, A., Andò, E., (2019), 'Sphericity measures of sand grains', Engineering Geology, 254, pp. 43–53. DOI: 10.1016/j.enggeo.2019.04.006.
- Rorato, R., Arroyo, M., Gens, A., Andò, E., and Viggiani, G. (2018), 'Particle shape distribution effects on the triaxial response of sands : a DEM study'. In micro to MACRO Mathematical Modelling in Soil Mechanics, Trends in Mathematics. Giovine P. et al. (Eds.). DOI: 10.1007/978-3-319-99474-1_28.

Table of Contents

Part I: Introduction and State of the Art **1**

1 Introduction **3**

1.1 Research motivation 3

1.2 Aim & Objectives 5

1.3 Outline of the thesis 6

2 Experimental Description of Particle Shape **9**

2.1 Introduction 9

2.2 Shape characterization 10

2.2.1 Form (or morphology) 11

2.2.2 Roundness 21

2.2.3 Surface Texture (roughness) 26

2.3 Summary 28

3 Influence of particle shape on Geotechnical Properties **31**

3.1 Introduction 31

3.2 Packing limits 31

3.3 Grain Size Distribution from sieve analysis 33

3.4 Shear strength 34

3.5 Stiffness 39

3.6 Liquefaction 40

3.7 Cone Penetration Test 42

3.8 Summary 43

4 Particle shape in Discrete Element Modelling 45

4.1 Introduction 45

4.2 DEM fundamentals 46

4.3 Particle shape modelling in DEM 50

4.3.1 Continuous analytical particle shape description 50

4.3.2 Polyhedral particles 51

4.3.3 Aggregates of spheres (clumps) 51

4.3.4 Other approaches 54

4.3.5 Rolling resistance contact models 56

4.4 Effects of particle shape observed in DEM-based studies 71

4.5 Summary 76

References Part I 77

Part II: Experimental dataset and image analysis 89

5 X-Rays micro-computed tomography for geomaterials 91

5.1 Introduction 91

5.2 X-rays tomographic equipment 92

5.3 Experimental campaign 94

5.3.1 Hostun sand 95

5.3.2 Caicos ooids 101

5.3.3 Ottawa sand 105

5.4 Image analysis procedure 107

5.5 Summary 109

6 Shape analysis of Sand Particles 111

6.1 Introduction 111

6.2 Numerical quantification of particle geometry 114

6.2.1 Volume and centre of mass 116

6.2.2 Volume – Particle Size Distribution 116

6.2.3 Surface Area 121

6.2.4 Inertia Tensor 124

6.2.5 Particle characteristic lengths 127

6.2.6 Convex hull 129

6.2.7 Maximum inscribed sphere 129

6.2.8 Minimum circumscribed sphere 130

6.3 Numerical quantification of the particles shape descriptors 131

6.4 3D shape descriptions: correlations 139

6.5 Projected (2D) measures of shape 143

6.6 Relation between 2D and 3D shape descriptors 145

6.7 Statistical convergence of sample size 147

6.8 Sphericity evolution during triaxial shearing 149

6.9 Summary 150

7 Study of grain kinematics during triaxial tests 151

7.1 Introduction 151

7.2 Digital image correlation for particle tracking 153

7.2.1 Single-image post-processing 156

7.2.2 Tracking grains kinematics with D-DVC 157

7.2.3 Validation of the D-DVC procedure 159

7.2.4 Shear band identification 161

7.3 Results from D-DVC 162

7.3.1 Shear band identification 162

7.3.2 Spatial distribution of grain shapes and shear localization 164

7.3.3 Overall grain kinematics 166

7.3.4 Axes of rotation 171

7.3.5 Relation between grain shape and magnitude of rotation 173

7.4 New definition of "local" porosity 179

7.5 Summary 185

References Part II 187

8 A rolling resistance contact model accounting for Particle Shape 197

8.1 Introduction 197

8.2 Contact rolling resistance model 198

8.3 Relating rolling resistance and particle shape 199

8.4 Model calibration 199

8.4.1 Target experimental data 200

8.4.2 Mapping function 201

8.4.3 Calibration procedure 202

8.5 Validation of the contact model 210

8.5.1 Validation 1: Triaxial test on Hostun and Caicos sands at 300kPa confining pressure 210

8.5.2 Validation 2: Triaxial test on Ottawa sand at 100kPa and 300kPa 212

8.5.3 Validation 3: Triaxial tests on dense, medium and loose Ticino sand at 100-200-300 kPa 215

8.6 Comparison with rolling frictions from particles eccentricity 215

8.7 Summary 218

9 Cone Penetration Test on a Virtual Calibration Chamber (VCC) using DEM 219

9.1 Introduction 219

9.2 Previous work 221

9.3 Microscopic calibration of DEM parameters: Drained triaxial test on Ticino sand 228

9.3.1 Acquisition of 2D perimeter sphericity from a table scanner (oriented projection) and determination of rolling friction from 2D sphericity 228

9.3.2 Results at 100-200-300kPa confining pressures 230

9.4 DEM simulations of CPT tests in the ENEL-ISMES calibration chamber 235

9.4.1 Chamber & cone geometry and properties 235

9.4.2 Multiscaling approach for particle size of Ticino sand 236

9.4.3 Comparison of macro-responses with physical dataset of Ticino sand 239

9.5 Effect of particle shape on penetration resistance: parametric study 243

9.5.1 Model properties 244

9.5.2 Results 248

9.6 Summary 254

References Part III 256

Part IV: Conclusions 261

10 Conclusions 263

10.1 Summary results 263

10.2 Recommendations for future work 264

10.2.1 Particle shape 264

10.2.2 Numerical simulations 265

10.3 Final remarks 267

References Part IV 268

Part V: Appendices 271

Appendix A: Scripts 273

Appendix A.1 Python script "GetAllGrains_MPI.py" 273

Appendix A.2 Python script “GetAllGrains_2Dprojection.py” 278

Appendix A.3 Python script “GetLabels_2Dimage.py” 281

Appendix A.4 PFC5 script “Make_initial.p3dat” 282

Appendix A.5 PFC5 script “Isotropic_compression.p3dat” 283

Appendix A.6 PFC5 script “Triaxial_compression.p3dat” 284

Appendix A.7 PFC5 script “Prepare_Cone.p3dat” 286

Appendix B: Dataset 289

Appendix C: Number of particles estimation in a cylindrical DEM sample 291

List of Figures:

Figure 2.1: Three independent aspects of shape (Barret, 1980) 11
Figure 2.2: Feret diameters of a particle outline 12
Figure 2.3: Zingg's shape classification based on the flatness and elongation indexes (Krumbein 1941) and relation between "intercept sphericity" and Zingg's classification (Krumbein and Sloss, 1963) 16
Figure 2.4: Sphericity-form diagram of Sneed and Folk (1958) (from (Lewis and McConchie, 1994)). 18
Figure 2.5: Illustration of the conception "roundness" (Wadell, 1932) 22
Figure 2.6: Power's chart for shape classification (Powers, 1953) 23
Figure 2.7: Chart used to characterise sphericity and roundness of particles (Krumbein and Sloss, 1963) 24
Figure 2.8: Self-affinity of a surface profile (Bhushan, 2001) 26
Figure 2.9: Roughness profiles with relative JCR value (Barton and Choubey, 1977) ... 27
Figure 2.10: Microscope image of glass ballottini (a) and relative surface texture profile measured by interferometer (b), from (Cavarretta, 2009) 28
Figure 3.1: Relation between shape parameters (roundness, sphericity, regularity) and void ratios (Santamarina and Cho, 2004) 33
Figure 3.2: GSD of gravel soil (4.75mm-8mm) with different shapes (Arasan and Akbulut, 2008) 34
Figure 3.3: Macro-mechanical responses of a dense and loose material 35
Figure 3.4: Rotational tendency in loose (low e) and dense (high e) packing (Santamarina, 2004) 36
Figure 3.5: Empirical correlation between particle shape (roundness) and φcv (Santamarina and Cho, 2004) 36

Figure 3.6: Empirical correlation between particle shape (roundness) and Γ (Cho, 2006) 38
Figure 3.7: Influence of shape (sphericity and roundness) on the parameters (α, β) (Santamarina, 2004) 40
Figure 3.8: Relationship between CSR (30^{th} cycle) and sphericity (S_A following the terminology presented in Table 2.1) (Ishibashi et al., 1982) 41
Figure 3.9: CPT tip resistance in the centrifuge test performed at g=50 and DR=0.8 (Liu and Lehane, 2013) 42
Figure 4.1: Calculation cycle in DEM, from PFC5 reference guide (Itasca Consulting Group Inc., 2014) 47
Figure 4.2: Single mass-spring system 47
Figure 4.3: Examples of 3D clumps (Yang et al., 2017) 52
Figure 4.4: Example of algorithm used for creating clumped particles (Das, 2007) 53
Figure 4.5: Particle representation using level set function. The black dots are the boundary node discretisation (Jerves et al., 2016). 55
Figure 4.6: Level-set DEM representation of HNEA01 sand specimen before and after triaxial shearing (Kawamoto et al., 2018) 55
Figure 4.7: Rolling resistance model proposed by (Iwashita and Oda, 1998) 58
Figure 4.8: Triaxial responses of DEM simulations performed on spherical particles with three different rotational constrains: free rolling, fixed rolling and rolling resistance (Iwashita and Oda, 1998) 58
Figure 4.9: Strain localisation after triaxial testing in the free rolling test (a), fixed rolling test (b) and rolling resistance test (c) using MDEM. 59
Figure 4.10a-b: Rolling resistance model proposed by (Jiang et al., 2005) 60
Figure 4.11: Moment-relative rotation response for the model introduced by (Jiang et al., 2005) 61
Figure 4.12: Angle of internal friction at peak and critical states in function of the shape parameter δ (Jiang et al., 2005) 62
Figure 4.13: Relationship between the rolling torque M and relative rotation ωr (Estrada et al., 2008) 63

Figure 4.14: Contour map of the internal friction coefficient (μ*) as function of the rolling friction (η) and sliding friction (μ) (Estrada et al., 2008) 63

Figure 4.15: Elastic part of the rolling resistance contact model (Ai et al., 2011) 65

Figure 4.16: Non-spherical particles in contact. The contact normal forces shows an eccentricity that induces a torque (Wensrich and Katterfeld, 2012) 67

Figure 4.17: Relationships between the coefficient of rolling friction (above) and rolling radius (below) as function of the aspect ratio of the spheroid (Wensrich and Katterfeld, 2012) 68

Figure 4.18: Tertiary clump with the spacing parameter δ used to vary the angularity (Wensrich and Katterfeld, 2012).. 68

Figure 4.19: Relationships between the coefficient of rolling friction (above) and rolling radius (below) as function of the spacing parameter δ for binary and tertiary clumps (Wensrich and Katterfeld, 2012).. 69

Figure 4.20: Measured angles of repose (AOF) for 150 simulations of different shaped particles in function of the rolling friction and the sliding friction (Wensrich and Katterfeld, 2012)... 70

Figure 4.21: Failure envelopes of DEM simulations performed on spherical and clumped particles (Das, 2007) 72

Figure 4.22: Values of the internal friction angles for Daytona Beach Sand and rounded particles (from 2D-3D simulations and experiments) (Das, 2007).................................... 72

Figure 4.23: Experimental (a) and numerical (b) models for the granular flow study... 73

Figure 4.24: Disc, square and triangular particles built using clumps 74

Figure 4.25: Stress-strain (a) and volumetric (b) responses of the DEM simulations using disks with different rolling resistance values and clumped particles (squares, triangles) 74

Figure 4.26: Accumulated shear strain at the critical state (10% axial strain) for spheres with increasing values of rolling resistance (a-b-c), and the clump samples made with squares (d) and triangles (e) as in Figure 4.24. 75

Figure 4.27: Cyclic stress ratio (CSR) versus number of cycles to liquefaction (N) for simulated samples prepared by static compaction (Ashmawy et al., 2003) 75

Figure 5.1: Laboratoire 3SR x-rays scanner equipment (Andò, 2013)............................... 93

Figure 5.2: Radiograph (1920 × 1536 pixels) of the Caicos ooids specimen (Andò, 2013) 94

Figure 5.3: Horizontal section of the scanned 3D Hostun sand specimen (on the left). On the right, a scanning with an Electron Microscope (Andò, 2013)..................................... 96

Figure 5.4: Grain Size Distribution of Hostun sand (Andò, 2013).................................... 96

Figure 5.5: Stress-strain responses of the triaxial tests on specimens HNEA01 and HNEA03 (Andò, 2013).. 98

Figure 5.6: Stress-strain responses of the triaxial tests on specimens HNEA02 and HNEA04.. 99

Figure 5.7: Stress-strain responses on specimens HNEA01, HNEA03, TS28D01 and TS28D03 (Andò, 2013) 100

Figure 5.8: Horizontal slice of COEA04 (left) and single radiograph of Caicos sand (right) (Andò, 2013) 102

Figure 5.9: Grain Size Distribution of Caicos ooids (Andò, 2013) 102

Figure 5.10: Stress-strain responses of the triaxial tests on specimens COEA01, COEA03 and COEA04 (Andò, 2013)... 103

Figure 5.11: Stress-strain curves of the triaxial tests on specimens COEA02 and COCV02 (Andò, 2013) 104

Figure 5.12: Stress-strain curves of the triaxial tests on specimens OUEA04 and OUEA06 (Andò, 2013) 106

Figure 5.13: Stress-strain curves of the triaxial tests on specimens OUEA02 and OUEA03 (Andò, 2013) 106

Figure 5.14: Flow chart showing how to go from a greyscale image to a labelled image in which individual particles can be extracted (Andò, 2013) 109

Figure 5.15: Matrix representation of the pixels of a labelled image's slice................... 109

Figure 6.1: Macro-mechanical responses of HNEA01 and COEA04 with associated loading steps 112

Figure 6.2: Vertical slices of HNEA01. On the left, the original labelled image. On the right, after the filter is applied.. 113

Figure 6.3: 3D representation of the specimen COEA04 114
Figure 6.4: Flow diagram of image treatment operations (Rorato et al., 2019) 115
Figure 6.5: VSD of HNEA01 at the beginning and the end of the (scanned) triaxial test 117
Figure 6.6: Histogram of the particles volume in specimen HNEA01............................ 117
Figure 6.7: VSD of COEA04 at the beginning and the end of the (scanned) triaxial test 118
Figure 6.8: Histogram of the particles volumes in specimen COEA01 and COEA04 .. 118
Figure 6.9: Comparison between the GSDs of HNEA01 and COEA04 during isotropic compression 118
Figure 6.10: GSDs of HNEA01 compared to the GSD measured by the manufacturer 119
Figure 6.11: Histogram of the equivalent diameter in the specimen HNEA01 120
Figure 6.12: GSDs of COEA04 compared to the GSD measured by Exxon and Laboratoire 3SR 120
Figure 6.13: Histogram of the equivalent diameter in the specimen COEA04.............. 120
Figure 6.14: Comparison between the GSDs of HNEA01 and COEA04 121
Figure 6.15: Visualisation of the Gaussian filter applied to grain number 46972 122
Figure 6.16: Mesh of grain 46972 from Marching Cubes algorithm............................... 123
Figure 6.17: On the left, slice of the initial binarised sphere. On the right, the same sphere after the Gaussian filter is applied 124
Figure 6.18: Surface mesh visualisation after application of the MC-algorithm 124
Figure 6.19: Paraview representation of the artificial spheroid with its principal inertia axis 126
Figure 6.20: Longest (a), intermediate (b) and shortest (c) lengths of grain 46972. 129
Figure 6.21: Normalised histogram of the "degree of true sphericity" for the three sands 134
Figure 6.22: Meshed surfaces of the grains having extreme values of Sphericity (ψ) .. 134
Figure 6.23: Histograms of the flatness index for HNEA01 and COEA04..................... 135
Figure 6.24: Histograms of the elongation index for HNEA01 and COEA04................ 135
Figure 6.25: Meshed surfaces of the grains having extreme values of Flatness indices 136

Figure 6.26: Meshed surfaces of the grains having extreme values of Elongation indices 136
Figure 6.27: Meshed surfaces of the grains having extreme values of 3D-Convexity .. 137
Figure 6.28: Comparison between the histograms of the Alshibli sphericity (see Table 6.2) of Hostun sand measured in this work with the data presented in (Alshibli et al., 2015) 138
Figure 6.29: Bivariate density plot of Hostun (a-c) and Caicos (b-d) shown on the Zingg form space with Blott & Pye (2008) classifications for Elongation (a-b) and Flatness (c-d). Isoline spacing is 10%. 139
Figure 6.30: Relation between true sphericity and particle volume for Hostun sand (a) and Caicos ooids (b). Marginal distributions are also shown alongside the axis 140
Figure 6.31: Linear regression line between true sphericity (3D) and perimeter sphericity (2D). The arrows show the ranges (5% and 95% percentiles) of the two sands. 147
Figure 6.32: Evolution of the first three sample moments (mean, standard deviation, skew) 148
Figure 7.1: Grey-scale images (slices) of specimen COEA04 at increments “01” (left) and “11” (right). It is clear how the bottom plates moved upwards, inducing axial shortening and failure in the specimen. 155
Figure 7.2: Vertical slices of Caicos sand showing grains vertical displacement (on the left) and rotations (on the right) measured from increment “01” (start of deviatoric load) to increment “11” (end of the test). Grains are coloured by the value of their measured z-displacement and total rotation at step “11”, although the image is referred to the loading step “01” (initial state). 155
Figure 7.3: Triaxial responses of the specimens HNEA01 and COEA04 with loading stages markers. The yellow stripes indicate loading stages that are later investigated in more detail 157
Figure 7.4: Spherical coordinates system adopted for the stereoplots (Wikipedia) 158
Figure 7.5a-b-c: (a) Histogram of measured rotation after rigid rotation of the specimen (b) Stereoplot showing the rotation versor of each grain (c) 2D histogram showing the correlation between grains sphericity and grains rotation. 161

Figure 7.6: Shear band identification for specimens COEA04 (a) and HNEA01 (b). Particles are coloured black if the "micro-strain" (Catalano et al., 2014) calculated on the Voronoi domain centred on the particle is greater than 0.10 (i.e., they belong to the shear band). 163

Figure 7.7: Local reference system for the shear band 163

Figure 7.8: Sphericity spatial distribution for Hostun and Caicos sand in two vertical sections: parallel and perpendicular to the shear band. 165

Figure 7.9: Histograms of true sphericity for Hostun (a) and Caicos (b) sands both inside and outside the shear bands. 166

Figure 7.10: Vertical slices of Caicos sand (specimen COEA04) showing grain vertical displacement (above) and rotation (below**) accumulated** during the test. Grains are coloured by the value of their measured z-displacement (above) and total rotation (below). Not all the increments are shown. 167

Figure 7.11: Vertical slices of Hostun sand (specimen HNEA01) showing grain vertical displacement (above) and rotation (below) **accumulated** during the test. Grains are coloured by the value of their measured z-displacement (above) and total rotation (below). Not all the increments are shown. 168

Figure 7.12: Histories of cumulated mean particle rotations inside and outside the shear bands (SB in the legend), measured by D-DVC throughout the triaxial tests. The green dots represent interpreted results from Alshibli and Alramahi (2006) for a triaxial experiment involving 400 plastic pearls. 168

Figure 7.13: Distribution of accumulated particle rotation magnitudes at different test stages (12-14-16) for particles within the shear band of the Hostun sand HNEA01 specimen. 170

Figure 7.14: Particles with correlation maximum below 98% as a percentage of total number of particles 170

Figure 7.15: Stereoplots showing the rotation versor directions at 5% shortening. The green dots indicate the orientation of vector b (see Figure 7.7) belonging to the shear bands of Hostun and Caicos sands. The stereoplot angles markers are not shown for readability, see Figure 7.5b for reference. 171

Figure 7.16: Stereoplots showing the rotation versor directions at 9% shortening. The green dots indicate the orientation of vector b (see Figure 7.7) belonging to the shear bands of Hostun and Caicos sands. Stereoplot grid not shown for readability, see Figure 7.5b for reference. 172

Figure 7.17: Normalised bivariate frequency density plots of **form** descriptors versus **cumulative** grain rotation magnitude at 5% shortening (loading stages HNEA01-09 and COEA04-06, respectively 48.612 and 65.056 grains). The contours colour bar is shown in Figure 7.5c. 174

Figure 7.18: Normalised bivariate frequency density plots of **sphericity** descriptors versus the **cumulative** grain rotations measured at 5% shortening (loading stages HNEA01-09 and COEA04-06, respectively 48.612 and 65.056 grains). The contours colour bar is shown in Figure 7.5c.......... 175

Figure 7.19: Normalised histograms showing the observed relation between the degrees of true sphericity and the total grains rotation measured at 5% sample shortening.... 176

Figure 7.20: Influence of the degree of true sphericity on the total grains rotation (at 5% shortening) outside the shear band. 177

Figure 7.21: Influence of the degree of true sphericity on the total grains rotation (at 5% shortening) inside the shear band.......... 178

Figure 7.22: Influence of the degree of true sphericity on the total grains rotation (at 9% shortening) outside the shear band. 178

Figure 7.23: Influence of the degree of true sphericity on the total grains rotation (at 9% shortening) inside the shear band.......... 179

Figure 7.24: Horizontal section (800 of 1750) of the labelled image of HNEA01-01 (a). Horizontal section (800 of 1750) of the labelled image with the built set voronois (b). All the voids have been filled preserving the grains labels.......... 180

Figure 7.25: Vertical slices showing the local porosity value for each grain of Caicos and Hostun sands. 181

Figure 7.26: Vertical slice perpendicular to the shear band of HNEA01 at 9% axial strain (a). Representation of the set-voronois for the same slice (b). 185

Figure 8.1: Rolling resistance contact model (Iwashita and Oda, 1998) (a) and elastic-perfectly plastic model accounting for rolling resistance at contact (b) 198

Figure 8.2: Power law relating the degree of true sphericity of a grain (known) with the rolling friction coefficient to apply to its spherical counterpart in the DEM simulation. The shaded area indicates the maximum 202

Figure 8.3: Comparison between the triaxial responses (100kPa confining pressure) of the experiments (specimens HNEA01 and HNEA03) and the numerical model (DEM) replicating Hostun sand. The mechanical responses from Kawamoto et al. (2018) are also reported for comparison.. 204

Figure 8.4: Comparison between the triaxial responses (100kPa confining pressure) of the experiments (specimens COEA03 and COEA04) and the numerical model (DEM) replicating Caicos sand.. 205

Figure 8.5: Shear band identification for the experiments and the DEM simulation for both sands (specimens HNEA01 and COEA04). Physical (a-c) and numerical (b-d) particles are coloured black if the "micro-strain" (Catalano et al., 2014) calculated on the Voronoi domain centred on the particle is greater than 0.10 (i.e. they belong to the shear band). The same threshold separates the grains from both sands and both physical and numerical samples.. 206

Figure 8.6: Z-displacements in a vertical section of the DEM sample representing Hostun sand compressed at 100kPa confining at 15% axial strain... 207

Figure 8.7: Mean particle rotations for the grains located inside the shear bands (the black grains of Figure 8.5) for both the experimental and numerical samples, throughout the execution of the triaxial test. The good fit ensures the kinematics at failure is respected. 208

Figure 8.8: Comparison between the triaxial responses (300kPa confining pressure) of the experiments (specimens HNEA02 and HNEA04) and the numerical model (DEM) replicating Hostun sand. 211

Figure 8.9: Comparison between the triaxial responses (300kPa confining pressure) of the experiment (specimen COEA02) and the numerical model (DEM) replicating Caicos sand. 212

Figure 8.10: Comparison between the triaxial responses (100kPa confining pressure) of the experiments (specimens OUEA04 and OUEA06) and the numerical model (DEM) replicating Ottawa sand. 214
Figure 8.11: Comparison between the triaxial responses (300kPa confining pressure) of the experiments (specimens OUEA02 and OUEA03) and the numerical model (DEM) replicating Ottawa sand. 214
Figure 8.12: Contact of un-spherical particles producing a torque (T) due to the eccentricity (e) of the normal contact force (F_n) (Wensrich and Katterfeld, 2012)........ 215
Figure 8.13: Rolling frictions of all particles involved in the simulation obtained from both eccentricity calculation and Equation 8.6. For high values of particle sphericity (i.e., ψ>0.90) the two approaches provide similar values. 216
Figure 8.14: Comparison between the triaxial responses (100kPa confining pressure) of the experiments (specimens HNEA01 and HNEA03) and the numerical DEM models exploiting rolling resistance obtained from Eq. 8.6 (red curves) and from the eccentricity calculation (Eq. 8.9, dark red curves). 217
Figure 9.1: Purpose of calibration chambers (from ISMGEO website)........ 220
Figure 9.2: ISMES calibration chamber located in Bergamo (Italy) and its cross-section geometry. 221
Figure 9.3: Representation of stresses and strains applied by the ISMES calibration chamber 222
Figure 9.4: Comparison of raw experimental and numerical tip resistances for both BC1-BC3 boundary conditions at σv = 122kPa, σh = 54kPa (Butlanska, 2014)........ 225
Figure 9.5: Comparison of raw experimental and numerical tip resistances for both BC1-BC3 boundary conditions at σv = 212kPa, σh = 88kPa (Butlanska, 2014)........ 225
Figure 9.6: Comparison of raw experimental and numerical tip resistances for both BC1-BC3 boundary conditions at σv = 313kPa, σh = 133kPa (Butlanska, 2014) 226
Figure 9.7: Virtual Calibration Chamber segment (30°) with three zones with different particle sizes (McDowell et al., 2012). 227

Figure 9.8: Top view of the VCC built by Sharif et al., (2019) exploiting multiple particle scales (7 zones) and the PCRM method showing ball sizes (a) and contact forces (b). Images from (Sharif et al., 2019). 227

Figure 9.9: Zoom on (a) the original scan and (b) the labelled image of Ticino sand... 229

Figure 9.10: Statistical distributions of 3D true sphericity for Hostun, Caicos and Ticino sands........ 229

Figure 9.11: Triaxial responses of loose Ticino sand at 100-200-300kPa........ 232

Figure 9.12: Triaxial responses of medium Ticino sand at 100-200-300kPa........ 233

Figure 9.13: Triaxial responses of dense Ticino sand at 100-200-300kPa........ 234

Figure 9.14: DEM-VCC model reconstruction 236

Figure 9.15: Visualisations of the multi-scaling technique for particle sizes in 3D (a) and 2D, from a vertical slice (b). The particles located closer to the VCC vertical axis are smaller compared to the others. The balls are coloured by the value of their radii. 238

Figure 9.16: Contact network at the initial anisotropic state (σv = 122kPa, σh = 54kPa) 239

Figure 9.17: Cumulative density functions (in log scale) of the normal contact forces in the three zones with different ball scaling factors. Normal forces are normalised with respect to the mean force........ 239

Figure 9.18: Comparison of raw experimental and numerical tip resistances (with fitting curves) respectively at 121-54kPa confinement for BC1 (a) and BC3 (b) and at 212-88kPa for BC1 (c) and BC3 (d)........ 242

Figure 9.19: Contact force network (a) and ball rotations (b) during cone penetration (hpenet = 40cm) 243

Figure 9.20: Contact visualisation near the cone tip for case **C**. Contacts are coloured by the value of their friction coefficient (red=0.60, blue=0.0, green=0.30)........ 245

Figure 9.21: Assigned values of true sphericity for Series 5 (a) and Series 6 (b) and resulting rolling frictions for Series 5 (c) and Series 6 (d)........ 248

Figure 9.22: Tip and shaft resistance of the CPT tests performed for the parametric study of particle shape effects under Cases A (a-b), B (c-d) and C (e-f)........ 249

Figure 9.23: Soil classification from Robertson & Campanella chart (Robertson et al., 1986) for Case A. The dots colours represent the Series from 1 to 6 and respect the colours of the legend in Figure 9.22, also reported here. 250

Figure 9.24: Soil classification from Robertson & Campanella chart (Robertson et al., 1986) for Case B. The dots colours represent the Series from 1 to 6 and respect the colours of the legend in Figure 9.22. 250

Figure 9.25: Soil classification from Robertson & Campanella chart (Robertson et al., 1986) for Case C. The dots colours represent the Series from 1 to 6 and respect the colours of the legend in Figure 9.22. 251

Figure 9.26: Vertical (top figures) and radials stress distributions induced by the cone penetration for simulation Case A for Series 1 (a), Series 3 (b), Series 4 (c) and Series 2 (d) 252

Figure 9.27: Vertical (top figures) and radials stress distributions induced by the cone penetration for simulation Case B for Series 1 (a), Series 3 (b), Series 4 (c) and Series 2 (d). 253

Figure 10.1: Rendering of (a) two high-resolutions (1 μm/px) Hostun sand grain in contact (Wiebicke et al., 2017) (b) a single particle of Mason sand scanned at a resolution of 2 μm/px (Amirrahmat et al., 2019) 265

List of Tables:

Table 2.1: 2D form parameters, terminology following (Zheng and Hryciw, 2015)....... 13

Table 2.2: Fundamental measures from which 2D sphericity proxies are derived......... 14

Table 2.3: Three dimensional form descriptors (see Table 2 for symbol definitions)..... 20

Table 2.4: Fundamental measures from which 3D shape descriptors are derived 20

Table 5.1: Triaxial tests performed on Hostun sand by Andò (Andò, 2013).................... 97

Table 5.2: Triaxial tests performed on Caicos sand by Andò (Andò, 2013) and Viggiani 103

Table 5.3: Triaxial tests performed on Ottawa sand by Andò (Andò, 2013).................. 105

Table 6.1: Description of the filters applied to the original labelled images.................. 113

Table 6.2: Shape descriptors for grain 46972 [V, S = volume and surface area of the grain. s_n = surface area of the equivalent sphere. V_{CS}, $D_{circ,min}$ = volume and diameter of the minimum circumscribed sphere. $D_{ins,max}$ = diameter of the maximum inscribed sphere. a, b, c = grain lengths. V_{CH} = volume of the convex hull].. 132

Table 6.3: Statistics of the 3D shape descriptors for the three sands at the initial state 133

Table 6.4: Correlation matrix of the shape parameters for Hostun sand (48.612 grains). 141

Table 6.5: Correlation matrix of the shape parameters for Caicos sand (65.056 grains). 142

Table 6.6: Correlation matrix of the shape parameters for Ottawa sand (112.411 grains) 143

Table 6.7: Statistics of the 2D shape descriptors for the two sands (obtained from randomly oriented projections).. 144

Table 6.8: Statistics of the 2D shape descriptors for the two sands (obtained from projections oriented along the minor principal axis) 145

Table 6.9: Correlation matrix between 3D and 2D sphericity parameters (obtained from randomly oriented projections). Merged data for Hostun and Caicos, 2000 grains for each one. 146

Table 6.10: Correlation matrix showing 3D and 2D sphericity parameters (obtained from projections oriented along the minor principal axis). Merged data for Hostun and Caicos, 2000 grains for each one. 146

Table 6.11: Statistics of the 3D shape descriptors for the two sands at the critical state on 2000 grains 150

Table 7.1: Pearson's correlation coefficients between the measured particles rotations (9% axial shortening) and the local porosity computed at the initial state with the known shape parameters for Caicos (a) and Hostun (b) sands. 182

Table 7.2: Pearson's correlation coefficients between the measured particles rotations and the local porosity (both measured at 9% axial shortening) with the known shape parameters for Hostun sand both outside (a) and inside (b) the shear band. 183

Table 7.3: Pearson's correlation coefficients between the measured particles rotations and the local porosity (both measured at 9% axial shortening) with the known shape parameters for Hostun sand both outside (a) and inside (b) the shear band. 184

Table 8.1: Parameters and input variables employed in the DEM simulations on Hostun, Caicos and Ottawa sands. 209

Table 8.2: Drained triaxial compression tests performed in this chapter. The relative density and porosity of each experimental/numerical test are reported. The symbol (*) means that a denser specimen could not be generated for the DEM simulation. 209

Table 9.1: Boundary conditions that can be applied by the ISMES calibration chamber 222

Table 9.2: List of DEM properties and parameters used by Butlanska (Butlanska, 2014) 224

Table 9.3: Drained triaxial compression tests performed on Ticino sand. The relative density and porosity of each experimental/numerical test are reported 231

Table 9.4: List of DEM properties and parameters used for the DEM-VCC CPT tests in this work 241

Table 9.5: Best fitting parameters for the numerical penetration curves. The representative values of qc, exp were selected at 50% of the total penetration depths.241

Table 9.6: Cases of study. Three different situations of frictions ball-ball, ball-tip, ball-shaft are considered in the parametric study. 244

Table 9.7: Scenarios that are considered for the parametric study of particle shape effects 246

Part I: Introduction and State of the Art

1 Introduction

1.1 Research motivation

In-situ soil testing is a very important branch of geotechnical engineering. While laboratory tests are executed on soil samples extracted from the field, *in-situ* tests are tests conducted on or in the soil at the site. Examples of *in-situ* tests are the Standard Penetration test (SPT), the Cone Penetration Test (CPT), the Flat Dilatometer Test (DMT), the Prebored Pressumeter Test (PMT) and the Vane Shear Test (VST).

There are many advantages to conducting *in-situ* geotechnical tests, for example, they allow (a) testing larger volumes of (undisturbed) soil, (b) recording continuously soil parameters with depth considering stratigraphy, (c) testing soils in which sampling is hard to perform, (d) faster and economical soil characterisation compared to laboratory tests. However, the interpretation of the testing results is a boundary value problem that is not easy to formulate and to solve mathematically in a rigorous manner. Moreover, the disturbance induced in the soil by the testing instruments permits only an empirical interpretation of the test results.

Calibration Chambers have been therefore developed to simulate full-scale *in-situ* tests in the laboratory, in which the sample size, properties and the boundary conditions are known *a priori*. Such equipment can be hence used to establish correlations between test results and geotechnical parameters of the soil, in order to calibrate the interpretations of *in-situ* tests. However, calibration chamber testing is extremely expensive and time consuming. Few calibration chambers exist around the world and each test requires the preparation of several tons of soil. Therefore, numerical models can provide an efficient alternative to simulate physical experiments in a computer, but numerical models need to be calibrated as well, though in a completely different way.

The initial motivation for this doctoral thesis was to improve the Cone Penetration Test (CPT) simulations performed in a Virtual Calibration Chamber (VCC) using DEM (*Distinct Element Method*) by Joanna Butlanska in her PhD thesis (Butlanska, 2014). As indicated in the recommendations for future work of her dissertation, she envisaged two main lines of future research. The first one was to include a particle-crushing model in the DEM simulations. This task has been successfully carried out by Ciantia who implemented a crushable double-porosity model in PFC framework, achieving satisfactory results (Ciantia et al., 2019a, 2015). The second issue was regarding particle rotations. All the DEM simulations there presented (Butlanska, 2014) were done with rigid spheres with inhibited particle rotations, in order to represent the angular shape of Ticino sand grains, as originally proposed -and still suggested- by Calvetti (Calvetti, 2008; Calvetti et al., 2004, 2003). Although the macro results were always satisfactory when compared with experimental data, this approach seemed unnecessarily reductive.

The current doctoral work here presented aims to overcome this limitation. A novel DEM contact that allows particle rotations, but also to consider particle shape effects is proposed. It is extensively described in the thesis that there are several techniques to run DEM simulations taking particle shape into account. Nowadays, the increment of computing power allows representing numerical particles with the exact shape of the physical grains. In a first approximation, this would seem the best approach to tackle the problem of particle shape in DEM. However, a geotechnical engineer with experience in DEM modelling may dissent. In some circumstances, for instance for large-scale geotechnical problems, it is important to consider a large number of particle. This is achievable only if spherical particles -for which the contact detection is very efficient- are used. When CPT DEM simulations are performed, it is essential to guarantee a high number of contacts between the cone and the granular material simulated. Therefore, a rolling resistance contact model is exploited to add rotational constrains at the contacts able to mimic particle shape effects without dramatically affect the computational time. However, this is not a straightforward operation. In this work, the resisting moments are applied depending on -beside other quantities- the shape of the particles in contacts. A systematic and exhaustive study about the quantification of particle shape is necessary and it is the starting point of this doctoral work. Moreover, an in-depth investigation about the influence of particle shape on the kinematics of shearing granular materials has to be made. This knowledge will be then used to calibrate the proposed DEM rolling resistance contact model, that was thereafter successfully validated under different conditions.

The contact detection remains economical and advanced algorithms are not required, maintaining low the computational time. This will open new possibilities to the use DEM for studying engineering applications at larger scales, especially in geotechnical problems in which the particulate nature of the soil cannot be ignored.

1.2 Aim & Objectives

The specific goals for this doctoral work are:

- Develop efficient and reliable image analysis algorithms to quantify the shape of thousands of sand particles in three dimensions;
- Measure accurately the kinematics (*i.e.,* displacements and rotations) of single grains during standard geotechnical tests by using *Digital Volume Correlation* (DVC);
- Understand the influence of particle shape on the kinematics of sheared granular materials exploring the statistical relation existing between shape and rotations of single grains;
- Select an appropriate DEM rolling resistance contact model to use as starting point for all the numerical simulations;
- Calibration and validation of a new advanced DEM rolling resistance contact model (*i.e.,* the resisting moment at each contact) based on the measured shape of particles in contact; able to represent particle shape effects in an efficient way, albeit respecting the measured kinematics at failure;

- Exploit the newly proposed DEM contact model to simulate large-scale geotechnical tests as the CPT test performed in a Virtual Calibration Chamber (VCC), reproducing physical experiments;
- Investigate numerically the effect of particle shape on the CPT tip and shaft penetration resistance.

1.3 Outline of the thesis

Each chapter starts with introductory remarks to recall some of the main aspects of the topic and to set the context for the following discussions. At the end of each chapter, the main outcomes are recapitulated in a concise summary. The main body of the text is divided in five parts, which gather ten chapters plus appendices as follows.

- *Part I: Introduction and State of the Art*

Chapter 1 presents the motivations behind this research doctoral project and the objectives to attain.
Chapter 2 details how the shape of soils particles has been historically measured and quantified in two and three-dimensions.
Chapter 3 describes the influence of particle shape on geotechnical properties observed during laboratory and field tests.
Chapter 4 presents the fundamentals of the Distinct Element Method (DEM) with particular focus on how particle shape is treated in previous researches.

- *Part II: Experimental dataset and image analysis*

Chapter 5 aims to describe in details the employment of x-rays microtomography for soil mechanics purposes. Moreover, the experimental data used as starting point for this doctoral work is presented, as well as the basis of image analysis.

Chapter 6 explains how the shape of a particle can be analysed and quantified in three-dimensions. The statistical correlations between three and bi-dimensional shape description are presented.
Chapter 7 describes the use of 3D Digital Volume Correlation (DVC) for particle tracking. The observed relation between particle shape and rotations is also illustrated and explained.

- *Part III: Numerical Simulations*

Chapter 8 introduces the rolling resistance contact model that is centrepiece of this doctoral project, detailing the microscopic calibration and relative validation under different conditions.
Chapter 9 explores the newly proposed contact model for large-scale Dem simulations, as the CPT test performed in a Virtual Calibration Chamber (VCC).

- *Part IV: Conclusions*

Chapter 10 summarizes the achievements, the lessons learned and presents suggestions for future work.

- *Part V: Appendices*

Appendices give complementary information that is too extensive to be included in the document's main body. The interested reader can consult them for further information on specific topics.
Appendix A lists the python scripts developed for the image analysis studies as well as the PFC scripts for the DEM simulations.
Appendix B provides some information about the dataset that has been used in this work. The most relevant data is available in open-access.

Appendix C presents an equation to estimate the number of particles involved in DEM simulations performed in a cylindrical chamber.

2

Experimental Description of Particle Shape

2.1 Introduction

It has been extensively shown in the geotechnical literature that particle shape has a significant influence on granular soil behaviour. However, even if such influences are generally acknowledged they remain very difficult to quantify and measure. Since the early 1900's, several authors tried to characterise the grain shape and to understand its influence on the overall soil behaviour. Among the most important, Wadell (Wadell, 1932) introduced the concept of "sphericity" that quantifies how a particle differs from a sphere, in terms of surface area. Krumbein (Krumbein, 1941) created the first chart to visually estimate shape from the grain length ratios ("flatness" and "elongation" indices). This and similar works were difficult to apply and develop, because particle shape measurements typically made by hand or eye, were tedious and not objective.

In recent years, this unsatisfactory situation has changed significantly. In particular, computer-based automated or semi-automated image analysis techniques are replacing measurements made by hands or eyes. Moreover, as computer performance increases, it has become increasingly feasible to move from the analysis of two-dimensional measurements -ultimately based on particular planar projections of volumes- to fully three-dimensional measurements. Taking profit of this to fully characterise grain shape, new 3D shape descriptors able to capture the tri-dimensional nature of particles have been recently developed.

The next Section gives an overview of how the shape of granular soil particles has been historically studied and described in literature: tracing the development from the bi-dimensional projection approaches of the 1920s, to the three-dimensional computational methods existing nowadays. While doing that the main terminology used on particle shape studies is introduced.

2.2 Shape characterization

Particle shape characterization can be based on two-dimensional or three-dimensional descriptors. Bi-dimensional shape descriptors can be obtained from the projection of a particle on a plane, that results is a particle outline drawn on a specified plane. The advantage of 3-D shape characterization is evident: a single 3D parameter can fully describe one aspect of the particle shape (*i.e.*, *sphericity*) whereas in bi-dimensional studies, a list of 2D parameters measured onto several projection planes is required. For example, a cylinder presents completely different outlines depending on the orientation of the projection plane. On the other hand, bi-dimensional studies are less demanding in terms of equipment. Even the naked eye can be employed to obtain two-dimensional shape data, whereas a three-dimensional image of a particle is much more difficult to obtain. It requires sophisticated equipment to scan the particles (*i.e.*, x-rays tomography) and to create and study a 3-D model of the grain.

Particle shape studies can be also organized according to the relative scale of analysis. Barret (Barret, 1980) defined shape as the combination of three *independent* aspects in function of the scale at which they are evaluated: *morphology/form*, measured at large scale, *roundness*, measured at the intermediate scale, and *surface texture*, measured at small scale. The three aspects are represented in Figure 2.1. The term "independent" in this context means that one aspect can change without affecting the others. The independence of the three aspects just described has been traditionally assumed, although recent approaches (e.g. Zhou et al. 2015) use functional bases to obtain a rigorous set of independent descriptors. These approaches, well suited to computer-based storage and reconstruction of grain images, will not be considered here in detail.

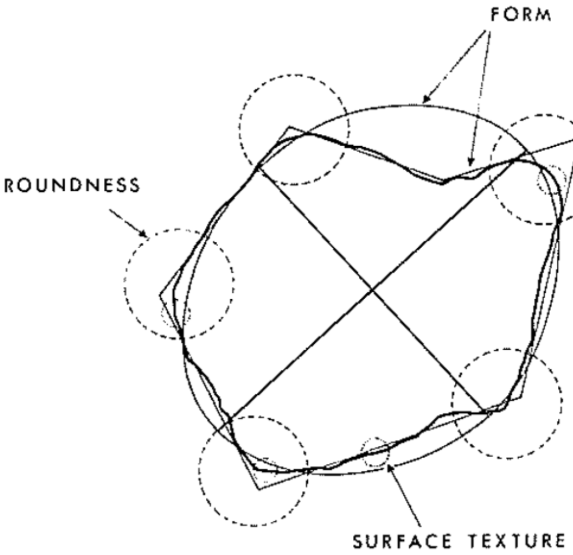

Figure 2.1: Three independent aspects of shape (Barret, 1980)

2.2.1 Form (or morphology)

At large scale the particle lengths (*a, b* and *c,* respectively the major, intermediate and minor axis dimension of the particle) are the most important ingredients for defining the overall morphology of a particle. Simply calculating their ratio, it is possible to quantify how a particle is *elongated* of *platy*, which is a first approach to characterise the form of the particle, irrespective of the sharpness of edges and corners. However, the most used term for shape description at large scale is *"sphericity"*.

Sphericity is the measure of the degree of conformity of particle shape to that of a sphere (circumference in 2D).

2.2.1.1 Two-dimensional form descriptors

A very large set of bi-dimensional descriptors of shape have been historically used. This dissertation is based on a three-dimensional study of particle shape, therefore only a short review of 2D descriptors is presented here. In particular, the descriptors listed below are defined in (ISO, 2006), and based on a 2D projection of a 3D particle.

The *Feret diameters* are defined as the distance between two parallel tangents to the particle outline. There are infinite parallel tangents that can be chosen, but only two of them are relevant: the *maximum Feret diameter,* also called the *maximum distance* in some references, is defined as the furthest distance between any two parallel tangents on the particle. Likewise, the *minimum Feret diameter,* also called the *minimum distance,* is defined as the shortest distance between any two parallel tangents on the particle.

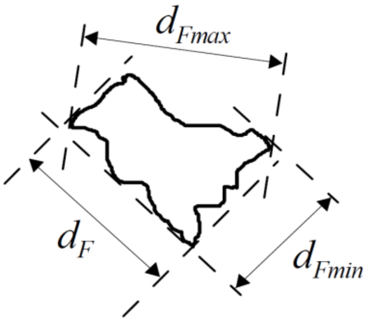

Figure 2.2: Feret diameters of a particle outline

The *aspect ratio (AR)* is the ratio of the Feret minimum length (d_{Fmin}) to the Feret maximum length (d_{Fmax}) as given in Equation (2.1). This is done to scale the aspect ratio such that the value is always in the range $0 < AR < 1$.

$$AR = \frac{d_{Fmin}}{d_{Fmax}} \tag{2.1}$$

The terminology of the following form descriptors is taken from Zheng and Hryciw (Zheng and Hryciw, 2016).

Area sphericity (s_a) is the ratio between the squares of the diameter (d_n) of the equivalent (same area as the particle) circle and the diameter (d_{cm}) of the maximum circumscribing circle.

Diameter sphericity (s_d) is the square root of *area sphericity*.

Circle ratio sphericity (s_c) is the ratio between the diameter of the maximum inscribed circle (d_{iM}) and the diameter of the minimum circumscribed circle (d_{cm}).

$$s_c = \frac{d_{iM}}{d_{cm}} \tag{2.2}$$

Perimeter sphericity (s_p) is a measure of the degree of conformity of a particle outline (having area a_n and perimeter *p)* to that of a circle. It is defined as the ratio between the perimeter (p_n) of the circle with the same area of the particle and the perimeter of the particle (p)

$$s_p = \frac{p_n}{p}\,. \tag{2.3}$$

KS sphericity (s_{KS}) is defined as the ratio between the minimum (d_1) and maximum (d_2) dimensions of the particle, originally proposed by (Krumbein and Sloss, 1951) and defined as

$$s_{KS} = \frac{d_2}{d_1}\,.$$

2D Convexity (Co-2D) is the measurement of the overall concavity of a particle. It is defined as the image area, a_n, divided by the convex hull area, a_{CH}, as given in Equation (2.4). Thus, as the particle becomes more solid, the image area and convex hull area approach each other, resulting in a solidity value of one. However, as the particle form digresses from a closed circle, the convex hull area increases and the calculated convexity decreases.

$$\text{Co-2D} = \frac{a_n}{a_{CH}} \tag{2.4}$$

Name	Symbol	Formula
Aspect Ratio	AR	$AR = \frac{d_{Fmin}}{d_{Fmax}}$
Area sphericity	s_A	$s_A = \frac{d_n^2}{d_{cm}^2}$
Diameter sphericity	s_D	$s_D = \frac{d_n}{d_{cm}} = \sqrt{s_A}$
Circle ratio sphericity	s_C	$s_D = \frac{d_{iM}}{d_{cm}}$
Perimeter sphericity	s_P	$s_P = \frac{p_n}{p}$
KS sphericity	s_{KS}	$s_{KS} = \frac{d_2}{d_1}$
2D Convexity	*Co-2D*	$Co\text{-}2D = \frac{a_n}{a_{CH}}$

Table 2.1: 2D form parameters, terminology following (Zheng and Hryciw, 2015)

Shape property	Symbol	Equivalent diameter	Equivalent perimeter
Feret's minimum diameter	d_{Fmin}		
Feret's maximum diameter	d_{Fmax}		
Projected area	a_n	d_n	p_n
maximum & minimum dimensions of projected area	d_1, d_2		
Diameter of minimum circumscribing circle	d_{cm}		
Diameter of maximum inscribed circle	d_{iM}		
Projected perimeter	p		
Area of the convex hull	a_{CH}		p_{CH}

Table 2.2: Fundamental measures from which 2D sphericity proxies are derived

2.2.1.2 Three-dimensional form description

Wadell was one among the first authors to study and quantify particle shape. Still today, Wadell's shape descriptors are widely used or taken as reference for comparisons with new ones. Wadell (Wadell, 1932) choose the sphere as standard and defined "*degree of true sphericity (ψ)*" as the as the ratio of the area (s_n) of a sphere with the same volume as the particle (V) to the particle surface area *(S)*.

$$\psi = \frac{s_n}{S} = \frac{\sqrt[3]{36\pi V^2}}{S} = true\ sphericity \qquad (2.5)$$

Although the definition was clear, this index has seen very little use because measuring the surface area on irregular particles is difficult. Only in recent years, the use of computer algorithms has made this task feasible (Fonseca et al., 2012; Hayakawa and Oguchi, 2005; Komba et al., 2013; Zhou et al., 2015). An interesting feature of this index is that, although it was originally proposed as a form descriptor, it is also sensitive to smaller scale features, like those associated with roundness, as long as those are captured by the measurement of particle surface area.

Krumbein (Krumbein, 1941) proposed another definition of sphericity, more suitable for operational purposes, as the ratio of the particle volume (V) and the volume of the minimum circumscribed sphere (V_{cm}), or equivalently, as the ratio of the diameter (D_n) of the sphere having the same volume as the particle diameter and that (D_{cm}) of the minimum circumscribed sphere. This value will be named in this work as "*operational sphericity*" and denoted by.

$$\psi_{op} = \sqrt[3]{\frac{V}{V_{cm}}} = \left[\frac{\left(\frac{\pi}{6}\right) D_n{}^3}{\left(\frac{\pi}{6}\right) D_{cm}{}^3}\right]^{\frac{1}{3}} = \frac{D_n}{D_{cm}} \approx \frac{D_n}{a} = operational\ sphericity \tag{2.6}$$

Equation (2.6) is more straightforward to apply than equation (2.5) because D_n and D_{cm} are easier to get rather than the particle surface area. D_{cm} has often been substituted by the major particle axis (a) for faster calculation (Krumbein, 1941).

As reported by Cavarretta (Cavarretta, 2009), the value of operational sphericity obtained from equation (2.6) cannot be considered as an exact alternative to true sphericity (ψ) and usually the two values differ. For example, the degree of true sphericity of a cube is 0.877, but its operational sphericity is 0.716.

Moreover, the relation between true and operational sphericity is not one-on-one. Indeed, all the particles having a given volume V (and therefore a given D_n) and a given D_{cm} have the same value of operational sphericity, which is not necessarily the case for true sphericity.

An alternative approximation is given by *intercept sphericity*, defined as (Krumbein, 1941) by:

$$\psi_{int} = \left[\frac{bc}{a^2}\right]^{\frac{1}{3}} = intercept\ sphericity \tag{2.7}$$

Zingg (Zingg, 1935) developed a more versatile shape characterisation based on relations amongst the three particle axes. Particles are classified into four class categories, as shown in Figure 2.3. The ratios between the particle axes are usually called in literature the "*flatness index*" and "*elongation index*", defined as:

$$flatness\ index = FI = \frac{shortest\ axis}{intermediate\ axis} = \frac{c}{b} \tag{2.8}$$

$$elongation\ index = EI = \frac{intermediate\ axis}{longest\ axis} = \frac{b}{a} \tag{2.9}$$

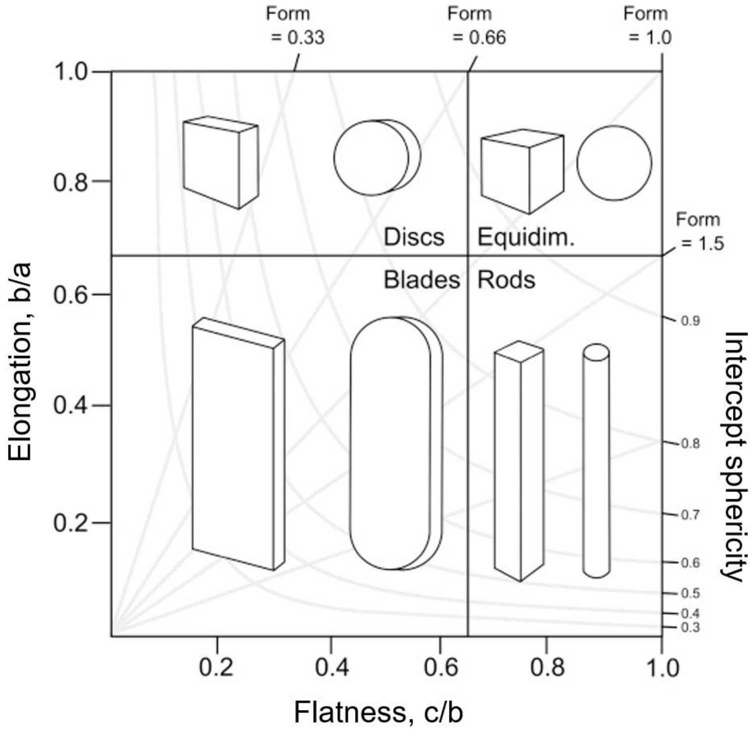

Figure 2.3: Zingg's shape classification based on the flatness and elongation indexes (Krumbein 1941) and relation between "intercept sphericity" and Zingg's classification (Krumbein and Sloss, 1963)

Flatness and elongation uniquely define intercept sphericity. Indeed *intercept sphericity* Eq. (2.7) may then be plot onto Zingg's chart Figure 2.3 as a family of hyperbolae with asymptotes the axis $b/a = 0$ and $c/b = 0$. Intercept sphericity can indeed also be defined as:

$$\psi_{int} = \sqrt[3]{\frac{bc}{a^2}} = \sqrt[3]{FI(EI)^2} = intercept\ sphericity \tag{2.10}$$

One of the most important outcomes of this comparison is that it clearly shows how particles having different form (e.g. disks and rollers) may have the same intercept sphericity. As Cavarretta (Cavarretta, 2009) notes: "*this lack of uniqueness seems more dependent on the ….simplification introduced in the definition of the intercept sphericity than a real feature of a 3D shape*".

Cailleux (Cailleux, 1945) developed his form index based upon the relationship between the particle dimensions along the three principal axes. The index is given by:

$$F_{cailleux} = \frac{a+b}{2c} \tag{2.11}$$

The index ranges from a minimum value of 1 for an equant particle and becomes progressively larger the flatter the particle. There is no maximum limit.

Aschenbrenner (Aschenbrenner, 1956) proposed another definition, called *working sphericity*, ψ_{work}:

$$\psi_{work} = \frac{12.8\sqrt[3]{\left(\frac{c}{b}\right)^2\left(\frac{b}{a}\right)}}{1+\left(\frac{c}{b}\right)\left(1+\frac{b}{a}\right)+6\sqrt[2]{1+\left(\frac{c}{b}\right)^2\left(1+\left(\frac{b}{a}\right)^2\right)}} = working\ sphericity \tag{2.12}$$

Sneed and Folk (Sneed and Folk, 1958) developed a different sphericity index, the *maximum projection sphericity*, ψ_{mps} , which they believed represented the hydrodynamic behaviour of particles in a fluid. The maximum projection sphericity of a particle is given by the equation:

$$\psi_{mps} = \left[\frac{c^2}{ab}\right]^{\frac{1}{3}} = maximum\ projection\ sphericity \tag{2.13}$$

Equation (2.13) is represented in the sphericity-form diagram of Sneed and Folk (1958) in Figure 2.4. As in the case of the Zingg's diagram Figure 2.3, lines of equal maximum projection sphericity span several form fields in the diagram.

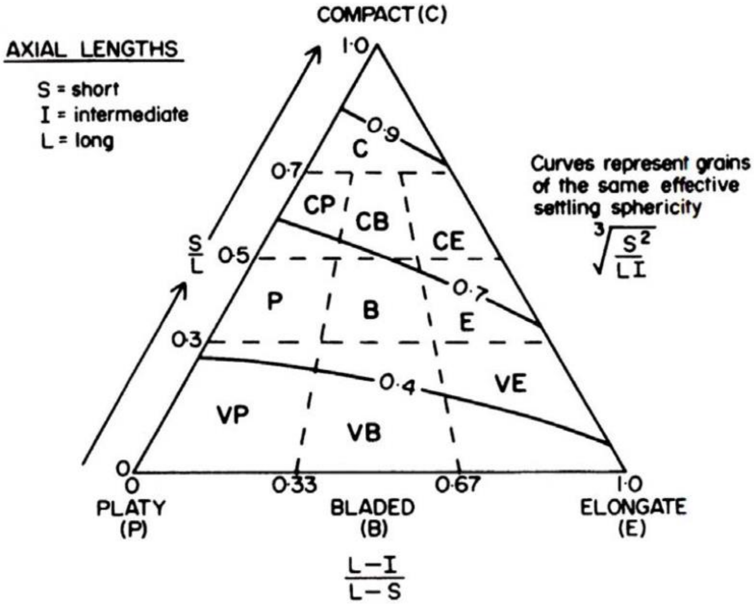
AXIAL LENGTHS
S = short
I = intermediate
L = long
COMPACT (C)
1·0
0·9
C
0·7
CP
CB
CE
S/L
0·5
P
B
0·7
E
0·3
0·4
VE
VP
VB
0
0
0·33
0·67
1·0
PLATY (P)
BLADED (B)
ELONGATE (E)
L−I / L−S
Curves represent grains of the same effective settling sphericity
∛(S²/LI)

Figure 2.4: Sphericity-form diagram of Sneed and Folk (1958) (from (Lewis and McConchie, 1994)).

Recently, new sphericity definitions have been proposed. Alshibli (Alshibli et al., 2015) defined the *sphericity index* (ψ_{al}) as the ratio between the volume (V) of the particle and the volume ($V_{d=c}$) of a sphere with a diameter equal to the shortest particle axes (c).

$$\psi_{al} = \frac{V}{V_{d=c}} \tag{2.14}$$

Jerves (Jerves et al., 2016) used the ratio between the diameters of the maximum inscribed (D_{cm}) and the minimum circumscribed spheres (D_{iM}) to describe sphericity. This value is usually referred as *irregularity* (IR_{2D}) in 2D analysis, where circles are used instead of spheres (Chapter 2.2.1.1).

$$IR_{3D} = \frac{D_{iM}}{D_{cm}} = irregularity3D \tag{2.15}$$

Other parameters along this line but requiring the use of more advanced 3D shape capture procedures are convexity and solidity. Both use the definition of *convex hull*, which is the minimal convex polytope (generalised polyhedron) covering of a 3-D object, as used by Fonseca (Fonseca et al., 2012). *Solidity* ($So3D$) can be defined as the ratio of the surface areas of the convex hull (S_{CH}) of the boundary and the original boundary (S).

$$So3D = \frac{S_{CH}}{S} \tag{2.16}$$

Convexity (Co3D) is defined as the ratio between the volume of the particle (V) and the volume of the convex hull bounding the particle (V_{CH})

$$Co3D = \frac{V}{V_{CH}} \tag{2.17}$$

Both the parameters range from zero to one (for a perfect convex grain).

Table 2.3 and Table 2.4 store respectively the 3D form descriptors and the fundamental measures from which they are derived.

Name	Symbol	Definition	Reference
True Sphericity	Ψ	$\frac{s_n}{S}$	(Wadell, 1932)
Operational Sphericity	Ψ_{op}	$\sqrt[3]{\frac{V}{V_{cm}}} = \frac{D_n}{D_{cm}} \approx \frac{D_n}{a}$	(Krumbein, 1941)
Intercept Sphericity	Ψ_{int}	$\sqrt[3]{\frac{bc}{a^2}} = \sqrt[3]{FI\left(EI\right)^2}$	(Krumbein, 1941)
Flatness index	FI	c/b	(Zingg, 1935)
Elongation index	EI	b/a	(Zingg, 1935)
Form Cailleux	$F_{cailleux}$	$\frac{a+b}{2c}$	(Cailleux, 1947)
Working Sphericity	Ψ_{work}	$\frac{12.8\sqrt[3]{\left(\frac{c}{b}\right)^2\left(\frac{b}{a}\right)}}{1+\left(\frac{c}{b}\right)\left(1+\frac{b}{a}\right)+6\sqrt[2]{1+\left(\frac{c}{b}\right)^2\left(1+\left(\frac{b}{a}\right)^2\right)}}$	(Aschenbrenner, 1956)
Maximum projection sphericity	Ψ_{mps}	$\left[\frac{c^2}{ab}\right]^{\frac{1}{3}}$	(Sneed and Folk, 1958)
Alshibli Sphericity	Ψ_{al}	$\frac{V}{V_{d=c}}$	(Alshibli et al., 2015)

Irregular-ity3D	IR_{3D}	$\frac{D_{iM}}{D_{cm}}$	(Jerves et al., 2016)
Convexity	$Co3D$	V/V_{CH}	(Fonseca et al., 2012)
Solidity	$So3D$	$\frac{S_{CH}}{S}$	

Table 2.3: Three dimensional form descriptors (see Table 2 for symbol definitions)

Shape property	Symbol	Equivalent diameter
Volume	V	D_n
Surface area	S	
Surface area of the equivalent sphere (same volume)	s_n	
Maximum, intermediate, minimum lengths	a, b, c	
Convex hull volume	V_{CH}	D_{CH}
Convex hull surface area	S_{CH}	
Volume of the maximum inscribed sphere	V_{iM}	D_{iM}
Volume of the minimum circumscribing sphere	V_{cm}	D_{cm}
Volume of the sphere with diameter the minimum length	$V_{d=c}$	c

Table 2.4: Fundamental measures from which 3D shape descriptors are derived

Other form and shape factors have been widely used in literature by several authors. Among the most important ones:

- $shape\ factor = \frac{c}{\sqrt{ab}}$ (Blott and Pye, 2008) (2.18)
- $shape\ factor = \begin{cases} 1 - \frac{ac}{b^2} & if \quad b^2 > ac \\ \frac{b^2}{ac} - 1 & if \quad b^2 \leq ac \end{cases}$ (Williams, 1965) (2.19)
- $form\ factor = \frac{c}{\sqrt{\frac{a^2+b^2+c^2}{3}}}$ (Janke, 1966) (2.20)

- $oblate - prolate\ index = \frac{10\left(\frac{a-b}{a-c}-0.5\right)}{\frac{c}{a}}$ (James E. Dobkins, Jr., 1970) (2.21)
- $shape\ factor = \frac{ac}{b^2}$ (Aschenbrenner, 1956) (2.22)
- $shape\ factor\ F = \frac{flatness\ ratio}{elongation\ ratio} = \frac{c/b}{b/a}$ (Lees, 1964) (2.23)

In other articles (e.g., (Zhao and Wang, 2016) and (Alshibli et al., 2015), as well as the manual of the image analysis Software ImageJ Fiji[1]), another parameter is mentioned using different names, here it will be called "$FormFactor3D$", defined as:

$$FormFactor3D = \frac{6\pi^{\frac{1}{2}}V}{S^{1.5}} \tag{2.24}$$

Where S is the particle surface area and V its volume.

2.2.2 Roundness

Roundness typically refers to second order approximations of shape, reflecting the variations on particle corners. Historically sphericity was treated as a three-dimensional concept, whereas roundness was only obtained by considering plane projections.

Wadell (Wadell, 1932) argued that roundness was a property independent on sphericity, but he was opposed by Wentworth (Wentworth, 1933). Wadell (Wadell, 1933) responded that a solid may possess a maximum degree of roundness and still not be a sphere, or have a high degree of sphericity and no roundness. He used Figure 2.5 to explain this concept.

---

[1] Open-source image processing package widely used in this work for image analysis.

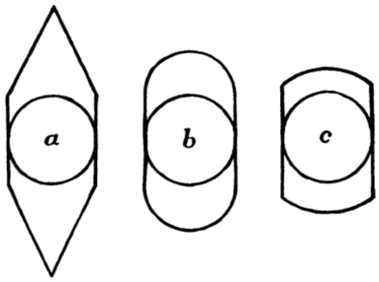

Figure 2.5: Illustration of the conception "roundness" (Wadell, 1932)

In stage "a" the particle has two sharp corners. Then, stage "a" evolves in stage "b" *(e.g.* because of erosion) where the extremities have reached the maximum degree of roundness, and finally it reaches stage "c" in which new corners are generated and roundness decreases. So, Wadell considered the ratio r/R_0 as descriptor of the roundness of the surface at a given point, where r is the corner's radius of curvature and R_0 the radius of the maximum inscribed sphere.

Since the radius of curvature of a corner may attain any value up to the maximum (which equals the value of the maximum inscribed circle), Wadell defined the *degree of roundness* as the arithmetic mean of the roundness of the individual corners in that plane, as in Equation (2.25).

$$degree\ of\ roundness = \frac{\sum_{i=1}^{N}\left(\frac{r_i}{R_0}\right)}{N} \tag{2.25}$$

Where N is the number of corners of radius r_i.

The degree of roundness thus defined has some evident inadequacies. Firstly, only the convex corners of the outline are considered in Eq. (2.25). Furthermore, if the particle is scaled up, the mean radius of curvature increases and vice-versa. In particular, at the smallest scale, a protruded mineral crystal may provide a highly curved corner, although it does not reflect gravel roundness.

Therefore, Wadell's roundness is a *scale dependent* parameter, contrary to sphericity. Measurement of roundness has always presented difficulties and the roundness definition has been controversial, especially because of its scale dependence.

Wentworth (Wentworth, 1919) proposed the ratio of the diameter (D_S) of the circle fitting the sharpest corner to the diameter (D_X) of the particle through that point, as in Eq. (2.26).

He later changed the divisor to the average of the long (L) and short (S) diameter of the particle in the maximum plane of projection (Wentworth, 1922), as in Eq. (2.27).

$$roundness\ of\ sharpest\ corner\ \text{(Wentworth, 1919)}\ = \frac{D_S}{D_X} \tag{2.26}$$

$$roundness\ of\ sharpest\ corner\ \text{(Wentworth, 1922)}\ = \frac{D_S}{(L+S)/2} \tag{2.27}$$

Cailleux (Cailleux, 1947) proposed a similar measure of roundness, expressed as the ratio between the radius of the most convex part and the longest axis, and many other authors proposed similar definitions (i.e. (Kuenen, 1956), (James E. Dobkins, Jr., 1970) (Swan, 1974)).

The application of these definitions of roundness (and shape) has been done traditionally by means of visual comparison with standard charts. Powers (Powers, 1953) developed a chart of reference using physical particles of different shapes. The chart offers a quick and easy way to estimate two-dimensional particle shape, based on six classes of roundness in which two classes of sphericity were considered, as in Figure 2.6.

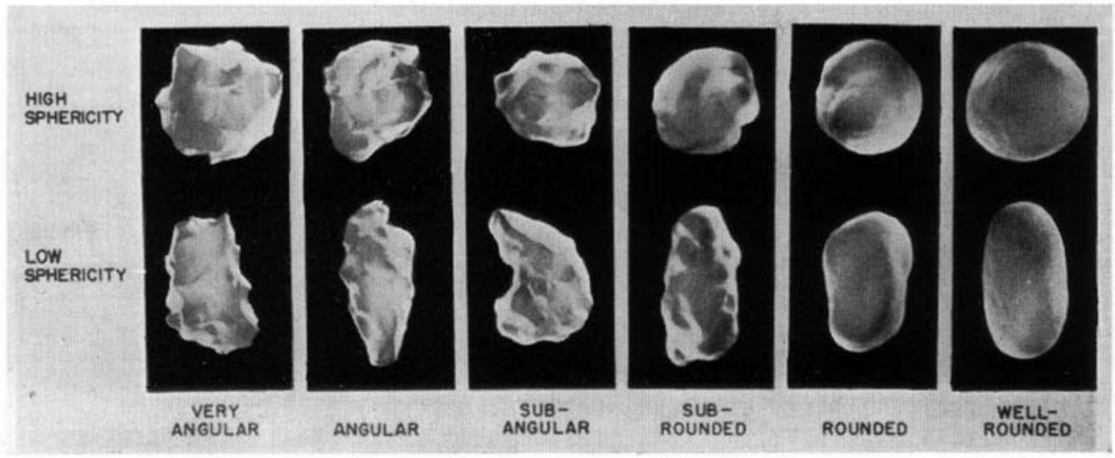

Figure 2.6: Power's chart for shape classification (Powers, 1953)

However, any comparing chart to describe particle shape has a high degree of subjectivity. Folk (Folk, 1955) claimed that when charts are used for classification, the risk of getting errors is negligible for sphericity but large for roundness.

Krumbein (Krumbein and Sloss, 1963) proposed another chart which had great impact on later studies of shape (Figure 2.7). Based on visual estimation of the particle shape, the chart provides the values of sphericity and roundness, scaled from 0 to 1.

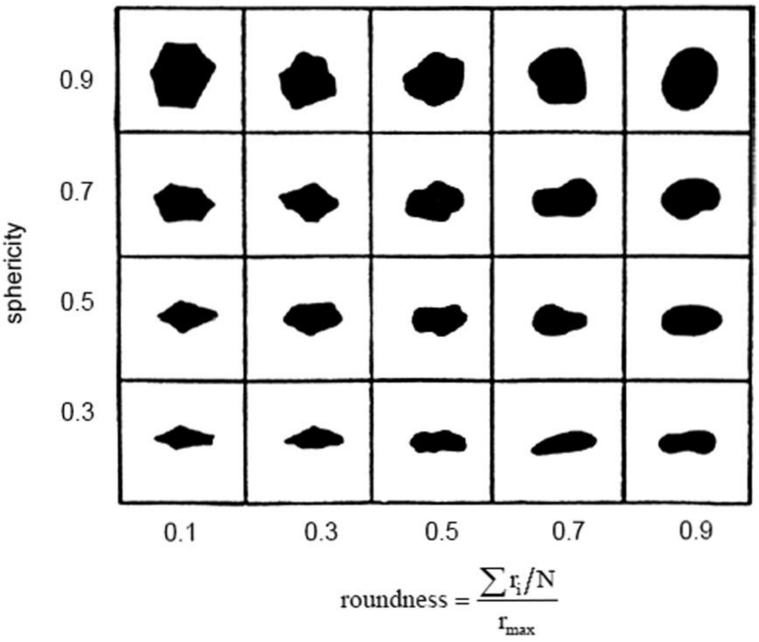

Figure 2.7: Chart used to characterise sphericity and roundness of particles (Krumbein and Sloss, 1963)

Some authors (*e.g.*, (Zheng and Hryciw, 2016) (Altuhafi et al., 2012) developed computational methods in order to replace the slower and un-objective chart methods, although always based on bi-dimensional projections. Beyond subjectivity, bi-dimensional roundness parameters also suffer from lack of uniqueness, as they are strongly dependent on the selected projection direction. Although the problem may be reduced by tight specification of the projection method. This can be for example projecting grains in order to minimise the projected area (a_n) or projecting grains lying on their plane of "greatest stability", that means with the minor length perpendicular to the horizontal plane). A fundamental alternative is to use 3D descriptors - which, of course, requires different image acquisition techniques. Along this line, some new three-dimensional descriptors of roundness have been recently defined.

Al-Raush (Al-Raoush, 2007) proposed another roundness index called:

$$I_R^P = \frac{S}{4\pi\left(\frac{D_{min}^p + D_{max}^p}{4}\right)^2} \tag{2.28}$$

Where S is the surface area of the particle p and D_{min}^p and D_{max}^p are respectively the minimum and maximum particle length. The surface area was here computed summing up the areas of the external faces of the external voxels. However this approach overestimates the measure of surface area.

Druckrey (Druckrey et al., 2016) slightly modified Eq. (2.28) in Eq. (2.29).

$$I_R = \frac{S}{4\pi\left(\frac{a + b + c}{6}\right)^2} \tag{2.29}$$

The denominator of Eq. (2.29) represents the surface area of a sphere having diameter equal to the average of a, b and c. I_R equals unity for a particle without asperities on the surface and having the same surface area as a sphere with an equivalent grain diameter.

Zhao (Zhao and Wang, 2016) used x-rays tomography to measure particle morphology. He claimed that existing 3D roundness indexes do not involve corner identification and curvature evaluation, so he proposed a novel method to evaluate 3D roundness based on the local curvatures on the reconstructed triangular surface mesh. A similar approach was also used by (Nadimi and Fonseca, 2017). The interest in this new method is that it goes back to the original idea of roundness proposed by Wadell (1932), but extending it to three dimensions.

To close this section it is worth mentioning another shape descriptor that mix aspects of form and roundness. Cho (Cho et al., 2006) proposed a new parameter called *regularity* (ρ) obtained by averaging the values of sphericity and roundness provided by the reference chart from Krumbein and Sloss (1963).

$$\rho = \frac{sphericity\ + roundness}{2} \tag{2.30}$$

They used this parameter for an exhaustive investigation about the influence of shape on the geotechnical properties, as it will later detailed in Chapter 3.

2.2.3 Surface Texture (roughness)

The third classical parameter of shape is measured at the smallest scale, the scale of the asperities. It is called *surface texture* (or *roughness*) and it has been long described by researchers but it always has been difficult to measure, however, the use of computer technology made this task realisable.

Roughness is a scale-dependent parameter, as well as roundness. As reported by Bhushan (Bhushan, 2001), a unique property of rough surfaces is that if a surface is repeatedly magnified, roughness is observed at every scale. In addition, the roughness at all scales present a simile structure, as shown in Figure 2.8, such behaviour can be characterized by fractal geometry. Therefore, when measurements of roughness are made, it should be specified which range of scales has been considered.

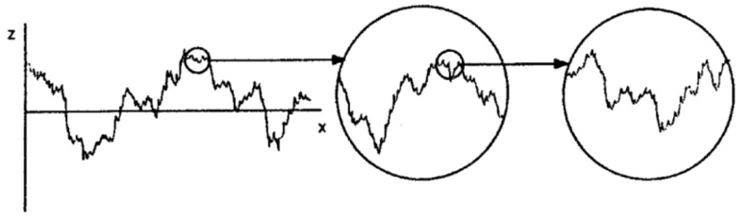

Figure 2.8: Self-affinity of a surface profile (Bhushan, 2001)

Several attempts have been done in the last century to quantify surface roughness. Wright (Wright, 1955) proposed a method to quantify the surface texture of particles of concrete aggregates. This method consisted in the direct comparison between the measures of the length of the particle profile (obtained using a map-measuring wheel) with the length of an unevenness line drawn as a series of chords. Similar approaches have been lately developed in rock mechanics to quantify the roughness of rock discontinuities (*i.e.*, JCR) (Barton and Choubey, 1977; Tse and Cruden, 1979), as shown in Figure 2.9.

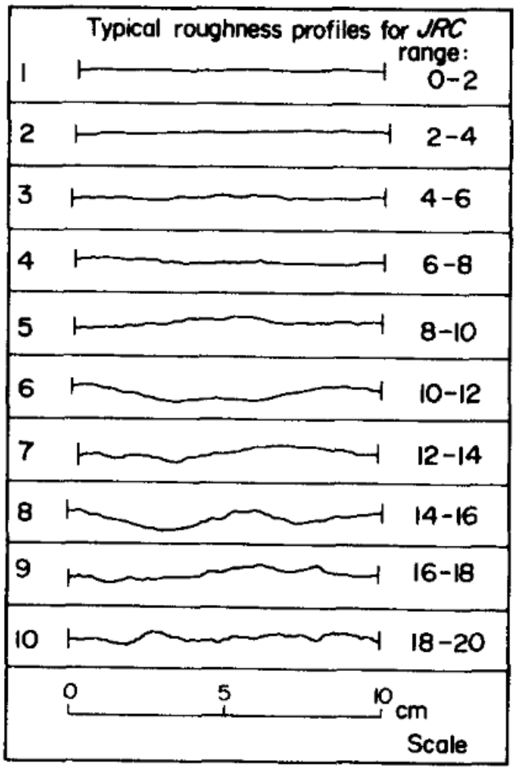
Typical roughness profiles for JRC range:
1
0-2
2
2-4
3
4-6
4
6-8
5
8-10
6
10-12
7
12-14
8
14-16
9
16-18
10
18-20
0
5
10
cm
Scale

Figure 2.9: Roughness profiles with relative JCR value (Barton and Choubey, 1977)

Some authors (*i.e.*, (Janoo, 1998) (Mora and Kwan, 2000) used the concept of convex hull (or perimeter in 2-D) for describing roughness, since a rough surface presents convexities at the small scale. Therefore, they claimed that the previously mentioned parameters *convexity* (Eq. (2.16)) and *solidity* (Eq. (2.17)) are suitable for measuring and quantifying roughness.

An alternative technique to measure roughness is to use an interferometer, capable of providing the optical profilometry of complex surfaces with a very high resolution of about 1 nanometre (Alshibli et al., 2015; Altuhafi and Coop, 2011; Cavarretta et al., 2010). An example of interferometer profile, from (Cavarretta, 2009), is shown in Figure 2.10.

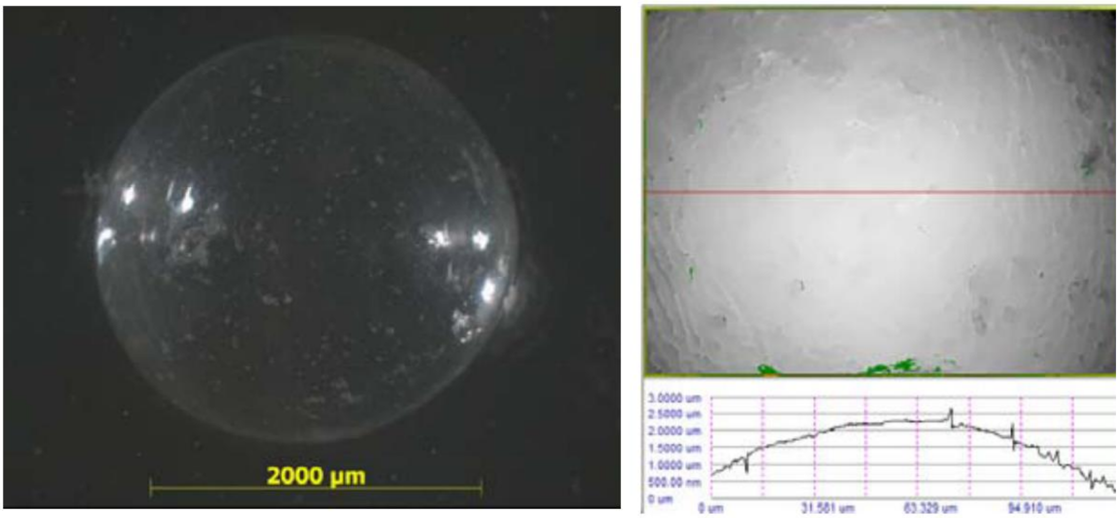

(a) *(b)*

Figure 2.10: Microscope image of glass ballottini (a) and relative surface texture profile measured by interferometer (b), from (Cavarretta, 2009)

An accurate measure of roughness is out of the scope of this dissertation, because the 3D images used in this study do not have the high resolution required to quantify properly the surface texture of sand particles.

2.3 Summary

In this Chapter, the state of the art of particle shape description in two and three dimension is reported. The main concepts can be summarised as follow:

- Particle shape has been historically quantified using 2-D descriptors and graphical charts (Krumbein and Sloss, 1963; Powers, 1953) but recent advances in computer power allow straightforward 3-D shape evaluations;
- According to Barret (Barret, 1980), particle shape is the combination of three *independent* aspects in function of the scale at which they are evaluated: *morphology/form*, measured at large scale, *roundness*, measured at the intermediate scale, and *surface texture*, measured at small scale.
- Wadell was one among the first authors to study and quantify particle shape. Still today, Wadell's shape descriptors are widely used or taken as reference for

comparisons with new ones. Wadell (Wadell, 1932) choose the sphere as standard and defined *"degree of true sphericity (ψ)"* as the as the ratio of the area (s_n) of a sphere with the same volume as the particle (*V*) to the particle surface area *(S)*.

- Roundness and roughness are scale-dependant parameters, therefore their use must be restricted to narrow ranges of particle size, which must be specified *a priori;*
- Particle roughness has not been studied in this current doctoral work.

3

Influence of particle shape on Geotechnical Properties

3.1 Introduction

The behaviour of granular soils depends on the re-arrangement of grains during loading. This re-arrangement is affected by particle shape, therefore particle shape plays an important role that must be investigated.

Small grains and large grains usually have different origin, the final shape depends on the material composition (mineralogy, chemical composition) but also the agent of transport affects grain shape. In particular, the shape of recently formed coarse grains firstly depends on the nature of the mother rock, then the size and shape can change with time because of mechanical and chemical effects: older sands tend to be more spherical and rounder. Moreover, large particles have a higher probability to present imperfections in their micro-structure, facilitating brittle fracture.

In the following sections, the influence of shape on some selected soil properties (*e.g.*, packing, grain size distribution) and geotechnical properties (*e.g.*; shear resistance) is investigated and detailed.

3.2 Packing limits

The *Void ratio (e)* is defined as the ratio of the volume of voids to the volume of solids.

$$e = \frac{V_V}{V_S} \tag{3.1}$$

Porosity (n) is the ratio of the volume of voids to the total volume of the soil.

$$n = \frac{V_V}{V} \tag{3.2}$$

The maximum and minimum void ratio that a granular material can reach are called e_{min} and e_{max}, respectively in its loosest and densest states. In soil mechanics practice, they are usually obtained in a geotechnical laboratory using standard established testing procedures (*i.e.,* ASTM D7263-09(2018)e2). For spheres these values have been studied by physicists and can be theoretically obtained even for random packings (Mackay, 1962; Scott and Kilgour, 1969; Torquato et al., 2000).

For a closed monodisperse packing of spheres, the loosest state is the cubic lattice model (coordination number 6) with a porosity of 0.4764 (e = 0.9099), whereas the densest models are the face-centred cubic (fcc) and the hexagonal closed packed (hcp) crystal lattices (coordination number 12) with a porosity of 0.2595 (e = 0.3504).

Holubec and D'Appollonia (Holubec and D'Appolonia, 1973) found a relation between the particle angularity and the void ratio. In particular, they found a direct proportionality between the maximum and minimum void ratio and true sphericity (ψ) - measuring the specific surface area of a sand on average, using an indirect method based on its permeability - given by the following relations:

$$e_{min} = 0.4549\psi^{0.434} \tag{3.3}$$

$$e_{max} = 0.6112\psi^{0.5152} \tag{3.4}$$

Santamarina and Cho (Santamarina and Cho, 2004) investigated how particle shape affects the packing limits . They investigated several sands for which shape was evaluated using the Krumbein's chart presented in Figure 2.7. The results are shown in Figure 3.1, including the relations they found. Denser packings are possible when roundness and sphericity increase. Note that also the void ratio difference ($e_{max} - e_{min}$) decreases as roundness and sphericity increase.

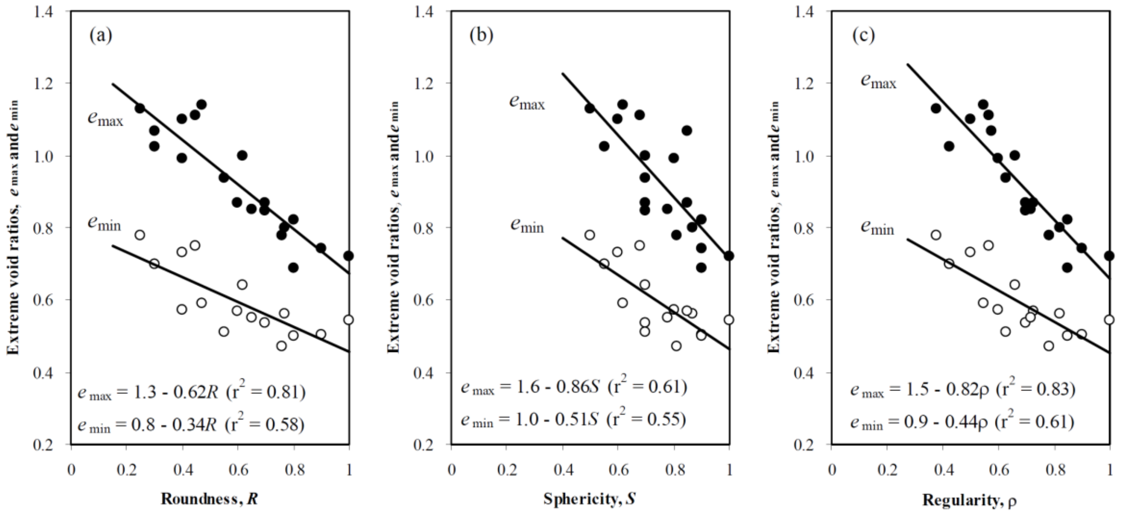

Figure 3.1: Relation between shape parameters (roundness, sphericity, regularity) and void ratios (Santamarina and Cho, 2004)

3.3 Grain Size Distribution from sieve analysis

The grain-size distribution (GSD) is one of the basic and most important properties of a soil. It is primarily used for soil classification and provided a first-order estimate of other soil engineering properties. The classical method, which is still standard (ISO 17892-4:2016), establishes the GSD of soils by sieve analysis. In this method the particle size is characterized by a single linear dimension representing the minimum square sieve aperture at which the particle just passes through. Therefore, particles passing through a sieve can actually have one dimension that is larger than the size of the sieve apertures. It follows that the standard GSD measure may be biased by grain shape.

Arasan et al. (Arasan et al., 2011) selected by hand size fractions of 4.75 – 8mm of flat (called *IA-Flat Particles*), elongated (*IA-Elongated Particles*) and spherical (*IA-Spherical Particles*) grains (classified using Zingg's diagram of Figure 2.3), and calculated the grain size distributions of these fractions; they also created new sand mixing the different shapes. Then, they compared the GSD of mixed particles (*IA-Mixed particles*) with the GSDs of flat and elongated particles. They noticed that there was a variation in the volume of the particles retained on the sieve: the GSD from elongated particles was farthest

(Figure 3.2) from the mixed one. Therefore, they concluded that particle shape is one of the most important factor affecting the GSD of soils, as previously showed also by (Fernlund, 1998) and (Mora et al., 1998) using image analysis techniques.

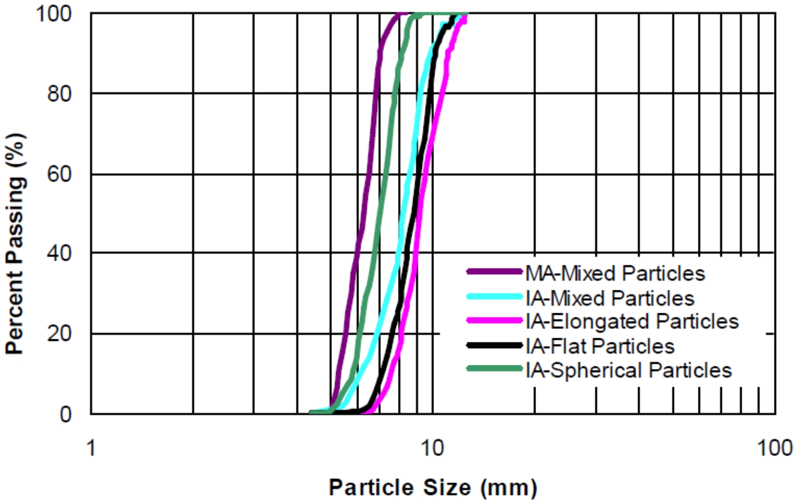

Figure 3.2: GSD of gravel soil (4.75mm-8mm) with different shapes (Arasan and Akbulut, 2008)

3.4 Shear strength

The shear strength of soils is usually expressed by the Mohr-Coulomb failure criterion. According to it, the failure is caused by a critical combination of normal (σ_n) and shear (τ_n) stresses, which induces a slippage if the following criterion is met.

$$\tau_n = \sigma_n \tan(\varphi) + c_0 \tag{3.5}$$

In which c_0 is the intercept of the failure criterion (*cohesion*), and φ is the slope of the envelope (*internal angle of friction*).

It is well known that the shear strength of a soil depends on the relative density. Indeed, a soil behaves differently depending on its state, which can be *dense*, *loose* and *critical*, as shown in Figure 3.3.

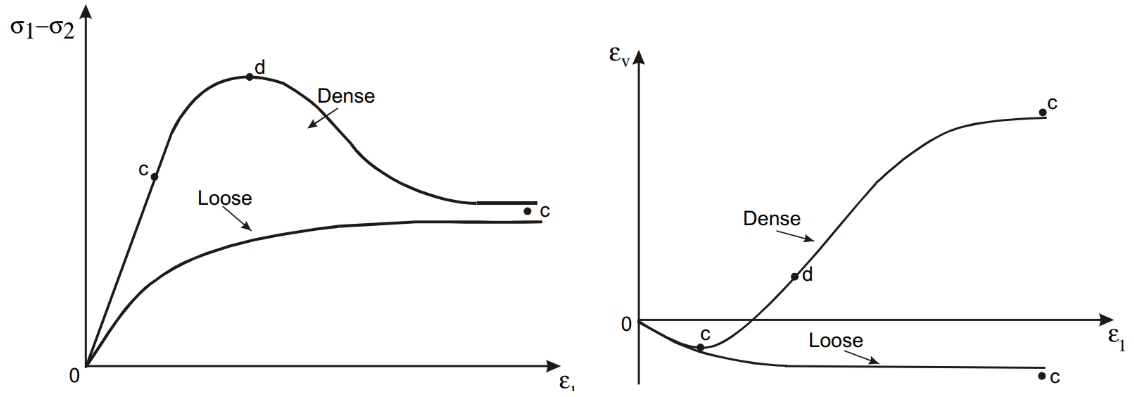

Figure 3.3: Macro-mechanical responses of a dense and loose material

A dense soil is stiffer than a loose soil and presents a *peak* resistance (at which the contribute of *dilatancy* is maximum) before reaching the *critical state* (Schofield and Wroth, 1968). After a short contractancy phase, which is prevented by granular interlocking (that depends on shape, as mentioned in Chapter 3.2), the soil increases its volume until failure. In dense soils rotation is frustrated because of the high number of contacts between particles (*coordination number*) therefore the energy applied during loading is dissipated in friction at contacts and in dilatation, in order to reduce the coordination number. Figure 3.4 illustrates the rotational inhibition existing in dense packings (Santamarina and Cho, 2004).

On the other hand, a loose soil will contract during shearing, without developing any peak strength. Therefore, the shear stress increases until the critical state is reached, arriving to the soil *critical state strength*.

Micromechanical reasons for this behaviour have been suggested: the coordination number is low in loose soils, therefore during shear loading the particle rotation is not inhibited as in dense soils (Figure 3.4) and the *particles bridges* (or *chains*), that may form in low density soils, can easily become instable and break (*buckling*), leading to a denser assembly.

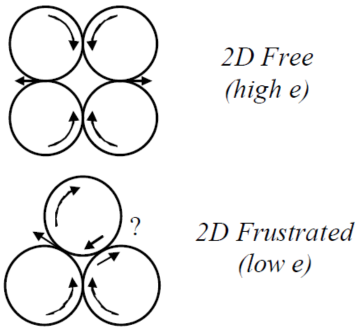

Figure 3.4: Rotational tendency in loose (low e) and dense (high e) packing (Santamarina, 2004)

Rothenburg and Bathurst (Rothenburg and Bathurst, 1989) claimed that the shear strength of a soil depends on its ability to develop internal forces and fabric anisotropy. But the particle shape strongly affects the tendency of particle to re-arrange and to form an anisotropic fabric. Therefore, it is possible to say that particle shape induces interlocking effects which reduce the possibility for particles to rotate easily, increase dilatancy and fabric anisotropy, resulting in a greater shear resistance.

Santamarina and Cho (Santamarina and Cho, 2004) studied the large strain response of sands, at the critical state. He plotted the friction angle at the critical state (φ_{cv}) against the particle roundness (R) for several sands and he found the empirical linear relation as in Figure 3.5. The value of roundness was obtained from the Krumbein chart, Figure 2.7.

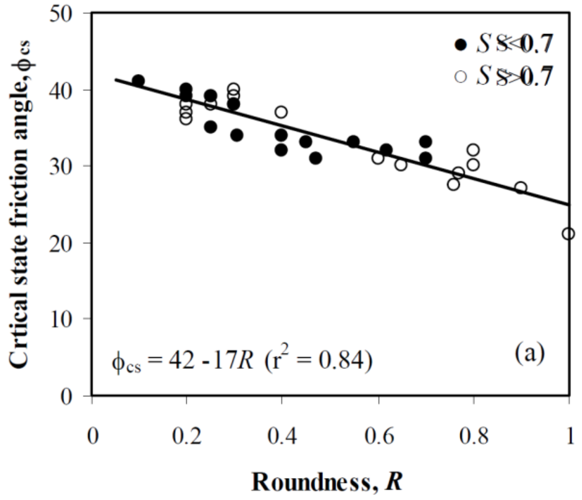

Figure 3.5: Empirical correlation between particle shape (roundness) and φ_{cv} (Santamarina and Cho, 2004)

$$\varphi_{cv} = 42 - 17R \tag{3.6}$$

Other authors (i.e. (Rousé et al., 2008)) proposed similar relationships:

$$\varphi_{cv} = 41.7 - 14.4R \tag{3.7}$$

where R is the roundness based on its original definition as proposed by (Wadell, 1932). Santamarina (2004) also claimed that the local dilatation ($\tan\psi$) of three horizontally aligned elliptical particles is proportional to the particle aspect ratio (L_N/L_T) in the shearing direction (sub index "T")

$$\tan\psi = \left(\frac{L_N}{L_T}\right)\tan 30° \tag{3.8}$$

Where the sub index N refers to the normal direction. Moreover, since the dilatancy angle ψ gives a contribution to the peak friction angle ($\varphi_p = \varphi_{cv} + 0.8\,\psi$, (Bolton, 1986)), as a result the peak friction angle also depends on the particle shape.

The role of shape parameters on shear strength is amply recognized in rock mechanics. For instance, Barton and Kjaernsli (Barton and Kjaernsli, 1981) suggested a model to predict the peak friction angle of rockfill:

$$\varphi_p = R_e \mathrm{Log}\left(\frac{S_e}{\sigma_n}\right) + \varphi_b \tag{3.9}$$

Where:

- S_e = equivalent strength of the particle
- R_e = equivalent roughness of the particle
- φ_b = base friction angle (calculated from basic tilting test)
- σ_n = normal stress

They provided charts for estimating the all the properties to use in their equation.

Cho (Cho et al., 2006) studied the effect of shape on the other critical state parameters. Roscoe (Roscoe et al., 1958) defined the *critical state line (CSL)* as the loci of the critical state conditions in the *e-p′-q* space, where *q* is the deviatoric stress. Its projection onto the *e*-log*p′* space defines the *slope* λ and the *intercept* Γ of the CSL.

$$e_{cs} = \Gamma - \lambda \log\left(\frac{p'_{cs}}{1\,kPa}\right) \tag{3.10}$$

The intercept Γ has been found to be dependent on their value of roundness rather that other shape parameters. In particular, this correlation is shown in Figure 3.6.

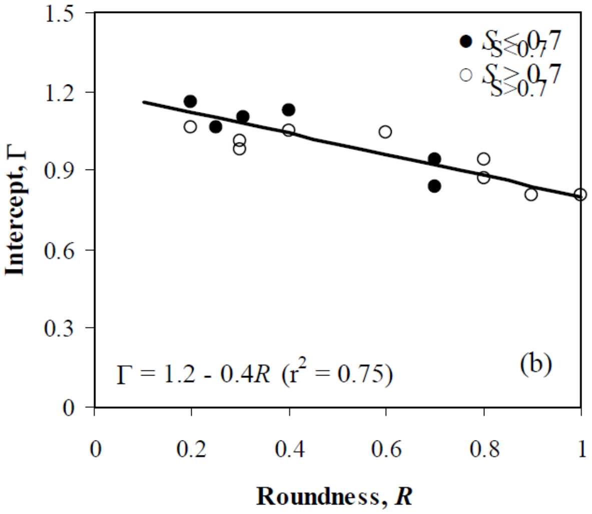

Figure 3.6: Empirical correlation between particle shape (roundness) and Γ (Cho, 2006)

$$\Gamma = 0.12 - 0.4\mathrm{R} \tag{3.11}$$

The slope λ was found to be not too dependent on shape parameters (a slight decrease is observed), however, the *critical state void ratio* (e_{cs100}) at a mean pressure p' of 100kPa presents dependency on *regularity* (ρ)

$$e_{cs100} = \Gamma - 2\,\lambda = 1.1 - 0.42\rho \tag{3.12}$$

In summary, the *critical state parameters* decrease when particles become more rounded and spherical. As a result, starting with the constant volume friction angle φ_{cv}, the soil strength decreases with regularity. In other words, particle irregularity contributes to the overall soil resistance.

Furthermore, the decrease of Γ with regularity implies that regular grains reach the CSL at denser states than irregular grains, which fail in a looser state because they activate a greater amount of dilatancy during shearing.

Finally, the slight decrease of λ means that the critical state of rounded sands is slightly less sensible to the mean stress.

3.5 Stiffness

Stiffness is a measure of the rigidity of an object, it quantifies how much a body resists deformation in response to an applied load. In soil mechanics, the stiffness of single grains is relevant mainly during small-strain deformation, when the strains are still elastic. At this strain level, the number of contacts between grains does not change, because grains have not started rotating and sliding with respect to the neighbours. In other words, fabric is invariant and governs the small strain response. Because fabric is dependent on grain shape, small strain stiffness will be also affected. Moreover, the internal deformation of a grain also depends on its shape, which introduces another dependency.

Santamarina and Cho (Santamarina and Cho, 2004) studied the effect of particle orientation on the shear-wave velocity (S-wave) anisotropy. They generated two specimens from flat particles (i.e. rice and flakes grains) having a preferential particle alignment, and then applied an isotropic pressure into a triaxial cell. The experiment showed that the S-wave velocity was higher (around 1.1-1.5 times) in the direction parallel to the main axis of the particles. It is known that the S-wave velocity (V_S) is controlled by the shear modulus (G), and it can be related to the mean stress (σ_0') on the polarisation plane. It is expressed by:

$$V_S = \sqrt{\frac{G}{\rho}} = \alpha \left(\frac{\sigma_0'}{1kPa} \right)^{\beta} \tag{3.13}$$

Where α is the shear wave velocity at 1kPa, and the exponent β reflects the sensitivity of V_S to the state of stress. Figure 3.7 shows the effect of shape (sphericity and roundness obtained from the Krumbein chart of Figure 2.7) on the (α, β) parameters.

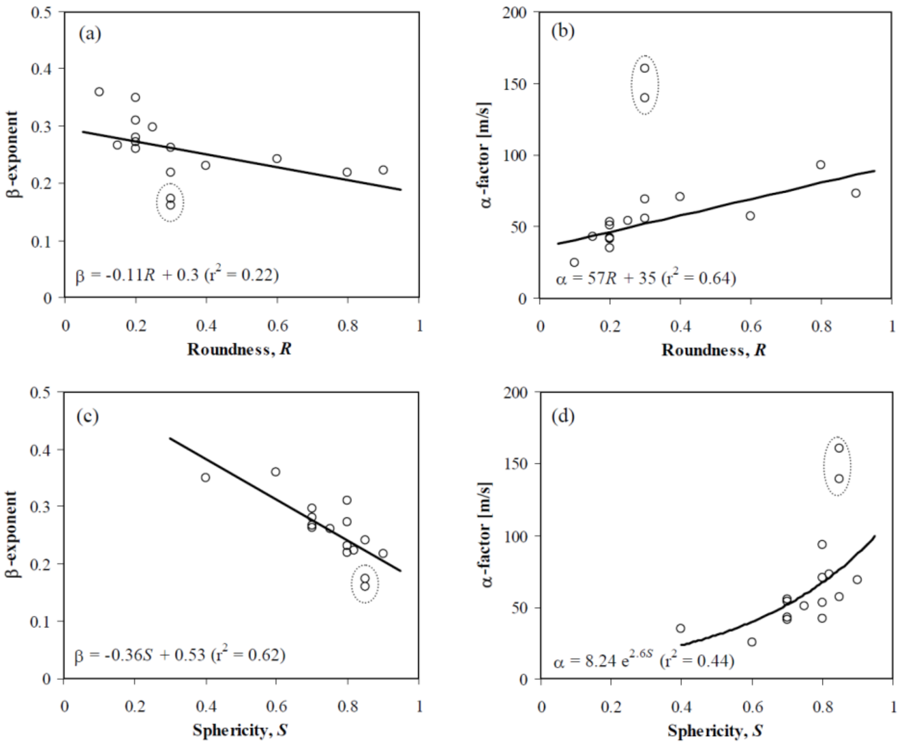

Figure 3.7: Influence of shape (sphericity and roundness) on the parameters (α, β) *(Santamarina, 2004)*

It is evident that when sphericity and roundness increase, the exponent β decreases and the parameter α increases. In other words, particle irregularity decreases the shear wave velocity (related to stiffness) but it increases the sensitivity of stiffness to the stress level.

3.6 Liquefaction

Liquefaction is a phenomenon in which a saturated or partially saturated soil loses a large percentage of its shear resistance and stiffness in response to an applied stress under undrained or partly drained conditions. Static and dynamic liquefaction may occur, but in both cases the fluid pressure inside the pores can increase inducing a decreasing of the effective pressure between particles. Liquefaction occurs if the effective stress between grains reaches zero, and all the stress is held by the fluid phase. Resistance to liquefaction is usually quantified through a direct comparison between the Cyclic Stress Ratio (CSR), with the Cyclic Resistance Ratio (CRR). When the resistance of the soil is less than the seismic demand (*i.e.,* CRR < CSR), liquefaction triggering occurs.

Ishibashi et al. (Ishibashi et al., 1982) showed a strong dependency between the particle sphericity (defined as 2D area sphericity, or S_A in Table 2.1) and the liquefaction potential. In particular, the CSR (after 30 cycles) significantly decreased as particle sphericity increased.

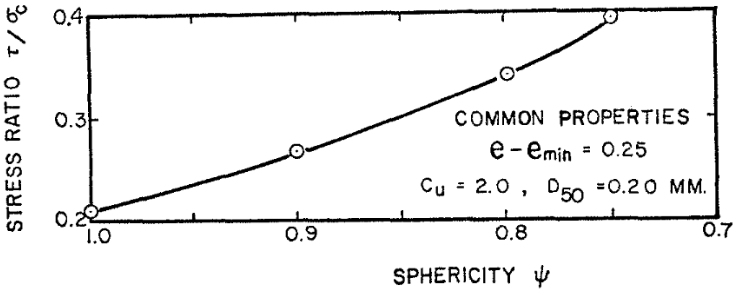

Figure 3.8: Relationship between CSR (30th cycle) and sphericity (S_A following the terminology presented in Table 2.1) (Ishibashi et al., 1982)

They claimed this increase in resistance to liquefaction might be due to the greater interparticle frictional resistance mobilised by angular sands under dynamic stresses.

A similar study was later presented by Vaid et al. (Vaid et al., 1985), who showed that particle angularity had an effect on liquefaction response even at higher confining pressures. In particular, they tested both rounded and angular sands with identical gradation, noting a decrease in resistance to liquefaction with increase in confining pressure. This reduction of resistance was stronger with increase in initial relative density and larger for angular particles. Indeed, angular sands can be susceptible to liquefaction even for very high relative densities and moderate earthquake, if the confining pressure is high. However, at low confining pressure, angular sands are more resistant to liquefaction for the entire range of relative densities. They claimed that this trend might be related to the breakage of particle corners in angular grains that happen at high confining pressure.

3.7 Cone Penetration Test

It has been proven experimentally that particle shape has an influence on the end resistance measured during the Cone Penetration Test (CPT) (Liu and Lehane, 2013). They conducted a series of centrifuge tests on four uniformly graded silica materials having different shape (in decreasing order of roundness: glass ballottini, UWA sand and two glass fragments). Since the primary mineral in all the specimens was silica, it was possible to attribute differences in the test results to the grain shape –although that assumed invariant shape properties during the tests. The CPTs were performed at three different centrifuge g-levels (g) and two different relative densities (D_R). At a given relative density and g-level, the tip resistance q_c varies with the sand type and therefore with particle shape. Values of q_c are higher for the angular glass fragments and lower for the more spherical glass ballottini. Figure 3.9 shows the CPT end resistance observed in a centrifuge test having g-level equal to 50 and relative density of 0.8. A similar trend was observed for every tested stress state and relative density.

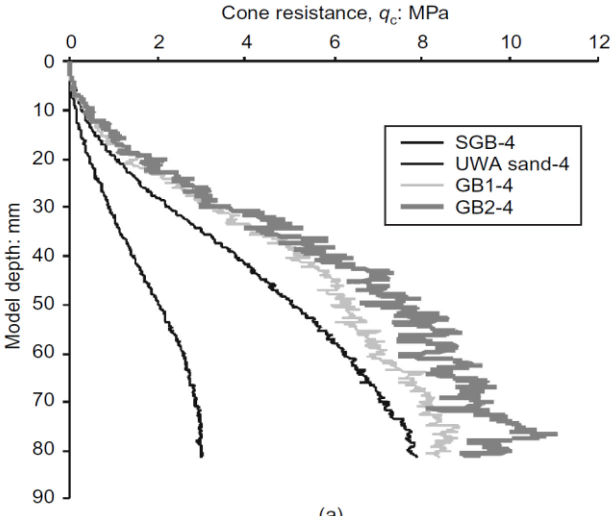

Figure 3.9: CPT tip resistance in the centrifuge test performed at g=50 and D_R=0.8 (Liu and Lehane, 2013)

3.8 Summary

In this Chapter, previous studies about the influence of particle shape on the geotechnical properties of granular soils are reported. The main concepts can be summarised as follow:

- The behaviour of granular soils depends on the re-arrangement of grains during loading. This re-arrangement is affected by particle shape;
- Particle shape affects both physical and mechanical properties of sands, and therefore it must be considered in numerical simulations.

4

Particle shape in Discrete Element Modelling

4.1 Introduction

Advances in computer technologies experienced in the last thirty years, have powered the expansion of numerical techniques able to simulate the behaviour of geomaterials, solving physical problems which have important features at multiple scales, both spatial and temporal. Some problems can be represented adequately by sets of differential equations that describe the system behaviour at the field points. Such systems are termed *continuous* and have infinite degrees of freedom.

In other situations, the global behaviour of the system may be difficult to formulate precisely in continuum terms, but can be determined through well-defined inter-relations between individually specified components (elements. Such approaches are termed *discrete*.

In this chapter, a synthetic overview on the most popular and widely used discrete numerical method is presented: The Discrete Element Method (DEM). Particular emphasis is given on the existing approaches used in practice for take into account the shape of particles into DEM simulations. As originally defined,

"The discrete element method is a numerical tool capable of describing the mechanical behaviour of assemblies of discs or spheres. The method is based on the use of an explicit numerical scheme in which the interaction of the particles is monitored contact by contact and the motion of the particle modelled particle by particle [...]" (Cundall and Strack, 1979)

The key concept of the Discrete Element Method is thus that the domain of interest is occupied by a set of rigid or deformable bodies –which are named either particles (e.g., PFC, YADE) or blocks (i.e. UDEC, 3DEC). Bodies and the contacts among them need to be identified and continuously updated during the entire deformation/motion process, and contact behaviour represented by contact models. The fundamental concepts lead naturally to three central issues:

- Identification of particles (or blocks) system topology based on particle shape assumptions within the domain of interest, or the fracture system geometry;
- Formulation and solution of equations of motion of the particles system;
- Detection and updating of varying contacts between the particles as the consequences of motion and deformations of the discrete system.

4.2 DEM fundamentals

Granular materials are modelled by a set of particles, that, for presentational purposes are assumed in this section to be spheres –see alternatives in the next section. Each sphere is identified by its own mass m, radius R and moment of inertia I_0. The calculation alternates between the application of Newton's second law to the particles and a force-displacement law at the contacts. Newton's second law is used to determine the motion of each particle arising from the contact and body forces acting upon it, whereas the force-displacement law is used to update the contact forces arising from the relative motion previously obtained.

The calculation cycle is therefore a time-stepping algorithm that requires the repeated application of the law of motion to each particle, a force-displacement law at each contact, and a constant updating of wall positions, being the wall the virtual entity acting as the boundary of the problem to be modelled. Contacts, which may exist between two balls, or between a ball and a wall, are formed and broken automatically during simulation.

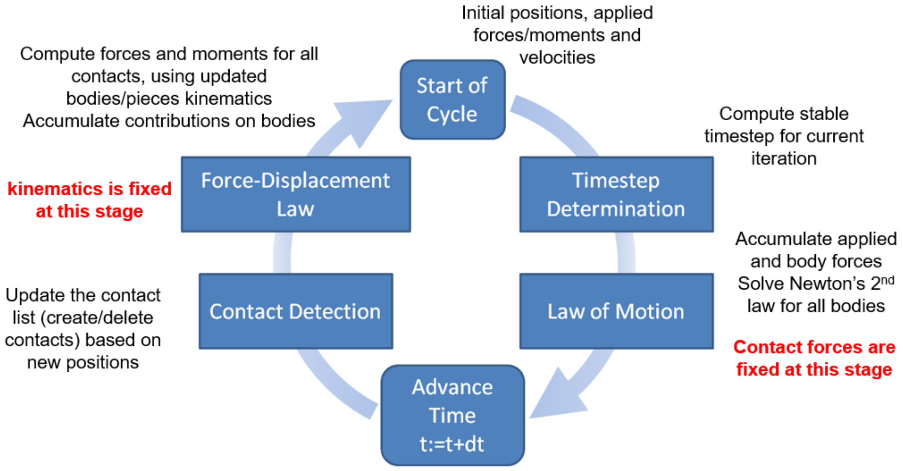
Initial positions, applied forces/moments and velocities
Start of Cycle
Compute stable timestep for current iteration
Timestep Determination
Accumulate applied and body forces Solve Newton's 2nd law for all bodies
Law of Motion
Contact forces are fixed at this stage
Advance Time t:=t+dt
Contact Detection
Update the contact list (create/delete contacts) based on new positions
Force-Displacement Law
kinematics is fixed at this stage
Compute forces and moments for all contacts, using updated bodies/pieces kinematics Accumulate contributions on bodies

Figure 4.1: Calculation cycle in DEM, from PFC5 reference guide (Itasca Consulting Group Inc., 2014)

All the process of calculation is represented in Figure 4.1 and detailed hereafter. At the start of each cycle, the timestep must be determined. The DEM methodology requires a finite timestep for the numerical integration of the Newton's laws, able to ensure the stability of the explicit algorithm employed in the numerical calculation. If the timestep is too large, contacts may not be identified, if it is too small the simulation time is penalized. Therefore, the timestep should be chosen as large as possible, as far as the stability is guaranteed. An efficient way is to calculate the critical timestep for all the degrees of freedom of the bodies and select the minimum one. The i-th timestep for the i-th body is estimated considering the one-dimensional mass-spring system of Figure 4.2.

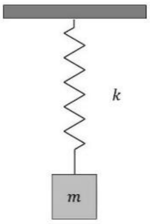

Figure 4.2: Single mass-spring system

The motion of the mass m is governed by the differential equation:

$$-k\boldsymbol{x} = m\ddot{\boldsymbol{x}} \tag{4.1}$$

Where k is the stiffness of the spring and x the displacement vector. The critical timestep can be written as (Bathe and Wilson, 1976):

$$t_{crit} = \frac{T}{\pi} \tag{4.2}$$

Being T the period of the system, defined as

$$T = 2\pi\sqrt{\frac{m}{k}} \tag{4.3}$$

In the case of an infinite series-connected set of identical masses and springs, the critical timestep for this system can be written as:

$$t_{crit} = 2\sqrt{\frac{m}{4k}} = \sqrt{\frac{m}{k}} \tag{4.4}$$

Concluding, the final critical timestep for the entire model (at a given cycle) is taken to be the minimum of all the timesteps calculated for all the degree of freedom of all the bodies.

Some other techniques to calculate the critical timestep exist in DEM literature. For instance, O'Sullivan and Bray (O'Sullivan and Bray, 2004) proposed an alternative method to estimate the critical timestep taking into account the particles arrangement configuration and the number of contacts per particle. They claimed it guarantees a more stable solution for simulations involving particles with high coordination numbers (*i.e.,* when clumps or non-convex particles are used). Another approach consider the Rayleigh wave speed to determine the timestep (Li et al., 2005; Thornton, 2000; Thornton and Randall, 1988).

Otsubo et al. (Otsubo et al., 2017) tested different DEM samples with different packing (i.e., monodisperse-polydisperse) and loading (constant-varying mean effective stress) conditions to see how the critical timestep was influenced. Their empirical study showed that some very simple methods used to calculate the critical timestep can result in simulations either unstable or having a very high computational cost. Therefore, they suggested that the critical timestep must be set with care depending on the situation.

Once the timestep for one calculation cycle has been fixed, the position and velocities of all bodies are calculated by integrating the Newton's laws of motion, using the contact forces of the previous cycle. This is done by integrating the equation:

$$m(\ddot{\boldsymbol{x}} - \boldsymbol{g}) = \boldsymbol{F} \tag{4.5}$$

Where $\boldsymbol{m}$ is the inertia mass matrix, $\ddot{\boldsymbol{x}}$ is the acceleration vector and $\boldsymbol{F}$ is the resultant force vector. The typical time integration method used in DEM is the Verlet algorithm (Verlet, 1967), in which the velocity at step $(t + \frac{\Delta t}{2})$ (half-step velocity) is computed as in equation (4.6):

$$\dot{\boldsymbol{x}}^{\left(t+\frac{\Delta t}{2}\right)} = \dot{\boldsymbol{x}}^{(t)} + \frac{1}{2}\left(\frac{\boldsymbol{F}^{(t)}}{m} + \boldsymbol{g}\right)\Delta t \tag{4.6}$$

This velocity is then used to calculate the position at step $t + \Delta t$ as:

$$\boldsymbol{x}^{(t+\Delta t)} = \boldsymbol{x}^{(t)} + \dot{\boldsymbol{x}}^{\left(t+\frac{\Delta t}{2}\right)}\,\Delta t \tag{4.7}$$

The velocity at $t + \Delta t$ is subsequently updated. It is not calculated at this step of the cycle sequence but after the application of the force-displacement law (when the contact forces are calculated) through:

$$\dot{\boldsymbol{x}}^{(t+\Delta t)} = \dot{\boldsymbol{x}}^{\left(t+\frac{\Delta t}{2}\right)} + \frac{1}{2}\left(\frac{\boldsymbol{F}^{(t+\Delta t)}}{m} + \boldsymbol{g}\right)\Delta t \tag{4.8}$$

Similar considerations apply to the rotational motion but are omitted here as they can be easily found in the PFC5 reference guide (Itasca Consulting Group Inc., 2014).

At this point the current timestep is updated to $(t + \Delta t)$, the contacts are detected based on the new bodies positions (from the applied law of motion) and the force-displacement law is applied to each couple of particles in contact. Here, assumptions on the constitutive contact model need to be done: the most common contact model used in DEM is the linear model, because of its simple formulation, but many other more advanced models exist (*e.g.,* parallel bond (Holt et al., 2005; Lu and McDowell, 2008), Hertzian (Ciantia et al., 2019b; Cundall, 1988a), rolling resistance (Iwashita and Oda, 1998; Jiang et al., 2005), etc.). The rolling resistance contact model will be detailed in Chapter 4.3.2.

In the linear contact model contact forces are proportional to the degree of the relative interpenetration between the bodies (usually named *overlap*, U_n) and the selected contact stiffness (k_n and k_s, respectively for the normal and tangential direction).

Regarding the tangential direction, the simplest approach is to assume the Coulomb friction model as yield criterion, in which μ is named the *coefficient of friction*. For the contact '*i*':

$$\boldsymbol{N}_{\boldsymbol{i}}^{t+\Delta t} = k_n U_n \quad \text{(along the normal direction)} \tag{4.9}$$

$$\Delta \boldsymbol{T}_{\boldsymbol{i}}^{t+\Delta t} = -k_s \Delta U_s, \quad \Delta \boldsymbol{T}_{\boldsymbol{i}}^{t+\Delta t} \leq \mu \boldsymbol{N}_{\boldsymbol{i}}^{t+\Delta t} \quad \text{(along the tangential direction)} \tag{4.10}$$

The tangential equation is defined in an incremental way, because it is important to take into account the cumulative shear displacement (ΔU_s) at the contact. Therefore, when a contact is created, the tangential force and displacements are set to zero. After some timesteps, the shear force depends on the cumulated displacement in the tangential direction, given as the sum of the incremental relative displacements of the particles at the contact point that occur at each timestep from the time of the contact creation. Moreover, the shear force presents an upper limit where the contact fails, given by the Coulomb criterion.

4.3 Particle shape modelling in DEM

There are several techniques to take the shape of particles into account in DEM simulations, which are briefly described hereafter. In broad terms, the problem of shape in DEM can be tackled either using *non-spherical* particles, either constraining the rotations of spherical particles.

4.3.1 Continuous analytical particle shape description

A first possibility to include particle shape into DEM simulations employs a continuous analytical description of the particles outlines. The most common non-spherical analytical geometries employed in DEM have been ellipses (in 2D) and ellipsoids (in 3D) (Gan et al., 2016; Jiang et al., 2016; Ng, 1994; Rothenburg and Bathurst, 1992). Elliptical particles are considered a good trade-off between computational time and shape complexity, indeed, they do introduce resistance to rotation (due to the non-collinearity of contacts) but only one contact may exist between each couple of particles. Others tried to model DEM particles with more complex superquadrics surfaces (G W Mustoe and Miyata, 2001; Podlozhnyuk et al., 2017). Superquadratics rely on analytical solution (complex closed-form expressions) for the detection of contacts, which can be computationally very expensive, especially when non-linear equations must be solved, limiting the practical applications of this method.

4.3.2 Polyhedral particles

Another school of thought exploits non-spherical particles (*e.g.*, triangles, squares, hexagons in 2D; polyhedrons in 3D) (Elias, 2013; Langston et al., 2013; Ouhbi et al., 2016) to generate complex-shaped particles. The contact detection is the most complex and expensive task to carry out for this methodology. Indeed, it requires the evaluation of the coordinates of the polygons vertices, the edges and the particle orientation, whereas only the radii and the positions of the centres are required for spheres. Moreover, the contact between two polyhedral particles can occur in six different situations (Cundall, 1988b): corner-corner, corner-edge, edge-edge, corner-face, edge-face and face-face; adding further complexities to the contact identification and calculation of the contact forces. Polyhedrons are defined by several vertices, edges and faces, and therefore they can well represent the shape of physical grains. Historically polyhedrons have seen limited use in DEM because of the difficulty to implement efficient contact detection algorithms. Recently, Itasca released the new version of their Particle Flow Code (PFC6), able to model polyhedrons using a variation of the Gilbert-Johnson-Keerthi algorithm (Gilbert et al., 1988) for the contact detection and resolution.

4.3.3 Aggregates of spheres (clumps)

Clumps are single entities of overlapping balls (used as “building blocks”) behaving as rigid bodies, used in DEM to create particles with more realistic geometries. The internal overlapping contacts are not considered in the calculations. The use of clumps provides an interlocking within the assembly leading to a more realistic overall stress-strain behaviour.

The advantages of clumps are the simplicity of the model creation and the possibility to refine the clump shape (depending on the number of spheres forming the clump), therefore clumps are widely used (e.g. (Lu and McDowell, 2007) (Lim and McDowell, 2005) (Sun et al., 2014)).

The main advantage of using clumps is that they do not require complex contact models to consider the effect of particle shape, since contact is always between spherical surfaces. However, the calculation time is strongly affected by the use of clumps, since each clump is formed by many spherical elements, and the number of possible contacts is controlled by the number of total spherical elements in the simulation, not by the number of clumps. As a result the number of clumps involved in the simulations must be kept relatively small, thus affecting the model size and therefore the physics of the systems that can be represented.

Figure 4.3 shows some examples of three-dimensional clumps, ranging from simple geometries to more complex ones.

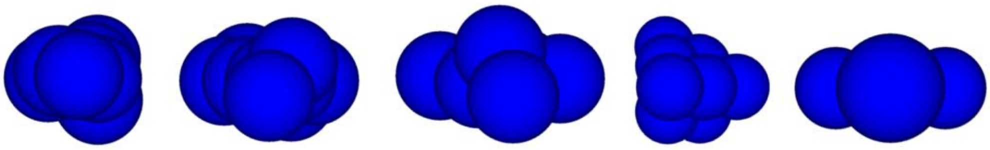

Figure 4.3: Examples of 3D clumps (Yang et al., 2017)

Several authors have proposed algorithms able to create clumps from digital images of real soil particles (Das, 2007) (Garcia et al., 2009). Usually, these algorithms try to fill the region delimited by the particle outline with several spheres of different sizes, as shown in Figure 4.4. An optimal target resolution must be set, in order to guarantee a realistic shape without using too many elements for each clump, increasing dramatically the calculation time.

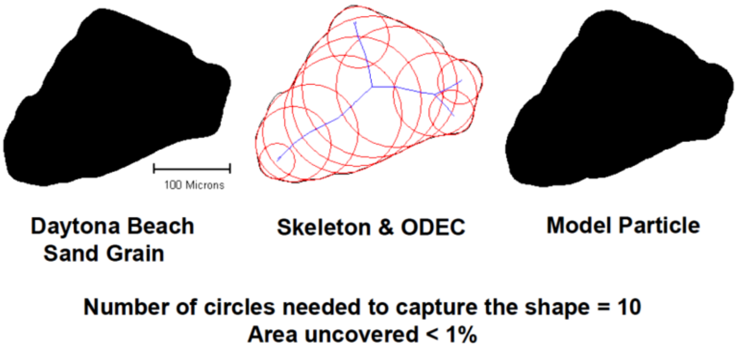

Figure 4.4: Example of algorithm used for creating clumped particles (Das, 2007)

The moment of inertia depends on the p-elements making up the single particle. It can be written as following (O'Sullivan, 2011), calculated about a local Cartesian axis centred at the cluster centroid $I^{cluster}$:

$$I_{ij}^{cluster} = \sum_{p=1}^{N_p} \left(I_{ij}^{p} \delta_{ij} + m^p a_i^p a_j^p \right) \tag{4.11}$$

Where N_p is the number of building blocks, each with mass m^p and inertia I^p, and δ_{ij} is the Kronecker delta. The vector a is given by the difference between the vectors defining the centroids of the p-element and the cluster respectively.

Similar approach can be done regarding the mass density and distribution. If the cluster is composed by non-overlapping particles, the total mass is simply given by the sum of the masses of the p-elements. In case of overlapping geometries, it is necessary to scale down the cluster density in order to avoid having huge masses in regions where several spheres overlap.

This can be done following a procedure used by (Ashmawy et al., 2003) and (Lu and McDowell, 2008), in which the density of the base spheres is scaled to a value ρ_{scaled}^{b} defined as:

$$\rho_{scaled}^{b} = \frac{\rho_p V_p}{\sum_{i=1}^{N^p} V_i^b} \tag{4.12}$$

Where ρ_p and V_p are the required density and volume of the target cluster, whereas V_i^b is the volume of the i-th base sphere.

4.3.4 Other approaches

Other approaches exist to take the shape of particles into account in DEM simulations (Coetzee, 2016; Lane et al., 2010), beside rotational constrains and aggregates of spheres. One of them, originally proposed by (Hentz et al., 2004), exploits the concept of "contact at distance": it means a contact between two particles can be created even if the particles are not actually in contact (do not overlap). This is done by defining a "proximity" distance under which the contact is created, even though there is no physical overlapping between the particles. The particle shape can be approximated by defining fictitious proximity distances to apply to the spheres depending on the angularity of the physical grain and on the contact orientation. It is an efficient way because it only introduces new terms into the force-displacement law but the "interaction range" is difficult to physically calibrate.

Calvetti et al. (Calvetti et al., 2004, 2003; Calvetti and Nova, 2004) proposed to inhibit the particle rotations, doing so the deformation of the assembly is entirely governed by the sliding between particles providing realistic results in an unrealistic framework. This approach can be seen as the extreme limit of the rolling resistance contact model described later, in which resistant torques are applied at the contacts in order to resist the relative rotation between spherical particles (see chapter 4.3.5).

Jerves et al. (Jerves et al., 2016) proposed a variation of the conventional DEM, called "level-set discrete element method (LS-DEM), able to take into account particle shape using level set to represent the grain geometry. Level-set is an implicit function representing the distance from a point to an interface (*i.e.*, the particle external surface). Therefore, each particle boundary can be related to a level set function, as illustrated in Figure 4.5.

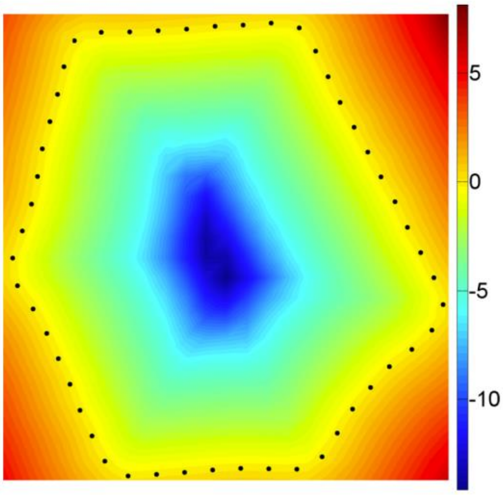

Figure 4.5: Particle representation using level set function. The black dots are the boundary node discretisation (Jerves et al., 2016).

This approach allows a high-level shape representation of each particle that can be input either analytically either from image-based methods, as shown in Figure 4.6. The main disadvantage of this shape representation is the huge computational time. Kawamoto (Kawamoto et al., 2018) simulated the triaxial test on Hostun sand (representing specimen HNEA01, having size 2×1 cm) in 17 hours on the San Diego Supercomputer Center's XSEDE cluster Comet, using 470 cores.

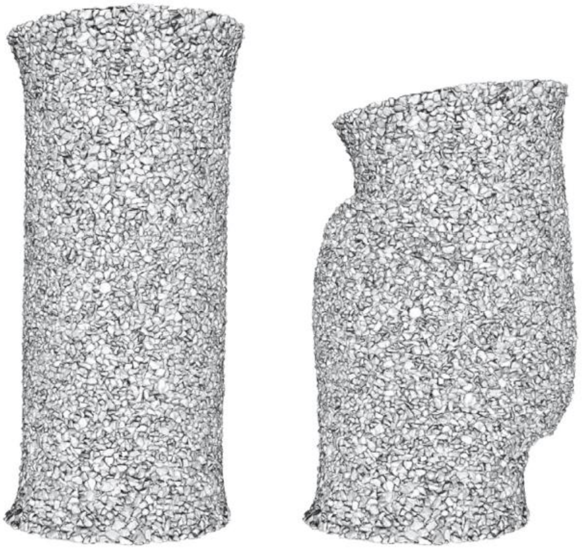

Figure 4.6: Level-set DEM representation of HNEA01 sand specimen before and after triaxial shearing (Kawamoto et al., 2018)

A similar methodology is adopted by Nadimi & Fonseca in their combined discrete-finite element model approach (Nadimi et al., 2019; Nadimi and Fonseca, 2018). They simulated a triaxial test performed on a granular sample filled with Martial regolith-like grains (scanned by x-rays and reproduced by micro-finite elements). A deformable numerical membrane (made by thin-shell elements) is also implemented to model more realistically the laboratory conditions. The results obtained appear promising, however only 3000 grains were included in the simulations.

4.3.5 Rolling resistance contact models

Traditional DEM simulations are based on smooth spherical particles with no resistance to rotation at the contact point. However, the surface irregularity, rugosity and particle angularity may add a resistance to rotation that may be taken directly into account, this resistance is usually referred as "rolling resistance".

4.3.5.1 Formulations

There are different implementations of the rolling resistance contact model. Iwashita & Oda (Iwashita and Oda, 1998) studied the microstructure of shear bands in two-dimensions noting that rolling, rather than sliding, is the major mechanism controlling the dilatancy into the shear bands, something that had also been demonstrated by Bardet (Bardet, 1994) using DEM. Moreover, since the contacts in real particles are not points but rather surfaces, rolling resistance provides a key contribution for a realistic shear band development at failure. Therefore, they proposed an elasto-plastic "Modified" version of the original DEM, called MDEM, able to take into account rolling resistance.
In conventional DEM, the contact (elastic and viscous) forces (normal N_i and tangential T_i) at the contact 'i' are defined as:

$$N_i = k_n U_n + C_n \frac{dU_n}{dt} \tag{4.13}$$

$$T_i = k_s U_s + C_s \frac{dU_s}{dt} \quad if \quad |T_i| \leq \mu N_i \tag{4.14}$$

Where k_n, k_s are the stiffness of the normal and tangential springs respectively; U_n, U_s are the relative normal and shear displacements at contacts, C_n, C_n are the viscous damping coefficients of the normal and shear dashpots, and μ is the coefficient of sliding friction.

In their proposed MDEM, illustrated in Figure 4.7, an additional equation is added to the contact model in order to provide the resistant torque termed as rolling resistance M_i:

$$M_i = -k_r\theta_r - C_r\frac{dU_r}{dt} \quad with \quad |M_i| \leq \eta N_i = \alpha B N_i \tag{4.15}$$

Where k_r is the *rolling stiffness*, θ_r the relative rotation, C_r the viscous coefficient and η the *coefficient of rolling friction* which has a dimension of length. The authors, in a subsequent publication (Iwashita and Oda, 2000), proposed η to be equal the product between an adimensional parameter α and half of the contact width B. The term dU_r is defined as the displacement due to the rolling component only, quantified studying the kinematics of the contact point of two disks (having radii r_1 and r_2) in contact (see (Iwashita and Oda, 1998), for more details). They concluded that $d\theta_r$ can be written as:

$$d\theta_r = \frac{dU_r}{r_{iwa}} \tag{4.16}$$

Where $r_{iwa} = \frac{r_1+r_2}{2}$ is named as *common radius*.

The authors argued that there was no obvious rationale to choose a value of the rolling stiffness k_r. However, they assumed k_r to be the same order of magnitude of k_s, leading to:

$$k_r = k_s r_{iwa}^2$$

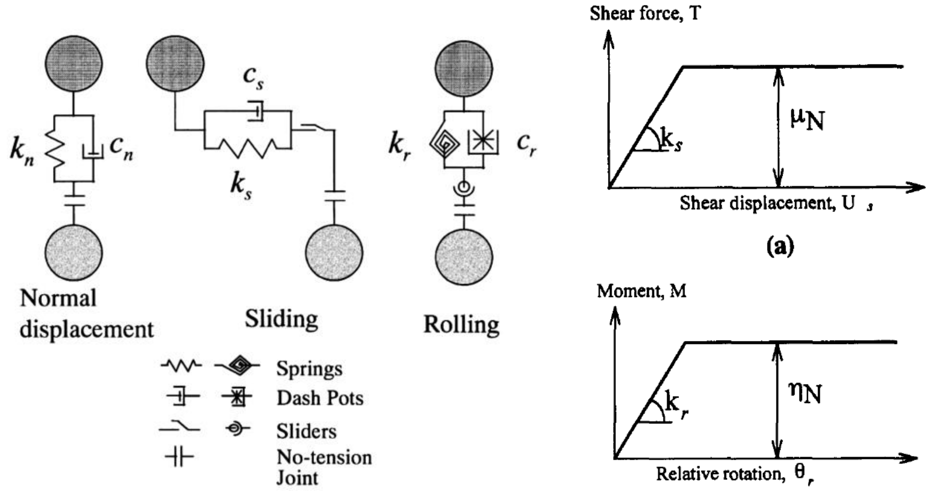

k_n
c_n
c_s
k_s
k_r
c_r
Normal displacement
Sliding
Rolling
Springs
Dash Pots
Sliders
No-tension Joint
Shear force, T
k_s
μN
Shear displacement, U_s
(a)
Moment, M
k_r
ηN
Relative rotation, θ_r

Figure 4.7: Rolling resistance model proposed by (Iwashita and Oda, 1998)

At this step, M_i and T_i can be substituted in the rotational dynamic equilibrium equation indicated in Eq. 4.17.

$$\sum_{i=1}^{m}(T_i r + M_i) = I\frac{d\omega}{dt} \tag{4.17}$$

Where m is the total number of contact forces and moments, I is the moment of inertia and ω the angular velocity, expressed in terms of displacements at contacts.

Their results showed that the use of rolling resistance had a large effect on both the peak and residual stresses at failure, the stress-strain curve lying between the free and fixed rolling tests, as shown in Figure 4.8. Moreover, when the MDEM is used, the specimen showed a strain localisation that was not visible in the other tests (Figure 4.9).

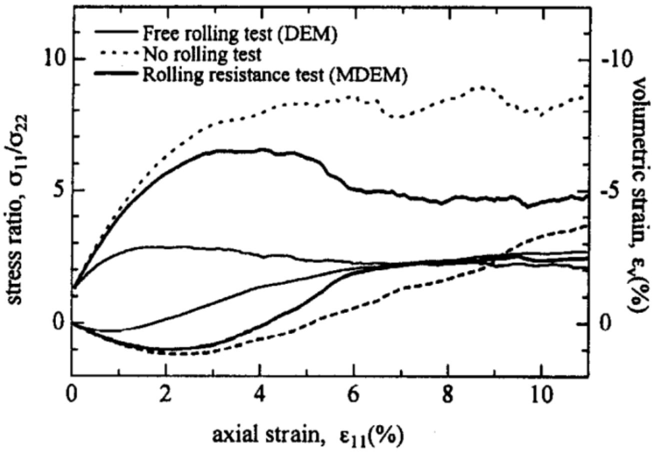

Figure 4.8: Triaxial responses of DEM simulations performed on spherical particles with three different rotational constrains: free rolling, fixed rolling and rolling resistance (Iwashita and Oda, 1998)

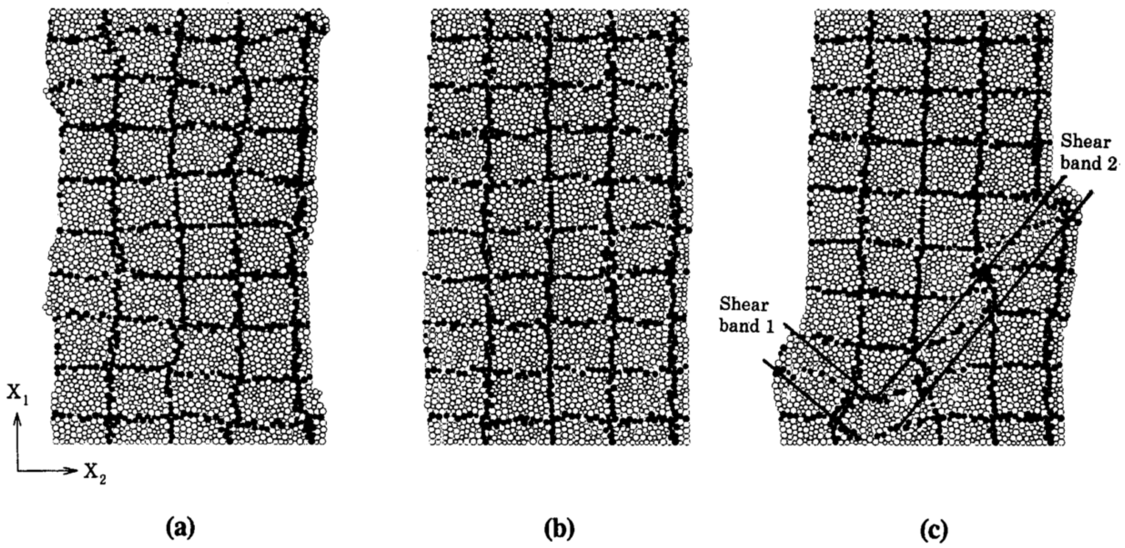

Figure 4.9: Strain localisation after triaxial testing in the free rolling test (a), fixed rolling test (b) and rolling resistance test (c) using MDEM.

Jiang et al. (Jiang et al., 2005) modified the Iwashita & Oda rotational model in order to solve its perceived limitations. In particular, the authors claimed that: 1) the kinematical model of Iwashita and Oda was stated for discs of equal radius only, without any theoretical proof for the decomposition of contact displacements and for the (empirical) relation with particle rotation; 2) the model introduced four additional parameters chosen separately by trial and error procedure; and 3) the angular motion equations were not linked to the equilibrium of the system.

Firstly, they proposed two new definitions of *pure sliding* and *pure rolling* in order to decompose in a unique manner the displacements at contacts. They provided theoretical proof that these decomposition leads to

$$dU_r = \frac{r_2 \mathrm{d}a - r_1 \mathrm{d}b}{r_1 + r_2} \; ; \quad dU_s = \frac{\mathrm{d}a + \mathrm{d}b}{2} \tag{4.18}$$

Where da and db are the arc length covered by the contact point along the two disks in contact, having radii r_1 and r_2.

These definitions are more rigorous and general than the ones proposed by Iwashita and Oda because they include the case in which $r_1 \neq r_2$ and the special case where both the disks rotate rigidly as a single body. The same considerations can be done for the relative particle rotation, $d\theta_r$, and the common radius r, which are similar to the definitions of (Iwashita and Oda, 1998).

$$d\theta_r = 2\frac{dU_r}{r_{jiang}} \tag{4.19}$$

Where:

$$r_{jiang} = \frac{2r_1 r_2}{r_1 + r_2} \tag{4.20}$$

Secondly, they defined a new contact width defined as:

$$B = \delta \cdot r_{jiang} \tag{4.21}$$

Where δ is a dimensionless geometrical parameter related to the grain shape. However, the authors did not provide any methodology to evaluate this shape parameter.

Subsequently, they represented the contact interaction through a series of springs and dashpots acting in parallel along its length B, as in Figure 4.10.

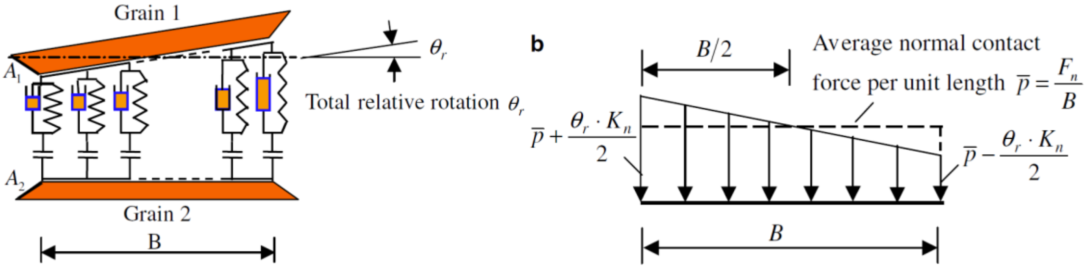
Grain 1
A_1
A_2
θ_r
Total relative rotation θ_r
Grain 2
B
b
$B/2$
Average normal contact force per unit length $\overline{p} = \frac{F_n}{B}$
$\overline{p} + \frac{\theta_r \cdot K_n}{2}$
$\overline{p} - \frac{\theta_r \cdot K_n}{2}$
B

Figure 4.10a-b: Rolling resistance model proposed by (Jiang et al., 2005)

The resistant torque is originated by a system of parallel springs placed along the contact (Figure 4.10a). The resulting distribution of the normal contact force is showed in Figure 4.10b. The normal and shear stiffness (for the normal and tangential motions) are computed as function of the contact length B.

In the framework of rational mechanics, it is straightforward to study the stress distribution along the element (Figure 4.10b), leading to an expression for the resistant moment M:

$$M = \frac{K_n B^2}{12}\theta_r = K_m \theta_r \tag{4.22}$$

Where K_m is the rolling stiffness, that can be written as Eq. (4.23) by substituting Eq. (4.21) into (4.22):

$$K_m = \frac{K_n B^2}{12} = \frac{K_n r^2}{12}\delta^2 \tag{4.23}$$

The proportionality between normal and rolling stiffness that was simply postulated by Iwashita & Oda appears here as a consequence of contact geometry. It can be noted that the condition $B = 0$, equivalent to $\delta = 0$ (it means the contact is a point), leads to $M = 0$. The authors proposed also an equation for modelling the plastic behaviour at the contact, described by the following equations:

$$M = M_0\left[3 - 2\left(\frac{\theta_r^0}{\theta_r}\right)^{0.5}\right] \tag{4.24}$$

Where M_0, θ_r^0 are the critical values of θ_r and M that separate the elastic and plastic zones, and are defined as

$$M_0 = \frac{1}{6}F_n B, \qquad \theta_r^0 = \frac{2F_n}{K_n B} \tag{4.25}$$

Where F_n is the normal contact force. Again all these quantities are only dependent on the normal contact properties and the shape parameter δ.

Eq. (4.24) and (4.25) constitute the elasto-plastic non-linear model of the rolling resistance contact model, shown in Figure 4.11.

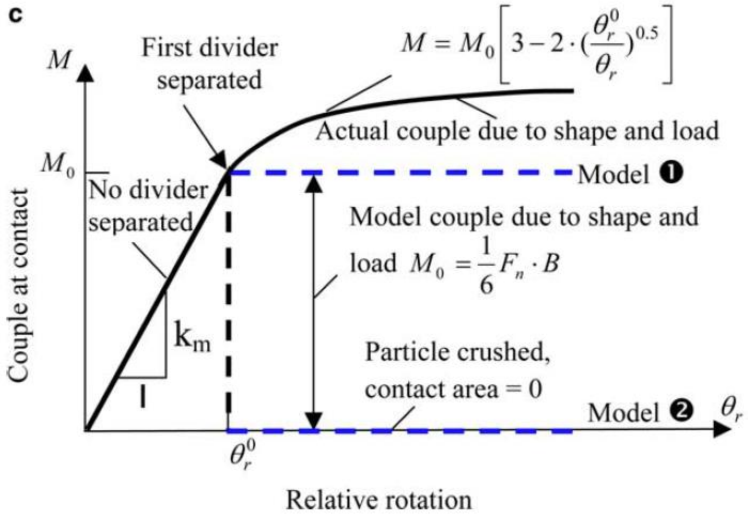

Figure 4.11: Moment-relative rotation response for the model introduced by (Jiang et al., 2005)

The non-linearity induces complexity in the numerical solution, and therefore they simplified the original model into two different idealized elastic-perfectly plastic models, (Model 1 and Model 2), as described in equations (4.26 – 4.28).

$$\begin{cases} M = \dfrac{K_n B^2}{12}\theta_r = K_m\theta_r, \quad \theta_r < \theta_r^0 \\ M = M_0 = \dfrac{1}{6}F_n B, \quad \theta_r > \theta_r^0 \ \text{(Model 1)} \\ M = 0, \quad \theta_r > \theta_r^0 \ \text{(Model 2)} \end{cases} \qquad (4.26 - 4.27 - 4.28)$$

Model 1 is similar to the one proposed by (Iwashita and Oda, 1998), but the approaches were different. Model 2 is meant for crushable grains, with an instant vanishing of the contact width and therefore the rolling resistance.

It worth to point out that both the model reduce to standard DEM if the shape parameter δ equals 0. Figure 4.12 shows the influence of the shape parameter δ on the shear resistance of the specimen.

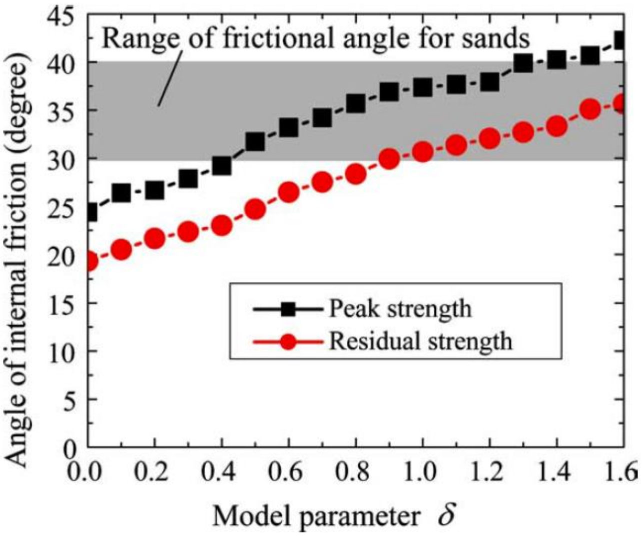

Figure 4.12: Angle of internal friction at peak and critical states in function of the shape parameter δ (Jiang et al., 2005)

Estrada et al. (Estrada et al., 2008) claimed that particles interlocking affects the force network by enhancing the arching effects, and that rolling resistance may imitate this phenomenon. They implemented a rolling resistance contact model in which a resistant torque M is applied depending on the sign (i.e., direction) of the relative angular velocity of the particles and it is a function of a parameter η, the radii of the spheres (r_1, r_2) and the normal force F_n.

$$M = \pm\eta(r_1 + r_2)F_n \qquad (4.29)$$

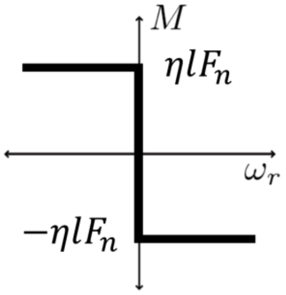

Figure 4.13: Relationship between the rolling torque M and relative rotation ω_r (Estrada et al., 2008)

The most important outcome of their work was to clearly show how the effects given by sliding (μ) and rolling (η) frictions are not independent but rather strongly coupled. It means, in order to reach high shear resistances, it is necessary to increase together μ and η, otherwise the shear resistance saturates independently on the magnitude of the single coefficient, if increased alone. The physical reason behind this observation is that two particles in contact tend to slide if the μ is low and η is large and tend to roll if vice versa.

They run 221 shear tests varying the values of μ (0-0.8) and η (0-0.6) and recorded the internal friction coefficient (μ^*). It is evident that μ^* tends to saturate very rapidly if both μ and η are not increased together, thus originating a narrow zone in which high shear resistance can be reached, as shown in Figure 4.14.

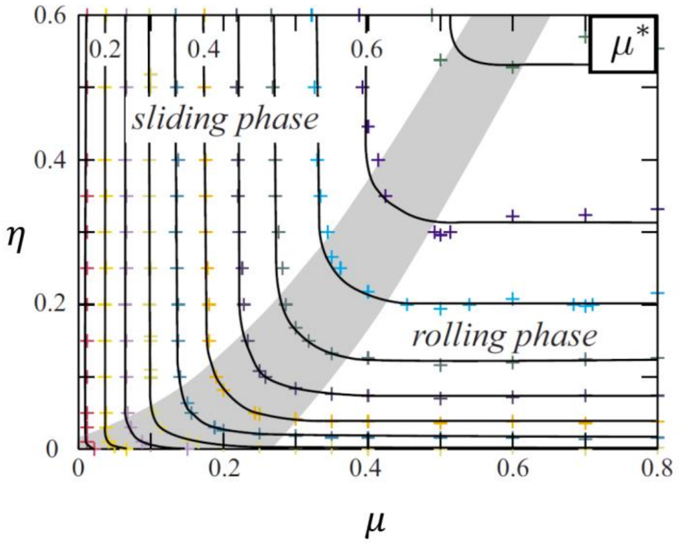

Figure 4.14: Contour map of the internal friction coefficient (μ^*) as function of the rolling friction (η) and sliding friction (μ) (Estrada et al., 2008)

Ai et al. (Ai et al., 2011) summarized previous work classifying rolling resistance models into four categories, highlighting the suitability of each model for different applications. First of all, they defined the coefficient of rolling resistance η as:

$$\eta = \tan(\beta) \tag{4.30}$$

Where β is the maximum slope angle at which the resistant rolling torque balances the torque induced by the body forces acting on the particle.

Regarding the rolling stiffness k_r, they used the 2D Hertzian formulation proposed by Bardet and Huang (Bardet and Huang, 1993).

$$k_r = 2J_n R_r F_n \tag{4.31}$$

Where J_n is a dimensionless coefficient usually between 0.25 and 0.5, and R_r is the common radius defined as $0.5r_{jiang}$

$$R_r = 0.5(r_{jiang}) = \frac{r_1 r_2}{r_1 + r_2} \tag{4.32}$$

The first category of models (Model A) they defined, is the *"directional constant torque models"*, that apply a constant resistant torque (*M)* on a particle, not depending on the relative angular velocity ($\omega_{rel} = \omega_1 - \omega_2$) or on the relative cumulated rotation between two particles (e.g. (Estrada et al., 2008; Zhou et al., 1999)).

$$M = -\frac{\omega_{rel}}{|\omega_{rel}|}\eta R_r F_n \tag{4.33}$$

The negative sign guarantees that the rolling torque *M* is applied in the opposite direction with respect to the relative rotation, in order to resist it.

The second category (Model B) are the *"viscous models"*, in which the rolling resistance moment is function of the angular velocity:

$$M = -\eta R_r F_n(\omega_1 r_1 - \omega_2 r_2) \tag{4.34}$$

The third category of rolling resistance contact models (Model C) are named *"elastic-plastic spring-dashpot"* models, in which there are two components that participate to the final resistant torque applied: the mechanical spring torque and the viscous damping torque. This is the approach used by Iwashita & Oda (1998) and (Jiang et al., 2005) described previously. However, Ai (Ai et al., 2011) argued that their model could work well only if rolling back or cyclic rolling were not involved. Therefore, he proposed a modification introducing a rolling backward part in the constitutive model, as shown in Figure 4.15.

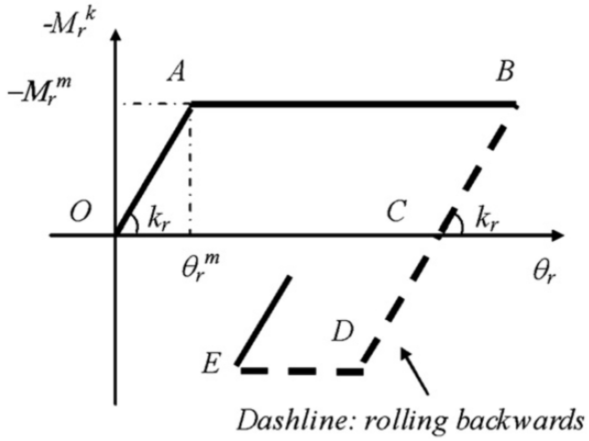

Figure 4.15: Elastic part of the rolling resistance contact model (Ai et al., 2011)

In Figure 4.15, M_r^k is the spring torque and M_r^m is the maximum limit value of the resistant torque having expression:

$$M_r^m = \eta R_r F_n \tag{4.35}$$

Details regarding the viscous part of the rolling resistant torque can be found in (Ai et al., 2011).

The fourth and last category (Model D) included models in which different resistant torques are applied to each particle of the couple in contact, thus violating the equilibrium. These models were not investigated in detail because of their clear inadequacy.

Their simulations were carried out on PFC^{2D} (Itasca, 2008) using the Hertz-Mindlin contact model for the normal and tangential directions and the rolling resistance model for the rotational part. The first set of simulations tried to model a disk rolling on a flat surface, applying an initial translational velocity to it. The second test case simulated a disk rolling up a slope and the third tried to replicate a sandpile formation.

Their outcomes were that the Models A produce a permanent oscillation when the system becomes quasi-stationary, therefore their use is recommended only in dynamic simulations. Models B are good when viscous effects are important, like in rapid motions. It is not suitable for simulations were static zones exist, since the resistant torque *M* goes to zero if there is no relative angular velocity between the particles.

Models C produced the best results in most situations. The viscous damping component can be switched off if the spring torque is fully mobilised in cases where the viscous hysteresis is not important.

4.3.5.2 Calibration approaches

Wensrich and Katterfeld (Wensrich and Katterfeld, 2012) tried to relate analytically the real shape of particles to the rolling resistance torque applied, by studying the effect of eccentricity of the contacts. In particular, they studied the similarity between the torque provided by the rolling resistance contact models previously described (Ai et al., 2011) and the torque produced by the eccentricity of a normal contact on a non-spherical particle.

The authors claimed that rolling resistance can mimic two different mechanisms for energy dissipation: attrition at the contact and the effect of shape, that they considered the main factor. They run several simulations in order to compare the angles of repose of angular shaped particles (clumps) with rolling resistant spheres, implementing the model C proposed by Ai (2010). However, they did not implement the damping torque because they argued that particles oscillation (contrasted by rolling damping, as mentioned by (Ai et al., 2011)) is not so important if the rolling stiffness is high. This is because, in this scenario, the shear damping is fully mobilised (plastic flow takes place) and oscillations are damped without the need of any further rotational damping. Moreover, rolling damping introduces a new parameter difficult to set and calibrate.

The maximum value for the rolling resistance moment is given by:

$$M_r^{max} = \eta R_r |F_n| \tag{4.36}$$

The starting point of their study was the consideration that there must be a physical sense of this applied torque that should be explained by Figure 4.16.

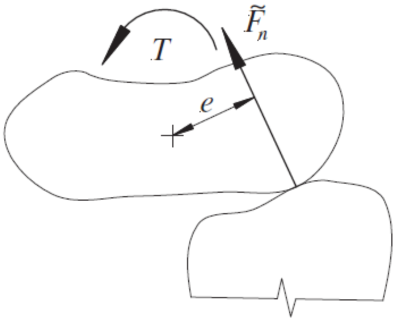

Figure 4.16: Non-spherical particles in contact. The contact normal forces shows an eccentricity that induces a torque (Wensrich and Katterfeld, 2012)

It is evident that the contact normal force does not pass through the particles centres of mass, therefore the eccentricity 'e' creates a rolling moment of magnitude

$$|M| = e \cdot |F_n| \tag{4.37}$$

That should be comparable to any value of rolling resistance torque provided by the mentioned contact models. A comparison between Eq. (4.36) and (4.37) inspires the following relationship:

$$\langle e \rangle \cong \eta R_r \ \rightarrow \eta \cong \frac{\langle e \rangle}{R_r} \tag{4.38}$$

Where $\langle e \rangle$ represents the average eccentricity of all the contacts. It is an easy and elegant method to assess the rolling friction coefficient η from the contact forces eccentricity, however caution must be adopted. In reality, particle shape may resist rotation as well as enhance it, whereas rolling resistance always acts to resist relative rolling between particles.

The first case study they considered are prolate and oblate spheroids, for which the eccentricity may be analytically evaluated, and therefore Eq. (4.38) can be exploited to evaluate rolling friction coefficient as function of the ellipsoids' axis (Figure 4.17). The resultant coefficients of rolling friction had values generally used in practice, encouraging the prosecution of their study.

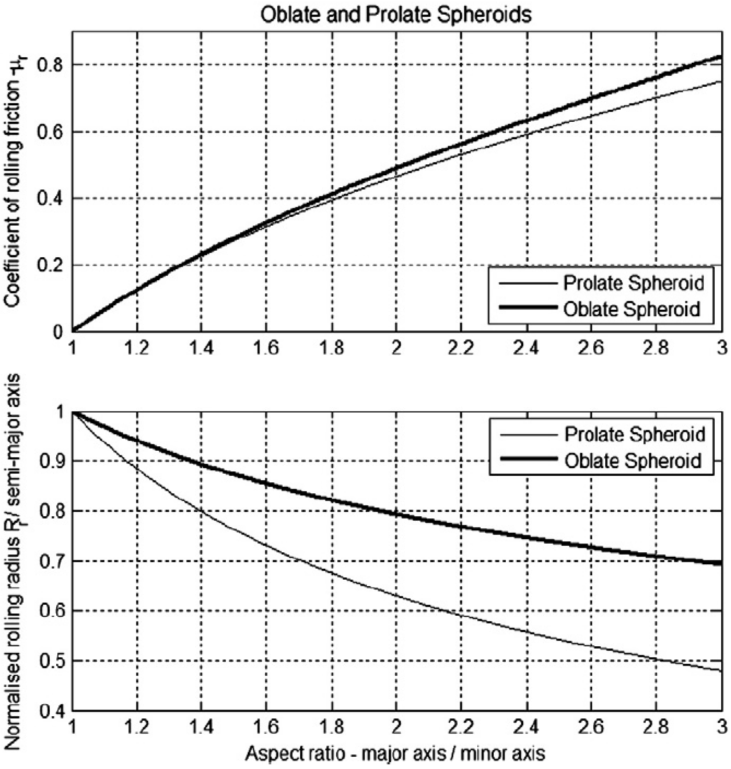

Figure 4.17: Relationships between the coefficient of rolling friction (above) and rolling radius (below) as function of the aspect ratio of the spheroid (Wensrich and Katterfeld, 2012)

In a second case study, Wensrich and Katterfeld took advantage of the simplicity of PFC3D (Itasca) to mimic shape through clumps. In particular, they created binary and ternary clumps of the same diameter for which the shape can be numerically varied from almost spherical to very angular, only playing with the spacing parameter δ shown in Figure 4.18.

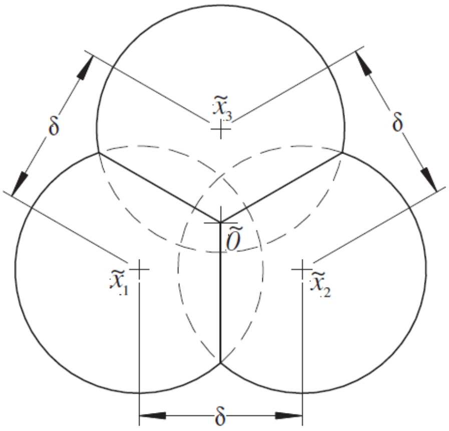

Figure 4.18: Tertiary clump with the spacing parameter δ used to vary the angularity (Wensrich and Katterfeld, 2012)

Then the calculation of the eccentricity of every contact is straightforward since the contact direction passes through the centre of the embedded sphere of the clump in contact, and the relative position of this centre and the clump centre is well known. The average eccentricity was calculated by a Monte-Carlo procedure in order to take into account some difficulties originated by the fact that not all the contact points are possible.

Again in this case, the results showed a good agreement between the coefficient of rolling friction obtained in this study (Figure 4.19) and typical values used in practice. The rolling radius shown in Figure 4.19 is defined as the radius of a sphere having the same volume of the clump.

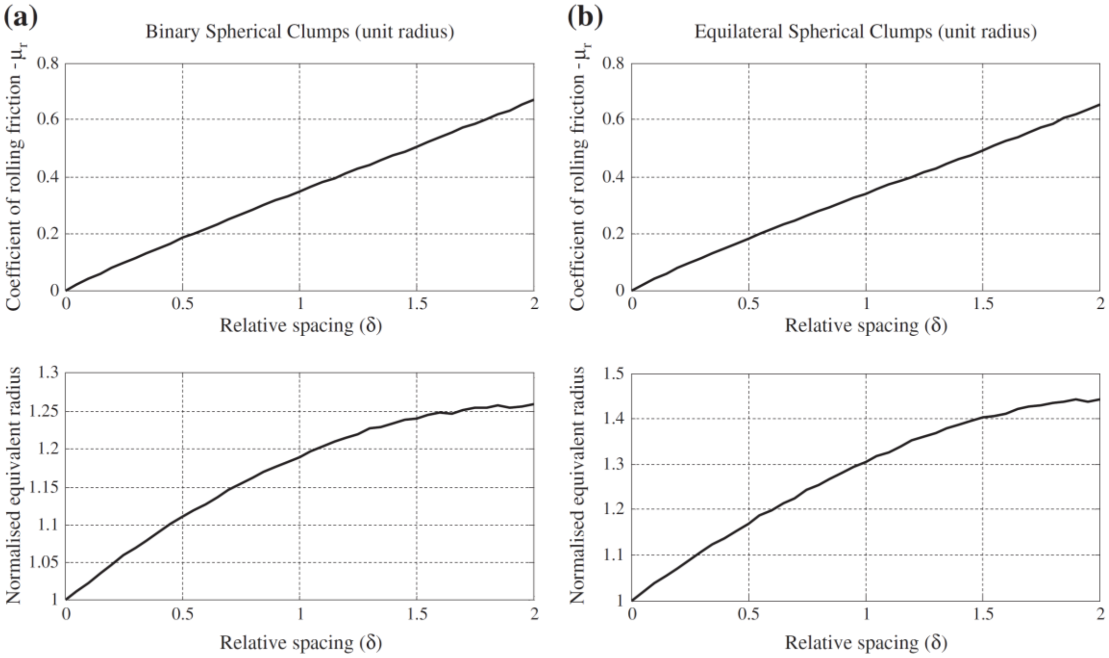

Figure 4.19: Relationships between the coefficient of rolling friction (above) and rolling radius (below) as function of the spacing parameter δ for binary and tertiary clumps (Wensrich and Katterfeld, 2012)

Finally, the validity of the rolling friction coefficient is evaluated by comparing the *angle of repose* (AOR) of three different types of numerical specimen (50 simulations each, varying the coefficient of inter-particle friction μ and initial packing) composed by binary, tertiary clumps and spheres with rolling friction.

Figure 4.20 summarises all the results. It is evident that the AOR is very sensible to shape ($\cong \eta$) for low values of η. Then, it becomes less and less dependent on η when η increases.

The explanation to this trend is that the mechanism of resist rolling must work together with the mechanism of resist sliding, in other words in order to reach high values of OAR both the coefficients of frictions (μ and η) must be high, as the work by (Estrada et al., 2008) highlighted as well.

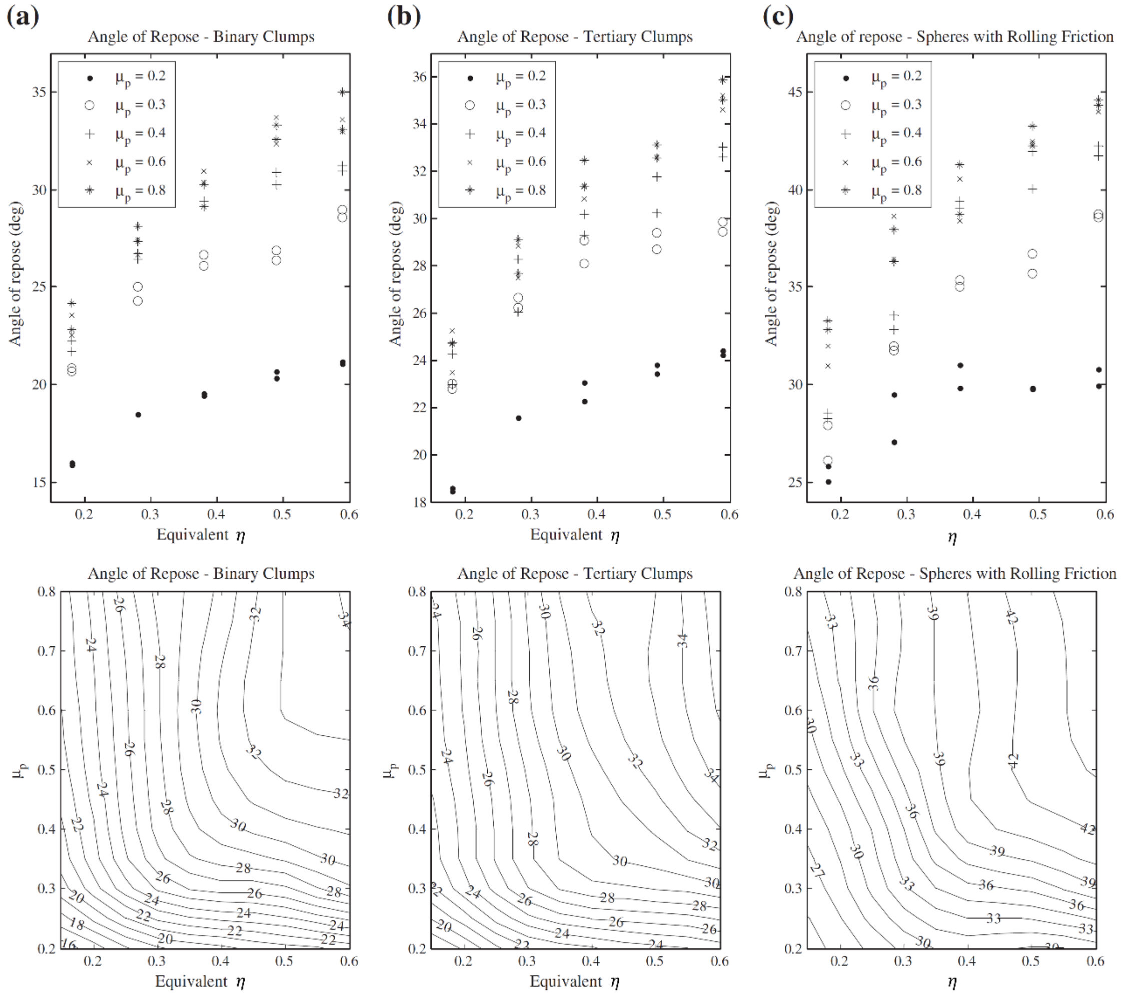

Figure 4.20: Measured angles of repose (AOF) for 150 simulations of different shaped particles in function of the rolling friction and the sliding friction (Wensrich and Katterfeld, 2012)

It can be concluded that rolling resistance induces a “shape-like” behaviour but it must be used with caution. Indeed, the AOR of spherical particles with rolling resistance are at least 10 degrees higher than the ones presented by clumped particles. In particular, it seems that the effect of rolling resistance is much stronger than what Eq. (4.38) provides for the clumps (and non-spherical particles): about half of rolling resistance is required to give similar AORs to the simulations involving clumps. The possible explanation to this evidence is that, as already mentioned, shape may resist as well as encourage rotation whereas rolling resistance always resists rotation.

Cheng (Cheng et al., 2017) proposed an alternative approach to calibrate the microscopic parameters for DEM (*i.e.,* Young modulus, Poisson ratio, rolling stiffness coefficient, sliding friction coefficient, rolling friction coefficient). Their approach, albeit attractive, requires several simulations to be run (at least one hundred) to calibrate one sand type, limiting the practical applicability of their method.

4.4 Effects of particle shape observed in DEM-based studies

Following the different approaches just explained, the effect of particle shape has been extensively investigated using DEM. It is not easy to quantify the influence of shape experimentally, since shape effects are coupled with those of many other parameters. However, DEM allows separating all of these properties (i.e. friction, shape, stiffness, confining pressure, initial porosity, etc.), so that that the effect of shape can be systematically studied.

Figure 4.21 shows the results of a Direct Shear Test (DST) performed by Das (Das, 2007) on two different types of assemblies one constituted by spherical particles, the other by clumps representing Daytona Beach. It is evident that the shear resistance is strongly affected by the use of clumps, that provide a better interlocking between the particles and therefore more resistance than spherical particles.

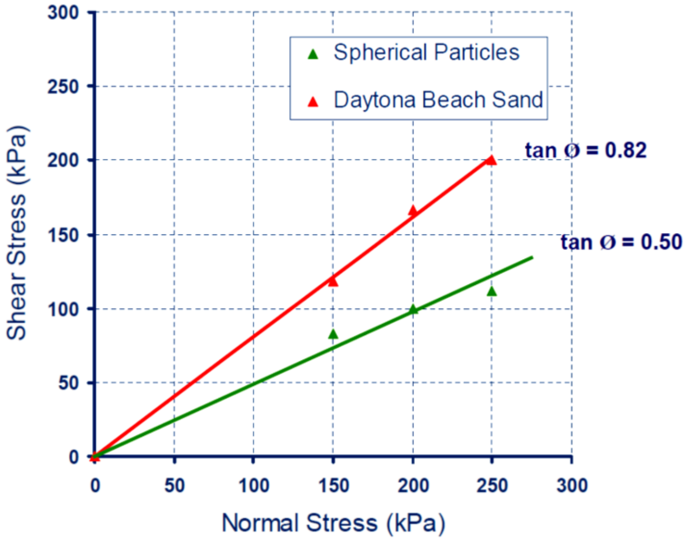

Figure 4.21: Failure envelopes of DEM simulations performed on spherical and clumped particles (Das, 2007)

Figure 4.22 lists the values of the internal friction for both the assemblies, in 2D and 3D. The 3-D simulations with clumps can provide very similar results with respect to the experimental ones.

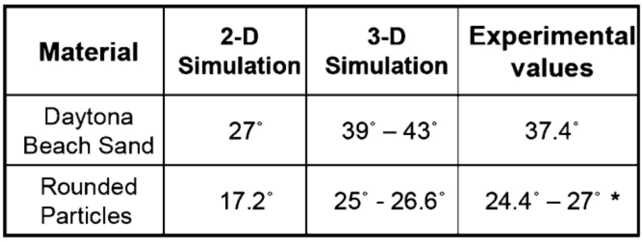

Material	2-D Simulation	3-D Simulation	Experimental values
Daytona Beach Sand	27°	39° – 43°	37.4°
Rounded Particles	17.2°	25° - 26.6°	24.4° – 27° *

Figure 4.22: Values of the internal friction angles for Daytona Beach Sand and rounded particles (from 2D-3D simulations and experiments) (Das, 2007)

Cleary (Cleary, 2008) investigated the effect of particle shape on simple shear flows, performing 2D DEM of flow in a Couette shear cell. The 3D Couette flow consists of a viscous fluid confined in the gap between two rotating cylinder, different flow regimes can start depending on their relative angular velocity. This flow is often studied in two-dimensions using two infinite flat plates, one of which moves tangentially relative the other, with the viscous fluid in the space between the surfaces.

Four different shapes were considered in the DEM study (*i.e.*, circular, squarish, ellipsoidal and brick), ranging from rounded to angular, built using super-quadrics. He showed that particle shape (Aspect Ratio, in particular) has an important effect on the shear flow of granulates. The shear strength of the material increased by a factor 15-30 because of the interlocking between grains and the higher number of contacts. In addition, the flow behaviour changed dramatically with particle shape. In particular, the aspect ratio change induces an effective change in the boundary layer which is reflected on the flow structure.

Similar considerations have been reported by Morigouchi et al. (Moriguchi et al., 2015). They tried to reproduce a granular flow experiment performed by Denlinger & Iverson (Denlinger and Iverson, 2001) using 3D-DEM, consisting in a rectangular flume with a bed surface inclined at 31.4 degrees adjoined to a horizontal runout surface, with a well-rounded quartz sand placed at the top. The comparison between the experimental setup (a) and the numerical model (b) is showed in Figure 4.23.

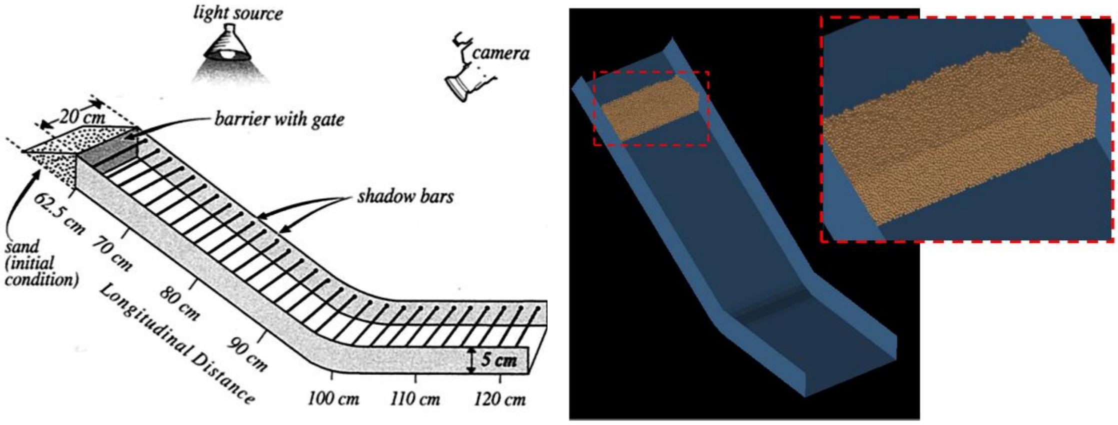

(a) (b)

Figure 4.23: Experimental (a) and numerical (b) models for the granular flow study

Spherical and non-spherical elements (built using clumps) were used in DEM to study the effect of particle shape on the granular flow. The obtained flow behaviours, in terms of velocity and runout distance, were very different depending on the shape of particles. They concluded that particle shape must be considered in numerical simulations to model a realistic granular flow.

Zhou et al. (Zhou et al., 2013) conducted a 2D DEM analysis to investigate the effect of particle shape on the mechanical behaviour of granular materials subjected to quasi-static shearing (*i.e.,* triaxial tests), with particular emphasis on the particles rotations mechanisms. They compared the mechanical responses of numerical samples comprised of (a) disc particles (testing different values of rolling resistance, exploiting the Iwashita & Oda contact model), (b) squared particles and (c) triangular particles, as showed in Figure 4.24.

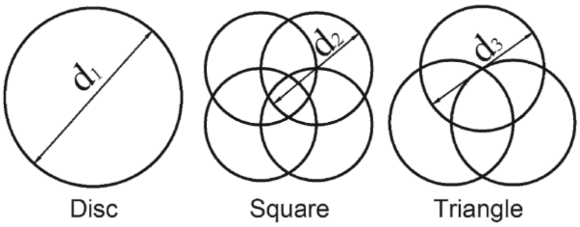

Figure 4.24: Disc, square and triangular particles built using clumps

They demonstrated that both the shear resistance and the volumetric strain are strongly affected by particle shape (Figure 4.25). Indeed, angular particles lead to higher material strength and more dilatant behaviour. In addition, they noted that the shear bands formed after shearing the clump samples present a more "uniform" localisation pattern compared to the more rounded samples that exhibit a clear shear band, as showed in Figure 4.26. Moreover, the strain localisation appears in an earlier stage for the disc samples.

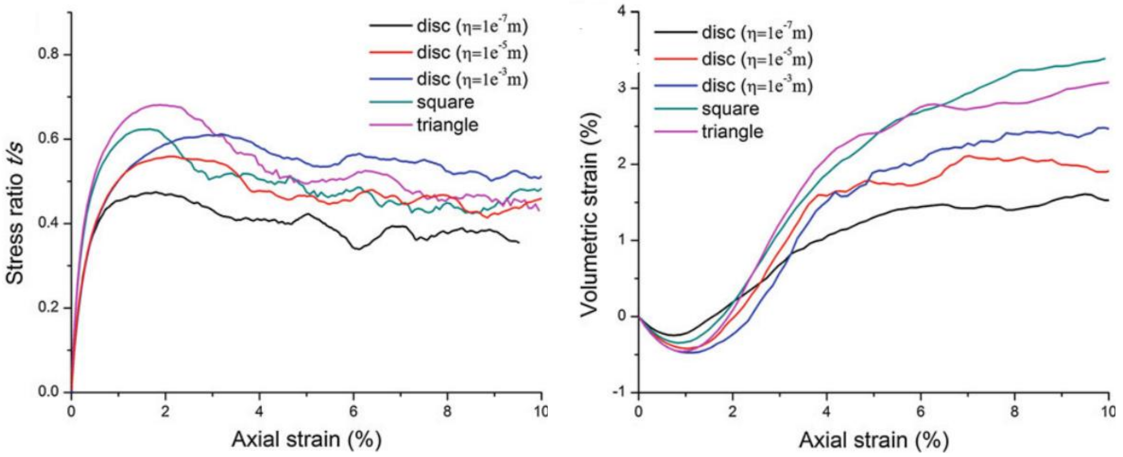

(a) (b)

Figure 4.25: Stress-strain (a) and volumetric (b) responses of the DEM simulations using disks with different rolling resistance values and clumped particles (squares, triangles)

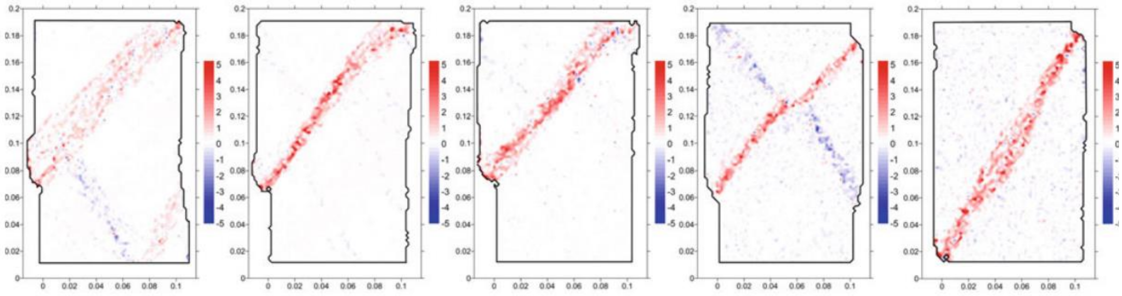
(a) (b) (c) (d) (e)

Figure 4.26: Accumulated shear strain at the critical state (10% axial strain) for spheres with increasing values of rolling resistance (a-b-c), and the clump samples made with squares (d) and triangles (e) as in Figure 4.24.

Ashmawy et al. (Ashmawy et al., 2003) studied the liquefaction susceptibility making use of 2D DEM. He created some numerical samples composed by grains with different shape, representing a range from Glass Beads to Ottawa angular sands. The angularity for a single discrete element representing a grain was obtained making use of a series of overlapping, rigidly connected elements (*i.e.,* clumps). They performed cyclic pure shear tests on the numerical samples and found that the liquefaction susceptibility has a strong relationship with particle shape, but only at low relative densities. Figure 4.27 shows the plot of the cyclic stress ratio (CSR) versus the number of cycles to liquefaction (N) for several samples prepared by static compaction, in order to induce a low void ratio equal to 0.245 for all the samples.

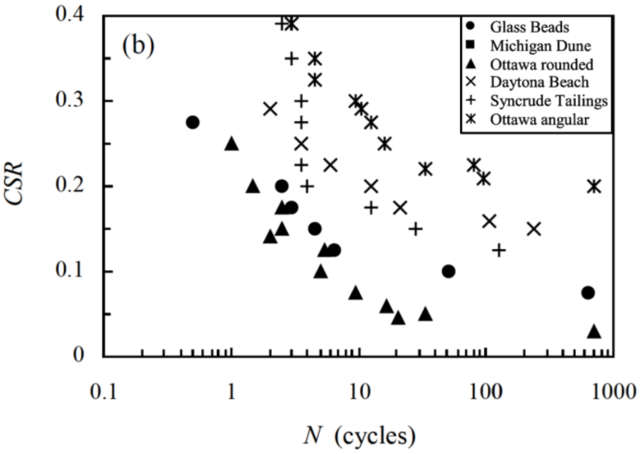

Figure 4.27: Cyclic stress ratio (CSR) versus number of cycles to liquefaction (N) for simulated samples prepared by static compaction (Ashmawy et al., 2003)

It is evident that the highest liquefaction susceptibility corresponds to Glass Beads and Ottawa rounded sand, whereas the angular sands exhibit a higher resistance to liquefaction. This tendency was not found for samples prepared at their maximum index densities.

4.5 Summary

In this Chapter, after a short part explaining the fundamentals of the DEM methodology, it is detailed how the shape of particles can be included in DEM simulations. The main concepts can be summarised as follow:

- Particle shape is computationally expensive to consider but cannot be neglected;
- Non-spherical particles (*i.e.,* superquadrics, polyhedrons, clumps) can be introduced in the simulations but the contact detections are inefficient;
- Freely rotating spheres give a behaviour that is not physical for soils;
- Rolling resistance contact model are widely used as alternative efficient technique to mimic particle shape, but are difficult to calibrate;
- The most popular rolling resistance contact model was proposed by Iwashita & Oda (Iwashita and Oda, 1998).

References Part I

Ai, J., Chen, J.F., Rotter, J.M., Ooi, J.Y., 2011. Assessment of rolling resistance models in discrete element simulations. Powder Technol. 206, 269–282. https://doi.org/10.1016/j.powtec.2010.09.030

Al-Raoush, R., 2007. Microstructure characterization of granular materials. Phys. A Stat. Mech. its Appl. 377, 545–558. https://doi.org/10.1016/j.physa.2006.11.090

Alshibli, K.A., Druckrey, A.M., Al-Raoush, R.I., Weiskittel, T., Lavrik, N. V., 2015. Quantifying Morphology of Sands Using 3D Imaging. J. Mater. Civ. Eng. 27. https://doi.org/10.1061/(ASCE)MT.1943-5533.0001246

Altuhafi, F., O'Sullivan, C., Cavarretta, I., 2012. Analysis of an image-based method to quantify the size and shape of sand particles. J. Geotech. Geoenvironmental Eng. 139, 1290–1307. https://doi.org/10.1061/(ASCE)GT.1943-5606.0000855.

Altuhafi, F.N., Coop, M.R., 2011. Changes to particle characteristics associated with the compression of sands. Géotechnique 61, 459–471. https://doi.org/10.1680/geot.9.P.114

Arasan, S., Akbulut, S., 2008. Determination of grain-size distribution of soils with image analysis, in: National Soil Mechanic and Foundation Engineering Congress. Konya, Turkey, pp. 323–332.

Arasan, S., Akbulut, S., Hasiloglu, A.S., 2011. Effect of particle size and shape on the grain-size distribution using Image analysis. Int. J. Civ. Struct. Eng. 1, 968–985. https://doi.org/10.6088/ijcser.00202010083

Aschenbrenner, B.C., 1956. A new method of expressing particle sphericity . J. Sediment. Res. 26, 15–31. https://doi.org/10.1306/74D704A7-2B21-11D7-8648000102C1865D

Ashmawy, A.K., Sukumaran, B., Hoang, V.V., 2003. Evaluating the influence of particle shape on liquefaction behavior using discrete element modeling, in: Proc. Offshore and Polar Engeneering Conference. Honolulu, Hawaii, pp. 1–8.

Bardet, J.P., 1994. Observations on the effects of particle rotations on the failure of idealized granular materials 18, 159–182.

Bardet, J.P., Huang, Q., 1993. Rotational stiffness of cylindrical particle contacts, in: 2nd International Conference on Micromechanics of Granular Media. A.A. Balkema, Birmingham, pp. 39–43.

Barret, P.J., 1980. The shape of rock particle, a critical review. Sedimentology 27, 291–303. https://doi.org/10.1111/j.1365-3091.1980.tb01179.x

Barton, N., Choubey, V., 1977. The shear strength of rock joints in theory and practice Extension fracturing in tunnels View project Illustrated guide to the Q-system View project. Rock Mech. 10, 1–54. https://doi.org/10.1007/BF01261801

Barton, N., Kjaernsli, B., 1981. SHEAR STRENGTH OF ROCKFILL. J. Geotech. Geoenvironmental Eng. 107, 873–891.

Bathe, K.-J., Wilson, E.L., 1976. Numerical methods in finite element analysis. Prentice-Hall.

Bhushan, B., 2001. Surface roughness analysis and measurement techniques, 1st ed.

Blott, S.J., Pye, K., 2008. Particle shape: A review and new methods of characterization and classification. Sedimentology 55, 31–63. https://doi.org/10.1111/j.1365-3091.2007.00892.x

Bolton, M.D., 1986. The strength and dilatancy of sands. Géotechnique 36, 65–78. https://doi.org/10.1680/geot.1986.36.1.65

Butlanska, J., 2014. Cone penetration tests in a virtual calibration chamber. PhD Thesis. Universitat Politecnica de Catalunya (UPC). https://doi.org/10.1680/geot.9.p.067

Cailleux, A., 1947. L'indice d'emoussé des grains de sable et grès. Rev. Géomorphologie Dyn. 3, 78–87.

Cailleux, A., 1945. Distinction des galets marins et fluviatiles. Bull. la Société géologique Fr. 15, 375–404.

Calvetti, F., 2008. Discrete modelling of granular materials and geotechnical problems. Eur. J. Environ. Civ. Eng. 12, 951–965. https://doi.org/10.3166/EJECE.12.951-965

Calvetti, F., Nova, R., 2004. Micromechanical approach to slope stability analysis, Degradations and Instabilities in Geomaterials. Springer Vienna, Vienna.

https://doi.org/10.1007/978-3-7091-2768-1_8

Calvetti, F., Prisco, C., Nova, R., 2004. Experimental and Numerical Analysis of Soil – Pipe Interaction. J. Geotech. Geoenvironmental Eng. 130, 1292–1299. https://doi.org/10.1061/(ASCE)1090-0241(2004)130

Calvetti, F., Viggiani, G., Tamagnini, C., 2003. A numerical investigation of the incremental behavior of granular soils. Riv. Ital. di Geotec. 37, 11–29.

Cavarretta, I., 2009. The influence of particle characteristics on the behaviour of coarse grained soils. Imperial College London. https://doi.org/10.1680/geot.2010.60.6.413

Cavarretta, I., Coop, M., O'Sullivan, C., 2010. The influence of particle characteristics on the behaviour of coarse grained soils. Géotechnique 60, 413–423. https://doi.org/10.1680/geot.2010.60.6.413

Cheng, K., Wang, Y., Yang, Q., Mo, Y., Guo, Y., 2017. Determination of microscopic parameters of quartz sand through tri-axial test using the discrete element method. Comput. Geotech. 92, 22–40. https://doi.org/10.1016/j.compgeo.2017.07.017

Cho, A.G., Dodds, J., Santamarina, J.C., 2006. Particle Shape Effects on Packing Density , Stiffness and Strength – Natural and Crushed Sands. J. Geotech. Geoenvironmental Eng. 132, 591–602. https://doi.org/10.1061/(ASCE)1090-0241(2006)132:5(591)

Ciantia, M.O., Arroyo, M., Calvetti, F., Gens, A., 2015. An approach to enhance efficiency of DEM modelling of soils with crushable grains. Géotechnique 65, 91–110. https://doi.org/10.1680/geot.13.P.218

Ciantia, M.O., Arroyo, M., O'Sullivan, C., Gens, A., Liu, T., 2019a. Grading evolution and critical state in a discrete numerical model of Fontainebleau sand. Géotechnique 69, 1–15. https://doi.org/10.1680/jgeot.17.P.023

Ciantia, M.O., Arroyo, M., O'Sullivan, C., Gens, A., Liu, T., 2019b. Grading evolution and critical state in a discrete numerical model of Fontainebleau sand. Géotechnique 69, 1–15. https://doi.org/10.1680/jgeot.17.p.023

Cleary, P.W., 2008. The effect of particle shape on simple shear flows. Powder Technol. 179, 144–163. https://doi.org/10.1016/j.powtec.2007.06.018

Coetzee, C.J., 2016. Calibration of the discrete element method and the effect of particle shape. Powder Technol. 297, 50–70. https://doi.org/10.1016/j.powtec.2016.04.003

Cundall, P.A., 1988a. Computer Simulations of Dense Sphere Assemblies, Studies in Applied Mechanics. Elsevier B.V. https://doi.org/10.1016/B978-0-444-70523-5.50021-7

Cundall, P.A., 1988b. Formulation of a three-dimensional distinct element model-Part I. A scheme to detect and represent contacts in a system composed of many polyhedral blocks. Int. J. Rock Mech. Min. Sci. Geomech. 25, 107–116. https://doi.org/10.1016/0148-9062(88)92293-0

Cundall, P.A., Strack, O.D.L., 1979. A discrete numerical model for granular assemblies. Géotechnique 29, 47–65. https://doi.org/10.1680/geot.1979.29.1.47

Das, N., 2007. Modeling Three-Dimensional Shape of Sand Grains Using Discrete Element Method. University of South Florida. https://doi.org/10.1017/CBO9781107415324.004

Denlinger, R.P., Iverson, R.M., 2001. Flow of variably fluidized granular masses across three-dimensional terrain 2. Numerical predictions and experimental tests. J. Geophys. Res. 106, 553–566.

Druckrey, A.M., Alshibli, K.A., Al-Raoush, R.I., 2016. 3D characterization of sand particle-to-particle contact and morphology. Comput. Geotech. 74, 26–35. https://doi.org/10.1016/j.compgeo.2015.12.014

Elias, J., 2013. DEM simulation of railway ballast using polyhedral elemental shapes, in: PARTICLES 2013 - III International Conference on Particle-Based Methods – Fundamentals and Applications. Barcelona, pp. 1–10.

Estrada, N., Taboada, A., Radjaï, F., 2008. Shear strength and force transmission in granular media with rolling resistance. Phys. Rev. E 78, 1–11. https://doi.org/10.1103/PhysRevE.78.021301

Fernlund, J.M.R., 1998. The effect of particle form on sieve analysis: a test by image analysis. Eng. Geol. 50, 111–124. https://doi.org/10.1016/S0013-7952(98)00004-0

Folk, R.L., 1955. Student Operator Error in Determination of Roundness, Sphericity, and Grain size. J. Sediment. Res. 25, 297–301.

Fonseca, J., O'Sullivan, C., Coop, M.R., Lee, P.D., 2012. Non-invasive characterization of particle morphology of natural sands. Soils Found. 52, 712–722. https://doi.org/10.1016/j.sandf.2012.07.011

G W Mustoe, B.G., Miyata, M., 2001. MATERIAL FLOW ANALYSES OF NONCIRCULAR-SHAPED GRANULAR MEDIA USING DISCRETE ELEMENT METHODS. J. Eng. Mech. 127, 1017–1026.

Gan, J.Q., Yu, A.B., Zhou, Z.Y., 2016. DEM simulation on the packing of fine ellipsoids. Chem. Eng. Sci. 156, 64–76. https://doi.org/10.1016/j.ces.2016.09.017

Garcia, X., Latham, J.-P., Xiang, J., Harrison, J.P., 2009. A clustered overlapping sphere algorithm to represent real particles in discrete element modelling. Géotechnique 59, 779–784. https://doi.org/10.1680/geot.8.T.037

Gilbert, E., Johnson, D., Keerthi, S., 1988. A fast procedure for computing the distance between complex objects in three space. J. Robot. Autom. 4, 193–203.

Hayakawa, Y., Oguchi, T., 2005. Evaluation of gravel sphericity and roundness based on surface-area measurement with a laser scanner. Comput. Geosci. 31, 735–741. https://doi.org/10.1016/j.cageo.2005.01.004

Hentz, S., Donzé, F. V, Daudeville, L., 2004. Discrete element modelling of concrete submitted to dynamic loading at high strain rates. Comput. Struct. 82, 2509–2524. https://doi.org/10.1016/j.compstruc.2004.05.016

Holt, R.M., Kjølaas, J., Larsen, I., Li, L., Gotusso Pillitteri, A., Sønstebø, E.F., 2005. Comparison between controlled laboratory experiments and discrete particle simulations of the mechanical behaviour of rock. Int. J. Rock Mech. Min. Sci. 42, 985–995. https://doi.org/10.1016/j.ijrmms.2005.05.006

Holubec, I., D'Appolonia, E., 1973. Effect of Particle Shape on the Engineering Properties of Granular Soils, in: Evaluation of Relative Density and Its Role in Geotechnical Projects Involving Cohesionless Soils. ASTM International, pp. 304–318. https://doi.org/10.1520/STP37879S

Ishibashi, I., Sherif, M.A., Cheng, W.-L., 1982. The effects of soil parameters on pore-pressure-rise and liquefactio prediction. Soils Found. 22, 39–48.

ISO, 2006. Representation of results of particle size analysis. Part 1-6. Part 6: Descrip- tive and quantitative representation of particle shape and morphology., in: Draft

International Standard ISO/DIS 9276. Geneve.

Itasca Consulting Group Inc., 2014. PFC — Particle Flow Code, Ver. 5.0. Minneapolis: Itasca.

Iwashita, K., Oda, M., 2000. Micro-deformation mechanism of shear banding process based on modified distinct element method. Powder Technol. 109, 192–205. https://doi.org/10.1016/S0032-5910(99)00236-3

Iwashita, K., Oda, M., 1998. Rolling resistance at contacts in simulation of shear band development by DEM. J. Eng. Mech. 124, 285–292. https://doi.org/10.1061/(ASCE)0733-9399(1998)124:3(285)

James E. Dobkins, Jr., R.L.F., 1970. Shape Development On Tahiti-Nui. J. Sediment. Res. 40, 1167–1203.

Janke, N.C., 1966. Effect of Shape Upon the Settling Velocity of Regular Convex Geometric Particles. J. Sediment. Res. 36, 370–376.

Janoo, V.C., 1998. Quantification of Shape , Angularity , and Surface Texture of Base Course Materials. US Army Corps of Engineers. Cold Region Research and Engineering Laboratory.

Jerves, A.X., Kawamoto, R.Y., Andrade, J.E., 2016. Effects of grain morphology on critical state: A computational analysis. Acta Geotech. 11, 493–503. https://doi.org/10.1007/s11440-015-0422-8

Jiang, M.J., Liu, J.D., Arroyo, M., 2016. Numerical evaluation of three non-coaxial kinematic models using the distinct element method for elliptical granular materials. Int. J. Numer. Anal. Methods Geomech. 40, 2468–2488. https://doi.org/10.1002/nag.2540

Jiang, M.J.J., Yu, H.-S., Harris, D., 2005. A novel discrete model for granular material incorporating rolling resistance. Comput. Geotech. 32, 340–357. https://doi.org/10.1016/j.compgeo.2005.05.001

Kawamoto, R., Andò, E., Viggiani, G., Andrade, J.E., 2018. All you need is shape: Predicting shear banding in sand with LS-DEM. J. Mech. Phys. Solids 111, 375–392. https://doi.org/10.1016/j.jmps.2017.10.003

Komba, J.J., Anochie-Boateng, J.K., van der Merwe Steyn, W., 2013. Analytical and Laser

Scanning Techniques to Determine Shape Properties of Aggregates. Transp. Res. Rec. J. Transp. Res. Board 2335, 60–71. https://doi.org/10.3141/2335-07

Krumbein, W.C., 1941. Measurement and Geological Significance of Shape and Roundness of Sedimentary Particles. J. Sediment. Res. 11, 64–72.

Krumbein, W.C., Sloss, L.L., 1963. Stratigraphy and Sedimentation, Second Edition. San Francisco.

Krumbein, W.C., Sloss, L.L., 1951. Stratigraphy and Sedimentation, in: W. H. Freeman & Co (Ed.), Geological Journal. John Wiley & Sons, Ltd, San Francisco. https://doi.org/10.1002/gj.3350010110

Kuenen, P.H., 1956. Experimental Abrasion of Pebbles: 2. Rolling by Current. J. Geol. 64, 336–368. https://doi.org/10.1086/626370

Lane, J.E., Metzger, P.T., Wilkinson, R.A., 2010. A Review of Discrete Element Method (DEM) Particle Shapes and Size Distributions for Lunar Soil, NASA Center for Aerospace information.

Langston, P., Ai, J., Yu, H.-S., 2013. Simple shear in 3D DEM polyhedral particles and in a simplified 2D continuum model. Granul. Matter 15, 595–606. https://doi.org/10.1007/s10035-013-0421-0

Lees, G., 1964. The measurement of particle shape and its influence in engineering materials. Br. Granite Whinstone Fed.

Lewis, D.W., McConchie, D., 1994. Practical Sedimentology.

Li, Y., Xu, Y., Thornton, C., 2005. A comparison of discrete element simulations and experiments for Fsandpiles_ composed of spherical particles. Powder Technol. 160, 219–228. https://doi.org/10.1016/j.powtec.2005.09.002

Lim, W.L., McDowell, G.R., 2005. Discrete element modelling of railway ballast. Granul. Matter 7, 19–29. https://doi.org/10.1007/s10035-004-0189-3

Liu, Q.B., Lehane, B.M., 2013. The influence of particle shape on the (centrifuge) cone penetration test (CPT) end resistance in uniformly graded granular soils. Géotechnique 60, 111–121. https://doi.org/10.1139/t06-037

Lu, G., Third, J.R., Müller, C.R., 2015. Discrete element models for non-spherical particle systems: From theoretical developments to applications. Chem. Eng. Sci. 127, 425–

465. https://doi.org/10.1016/j.ces.2014.11.050

Lu, M., McDowell, G.R., 2008. Discrete element modelling of railway ballast under triaxial conditions. Geomech. Geoengin. An Int. J. 3, 37-257–270. https://doi.org/10.1007/s10035-016-0663-8

Lu, M., McDowell, G.R., 2007. The importance of modelling ballast particle shape in the discrete element method. Granul. Matter 9, 69–80. https://doi.org/10.1007/s10035-006-0021-3

Mackay, A.L., 1962. A dense non-crystallographic packing of equal spheres. Acta Crystallogr. 15, 916–918. https://doi.org/10.1107/s0365110x6200239x

Mora, C.F., Kwan, A.K.H., 2000. Sphericity , shape factor and convexity measurement of coarse aggregate for concrete using digital image processing. Cem. Concr. Res. 30, 351–358.

Mora, C.F., Kwan, A.K.H., Chan, H.C., 1998. Particle size distribution analysis of coarse aggregate using digital image processing. Cem. Concr. Res. 28, 921–932. https://doi.org/http://dx.doi.org/10.1016/S0008-8846(98)00043-X

Moriguchi, S., Terada, K., Kato, J., Takase, S., 2015. Effects of grain size and grain shape in granular flow simulations 1453–1458.

Nadimi, S., Fonseca, J., 2018. A micro finite-element model for soil behaviour. Geotechnique 68, 364–369. https://doi.org/10.1680/jgeot.16.P.163

Nadimi, S., Fonseca, J., 2017. Single-Grain Virtualization for Contact Behavior Analysis on Sand. J. Geotech. Geoenvironmental Eng. 143, 06017010. https://doi.org/10.1061/(ASCE)GT.1943-5606.0001740

Nadimi, S., Fonseca, J., Andò, E., Viggiani, G., 2019. A micro finite-element model for soil behaviour: experimental evaluation for sand under triaxial compression. Géotechnique. accepted m. https://doi.org/10.1680/jgeot.18.t.030

Ng, T.T., 1994. Numerical simulations of granular soil using elliptical particles. Comput. Geotech. 16, 153–169. https://doi.org/10.1016/0266-352X(94)90019-1

O'Sullivan, C., 2011. Particulate Discrete Element Modelling: A geomechanics perspective. Taylor & Francis.

O'Sullivan, C., Bray, J.D., 2004. Selecting a suitable time step for discrete element simulations that use the central difference time integration scheme. Eng. Comput. 21, 278–303. https://doi.org/10.1108/02644400410519794

Otsubo, M., O'Sullivan, C., Shire, T., 2017. Empirical assessment of the critical time increment in explicit particulate discrete element method simulations. Comput. Geotech. 86, 67–79. https://doi.org/10.1016/j.compgeo.2016.12.022

Ouhbi, N., Voivret, C., Perrin, G., Roux, J.-N., 2016. Railway Ballast: Grain Shape Characterization to Study its Influence on the Mechanical Behaviour. Procedia Eng. 143, 1120–1127. https://doi.org/10.1016/J.PROENG.2016.06.150

Podlozhnyuk, A., Pirker, S., Kloss, · Christoph, 2017. Efficient implementation of superquadric particles in Discrete Element Method within an open-source framework. Comput. Part. Mech. 4, 101–118. https://doi.org/10.1007/s40571-016-0131-6

Powers, M.C., 1953. A New Roundness Scale for Sedimentary Particles. J. Sediment. Res. 23, 117–119.

Roscoe, K.H., Schofield, a. N., Wroth, C.P., 1958. On the yielding of soil. Géotechnique 8, 22–52. https://doi.org/10.1680/geot.1958.8.1.22

Rothenburg, L., Bathurst, R.J., 1992. Micromechanical features of granular assemblies with planar elliptical particles. Géotechnique 42, 79–95. https://doi.org/10.1680/geot.1992.42.1.79

Rothenburg, L., Bathurst, R.J., 1989. Analytical study of induced anisotropy granular materials in idealized. Geotechnique 39, 601–614.

Rousé, P.C., Fannin, R.J., Shuttle, D.A., 2008. Discussion: Influence of roundness on the void ratio and strength of uniform sand. Géotechnique 58, 681–681. https://doi.org/10.1680/geot.2008.58.8.681

Santamarina, J., Cho, G., 2004. Soil behaviour: The role of particle shape, in: Advances in Geotechnical Engineering. Proceedings of the Skempton Conference. London, pp. 1–14. https://doi.org/http://pmrl.ce.gatech.edu/tools/santamarina_cho_2004.pdf

Schofield, A.N., Wroth, C.P., 1968. Critical State Soil Mechanics. https://doi.org/10.1111/j.1475-2743.1987.tb00718.x

Scott, G.D., Kilgour, D.M., 1969. The density of random close packing of spheres. J. Phys.

D. Appl. Phys. 2, 311. https://doi.org/10.1088/0022-3727/2/6/311

Sneed, E.D., Folk, R.L., 1958. Pebbles in the Lower Colorado River, Texas. A Study in Particle Morphogenesis. J. Geol. 66, 114–150.

Sun, Y., Indraratna, B., Nimbalkar, S., 2014. Three-dimensional characterisation of particle size and shape for ballast. Geotech. Lett. 4, 197–202. https://doi.org/10.1680/geolett.14.00036

Swan, B., 1974. Measures of Particle Roundness: A NOTE. J. Sediment. Res. 44, 572–577.

Thornton, C., 2000. Numerical simulations of deviatoric shear deformation of granular media. Géotechnique 50, 43–53. https://doi.org/10.1680/geot.2000.50.1.43

Thornton, C., Randall, C.W., 1988. Applications of Theoretical Contact Mechanics to Solid Particle System Simulation. Stud. Appl. Mech. 20, 133–142. https://doi.org/10.1016/B978-0-444-70523-5.50023-0

Torquato, S., Truskett, T.M., Debenedetti, P.G., 2000. Is Random Close Packing of Spheres Well Defined? Phys. Rev. Lett. 84, 2064–2067.

Tse, R., Cruden, D.M., 1979. Estimating joint roughness coefficients. Int. J. Rock Mech. Min. Sci. 16, 303–307. https://doi.org/10.1016/0148-9062(79)90241-9

Vaid, Y., Chern, J., Tumi, H., 1985. Confining pressure, Grain angularity and Liquefaction. J. Geotech. Eng. 111, 1229–1235.

Verlet, L., 1967. Computer “Experiments” on Classical Fluids. I. Thermodynamical Properties of Lennard-Jones Molecules. Phys. Rev. 159, 98–103.

Wadell, H., 1933. Sphericity and Roundness of Rock Particles. J. Geol. 41, 310–331. https://doi.org/10.1086/624040

Wadell, H., 1932. Volume, Shape, and Roundness of Rock Particles. J. Geol. 40, 443–451.

Wensrich, C.M., Katterfeld, A., 2012. Rolling friction as a technique for modelling particle shape in DEM. Powder Technol. 217, 409–417. https://doi.org/10.1016/j.powtec.2011.10.057

Wentworth, C.K., 1933. The Shapes of Rock Particles: A Discussion. J. Geol. 41, 306–309.

Wentworth, C.K., 1922. The shapes of beach pebbles. US Geol. Surv. Prof. Pap. 131, 75–83.

Wentworth, C.K., 1919. A Laboratory and Field Study of Cobble Abrasion. J. Geol. 27, 507–521.

Williams, E.M., 1965. A Method of Indicating Pebble Shape with One Parameter: NOTES. J. Sediment. Res. 35, 993–996.

Wright, P.J.F., 1955. A method of measuring the surface texture of aggregate. Mag. Concr. Res. 7, 151–160. https://doi.org/10.1680/macr.1955.7.21.151

Yang, X., You, Z., Hu, J., 2017. Three-Dimensional Finite-Element Modeling for Asphalt Concrete Using Visual Cross-Sectional Imaging and Indirect Element Meshing Based on Discrete-Element Models. J. Mater. Civ. Eng. 29, 04016182. https://doi.org/10.1061/(ASCE)MT.1943-5533.0001704

Zhao, B., Wang, J., 2016. 3D quantitative shape analysis on form, roundness, and compactness with micro-CT. Powder Technol. 291, 262–275. https://doi.org/10.1016/j.powtec.2015.12.029

Zheng, J., Hryciw, R.D., 2016. Roundness and Sphericity of Soil Particles in Assemblies by Computational Geometry. J. Comput. Civ. Eng. 30, 1–13. https://doi.org/10.1061/(ASCE)CP.1943-5487.0000578.

Zheng, J., Hryciw, R.D., 2015. Traditional soil particle sphericity, roundness and surface roughness by computational geometry. Géotechnique 65, 494–506. https://doi.org/10.1680/geot.14.P.192

Zhou, B., Huang, R., Wang, H., Wang, J., 2013. DEM investigation of particle anti-rotation effects on the micromechanical response of granular materials. Granul. Matter 15, 315–326. https://doi.org/10.1007/s10035-013-0409-9

Zhou, B., Wang, J., Zhao, B., 2015. Micromorphology characterization and reconstruction of sand particles using micro X-ray tomography and spherical harmonics. Eng. Geol. 184, 126–137. https://doi.org/10.1016/j.enggeo.2014.11.009

Zhou, Y.C., Wright, B.D., Yang, R.Y., Xu, B.H., Yu, A.B., 1999. Rolling friction in the dynamic simulation of sandpile formation". Phys. A Stat. Mech. its Appl. 269, 536–553. https://doi.org/10.1016/j.physa.2005.01.019

Zingg, T., 1935. Beitrag zur Schotteranalyse. Schweizerische Mineral. Petrogr. Mitteilungen. https://doi.org/10.3929/ethz-a-000103455

Part II: Experimental dataset and image analysis

5

X-Rays micro-computed tomography for geomaterials

5.1 Introduction

The aim of this Chapter is to give a short overview on the methods, procedures and materials that were used to procure the data that was taken as starting point for the work described in the next two chapters. It is based on previous work, not done by the author, but it is reported here to give the reader adequate understanding of the thesis contribution. A full detailed explanation of the aspects treated in the current Chapter can be found in the doctoral thesis by Edward Andò (Andò, 2013), specifically in Chapters 2, 3 and 4.

The first part of this Chapter (5.2) describes the basis of x-rays tomography, with emphasis on the experimental equipment located at Laboratoire 3SR of "Université Grenoble Alpes" (France).

The second part (Chapter 5.3) aims to detail the experimental campaign which is used as starting point of this doctoral work. In particular, the experimental data consists in a series of triaxial tests and relative 3D x-rays scans performed on different sands. Andò (2013) performed a series of test at different confining pressures (100kPa and 300kPa) on three different sands (Caicos, Hostun and Ottawa sands) having considerably different grain shape. In this work, the two extreme ranging angular and rounded sands are deeply investigated, respectively Hostun sand (Chapter 5.3.1) and Caicos ooids (Chapter 5.3.2). Some results about Ottawa sand (medium angular sand) have also been reported in Chapter 5.3.3 because then used for validation in a subsequent stage of the project (the numerical simulations presented in Chapter 8).

All the triaxial tests have been scanned during time using x-ray micro-tomography. It means the triaxial experiments were performed into the triaxial cell which is located into the 3SR Laboratory's x-rays scanner. Several x-rays images are taken during the execution of each test, resulting in a series of 3-D scans of the specimen for several loading steps.

Subsequently, each 3D x-rays image can be studied by image analysis procedures. Chapter 5.4 briefly describes how the images are *binarised* in order to separate the solid phase and the voids, *segmented*, in order to separate the single inter-connected solid phase in individual particles, and finally *labelled*, in order to assign an integer value (a name) to each grain within the specimen.

5.2 X-rays tomographic equipment

The use of x-rays micro-tomography for studying geomaterials is relatively recent, the main advantage of x-rays in every field of science is the fact that it is a *non-destructive* technique. In other words, it is possible to extract many useful information from an object without physically touching it, thus without inducing irreversible damage. Moreover, x-rays are sensitive to the mass density, therefore the solid and void phases of granular materials, like the ones studied in this doctoral work, can be easily detected and distinguished. Indeed, the grains stop x-rays transmission more than the surrounding air, resulting in different grey-scale values on a radiograph. The same concept is applied in medicine, allowing distinguishing the bones from the flesh. However, a radiograph is a two-dimensional measurement representing the amount of photons which are adsorbed by each point of an object. X-ray tomography was developed during the 1960s. Tomography is a technique that consists in taking a series of radiograph of the object, in order to reconstruct a three-dimensional image of it. Usually, in industrial/laboratory applications, the object is rotated around one axis allowing the sequence of image to be taken from different perspectives.

The x-ray source emits a cone beam that travels through the specimen and terminates on the x-ray detector. The specimen can be approached to the source allowing the scan to be enlarged without losing resolution, although the field of view is then reduced.

Figure 5.1 shows a photograph of the experimental equipment of the Laboratoire 3SR x-ray scanner.

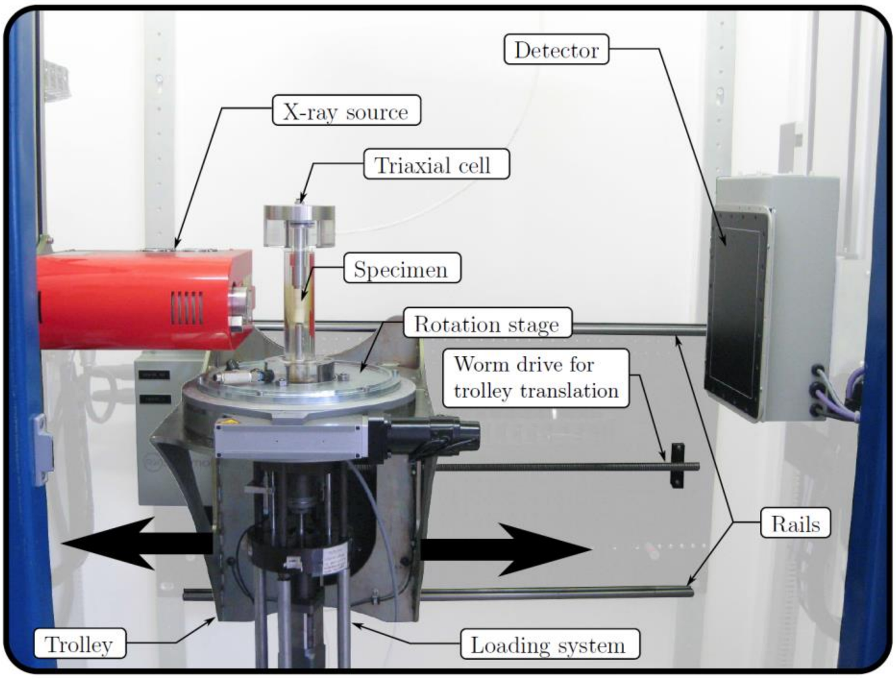
Detector
X-ray source
Triaxial cell
Specimen
Rotation stage
Worm drive for trolley translation
Rails
Trolley
Loading system

Figure 5.1: Laboratoire 3SR x-rays scanner equipment (Andò, 2013)

The specimen is located into the triaxial cell, which is mounted onto the rotation stage. This element is hollow, so that the experimental equipment can pass through it for being scanned.

The detector governs the special resolution of the radiographs, indeed the number of pixels in the detector is fixed (in the Laboratoire 3SR's detector, a pixel measures 127 µm). However, it is possible to zoom in the specimen by translating it closer to the source, as mentioned above. As an example, a radiograph of a cylindrical specimen ready to be tested in triaxial conditions is shown in Figure 5.2.

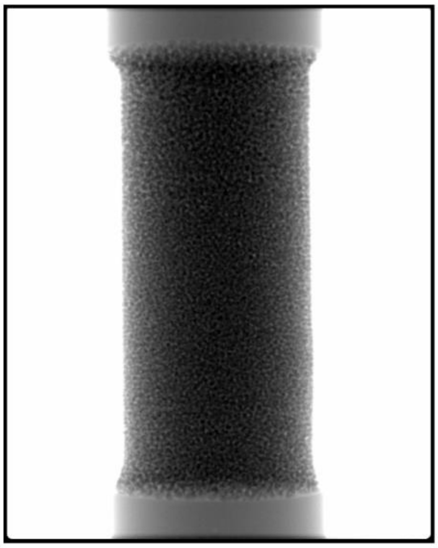

Figure 5.2: Radiograph (1920 × 1536 pixels) of the Caicos ooids specimen (Andò, 2013)

The radiograph is taken from a specimen containing around eighty thousand grains of Caicos sand. It is evident that the centre of the specimen is darker, because more x-rays have been adsorbed by the grains located on that central vertical section.

Once a series of radiograph is taken, it is possible to *reconstruct* the 3-D volume of the specimen. This is done making use of a mathematical tool, the *Radon transform*. It describes how a function can be reconstructed from an infinite number of projections of the function itself. In our case, the projections are the radiographs acquired at different angles and the function to be reconstructed is the one describing the field of x-rays attenuation coefficients inside the object. The software used for the *reconstruction* process is “DigiCT” from Digisens. The files coming out from this process are three-dimensional images in which the grey-scale values are stored in each voxel. These images have been used as starting points in the following Chapters.

5.3 Experimental campaign

A triaxial test campaign was performed on several sand specimens. The goal was to follow the evolution of the micro-structure during the deformation process, at the scale of the grains. The triaxial tests are scanned by x-rays at some loading steps, in order to capture the macroscopic results during time (from the triaxial experiment), as well as the microscopic information (from x-rays tomography, without disturbance of the specimen).

In order to visualise individual grains from the tomographic images, the specimen must be positioned relatively close to the laser beam. Consequently, the typical cylindrical cell size historically used in soil mechanics for triaxial testing (10 cm diameter × 20 cm height) is excessively large to be used for this purpose. Therefore, the specimens used in this work were cylinders of approximately 22 mm height and 11 mm diameter. All the test are performed in drained conditions, therefore $\sigma' = \sigma$.

The pixel size selected to image the studied sands is 15.56 μm, in order to ensure the field of view of the detector to be approximately 30.5 mm × 23.0 mm. Doing so, that the specimens can fit inside this area, as detailed above. This pixel size guarantees an average of 30 pixels across the thickest section of a grain, allowing distinguishing individual grains.

5.3.1 Hostun sand

Hostun sand is produced in a quarry located in the commune of Hostun in the Rhone-Alpes region of France, the particles are very angular and elongated (see Figure 5.3) because they are generated by crushing and have not been transported very far, since they were crushed in-situ. Hostun is a quartz sand used in many previous laboratory studies (Calvetti et al., 2004; Desrues et al., 1996; Schanz and Vermeer, 1996).

On the left of Figure 5.3, a horizontal radiograph section of the Hostun sand specimen is shown, on the right, the image shows a microscope image of few grains of Hostun sand, scanned by an electron microscope.

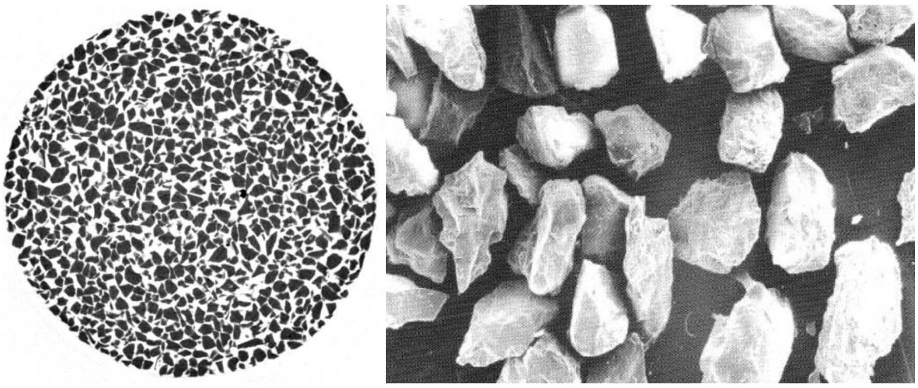

Figure 5.3: Horizontal section of the scanned 3D Hostun sand specimen (on the left). On the right, a scanning with an Electron Microscope (Andò, 2013)

The Grain Size Distribution of Hostun sand is shown in Figure 5.4, it was provided by the manufacturer "Sibleco France".

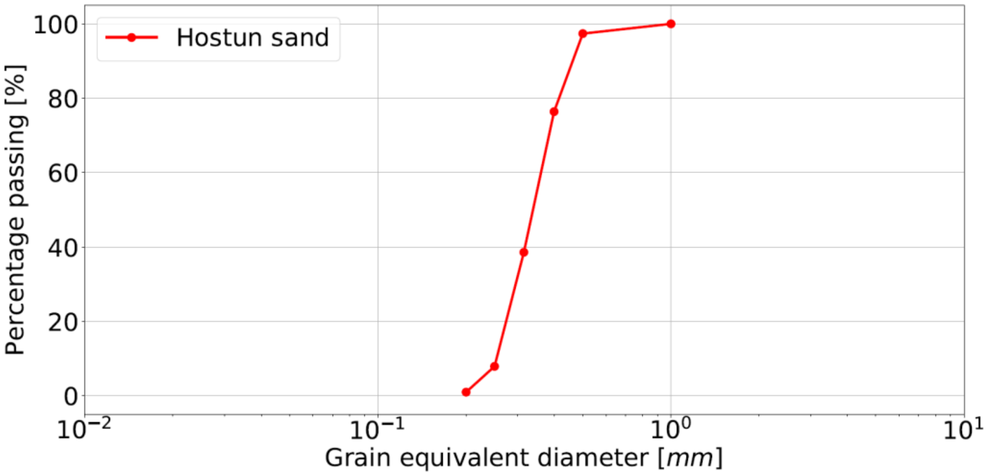

Figure 5.4: Grain Size Distribution of Hostun sand (Andò, 2013)

The grain size distribution is very narrow ($C_U = 1.41$) because the particles were already sorted by grain size after quarrying. The D_{50} is equal to 338 μm.

The triaxial test were performed at a strain rate of 0.1% per minute: it means the ram is driven up at 21 μm/min, considering that the specimen is 22 mm height. The x-rays scans are taken at around every 1% of axial shortening, but some other criterion was adopted for specific purposes at some steps (*i.e.,* the onset of the critical state of Caicos).

Obviously, loading is interrupted when a scan is performed, because the scanning process takes time (the specimen makes a revolution around its vertical axis during which radiographs are taken for each rotation angle).

Four tests were carried out on Hostun sand by Edward Andò (Andò, 2013) in Grenoble at different confining pressure, as summarised in Table 5.1.

Confining Pressure	**Experiment name**
100 kPa	**HNEA01** **HNEA03**
300 kPa	**HNEA02** **HNEA04**

Table 5.1: Triaxial tests performed on Hostun sand by Andò (Andò, 2013)

The name of the experiment is labelled as six characters where the first two letters (**HN**) denotes the material (Hostun), the second two letters designate the researcher in charge of the test (**EA**: Edward Andò, **CV**: Cino Viggiani), and finally the two numbers (*i.e.,* **01**) indicate the number of the specimen under testing.

As can be seen in Figure 5.5, the stress strain material responses show some sharp fluctuation during the deformation, characterised by a rather regular strain rate. This is due to the scanning stages, indeed the stress ratio is kept constant during scanning and a redistribution of the grains contacts may induce a rapid variation of the measured stress ratio. The "instant" (although actually it is not an instant) at which images are taken is named using two further numbers added at the end of the specimen name. For instance, HNEA01-**01** represents the loading step "01" (the end of the isotropic compression) of specimen HNEA01. Moreover, a single loading step *increment* is named as HNEA01-**01-02**. In this case, it refers to the loading phase between the incremental states "01" and "02" of specimen HNEA01. Therefore, the response of specimen HNEA01 during the whole experiment, from the isotropic compression (step "01") until failure (step "16"), is named HNEA01-01-16.

The four specimens were prepared by dry pluviation and the final relative densities achieved were similar, however there is some variability because of the difficulty to create small size specimens. Figure 5.5 shows the macroscopic result of the triaxial tests performed at 100kPa confining pressure on two specimens: HNEA01 and HNEA03. The initial densities are equal respectively to 83.2% and 73.1%, hence they can be classified as dense.

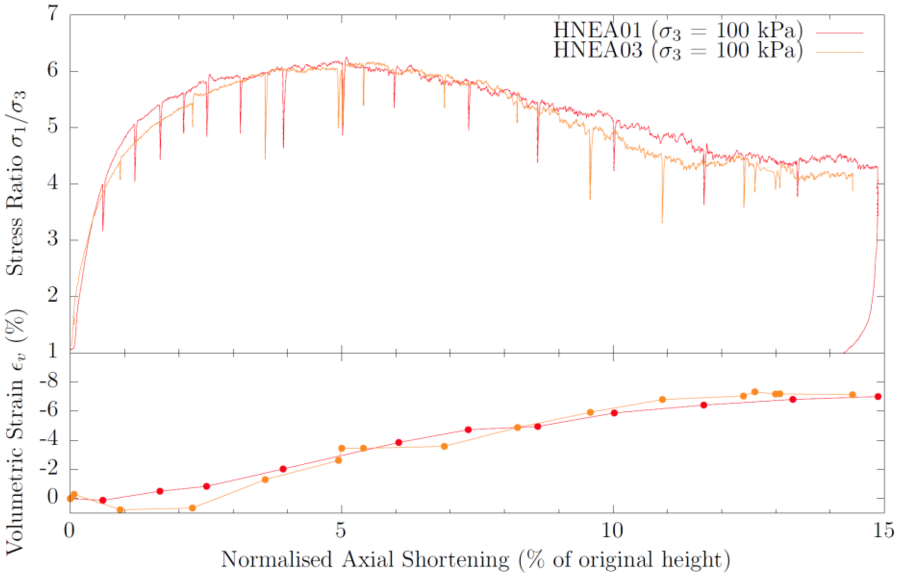

Figure 5.5: Stress-strain responses of the triaxial tests on specimens HNEA01 and HNEA03 (Andò, 2013)

The stress-strain curves are moderately similar, both present a peak followed by a softening phase until the critical state is reached. The peak corresponds to a stress ratio $\left(\frac{\sigma_1}{\sigma_3}\right)$ around 6.15 (615kPa) and an axial strain of 5% for both specimens, whereas the residual stress ratio is 4.15 (415kPa) at 13% shortening for HNEA03 and 4.4 (440kPa) at 13.3% for HNEA01, which resists longer. Therefore, the peak (φ_P) and the residual (φ_{CS}) friction angles are respectively 46.1° and 37.7° for both the specimens.

The dilatancy angle at the peak is 17.0° for HNEA01 and is 18.3° for HNEA03, it reaches zero at the end of the test, thus confirming that both the specimens reached the critical state, although recent numerical works (Kawamoto et al., 2018) casted some doubts on this aspect, pointing out the stress state was still rotating when the experiment was stopped.

The specimens tested at 300kPa confining pressure (HNEA02 and HNEA04) have similar responses as well, as shown in Figure 5.6. The initial relative densities are very high and respectively equal to 95.4% and 84.3%.

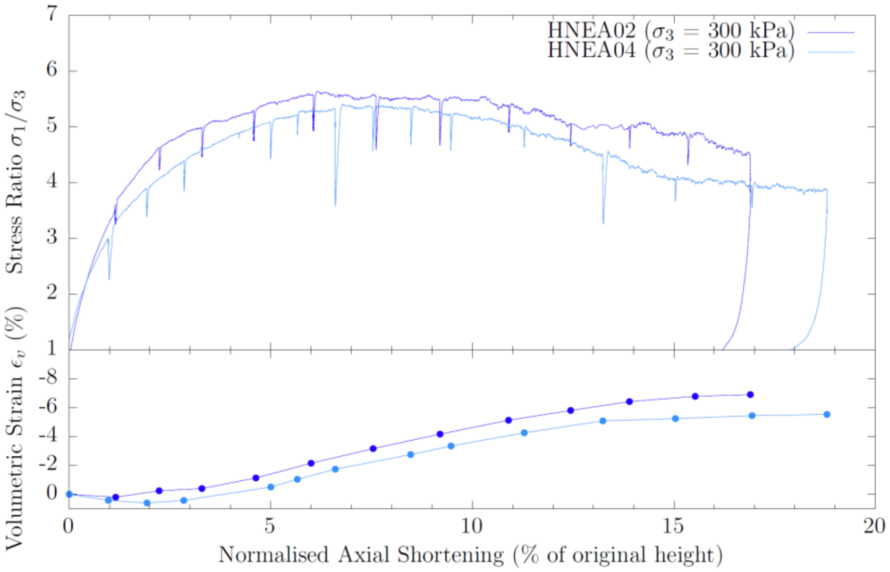

Figure 5.6: Stress-strain responses of the triaxial tests on specimens HNEA02 and HNEA04 (Andò, 2013)

The peaks state for HNEA02 and HNEA04 correspond to a stress ratio $\left(\frac{\sigma_1}{\sigma_3}\right)$ respectively equal to 5.50 and 5.35, which give a peak friction angle of 43.8° and 43.2°, at approximately the same axial strain of 7.2%.

The critical state is not reached at the end of the tests, indeed the dilatancy angle never reaches zero, however it seems that HNEA02 reaches a critical stress ratio greater than HNEA04. The higher resistance of HNEA02 at both peak and critical states can be due to its higher initial density.

In order to test the representativeness of the small specimens such the ones used in this study, the material responses were compared to the responses of larger specimens. If the small specimens' responses are comparable to the larger ones, it means the samples used in this work can represent well the behaviour of the sand tested at larger scale.

In particular, the results of Combe (Combe, 1998) are used in the comparisons. First of all, the material tested at large scale was found to deform in the same way as the small size specimens: both present a single shear band. Figure 5.7 shows the comparison between the responses of the Hostun samples tested at 100kPa and 300kPa confining pressure at both scales, small (respectively HNEA01 and HNEA02, tested by Andò) and large (respectively called TS28D01 and TS28D03, tested by Combe). The slenderness ratio of the sample tested at large scale is 1 (the diameter, 100 mm, equals the height), unlike the small specimens that have a slenderness ratio equal to 2 (22 mm ÷ 11 mm).

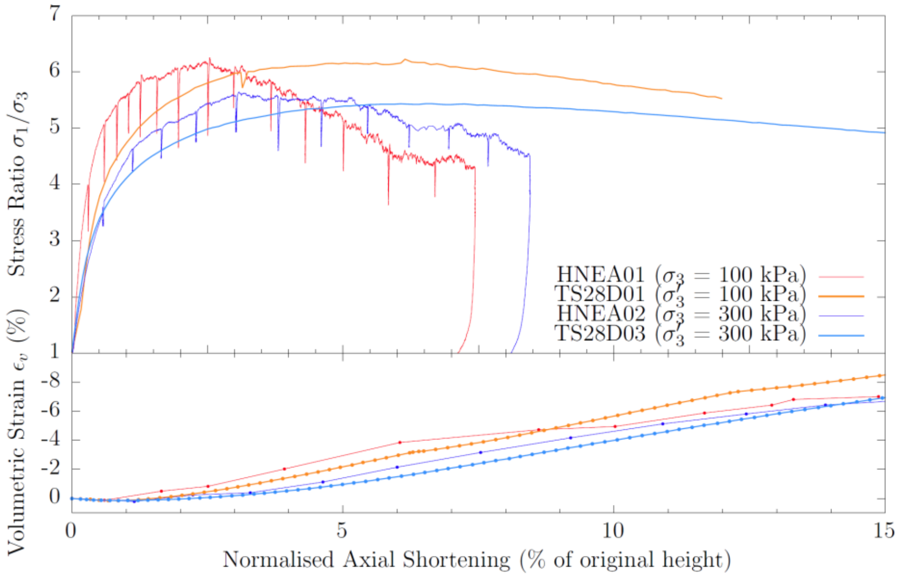

Figure 5.7: Stress-strain responses on specimens HNEA01, HNEA03, TS28D01 and TS28D03 (Andò, 2013)

The first evident fact is that both the peak and the critical states are reached for much larger axial strain for the large size specimens, at both the confining pressures. However, at 100kPa confining pressure the stress ratio at the peak is 6.15 for HNEA01 and 6.16 for TS28D01. Also at higher confinements (300kPa) the peak stress ratios are comparable: 5.50 for HNEA02 and 5.46 for TS28D02. Also the dilatancy angles at the peak state are very similar.

Moreover, the small size specimen tested at 100kPa confining pressure shows an initial stiffness higher than its relative large size specimen TS28D01, however this tendency is not occurring in the high confined tests.

In conclusion, the main difference between the responses is that small size specimens approach the peak and the residual state much faster than the large size ones, approaching failure more rapidly.

Nevertheless, it is important to point out that the geometry of the small specimen created by dry pluviation is less homogenous compared to the large specimen. As a consequence, particles bridges can be determinant in the material response and potential strain localisation phenomenon can arise earlier. In addition, the greater slenderness ratio of small specimens may anticipate the failure in compare to a specimen with slenderness ratio 1. Indeed, the shear banding formation is geometrically more difficult to achieve in a sample in which the ends are relatively close.

Considering the previous results and remarks, it can be concluded that the small specimens response can represent with satisfying accuracy the mechanical response of the material tested at larger scale.

5.3.2 Caicos ooids

Caicos ooids is a much rarer material that has not been extensively studied and tested, for which little data available beyond that is reported by Andò (Andò 2013).
It is generated from small seeds like shell fragments or calcite grains that subsequently become larger because some material gets attached to the grain while rolling or by precipitation over the surface. Ooids grow in marine environment, where the sea waves facilitate this phenomenon. In particular, the material tested comes from the Caicos Islands, in the British West Indies.
The mentioned mechanisms tend to generate rounded particles, as evident in the horizontal section of the tomographic image of Caicos sand (Figure 5.8 on the left) and on the radiograph of a single Caicos particle (Figure 5.8 on the right).

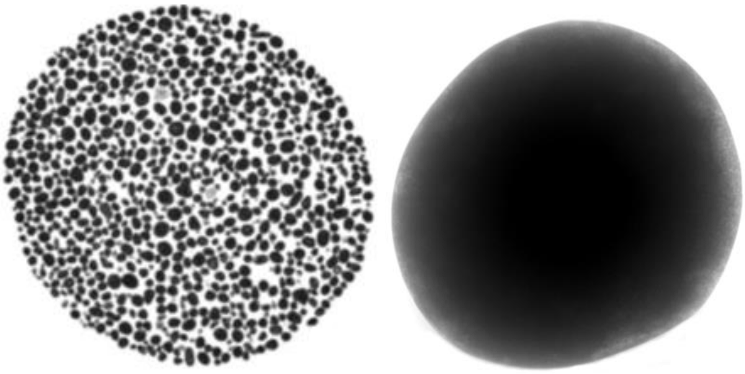

Figure 5.8: Horizontal slice of COEA04 (left) and single radiograph of Caicos sand (right) (Andò, 2013)

The microstructure of this material is calcium carbonate ($CaCO_3$), the 96% is aragonite and the rest is calcite.

Even in this case, the ooids under analysis were previously cleaned and sieved, therefore the sand is poorly graded $C_U = 1.39$ and the grain size distribution is tight, as shown in Figure 5.9.

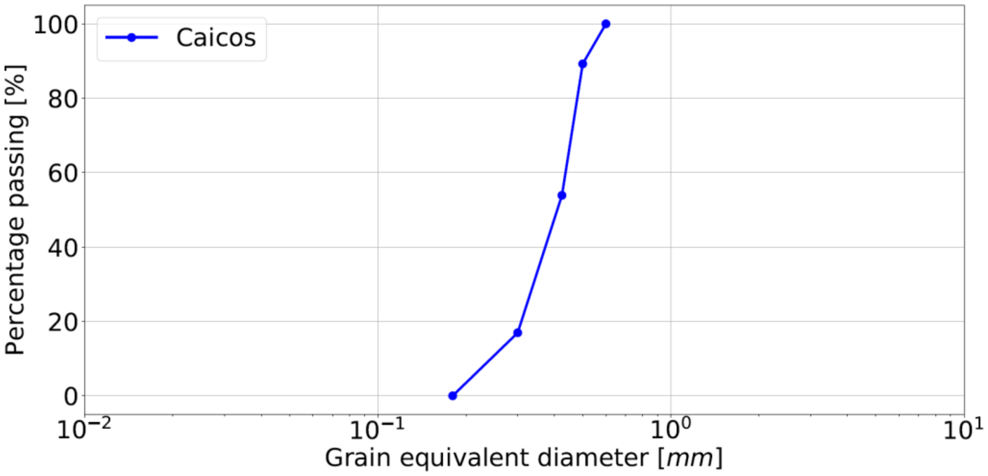

Figure 5.9: Grain Size Distribution of Caicos ooids (Andò, 2013)

The triaxial experiments were performed at 100kPa and 300kPa confining pressure as well as Hostun, as shown in Table 5.2.

Confining Pressure	Experiment name
100 kPa	**COEA01**
	COEA03
	COEA04
300-400 kPa	**COEA02** (300 kPa)
	COCV02 (400 kPa)

Table 5.2: Triaxial tests performed on Caicos sand by Andò (Andò, 2013) and Viggiani

Unfortunately, the relative densities are not reported because the material was not systematically studied. However, specimen COEA01 seems having a higher relative density compared to the others, since it was prepared by pluviation from a different height. Three specimens were tested at 100kPa confining pressure because the response of the first two (COEA01 and COEA03) were quite different, therefore a third test was performed (COEA04). The macroscopic response of the three tests is shown in Figure 5.10.

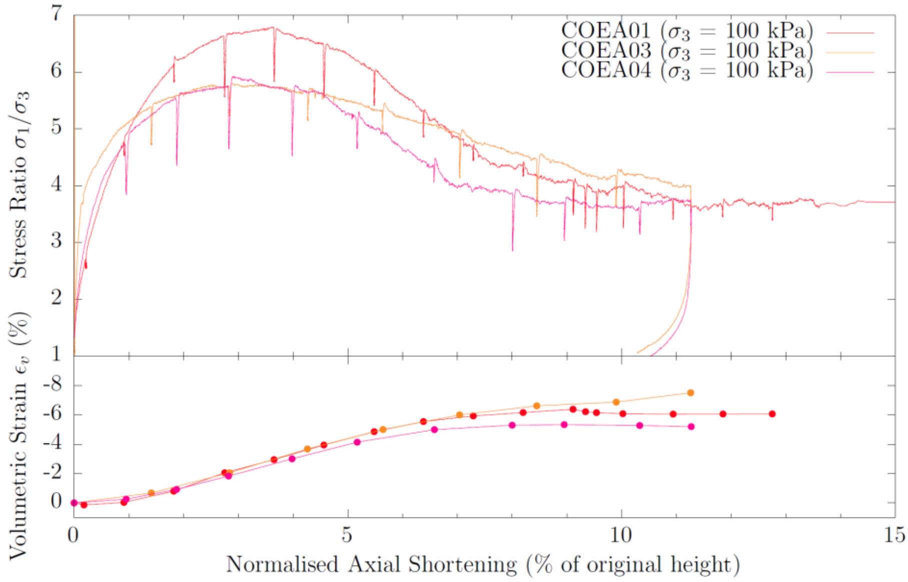

Figure 5.10: Stress-strain responses of the triaxial tests on specimens COEA01, COEA03 and COEA04 (Andò, 2013)

The three specimens behave as a dense material, showing a peak state followed by softening. In particular, COEA01 presents a very high peak stress with respect to the others: the stress ratios are respectively 6.79 and 5.77. In addition, the axial strain corresponding to the peak is higher for COEA01 than COEA03 and COEA04: 3.64% versus 3.4% shortening. It means the peak friction angles are respectively 48° and 44.8°.

After the peak stress, specimens COEA01 and COEA04 reach the critical state at around 11% shortening, confirmed by a dilatancy angle that goes to zero in both test. Specimen COEA03 seems more resistant in approaching the critical state, which indeed is not reached at the end of the test. The residual stress ratio is around 3.70 for the three specimens.

The volumetric response is quite similar for the three tests: the dilatancy angle at the peak is 20.4° for COEA01 and COEA04, whereas it is 19.3° in COEA03.

The shear resistance for all the three specimens is relatively high for a rounded sand, especially for COEA01 that was though presenting a higher initial density. The variance in the responses can be due to the small size of the specimens that may induce large differences in the initial porosity and anisotropy, because of the small amount of grains involved in the experiment. However, carbonate sand are known to present high friction angles as reported by Coop (Coop, 1990).

Regarding the specimens tested at higher confining pressures, although the confining pressure are not the same (COEA02 is tested at 300kPa whereas COCV02 at 400kPa), the macroscopic responses are plotted together in Figure 5.11.

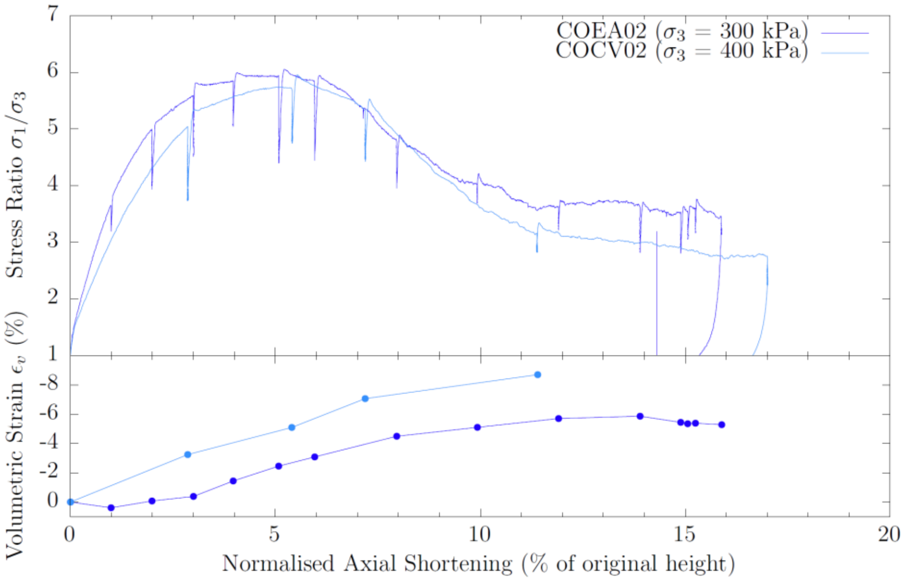

Figure 5.11: Stress-strain curves of the triaxial tests on specimens COEA02 and COCV02 (Andò, 2013)

Both specimens present an initial stiffer response in compare to the materials tested at lower confining pressure. Indeed, the stress peak is reached at around 5.2% shortening for COEA01 and 5.85% for COCV02. Therefore, the stress ratios $\left(\frac{\sigma_1}{\sigma_3}\right)$ are respectively 5.97 ($\varphi_P = 44.5°$) and 5.85 ($\varphi_P = 45.1°$).

The critical state seems to be reached by both specimens after 11% shortening, although the critical stress ratio is different: 3.65 for COEA02 and 3.11 for COCV02.

5.3.3 Ottawa sand

Ottawa sand is a siliceous sand made up of quartz grains. Grains are less angular compared to Hostun because of the anterior deposition process. The material studied is Ottawa 50-70. The D_{50} is about 310μm and the PSD is narrow because the material was previously sieved. In particular, the coefficient of uniformity (C_u) and the coefficient of curvature (C_c) are respectively equal to 1.31 and 0.95.

Four specimens have been tested in triaxial conditions by Andò (Andò, 2013), according to Table 5.3. The triaxial responses, respectively for 100kPa and 300kPa confinements, are showed in Figure 5.12 and Figure 5.13.

Confining Pressure	Experiment name
100 kPa	**OUEA04**
	OUEA06
300 kPa	**OUEA02**
	OUEA03

Table 5.3: Triaxial tests performed on Ottawa sand by Andò (Andò, 2013)

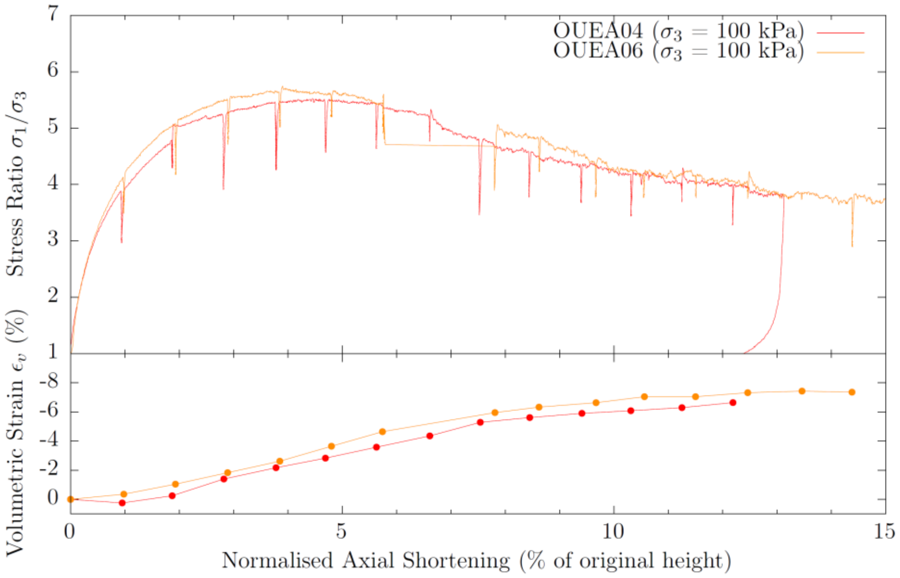

Figure 5.12: Stress-strain curves of the triaxial tests on specimens OUEA04 and OUEA06 (Andò, 2013)

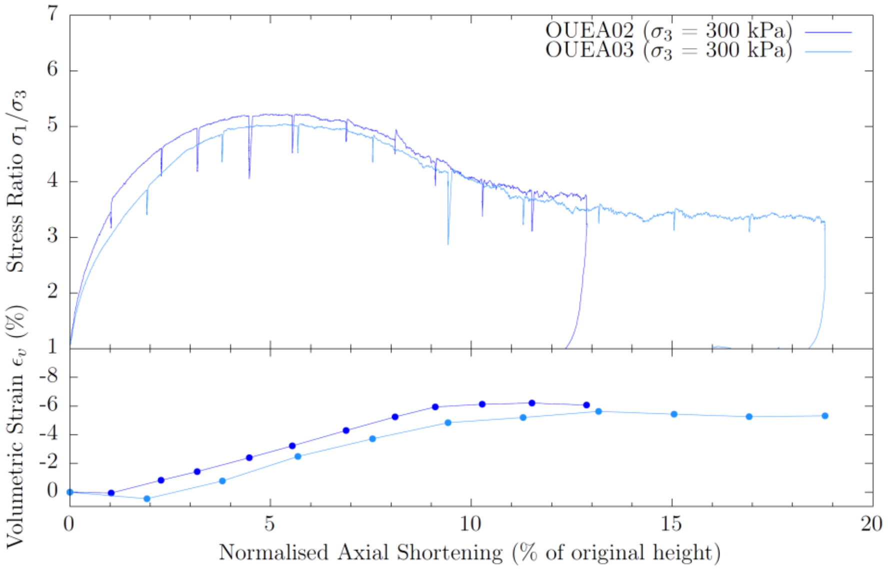

Figure 5.13: Stress-strain curves of the triaxial tests on specimens OUEA02 and OUEA03 (Andò, 2013)

The responses of OUEA04 and OUEA06 (100kPa - Figure 5.12) are very similar. The peak stress of about 550kPa (φ_P = 44°) is reached at around 4.5% shortening. A plateau stress ratio of 3.75 (φ_{CS} = 36°) is reached at around 13% axial shortening, although the critical state of OUEA04 has not been perfectly reached, since the dilatancy does not equals zero at the end of the test. The dilatancy angles at the peak are respectively 16.1° and 20.2° for OUEA04 and OUEA06. The sample OUEA06 presents a slightly more contractive volumetric behaviour compared to OUEA04.

Regarding the tests performed at 300kPa (OUEA02, OUEA03 - Figure 5.13), again the macroscopic response are similar, although OUEA02 presents a stiffer response before reaching the peak stress ratio of 5.2 (5.02 for OUEA03), that means respectively φ_P = 42.6° and φ_P = 41.9°. The critical state has been reached for both samples, with a stress ratio of 3.7 and 3.5 respectively for OUEA02 and OUEA03, at around 11.6% shortening. The dilatancy angles at the peak are 16.1° and 17.1°.

5.4 Image analysis procedure

After performing the triaxial tests into the x-rays scanner of Laboratoire 3SR, and after having taken some radiographs (resulting in 3D tomographic images after *reconstruction*) at some established loading steps, it is possible to start analysing these images.

The 3D tomographic images are simply stored as *grey-scale* images, in which the only variable (the greyscale of each pixel) represents the x-rays attenuation coefficient evaluated all over the specimen, as evident in Figure 5.8, showing an horizontal slice and a radiograph of a single grain.

However, such a grey-scale assembly of pixels (or voxels in 3D) makes impossible to study single grains. The eyes can do what a computer cannot: distinguish one grain from the others and from the void phase. It is possible to numerically extract single grains from the 3D images only if individual particles are previously defined. Subsequently, some geometrical properties can be calculated (as it will be detailed in Chapter 6.2, e.g. volume, surface area, inertia tensor).

This section shortly details how an image can be processed in order to define individual grains from a 3D grey-scale image coming from tomography. It consists in three steps: *Binarisation*, *separation* (or *segmentation*) and *labelling*.

- *Binarisation* is the process in which the solid phase is separated by the void phase. It creates a *binary* image in which all the voxels representing the solid phase are labelled with one single value (*i.e.*, 1 = white) as well as the "void" voxels (*i.e.*, 0

= black). The choice of a threshold value is very important in order to separate the two phases of the image with satisfying accuracy. In particular, the threshold was determined from a physical measurement: the volume of the solid phase can be easily measured from the real specimen if the grains densities are known. Therefore, the threshold was chosen so that it includes the number of voxels corresponding to the measured solid volume.

- *Separation* (or *segmentation*) is the process applied to the black-and-white images coming from binarisation in order to *separate* the single interconnected solid phase into individual grains. This is a crucial procedure for all the next studies on grain shape, since it determines the final geometry of each particle.
  This work was carried out by the watershed algorithm implemented in Visilog® (Bernard et al., 2011). The final goal of the watershed is to assign a marker for each individual grain that at this stage still belong to a unique solid skeleton. This is achieved by computing a Euclidean Distance Map to find the local maxima at which the markers are placed. The result of the segmentation process is always a binarised image, but where the individual particles are separated, storing a marker, and can be individually extracted from the whole numerical specimen. The separation algorithm may fail under some circumstances because of the huge amount of grains and the variety of sizes and shapes. In particular, if two markers are placed in one single grain, there is an "over-segmentation" error. An "under-segmentation" error occurs if one single marker is assigned to multiple grains. These errors cannot be avoid completely, but only few grains were affected as reported in (Andò, 2013). Other separation algorithms exist in literature, for example the "inter-pixel" (*i.e.*, the separated grains can touch) watershed algorithm implemented in the external open-source Python package SPAM (Andò et al., 2017) or the adaptive watershed algorithm recently proposed by Kong & Fonseca (Kong and Fonseca, 2018).
- *Labelling* is the last procedure which is applied to the 3D images coming from the separation process. It consists in assigning a unique value to all the voxels belonging to an individual particle. In other words, it assigns a "name" (a positive

integer assigned in ascending order starting from one) to each grain contained in the 3D image.

Figure 5.14 summarises the three described procedures as flow chart.

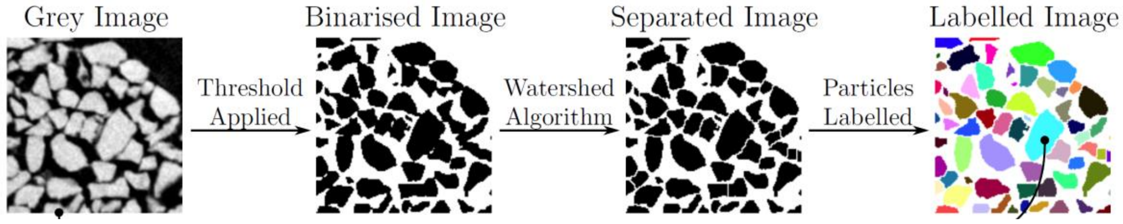
Grey Image
Threshold Applied
Binarised Image
Watershed Algorithm
Separated Image
Particles Labelled
Labelled Image

Figure 5.14: Flow chart showing how to go from a greyscale image to a labelled image in which individual particles can be extracted (Andò, 2013)

Figure 5.15 illustrates the information contained into a labelled image. The pixels (it is a slice) representing the void phase have value 0, whereas the pixels making up single particles (*i.e.*, 1, 2 and 3 in the figure) have value equal to the "grain name": a positive integer number.

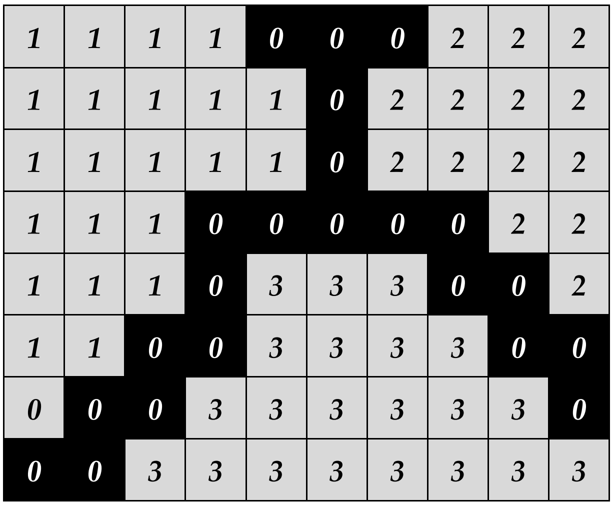

1	1	1	1	0	0	0	2	2	2
1	1	1	1	1	0	2	2	2	2
1	1	1	1	1	0	2	2	2	2
1	1	1	0	0	0	0	0	2	2
1	1	1	0	3	3	3	0	0	2
1	1	0	0	3	3	3	3	0	0
0	0	0	3	3	3	3	3	3	0
0	0	3	3	3	3	3	3	3	3

Figure 5.15: Matrix representation of the pixels of a labelled image's slice

5.5 Summary

This Chapter aimed at giving some basis about the use of x-rays tomography to study granular materials, as widely described by Edward Andò in his PhD dissertation (Andò, 2013). The main concepts can be summarized as follows:

- The tomographic equipment of 3SR Laboratory (Grenoble) allows scanning (with time) entire deforming cylindrical sand samples of small size (22 mm height and 11 mm diameter);
- A triaxial test campaign (scanned with x-rays) has been carried out by Andò (Andò, 2013) on three different sands, ranging from rounded to very angular (Caicos ooids, Ottawa sand, Hostun sand);
- The triaxial responses of the three materials are different, although prepared with the same procedure, achieving similar initial porosities, and tested at the same confining pressures, because of particle shape;
- An image analysis procedure (in order, *binarisation, segmentation* and *labelling*) allows extracting single particles from the entire 3D raw images coming from x-rays;
- Individual grains are now ready to be studied in three-dimensions.

6

Shape analysis of Sand Particles

6.1 Introduction

The objective of this chapter is to explain how the shape of a particle was established starting from the 3-D *labelled* images coming from the image analysis procedures described in Chapter 5.4.

Every grain is composed by an assembly of voxels (a "tri-dimensional pixel") that can be numerically studied in order to get some properties (*i.e.*, volume, surface area, inertia tensor, etc., in section 6.2) which are used to quantify shape parameters (*i.e.*, sphericity, elongation, convexity, etc., in section 6.3).

Not all the specimens mentioned in Chapter 5 are considered. In particular, two specimens were initially selected for detailed morphological study: HNEA01 and COEA04. Results obtained from examination of these two specimens constitute the backbone of this chapter. However, at a later stage in the project, motivated by the numerical modelling described in Chapter 8, data from the Ottawa sand specimen OUEA02 was also examined. For completeness, relevant results from this sand specimen are also presented hereafter, where available.

The HNEA01 and COEA04 specimens were tested in triaxial conditions at 100kPa confining pressure, and the macro-mechanical responses of the two materials are reported in Figure 5.5 and Figure 5.10. A direct comparison of the responses is illustrated in Figure 6.1, as well as the loading steps at which the x-rays scans are performed.

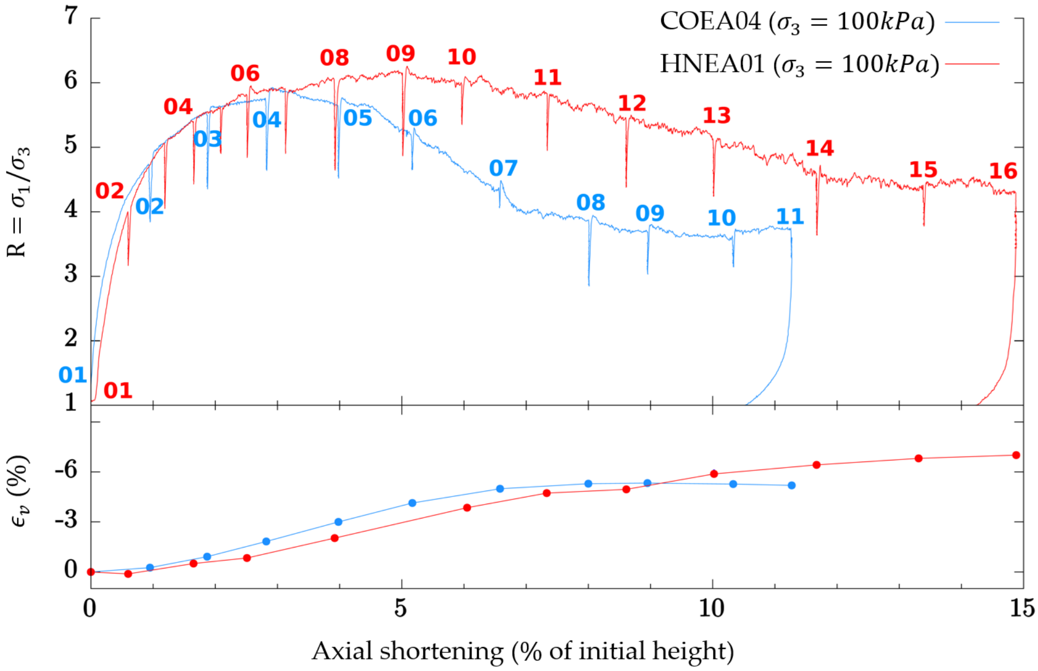

Figure 6.1: Macro-mechanical responses of HNEA01 and COEA04 with associated loading steps

It is interesting to note that the peak stress ratio of Caicos ooids is greater than Hostun sand. Chapter 5.3.2 detailed the experiments performed on Caicos sand, and all the specimens (tested at different confining pressure) exhibited high resistance, despite considerable variation due to initial anisotropy of the small sample. A large inter-particle friction may be a reason that can explain such high resistance.

The labelled images studied in this Chapter are referred to the first loading steps of both specimens, at the end of the consolidation phase at which the stress state is isotropic. These imaged are named "HNEA01-01" and "COEA04-01", following the convention described in Chapter 5.3.1, and have size (in pixels) respectively 960 × 960 × 1750 and 950 × 950 × 1600.

In addition, before being analysed, the images are slightly modified in order to enhance the efficiency of the algorithms described below. In particular, some filters (based on the particles barycentre positions, see Table 6.1) were applied in order to remove the loading platens (which are erroneously labelled as particles), as well as particles excessively close to the loading platens, as shown in Figure 6.2.

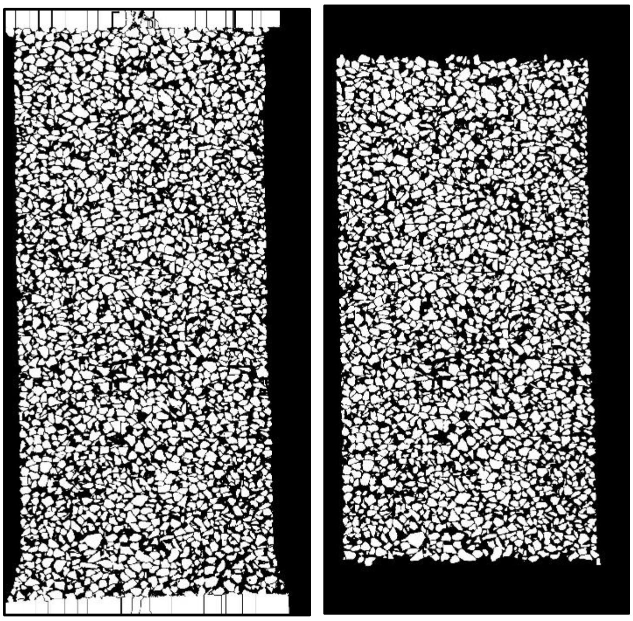

Figure 6.2: Vertical slices of HNEA01. On the left, the original labelled image. On the right, after the filter is applied

Moreover, another filter was applied on the particle volume (see Table 6.1). Only grains having volume greater than 50 voxels (0.00019 mm^3) (see Chapter 6.2.1) are included in the new 3D filtered image. This is done to exclude very small grains (some particles are composed by 1 single voxel) from the calculations: a numerical analysis such as described in Chapter 6.2 is impossible or misleading if applied to such particles. Table 6.1 lists the filters applied to the 3D labelled images representing the specimens, as well as the number of grains contained before and after the application of the filters.

	Hostun sand	**Caicos ooids**
Number of grains before filters (original labelled image size: x-y-z)	54.889 960 × 960 × 1750	72.680 950 × 950 × 1600
Filters applied	volume < 50 vox $150\ \text{px} < z < 1600\ \text{px}$	volume < 50 vox $50\ \text{px} < z < 1550\ \text{px}$
Number of grains after filters	48.612	65.056

Table 6.1: Description of the filters applied to the original labelled images

The following Chapters use the filtered labelled images as reference, therefore every particle that will be mention and studied is extracted from these filtered labelled images. Figure 6.3 shows the top of the 3-D reconstructed numerical filtered specimen COEA04 visualised on Paraview. From a similar visualisation, it is easier to appreciate the resolution of the images used in this work, in which each grain can be clearly distinguished by the others.

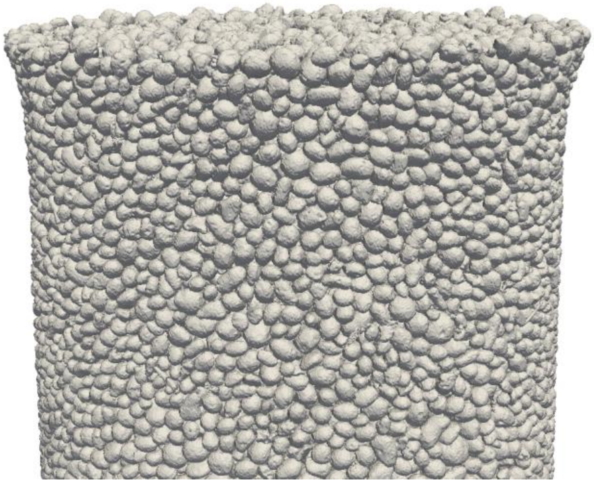

Figure 6.3: 3D representation of the specimen COEA04

6.2 Numerical quantification of particle geometry

Particle images have been numerically analysed using dedicated scripts written in Python programming language and its related scientific packages: *Numpy* (Oliphant, 2006) and *Scipy* (Jones et al., 2001). The main advantage of the Python language is its open-source philosophy; every researcher can run a script in every computer without compatibility problems. Moreover, many open-source external packages (*i.e.,* for image analysis) exist and can be easily downloaded and installed. Every algorithm of every external packages can be accessed and explored in order to understand the implementation and modify it in case of need.

The shape properties are calculated starting from the 3D labelled image representing the whole sand specimens, as shown in Chapter 5.4.

To give an idea about the efficiency of each algorithm used, the calculation time for one selected grain is indicated in each of the following sections. The reference grain is the number “46972”, it has been extracted from the labelled image representing the Hostun specimen at the beginning of the triaxial test (HNEA01-01). It is one of the most computationally expensive grains, giving the fact that its volume is larger than the 92% of all the grains contained within the specimen. The calculations were carried out on an Intel Core i7-6820HQ CPU 16GB RAM laptop, with Linux O.S.

A python function allows extracting a single grain (or rather, a single assembly of voxels) from the specimen and studying it. This step is by far the most computationally expensive, because the selected grain must be searched within the entire 3-D volume, composed by more than one billion voxels. The computational time requested by this operation for the example case was 3.7068 seconds, which means 84.1% of the total calculation time for this grain.

In the following, a detailed description of each grain property is presented, as well as the technique used to calculate it. For validation purposes, some algorithms are tested on artificial 3-D images representing fictitious grains with perfect spherical (or spheroidal) shape, so that the numerical results can be compared with the analytical solutions.

The general flow diagram of the operations is presented in Figure 6.4.

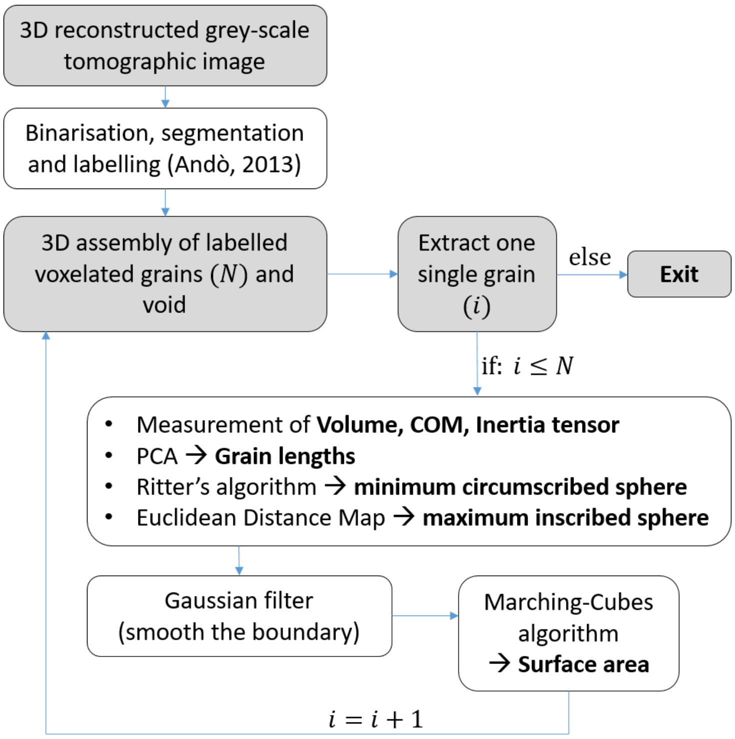
3D reconstructed grey-scale tomographic image
Binarisation, segmentation and labelling (Andò, 2013)
3D assembly of labelled voxelated grains (N) and void
Extract one single grain (i)
else
Exit
if: $i \leq N$
Measurement of Volume, COM, Inertia tensor
PCA → Grain lengths
Ritter's algorithm → minimum circumscribed sphere
Euclidean Distance Map → maximum inscribed sphere
Gaussian filter (smooth the boundary)
Marching-Cubes algorithm → Surface area
$i = i + 1$

Figure 6.4: Flow diagram of image treatment operations (Rorato et al., 2019)

6.2.1 Volume and centre of mass

The volume of a grain is the easiest property to get from a labelled 3-D image: it is equal to the sum of all the voxels making up the grain. Doing so, the volume is expressed as number of voxels but, since the scans resolution is known, it is possible to convert it in [mm^3]. The reference grain labelled as "46972" from HNEA01-01 has 13860 voxels, which means 0.052 mm^3, given the scan resolution of 15.56 μm per pixel size.

The grain centre of mass is calculated making use of the *Scipy* function called "*scipy.ndimage.measurements.center_of_mass*". Since all the voxels are considered having the same unitary mass and the voxels absolute coordinates are known, the coordinates of the grain's centre of mass are given as vector addition of the position vectors which point to the same global reference origin of the whole 3-D image containing all the grains. The computational time requested by these two operations on the reference grain was only 0.0027 seconds, which means 0.1% of the total calculation time for this grain.

6.2.2 Volume – Particle Size Distribution

If the particle volume is known, it is straightforward to calculate the Volume Size Distribution (VSD) of the numerical specimen, and also a first attempt to get the Particle Size Distribution (PSD) can be done. In particular, the diameter of the equivalent sphere (having the same number of voxels as the particle) can be obtained, hence the PSD can be calculated and compared to the GSDs of the physical specimens HNEA01 and COEA04, shown in Figure 5.4 and Figure 5.9.

The volume size distribution of HNEA01 is shown in Figure 6.5. The x-axis represents the particle's volume (expressed in mm^3 after conversion from the number of voxels), whereas the y-axis represents the percentage of grains passing a certain value. Two curves are plotted in Figure 6.5: the VSD of specimen HNEA01 at the beginning of the deviatoric phase (HNEA01-01) and at the critical state (HNEA01-16). It is clear that the curves are very close to each other, therefore it is possible to claim that grain crushing is not significant during the experiment, as expected.

Figure 6.6 shows the grains volume histogram of HNEA01 at the loading step "01", which is expected to be equal to step "16". The mean volume is equal to 0.027 mm^3 and the median is 0.022 mm^3.

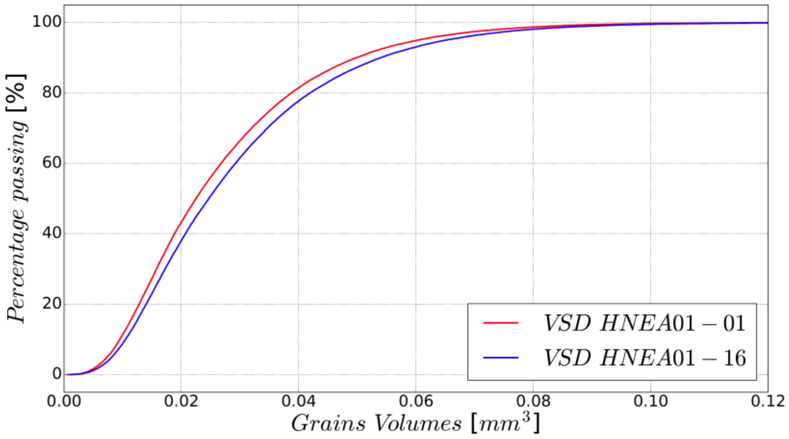

Figure 6.5: VSD of HNEA01 at the beginning and the end of the (scanned) triaxial test

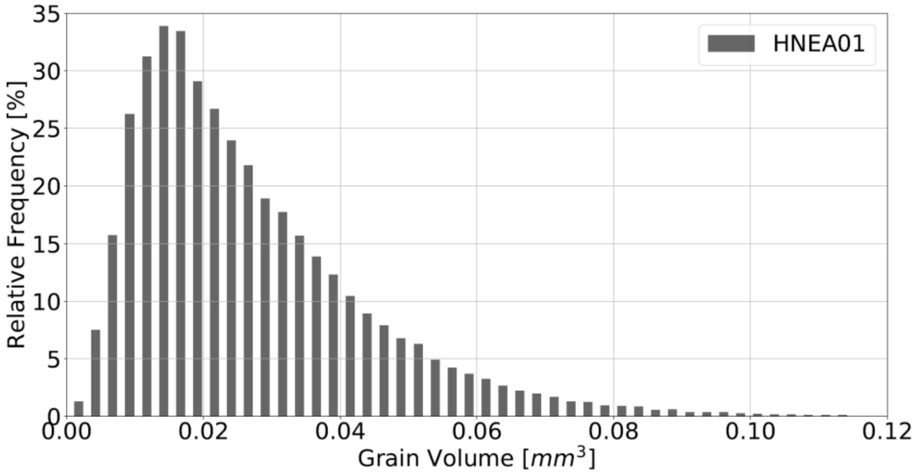

Figure 6.6: Histogram of the particles volume in specimen HNEA01

The same considerations can be done for Caicos sand. Figure 6.7 shows the VSD of the specimen COEA04 at the beginning (step "01") and at the end (step "11") of the triaxial test. The curves coincide perfectly, therefore grain crushing did not occur at all in this case. The histogram of the volumes is illustrated in Figure 6.8, the mean volume is 0.025 mm^3 and the median is 0.021 mm^3.

Figure 6.9 shows the comparison between Hostun sand (HNEA01) and Caicos ooids (COEA01 and COEA04) calculated at the loading step "01".

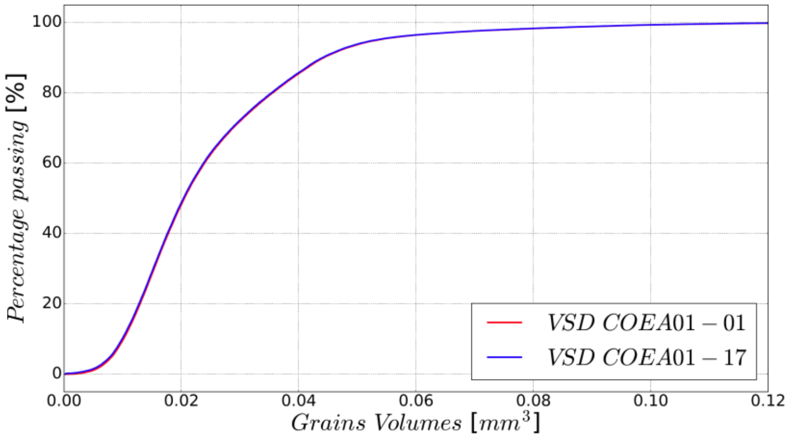

Figure 6.7: VSD of COEA04 at the beginning and the end of the (scanned) triaxial test

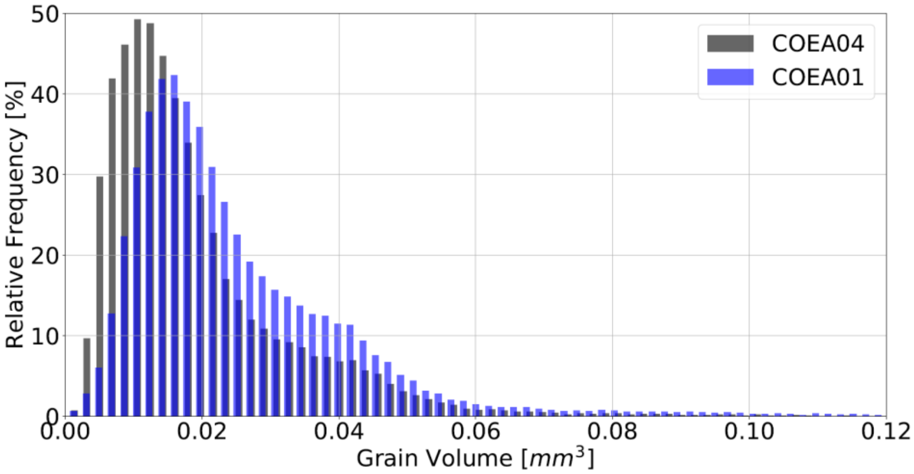

Figure 6.8: Histogram of the particles volumes in specimen COEA01 and COEA04

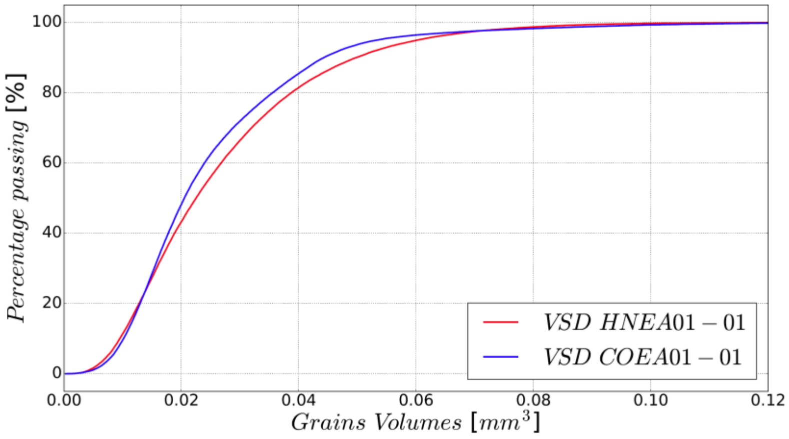

Figure 6.9: Comparison between the GSDs of HNEA01 and COEA04 during isotropic compression

(step "01")

In the next plots, the grains volumes have been substituted with the *equivalent grain diameter* (the diameter of the sphere having the same volume as the grain), in order to compare the numerical GSDs with the experimental ones, presented in Chapter 5.3.

Regarding Hostun sand (Figure 6.10) the numerical GSDs fit well with the experimental one measured by the manufacturer "Sibleco France". Moreover, the equivalent diameters seem extracted from a normal distribution (Figure 6.11) having mean equal to 0.356 mm and median (D_{50}) 0.350 mm, which is very close to the value indicated by the manufacturer: 0.338 mm.

Regarding Caicos ooids (Figure 6.12 and Figure 6.13), the same considerations can be done. The numerical GSDs are compared with the experiments performed by Exxon and Laboratoire 3SR: the curves are similar, however there is a slight difference given by the fact that the numerical GSDs are calculated with a continuous approach, whereas the experimental GSDs are obtained from sieve analysis, hence presenting steps. In addition, it worth to point out that the x-axis of Figure 6.12 only ranges from 0.0 mm to 0.7 mm, and is drawn in linear scale, unlike typical GSD in log-scale, thus emphasizing the gaps.

In conclusion, the comparison between the numerical GSDs of Hostun sand and Caicos ooids at the first loading step "01" is shown in Figure 6.14.

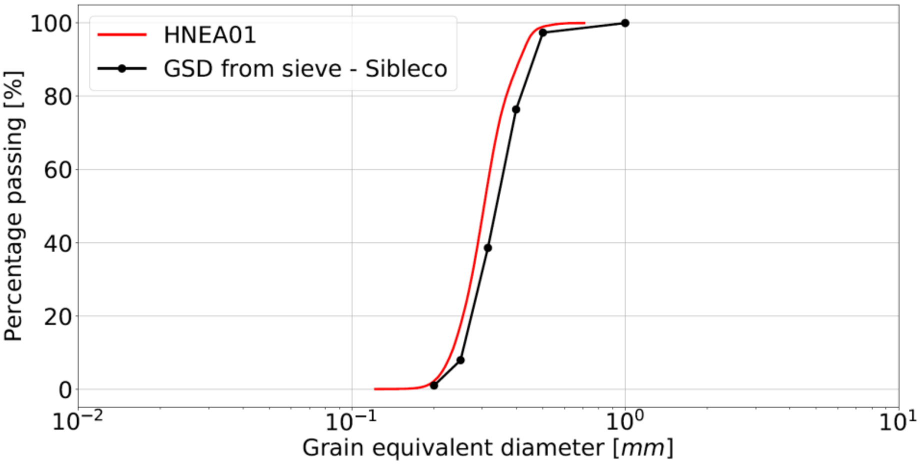

Figure 6.10: GSDs of HNEA01 compared to the GSD measured by the manufacturer

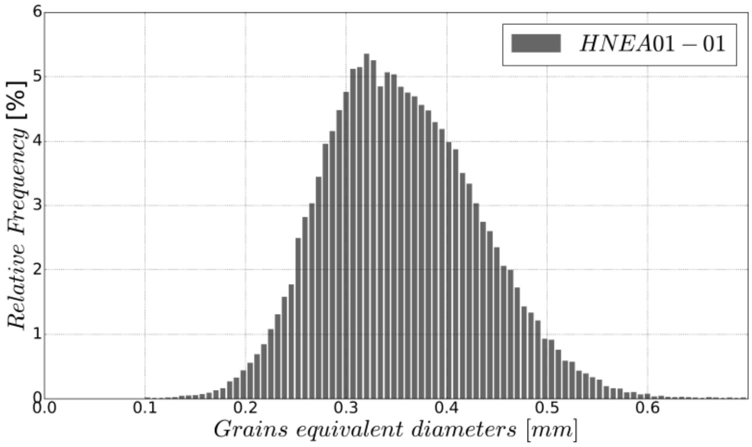

Figure 6.11: Histogram of the equivalent diameter in the specimen HNEA01

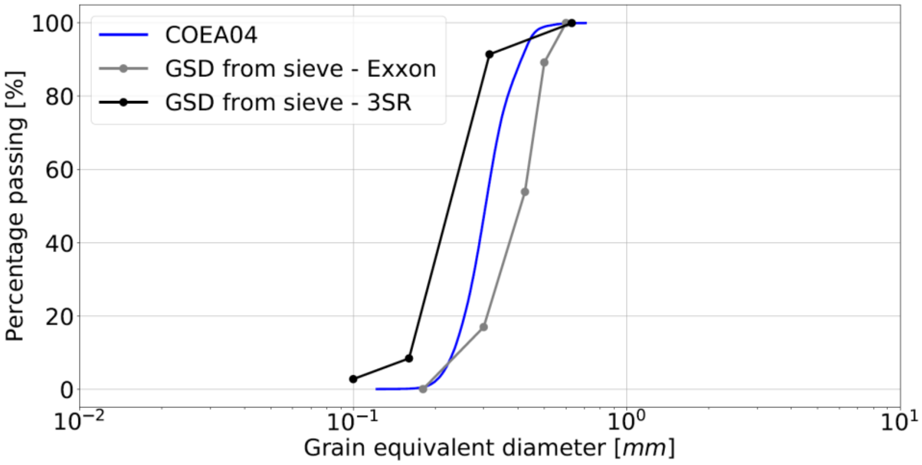

Figure 6.12: GSDs of COEA04 compared to the GSD measured by Exxon and Laboratoire 3SR

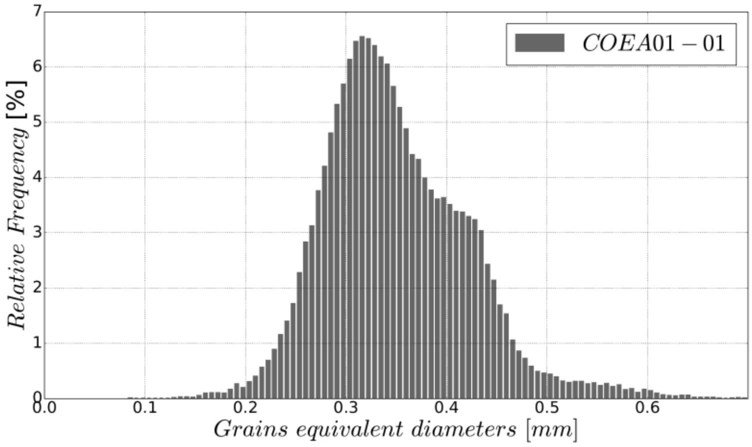

Figure 6.13: Histogram of the equivalent diameter in the specimen COEA04

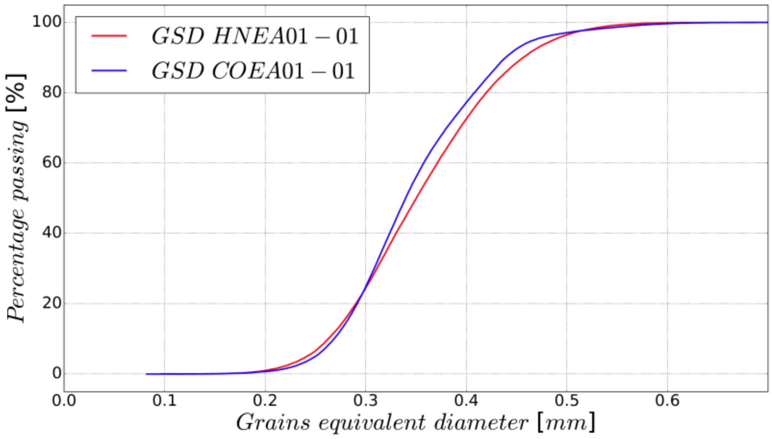

Figure 6.14: Comparison between the GSDs of HNEA01 and COEA04

6.2.3 Surface Area

Accuracy of particle surface area measurement is important, since it is used in many shape descriptors, as detailed in Chapter 2.2. There are different ways to calculate the surface area of a particle. One approach is to sum up all the external faces of the external voxels making up the particle. This solution is conceptually easy and computationally convenient but results in large overestimations of the actual grain surface area. Some codes (*i.e.*, Visilog® (Bernard et al., 2011)) apply a reducing coefficient calculated based on the configuration to every external voxel face. No more details are given in the reference guide of this commercial software about how those coefficients are computed.

In this work, the *"Marching Cubes (MC) algorithm"* (Lorensen and Cline, 1987) is used to create a surface mesh composed of n triangular elements whose n-areas can be sum up in order to get the surface area. The Marching cubes algorithm takes as input a three-dimensional array, representing a single particle. An initial surface is defined for all points where the scalar field (*i.e.*, the grey-scale value) is equal to a certain value. Then, the whole space is divided into a grid of little cubes and the intersection of each cube with the surface is studied. The corners of each cube can be either inside or outside the mentioned surface, therefore a Boolean value is assigned to them. For 8 corner points, there are 2^8 possible configurations. If all the corners are entirely inside or outside the space, it means the surface is not intersected and therefore there is nothing to do. However, if some corners are inside and some others are outside, it means the initial surface is intersected and therefore it is necessary to position the mesh vertex by determining the intersection configuration, in order to find the exact intersection point. This step is usually done by linearly interpolating the two scalar values that are connected by that edge. A detailed explanation of the algorithm can be found in the original paper published in 1987 by Lorensen and Cline (Lorensen and Cline, 1987).

In this study, before applying the MC-algorithm, a Gaussian filter is applied to the particles, in order to smooth its external surface, as exemplified in Figure 6.15.

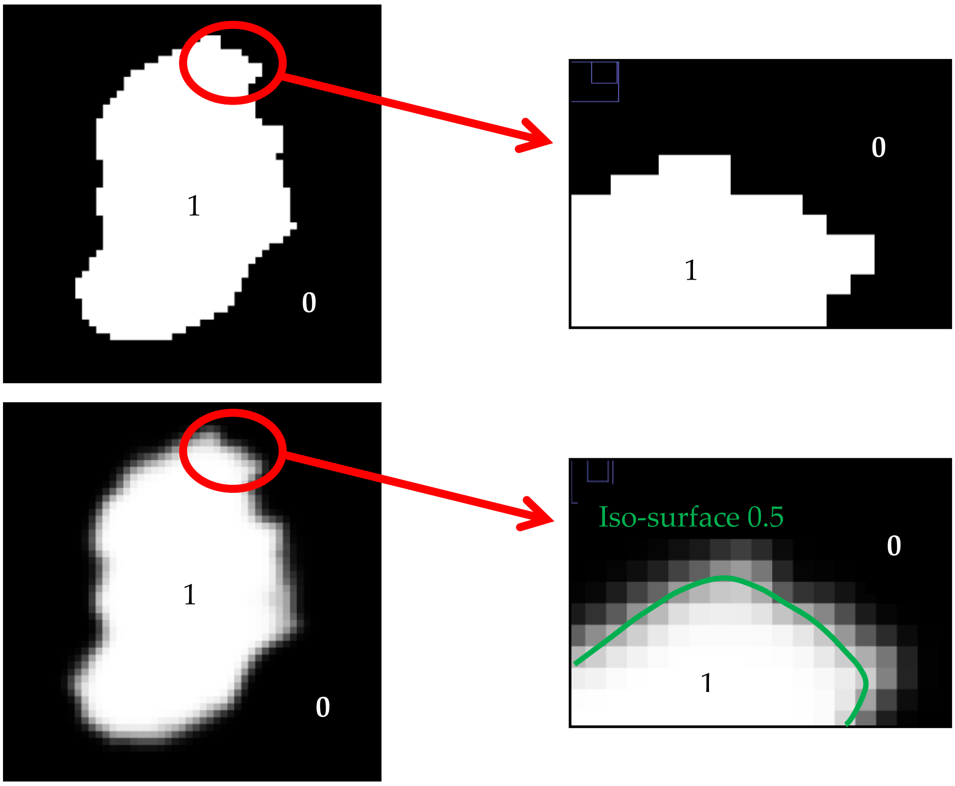

Figure 6.15: Visualisation of the Gaussian filter applied to grain number 46972

The external surface of the binarised grain on the top of Figure 6.15 is very irregular because of its pixels and the MC-algorithm cannot provide a good mesh. The Gaussian filter origins a wide range of grey-scale values on the surface, ranging from 1 (the grain, in white) to 0 (the void phase, in black), as shown in the bottom of Figure 6.15. A smooth surface between the solid and void phases is obtained as the iso-surface which connects all the voxels having a grey-scale value of 0.5 (exactly between the grain and the void phase). The Marching Cubes algorithm can now be applied on the iso-surface, coloured in green in Figure 6.15. The resulting Marching Cubes mesh of grain number 46972 is represented in Figure 6.16.

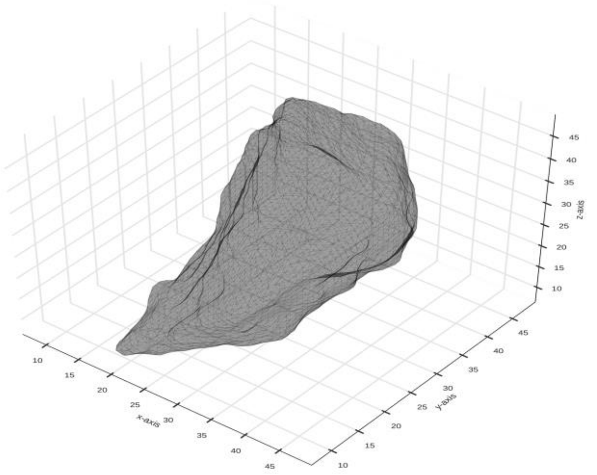

Figure 6.16: Mesh of grain 46972 from Marching Cubes algorithm

Finally, once the mesh is created, it is possible to sum up the area of all the triangles composing the mesh.

This procedure has been carried out using an external package for Python, called "*scikit-image*". In particular, the function "*skimage.measure.marching_cubes*" provides the list of vertices and faces of the final mesh. The final surface area of the example particle is $3757.10\ \mathrm{px}^2$.

The result coming from the Marching Cubes algorithm and its related surface area are compared to the result of a commercial software (*Visilog*®), that uses a completely different algorithm as already mentioned. The surface area of grain 46972 computed with Visilog® is equal to $3854.16\ \mathrm{px}^2$, higher by 2.6%.

The MC-algorithm was tested on a sphere to compare the numerical and the analytical results. A binarised sphere with volume equal to $\frac{4}{3}\pi(25)^3$ voxels was artificially built (Figure 6.17), the surface of this sphere is intentionally "rough" (*i.e.*, voxelated), as the labelled grains of the images. The same procedure used for grains was applied to this sphere: firstly, the Gaussian filter (Figure 6.17 on the right), secondly, the MC-algorithm (Figure 6.18) and finally the surface area was calculated.

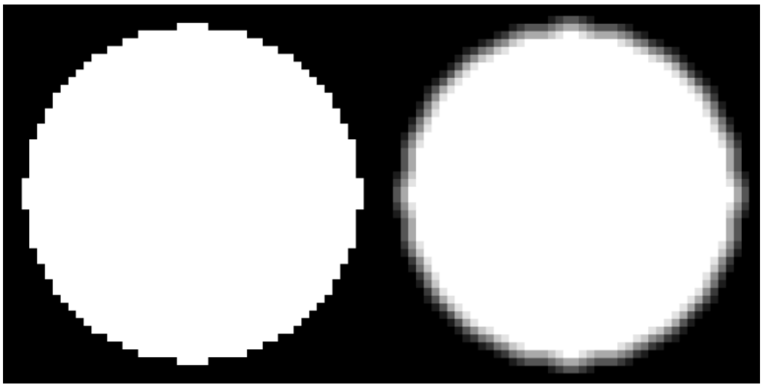

Figure 6.17: On the left, slice of the initial binarised sphere. On the right, the same sphere after the Gaussian filter is applied

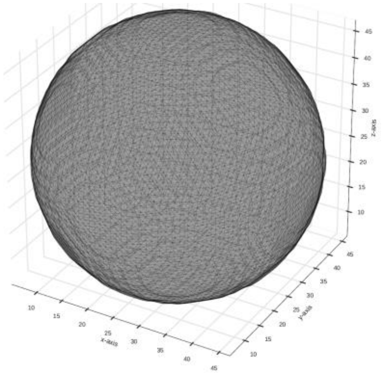

Figure 6.18: Surface mesh visualisation after application of the MC-algorithm

The surface area (analytical solution) of a sphere having radius equal to 25 pixels is 7853.98 px^2, whereas the surface area of the equivalent numerical sphere from the MC-algorithm is 7815.38 px^2, therefore the difference is only 0.49%. Discrepancies of similar magnitude were measured for an ellipsoid having axis a, b, and c respectively equal to 50, 50 and 25 pixels.

The computational time requested by this operation is relatively low: 0.0845 seconds, which means 1.9% of the total calculation time for this grain.

6.2.4 Inertia Tensor

The *Inertia tensor* quantifies the tendency of a body to rotate in the space around a given axis of rotation, it contains the information about its mass spatial distribution. In a three-dimensional framework it is a 3 × 3 matrix that can be expressed as:

$$I = \begin{bmatrix} I_{xx} & I_{xy} & I_{xz} \\ I_{yx} & I_{yy} & I_{yz} \\ I_{zx} & I_{zy} & I_{zz} \end{bmatrix} \tag{6.1}$$

Where I_{xx}, I_{yy}, I_{zz} are called the *moments of inertia* along respectively x, y and z axis. The other terms are called the *products of inertia*. It is important to point out that the inertia tensor is symmetric, therefore $I_{ij} = I_{ji}$.

The inertia tensor can be re-written in a computationally efficient form as:

$$I = \sum_{n} m_n \left[(x_n \cdot x_n)I_3 \text{-} (x_n \cdot x_n{}^T)\right] \tag{6.2}$$

Where x_n is the position vector of the point *"n"* having mass m_n, and I_3 is the *identity matrix*.

The labelled grains of the 3-D images are assumed homogeneous in terms of density ρ, therefore the inertia tensor for a single particle only depends on the spatial distribution (and amount, *V*) of the voxels making up the grain, and not on m_n.

$$I = \rho\left[(x_n \cdot x_n)I_3 \text{-} (x_n \cdot x_n{}^T)\right] \cdot V$$

Once the inertia tensor is known, it can be diagonalised in order to get the *principal axes of inertia* and the *principal moments of inertia*. These axes provide a unique coordinate orientation for which $I_{xy} = I_{xz} = I_{yz} = 0$. This is an eigenvalue problem that can be easily numerically solved by the *numpy* function *"numpy.linalg.eig"*, the resulting eigenvalues (I_1, I_2, I_3) are the *principal moments of inertia,* whereas the resulting eigenvectors are the *principal directions of inertia* (w_1, w_2, w_3).

The *inertia tensor* of grain 46972 (all quantities are expressed in px^4) is:

$$I = \begin{bmatrix} 2542149 & 198137 & 44756 \\ 198137 & 1062625 & 33326 \\ 44756 & 33326 & 1980036 \end{bmatrix}$$

The inertia tensor eigenvectors (*principal directions of inertia*) are:

$$w_1 = [\,0.9879 \quad 0.1315 \quad 0.0821]$$
$$w_2 = [-0.0851 \quad 0.0179 \quad 0.9962]$$
$$w_3 = [0.1295 \quad -0.9912 \quad 0.0288]$$

The inertia tensor eigenvalues (*principal moments of inertia*) are:

$$I_{11} = 2572235.56\ px^4$$
$$I_{22} = 1976809.18\ px^4$$
$$I_{33} = 1035765.26\ px^4$$

The validation of the inertia tensor calculated in Python has been done by comparing the analytical and numerical results for a spheroidal shaped particle.

For a spheroid with the *z*-axis along the axis of symmetry, characterised by the equatorial radius (*a*) equal to 50 and the polar radius (*c*) equal to 25, the inertia tensor is given by:

$$I = \frac{1}{5}\begin{bmatrix} a^2 + c^2 & 0 & 0 \\ 0 & a^2 + c^2 & 0 \\ 0 & 0 & 2a^2 \end{bmatrix} = \begin{bmatrix} 625px^4 & 0 & 0 \\ 0 & 625px^4 & 0 \\ 0 & 0 & 1000px^4 \end{bmatrix} \tag{6.3}$$

An artificial, binarised *oblate spheroid* (a > c) has been created, implementing its equation with a python code, for comparison with the analytical solution. The lengths a and c are respectively set equal to 50 and 25 pixels. Figure 6.19 shows the voxelated spheroid and the *principal axis of inertia* centred in the particle's centre of mass, the colours of the arrows, as well as their length, represent the magnitude of the *principal moment of inertia*.

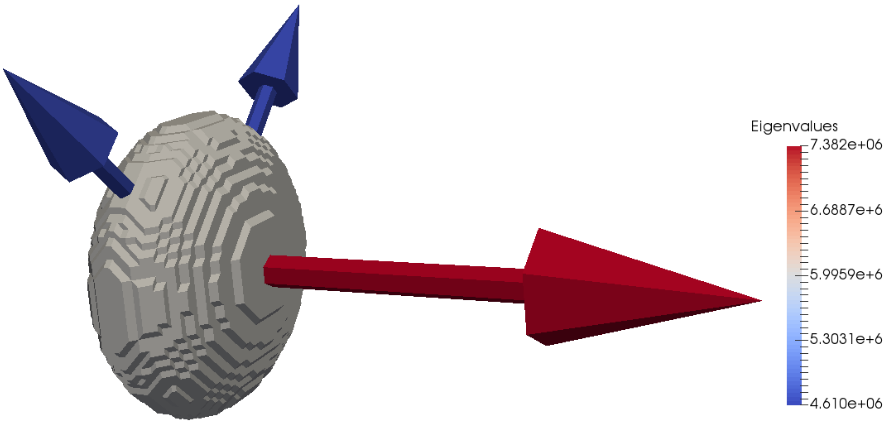

Figure 6.19: Paraview representation of the artificial spheroid with its principal inertia axis

As shown in Figure 6.19, the principal directions are properly individuated by the numerical algorithm. Moreover, the ratio between the eigenvalues of the inertia tensor is practically identical to the analytical result:

$$\left(\frac{I_1}{I_3}\right)_{numerical} = \frac{7381514.568px^4}{4610245.433px^4} = 1.601 \cong 1.600 = \frac{1000}{625} = \left(\frac{I_1}{I_3}\right)_{analytical} \tag{6.4}$$

The computational time requested by this operation is 0.3977 seconds, which means 9.0% of the total calculation time for this grain: it is the second most expensive operation.

6.2.5 Particle characteristic lengths

The calculation of characteristic lengths for a grain poses several problems. Firstly, it is necessary to define in a three-dimensional framework what are those characteristic lengths. For instance, one possibility is to use the *Feret diameters*, as defined in Chapter 2.2.1.1. The *maximum* and *minimum Feret diameters* can be obtained from 2-D projections of a 3-D body, otherwise they can be directly measured on the 3D object, by rotating two parallel tangents to the grain of a 4π steradians solid angle. However, Feret diameters are not the length measures used in the most relevant particle shape descriptors.

In this work, the characteristic lengths are defined as three perpendicular dimensions called respectively the *maximum*, the *intermediate* and the *minimum* grain lengths. Many researchers (Alshibli et al., 2015; Druckrey et al., 2016; Fonseca et al., 2012; Kong and Fonseca, 2018; Zhao and Wang, 2016) obtained these three dimensions making use of a statistical procedure called *Principal Component Analysis (PCA)*. Principal component analysis is a procedure for identifying a smaller number of uncorrelated variables, called *"principal components"*, from a large set of data. They are obtained from the eigendecomposition of the *variance-covariance matrix* C of the initial dataset.

In the context of particles lengths, the variables (for each grain voxel) are three, and the *ranges* of the dataset (after reference frame rotation) along the three different principal components $(\mathrm{pc}_1, \mathrm{pc}_2, \mathrm{pc}_3)$ give respectively the *maximum, intermediate* and *minimum* lengths of the particle.

In this current work, we obtained the orientations of the particles from the eigenvectors of the inertia tensor (*i.e.,* the principal directions of inertia), following the procedure explained in the previous section. The two approaches to obtain the grains lengths (PCA and inertia tensor) are equivalent. Indeed the inertia tensor reported in Eq. (6.2) can be rewritten as:

$$\begin{aligned} \mathrm{I} &= \sum_{\mathrm{n}} \mathrm{m_n} \cdot \left[(\mathrm{x_n} \cdot \mathrm{x_n})\mathrm{I_3} - (\mathrm{x_n} \cdot \mathrm{x_n}^{\mathrm{T}})\right] = \sum_{\mathrm{n}} \mathrm{m_n} \cdot (\mathrm{x_n} \cdot \mathrm{x_n})\mathrm{I_3} - \sum_{\mathrm{n}} \mathrm{m_n} \cdot \mathrm{x_n} \cdot \mathrm{x_n}^{\mathrm{T}} = \\ &= \mathrm{I_3} \cdot \mathrm{tr(C)} - \mathrm{C} \end{aligned} \tag{6.5}$$

where C is the mass-weighted variance-covariance matrix defined as

$$C = \sum_{n} m_n x_n \cdot {x_n}^T \tag{6.6}$$

The variance-covariance matrix C is symmetric, and therefore it can be diagonalised (obtaining the matrix D) by the matrix R (*i.e.,* the rotation matrix), as

$$C = RDR^{-1} = RDR^T\,. \tag{6.7}$$

It is now possible to rewrite the inertia tensor I as:

$$I = I_3 \cdot tr(C) - C = RR^T \cdot tr(C) - RDR^T = R[tr(C)I_3 - D]R^T \tag{6.8}$$

and since the matrix $[tr(C)I_3\text{-}D]$ is diagonal, it follows both the I and C are diagonalised by the same rotation matrix R**.** Therefore the eigenvectors, which are the body orientation in space, are the same for both approaches: PCA and inertia tensor. This has also been verified numerically, comparing both techniques in the validation that follows, obtaining exactly the same results.

The validation of the numerical algorithm has been done with the same oblate spheroid used for the validation of the inertia tensor. The only difference from the previous is that the spheroid is progressively rotated around one axis in order to test the ability of the algorithm to capture the exact spheroid diameters when its special orientation varies. Seven different orientations are tested: 0, 15, 30, 45, 60, 75 and 90 degrees of rotation around the *z*-axis, the spheroid lengths never differ more than 2% from the actual radius of the analytical spheroid.

For grain 46972 the gran lengths (L_1, L_2, L_3) are listed below, as well as their visual representation in Figure 6.20.

$$L_1 = 50.75\text{ px}$$
$$L_2 = 38.04\text{ px}$$
$$L_3 = 18.96\text{ px}$$

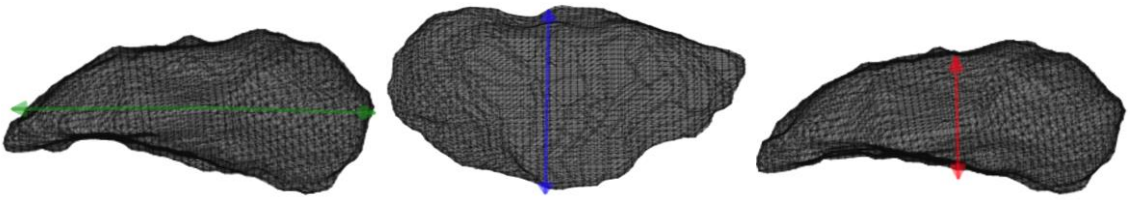

Figure 6.20: Longest (a), intermediate (b) and shortest (c) lengths of grain 46972.

The three arrows representing the grain lengths are perpendicular, as expected. They are drawn passing through the grain's centre of mass, however the dimensions calculated numerically do not intersect inevitably from this point: this is why the arrows' ends can fall outside the grain's surface.

The computational time requested by this operation is 0.0040 seconds, which means only 0.1% of the total calculation time for this grain.

6.2.6 Convex hull

The convex hull is defined as the minimal convex polytope (generalised polyhedron) covering of a 3-D object.

The calculation of the convex hull is carried out by the *scipy* function "*scipy.spatial.ConvexHull*". It takes as input an array of points (the voxels coordinates) to construct the convex hull from.

Then, the embedded functions "*hull.volume*" and "*hull.area*" allow calculating the volume surrounded by the convex hull and its surface area.

The computational time requested by this operation is 0.0075 seconds, which means 0.2% of the total calculation time for this grain.

6.2.7 Maximum inscribed sphere

The maximum inscribed sphere is obtained by calculating the *Euclidean distance transform* (also called *distance map*) on the 3-D array representing the labelled grain (the assembly of voxels). In particular, the scalar value into each cell of the array (a Boolean value *i.e.,* "1" if the grain, "0" if the void) is substituted with the value of the Euclidean distance measured from the cell itself to the grain boundary, individuated by the Boolean value "0". As a result, the maximum distance into this *transformed* array represents the radius of the maximum inscribed sphere, whereas the position of this voxel represents the co-ordinates of the sphere`s centre.

The transformed array has been calculated in Python by the *scipy* function "*scipy.ndimage.morphology.distance_transform_edt*" giving as input the binarised grain.

For grain 46972 the maximum inscribed sphere radius is equal to 8.60 pixels. Note that the diameter is relatively close to the shortest characteristic grain length (L_3) previously calculated.

The computational time requested by this operation is 0.0942 seconds, which means 2.1% of the total calculation time for this grain.

6.2.8 Minimum circumscribed sphere

The minimum circumscribed sphere (also called *bounding sphere*) can be obtained by means of different algorithms characterised by a different efficiency and precision. The implementation chosen in this work is the *Ritter's algorithm* (Ritter, 1990). It is computationally efficient, although it can slightly overestimate the bounding sphere's radius.

Given a list of points (*i.e.,* the grain voxels), the algorithm works as follows:

1. Pick a point x from the list of points and search the point y having the maximum distance from x.
2. Search another point z having the maximum distance from y. The midpoint between y and z is the centre of the first *trial sphere*, and the distance between the two points is the diameter.
3. If all the points of the initial list are contained within the *trial sphere*, this is the bounding sphere. Otherwise, let p be a point outside the *trial sphere*, construct a new *trial sphere* including the point p and the old *trial sphere*. Repeat this procedure until all points are covered in order to get the bounding sphere.

Making use of the Ritter's algorithm on grain 46972, it is possible to obtain the radius of the minimum circumscribed sphere, equal to 26.32 pixels.
The computational time requested by this operation is 0.1083 seconds, which means 2.5% of the total calculation time for this grain.

The total computational time for calculating the geometric properties for all the grains within each specimen is around 40 hours on an Intel Xeon CPU E5-1620 3.5GHz with 48GB RAM. Nevertheless, it is a calculation that needs to be done only once for each specimen.

6.3 Numerical quantification of the particles shape descriptors

After evaluating the particles geometric properties particle shape descriptors (explained in Chapter 2) were evaluated. Not all the shape descriptors mentioned in Chapter 2 were computed. The selected shape descriptors for the study that follows are focused on sphericity and are listed below.

- *Degree of true sphericity,* Eq. (2.5)
- *Flatness index,* Eq. (2.8)
- *Elongation index,* Eq. (2.9)
- *Intercept sphericity,* Eq. (2.7)
- *Operational sphericity,* Eq. (2.6)
- *Convexity*, Eq. (2.17)
- *Alshibli sphericity,* Eq. (2.14)

The table below lists the mentioned shape descriptors calculated for grain 46972.

Shape descriptor	**Equation**	**Value**
Degree of true sphericity, Ψ	$\frac{\mathrm{s_n}}{\mathrm{S}}$	0.7427
Flatness index, FI	$\mathrm{c/b}$	0.4982
Elongation index, EI	$\mathrm{b/a}$	0.7496

Shape descriptor	Equation	Value
Intercept sphericity, Ψ_{int}	$\sqrt[3]{\frac{bc}{a^2}} = \sqrt[3]{FI\left(EI\right)^2}$	0.6542
Operational sphericity, Ψ_{op}	$\sqrt[3]{\frac{V}{V_{CS}}}$	0.5661
Convexity, Co	V/V_{CH}	0.8274
Alshibli Sphericity, Ψ_{al}	$\frac{V}{V_{d=c}}$	3.8868

Table 6.2: Shape descriptors for grain 46972 [V, S = volume and surface area of the grain. s_n = surface area of the equivalent sphere. V_{CS}, $D_{circ,min}$ = volume and diameter of the minimum circumscribed sphere. $D_{ins,max}$ = diameter of the maximum inscribed sphere. a, b, c = grain lengths. V_{CH} = volume of the convex hull]

These shape descriptors were calculated for all the grain contained within both the specimens of Caicos, Hostun and Ottawa sands. Therefore, it is possible to plot the histograms of the sands on the same graph and calculate some statistical values, as reported below. The statistical data of the Ottawa sand sample OUEA02 are also reported in Table 6.3.

Name	**Mean**	**St. Dev.**	**Skew**	**CV**
	Hostun	*Hostun*	*Hostun*	*Hostun*
	Caicos	*Caicos*	*Caicos*	*Caicos*
	Ottawa	*Ottawa*	*Ottawa*	*Ottawa*
Volume (mm^3)	0.027	0.017	1.53	0.63
	0.025	0.017	2.31	0.68
	0.014	0.005	3.21	0.39
True Sphericity	0.82	0.06	-0.75	0.07
	0.94	0.04	-1.89	0.04
	0.88	0.05	-1.55	0.06
Flatness index	0.73	0.14	-0.22	0.19
	0.85	0.09	-0.65	0.11
	0.78	0.11	-0.24	0.14
Elongation index	0.76	0.12	-0.24	0.16
	0.80	0.11	-0.65	0.14
	0.79	0.11	-0.28	0.14
Intercept sphericity	0.74	0.09	-0.18	0.12

Name	**Mean**	**St. Dev.**	**Skew**	**CV**
	Hostun	*Hostun*	*Hostun*	*Hostun*
	Caicos	*Caicos*	*Caicos*	*Caicos*
	Ottawa	*Ottawa*	*Ottawa*	*Ottawa*
	0.81	0.08	-0.64	0.10
	0.779	0.07	-0.21	0.09
Operational Sphericity	0.58	0.07	-0.09	0.12
	0.71	0.09	-0.45	0.13
	0.64	0.06	-0.31	0.10
Convexity	0.79	0.08	-1.00	0.10
	0.92	0.06	-2.10	0.06
	0.84	0.07	-1.88	0.09
Alshibli Sphericity	2.08	1.05	2.34	0.51
	0.75	0.09	-0.18	0.12
	1.90	0.69	1.62	0.36

Table 6.3: Statistics of the 3D shape descriptors for the three sands at the initial state

For instance, the normalised histogram of the "*degree of true sphericity (ψ)*" is reported in Figure 6.21. As expected, it is clear from the plot that the mean value of Caicos sand sphericity (0.9426) is higher than the value of Hostun sand (0.8184). Moreover, the histogram of Caicos is more asymmetric and presents a lower variance, whereas the Hostun histogram seems representing a normal distribution. The true sphericity of Ottawa sand (specimen OUEA02) is located between the histograms of Caicos and Hostun sands (mean = 0.88), as expected.

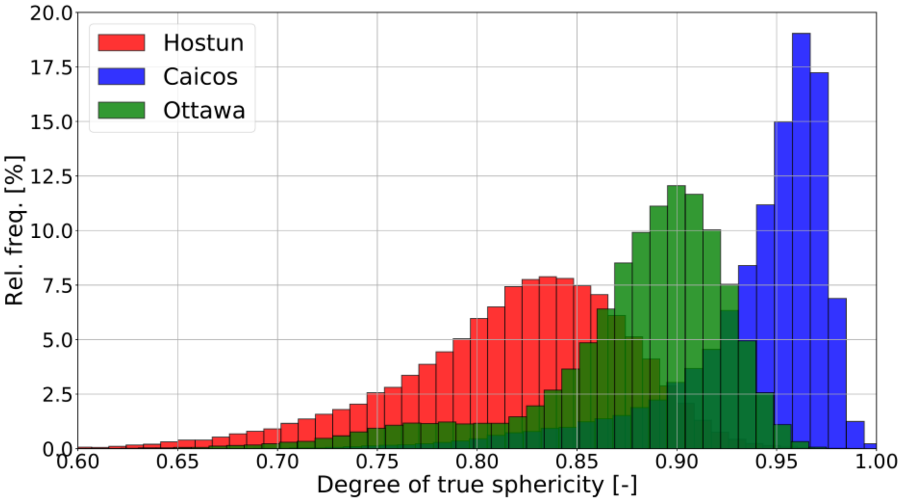

Figure 6.21: Normalised histogram of the "degree of true sphericity" for the three sands

In addition, the meshed surface of four selected grains characterised by the lowest and highest *degree of true sphericity* (ψ) for both, Caicos ooids and Hostun sand, are plotted in Figure 6.22.

	Minimum ψ	**Maximum ψ**
Hostun	Grain "38536" : ψ = 0.5075 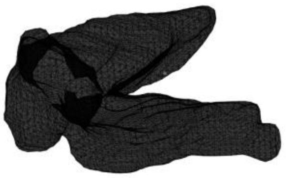	Grain "25161" : ψ = 0.9753 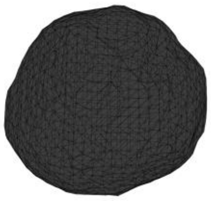
Caicos	Grain "1536" : ψ = 0.5667 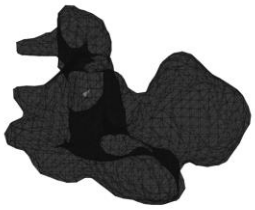	Grain "5866" : ψ = 0.9998 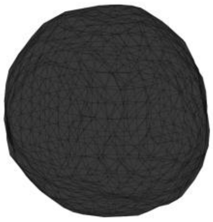

Figure 6.22: Meshed surfaces of the grains having extreme values of Sphericity (ψ)

The grains characterised by the minimum ψ are errors coming from the segmentation post-processing in image analysis (described in Chapter 5.4) in particular, probably they are multiple grains which have not been separated (this error is called *under-segmentation*). However, it is evident how the numerical algorithms are able to capture the desired quantity (sphericity) as they are intended for, with satisfying quality.

The same approach can be done with all the others shape parameters, for example the normalised histograms of the *flatness* and *elongation index* are presented in Figure 6.23 and Figure 6.24. In addition, the meshed surfaces of the grains having the maximum and minim value of the *flatness/elongation indices* are plotted in Figure 6.25 and Figure 6.26.

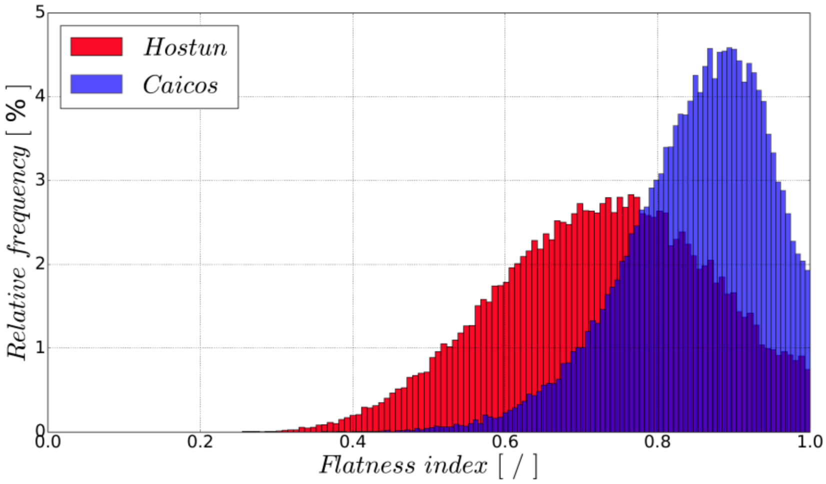

Figure 6.23: Histograms of the flatness index for HNEA01 and COEA04

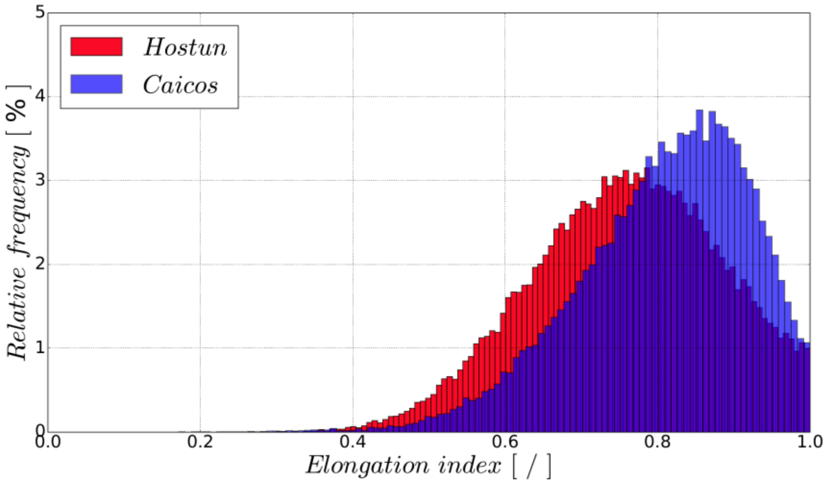

Figure 6.24: Histograms of the elongation index for HNEA01 and COEA04

	Minimum *flatness index (FI)*	**Maximum *flatness index (FI)***
Hostun	Grain "48612" : FI = 0.2551 ("coin" shaped) 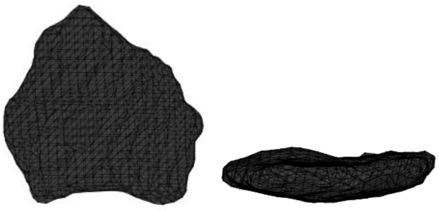	Grain "37522" : FI = 0.9999 ($L_3 \cong L_2$) 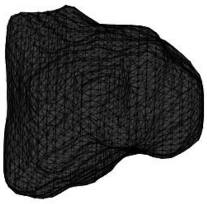
Caicos	Grain "50892" : FI = 0.3597 ("coin" shaped) 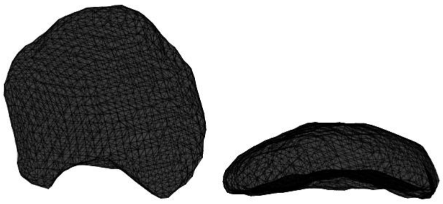	Grain "15119" : FI = 0.9999 ($L_3 \cong L_2$) 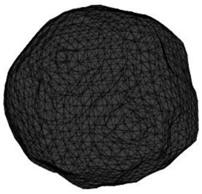

Figure 6.25: Meshed surfaces of the grains having extreme values of Flatness indices

	Minimum *elongation index (EI)*	**Maximum *elongation index (EI)***
Hostun	Grain "223" : EI = 0.2993 ("stick" shaped) 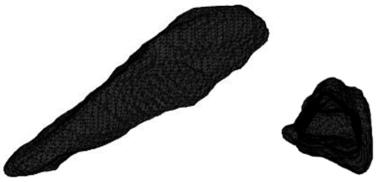	Grain "5544" : EI = 0.9999 ($L_1 \cong L_2$) 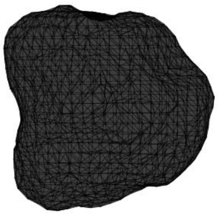
Caicos	Grain "10338" : EI = 0.1716 ("stick" shaped) 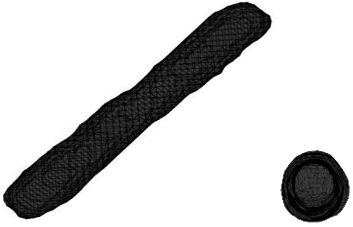	Grain "4909" : EI = 0.9999 ($L_1 \cong L_2$) 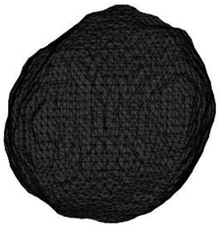

Figure 6.26: Meshed surfaces of the grains having extreme values of Elongation indices

Convexity is defined as the ratio between the particle volume and the volume of the convex hull bounding the particle itself. The meshed surface of four selected grains characterised by the lowest and highest values of convexity, are plotted in Figure 6.27.

	Minimum 3D-Convexity	**Maximum** 3D-Convexity
Hostun	Grain “21805” : S-3D = 0.2129 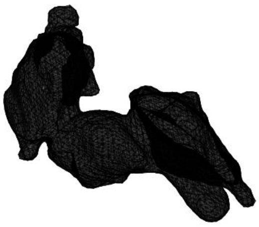	Grain “34437” : S-3D =0.9999 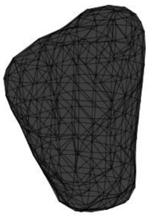
Caicos	Grain “2690” : S-3D = 0.2692 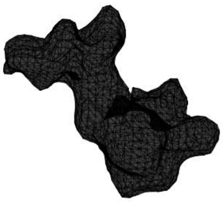	Grain “11130” : S-3D = 0.9999 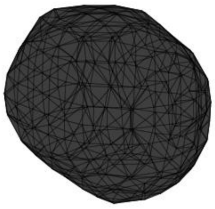

Figure 6.27: Meshed surfaces of the grains having extreme values of 3D-Convexity

It is important to note that the grains having a high value of convexity are not necessarily spherical, but rather that their surface is “convex”, without asperities. On the other hand, grains with very low value of convexity (as the ones in Figure 6.27), are also likely errors of the *segmentation* process described in Chapter 5.4.

Alshibli et al. (Alshibli et al., 2015) presented some shape data for Hostun sand. The mean true sphericity obtained here for Hostun is not far from the 0.77 value they reported. Figure 6.28 shows a more detailed comparison, now between the histogram of the Alshibli sphericity index (Ψ_{al}) as reported by Alshibli (2015) and that obtained from this study. Somewhat higher values are obtained here, but taking into account that different sand specimens, image acquisition systems and data treatment algorithms are employed, the agreement between the two distributions is satisfactory.

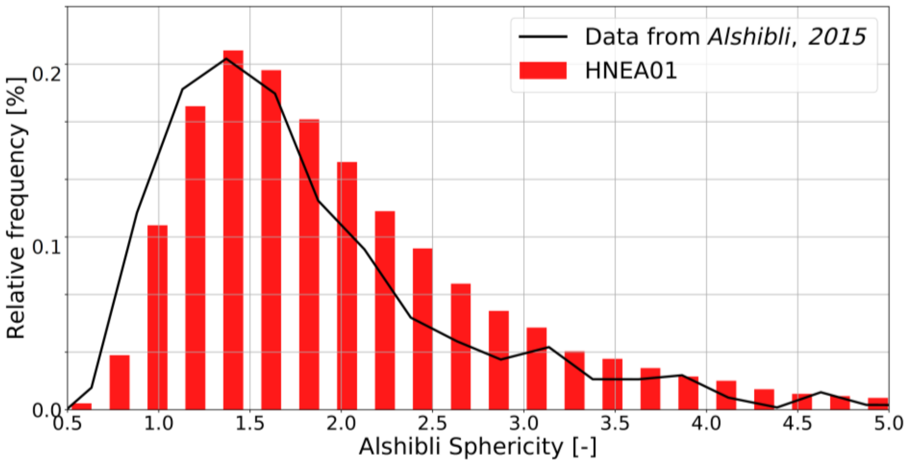

Figure 6.28: Comparison between the histograms of the Alshibli sphericity (see Table 6.2) of Hostun sand measured in this work with the data presented in (Alshibli et al., 2015)

The larger spectrum of shapes contained in the Hostun specimen is also visible in Figure 6.29, where the Zingg diagram (Zingg, 1935) is used to represent a bivariate distribution of *flatness* and *elongation indexes*. The Hostun specimen data spans three flatness Blott & Pye classes (Blott and Pye, 2008), whereas Caicos is contained in just two classes.

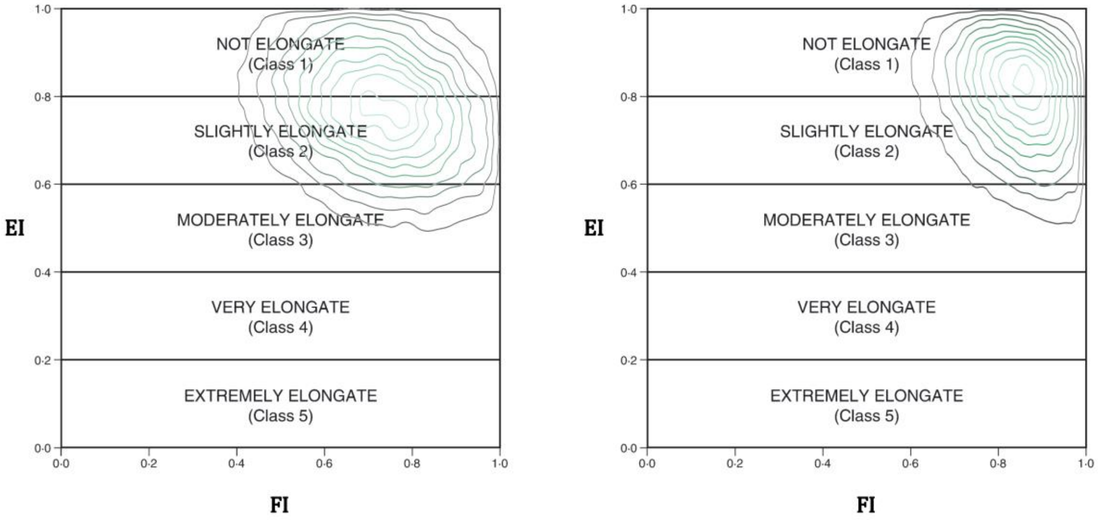

(a) (b)

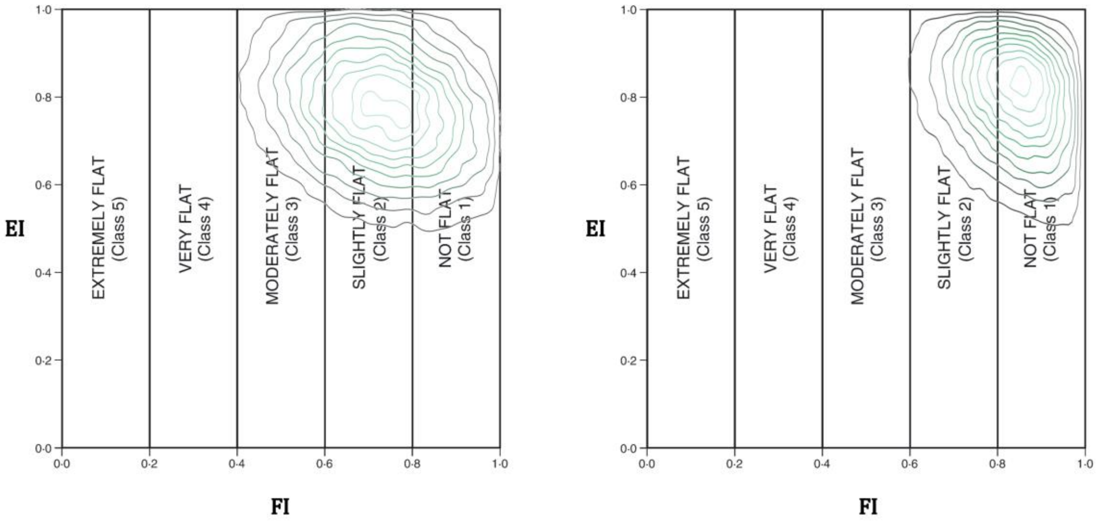

(c) (d)

Figure 6.29: Bivariate density plot of Hostun (a-c) and Caicos (b-d) shown on the Zingg form space with Blott & Pye (2008) classifications for Elongation (a-b) and Flatness (c-d). Isoline spacing is 10%.

6.4 3D shape descriptions: correlations

The correlations existing between some shape descriptors can be investigated simply plotting a couple of shape descriptors onto different axis in order to explore their distribution on a scatter plot. Since particle shape should convey geometrical information distinct from grain size, shape descriptors independent of particle volume are desirable. In Figure 6.30, 2D bivariate frequency distributions showing the mutual relationship between the degree of true sphericity and particle volume are plotted. The width of the sphericity marginal distribution at constant volume reduces as volume increases and the number of particles reduces. The mode, on the other hand, appears rather stable despite a slight negative bias towards lower Ψ with size for the artificial Hostun sand (Figure 6.30a).

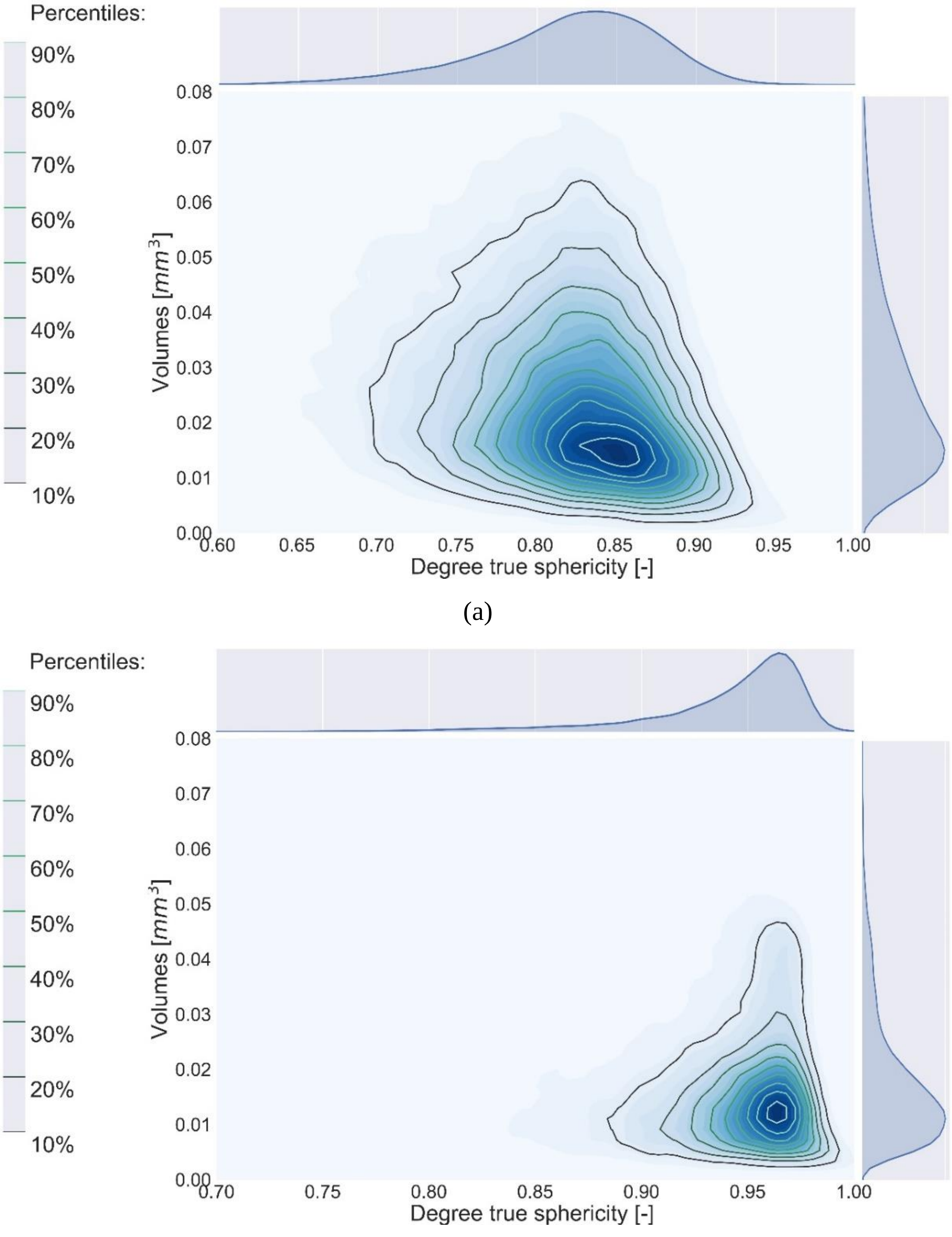

Figure 6.30: Relation between true sphericity and particle volume for Hostun sand (a) and Caicos ooids (b). Marginal distributions are also shown alongside the axis

Pearson product-momentum correlation coefficients for the shape parameters in specimens HNEA01 and COEA04 are summarized in correlation matrices presented in Table 6.4 and Table 6.5. The correlation matrix for the Ottawa specimen OUEA01 is reported also in Table 6.7. It appears that the correlation values for the three sands are similar, particularly for the stronger correlations. It is interesting that the *degree of true sphericity* shows a relatively good correlation with a simple measure like *Operational sphericity.* However, the stronger correlation is with *Convexity*. That strong correlation is indicative of a relatively rotund shape for these sand grains.

On the other hand, Krumbein *intercept sphericity*, Ψ_{int} is not as satisfactory as it is closer to Elongation Index than to either true or operational sphericity. The slight negative correlation between flatness and elongation indexes was already visible in Figure 6.29. The behaviour of other descriptors is more unexpected: for instance, the sphericity proposed by Alshibli (Ψ_{al}) appears negatively correlated with most other descriptors.

SHAPE DESCRIPTOR	V	Ψ	*FI*	*EI*	Ψ_{int}	Ψ_{op}	*Co*	Ψ_{al}
Grain volume	1.00	-0.26	0.13	0.09	0.16	0.03	-0.39	-0.20
True Sphericity	-0.26	1.00	0.37	0.26	0.47	0.62	0.84	-0.31
Flatness index	0.13	0.37	1.00	-0.21	0.36	0.34	0.05	-0.80
Elongation index	0.09	0.26	-0.21	1.00	0.83	0.32	0.10	-0.17
Intercept sphericity	0.16	0.47	0.36	0.83	1.00	0.51	0.12	-0.62
Operational sphericity	0.03	0.62	0.34	0.32	0.51	1.00	0.43	-0.33
Convexity	-0.39	0.84	0.05	0.10	0.12	0.43	1.00	0.11
Alshibli Sphericity	-0.20	-0.31	-0.80	-0.17	-0.62	-0.33	0.11	1.00

Table 6.4: Correlation matrix of the shape parameters for Hostun sand (48.612 grains).

SHAPE DESCRIPTOR	***V***	***Ψ***	***FI***	***EI***	$\boldsymbol{\Psi_{int}}$	$\boldsymbol{\Psi_{op}}$	***Co***	$\boldsymbol{\Psi_{\mathrm{al}}}$
Grain volume	1.00	-0.07	0.08	0.07	0.10	0.13	-0.28	-0.11
True Sphericity	-0.07	1.00	0.30	0.46	0.59	0.70	0.86	-0.32
Flatness index	0.08	0.30	1.00	-0.22	0.17	0.25	0.15	-0.69
Elongation index	0.07	0.46	-0.22	1.00	0.92	0.56	0.18	-0.37
Intercept sphericity	0.10	0.59	0.17	0.92	1.00	0.67	0.24	-0.65
Operational sphericity	0.13	0.70	0.25	0.56	0.67	1.00	0.48	-0.39
Convexity	-0.28	0.86	0.15	0.18	0.24	0.48	1.00	0.04
Alshibli Sphericity	-0.11	-0.32	-0.69	-0.37	-0.65	-0.39	0.04	1.00

Table 6.5: Correlation matrix of the shape parameters for Caicos sand (65.056 grains).

SHAPE DESCRIPTOR	V	Ψ	*FI*	*EI*	Ψ_{int}	Ψ_{op}	*Co*	Ψ_{al}
Grain volume	1.00	-0.65	0.08	-0.24	-0.20	-0.29	-0.68	-0.13
True Sphericity	-0.65	1.00	0.20	0.42	0.53	0.63	0.91	-0.16
Flatness index	0.08	0.20	1.00	-0.27	0.26	0.22	-0.03	-0.81
Elongation index	-0.24	0.42	-0.27	1.00	0.85	0.39	0.31	-0.12
Intercept sphericity	-0.20	0.53	0.26	0.85	1.00	0.51	0.30	-0.57
Operational sphericity	-0.29	0.63	0.22	0.39	0.51	1.00	0.52	-0.23
Convexity	-0.68	0.91	-0.03	0.31	0.30	0.52	1.00	0.15
Alshibli Sphericity	-0.13	-0.16	-0.81	-0.12	-0.57	-0.23	0.15	1.00

Table 6.6: Correlation matrix of the shape parameters for Ottawa sand (112.411 grains)

6.5 Projected (2D) measures of shape

2D measures of shape were acquired on all particles using as projection direction that of the minor principal axis (*i.e.,* projecting the particle outline on the plane containing the larger and intermediate axes, also called the "*plane of greatest stability*"). Suh et al. (Suh et al., 2017) demonstrated that this kind of projection results in 2D shape measures within 5% of the values obtained when particles are displayed on a flat surface (*i.e.,* when they are under equilibrium under self-weight).

For comparison purposes, randomly oriented particle projections were also obtained for a subset of particles of each sand. To do so, all the particles have been projected on a fixed vertical plane, but maintaining the particle in-specimen orientation. The specimens were built using a dry pluviation procedure (Andò, 2013) and it is assumed that this resulted in random particle orientations. Once the projected outline of the particle was obtained, similar (simplified) algorithms employed for the three-dimensional case (Chapter 6.2) were used to measure bi-dimensional geometrical quantities (Chapter 2.2.1.1) that, when combined, result in the 2D sphericity descriptors listed in Table 6.7 and Table 6.8, respectively for the randomly and oriented particles projections.

Name	**Mean** ***Hostun*** ***Caicos***	**St. Dev.** ***Hostun*** ***Caicos***	**Skew** ***Hostun*** ***Caicos***	**CV** ***Hostun*** ***Caicos***
Area sphericity	0.60	0.12	-0.36	0.20
	0.75	0.12	-0.68	0.16
Diameter sphericity	0.76	0.08	-0.63	0.11
	0.88	0.07	-0.95	0.08
Circle ratio sphericity	0.59	0.11	-0.43	0.19
	0.72	0.11	-0.75	0.15
Perimeter sphericity	0.84	0.05	-0.64	0.06
	0.92	0.04	-1.22	0.04
KS sphericity	0.65	0.12	-0.22	0.18
	0.70	0.13	-0.70	0.19

Table 6.7: Statistics of the 2D shape descriptors for the two sands (obtained from randomly oriented projections)

Name	**Mean**	**St. Dev.**	**Skew**	**CV**
	Hostun	*Hostun*	*Hostun*	*Hostun*
	Caicos	*Caicos*	*Caicos*	*Caicos*
Area sphericity	0.66	0.10	-0.39	0.15
	0.77	0.10	-0.82	0.13
Diameter sphericity	0.81	0.07	-0.61	0.09
	0.88	0.06	1.05	0.07
Circle ratio sphericity	0.65	0.09	-0.37	0.14
	0.75	0.11	0.86	0.15
Perimeter sphericity	0.85	0.05	-0.86	0.06
	0.92	0.05	-1.70	0.05
KS sphericity	0.76	0.12	-0.25	0.16
	0.80	0.12	-0.78	0.15

Table 6.8: Statistics of the 2D shape descriptors for the two sands (obtained from projections oriented along the minor principal axis)

Random orientation introduced a significant bias, decreasing the mean values for all 2D parameters. Random particle orientation also increased the variability of almost all 2D shape measures, except that of perimeter sphericity.

6.6 Relation between 2D and 3D shape descriptors

In both cases (*randomly* and *not-randomly* oriented grain projections), the grain label is preserved from the three-dimensional sample, therefore 2D and 3D shape parameters can be directly compared and statistically studied in order to explore potential correlates between them.

Table 6.9 and Table 6.10 show the correlation matrices of true sphericity (3D) and the 2D sphericity proxies listed in Table 6.7 and Table 6.8, as measured, respectively, on the *randomly* and *non-randomly* oriented particle projections. Data for Caicos and Hostun is merged in this analysis.

SHAPE DESCRIPTOR	Ψ	S_A	S_D	S_C	S_P	S_{KS}
True Sphericity 3D	1.00	0.58	0.61	0.66	0.55	0.49
Area sphericity 2D	0.58	1.00	0.99	0.95	0.72	0.81
Diameter sphericity 2D	0.61	0.99	1.00	0.93	0.65	0.80
Circle ratio sphericity 2D	0.66	0.95	0.93	1.00	0.71	0.77
Perimeter sphericity 2D	0.55	0.72	0.65	0.71	1.00	0.34
KS sphericity 2D	0.49	0.81	0.80	0.77	0.34	1.00

Table 6.9: Correlation matrix between 3D and 2D sphericity parameters (obtained from randomly oriented projections). Merged data for Hostun and Caicos, 2000 grains for each one.

SHAPE DESCRIPTOR	Ψ	S_A	S_D	S_C	S_P	S_{KS}
True Sphericity 3D	1.00	0.70	0.69	0.72	0.83	0.36
Area sphericity 2D	0.70	1.00	1.00	0.96	0.80	0.81
Diameter sphericity 2D	0.69	1.00	1.00	0.96	0.80	0.81
Circle ratio sphericity 2D	0.72	0.96	0.96	1.00	0.82	0.79
Perimeter sphericity 2D	0.83	0.80	0.80	0.82	1.00	0.45
KS sphericity 2D	0.36	0.81	0.81	0.79	0.45	1.00

Table 6.10: Correlation matrix showing 3D and 2D sphericity parameters (obtained from projections oriented along the minor principal axis). Merged data for Hostun and Caicos, 2000 grains for each one.

It is noteworthy, but not surprising – given its close relation to elongation – that the Krumbein-Sloss sphericity 2D proxy offers the poorest correlation with the 3D true sphericity measure. Correlation strength increases significantly for all other 2D proxies when the 2D measurements are taken on oriented (*i.e.,* maximum area) projections. In particular, *perimeter sphericity* (S_P) is the 2D descriptor that appears best correlated with true sphericity (Pearson correlation coefficient equal to 0.83). This perhaps reflects the fact that the definition of *perimeter sphericity* (Eq. 2.3 and Table 2.1) is equivalent to that of true sphericity for the 2D case. For practical purposes, a linear regression line can be drawn (Figure 6.31) through the data to link the 3D true sphericity with the 2D perimeter sphericity resulting in the expression

$$\psi = 1.075(S_P)\text{-}0.067 \tag{6.8}$$

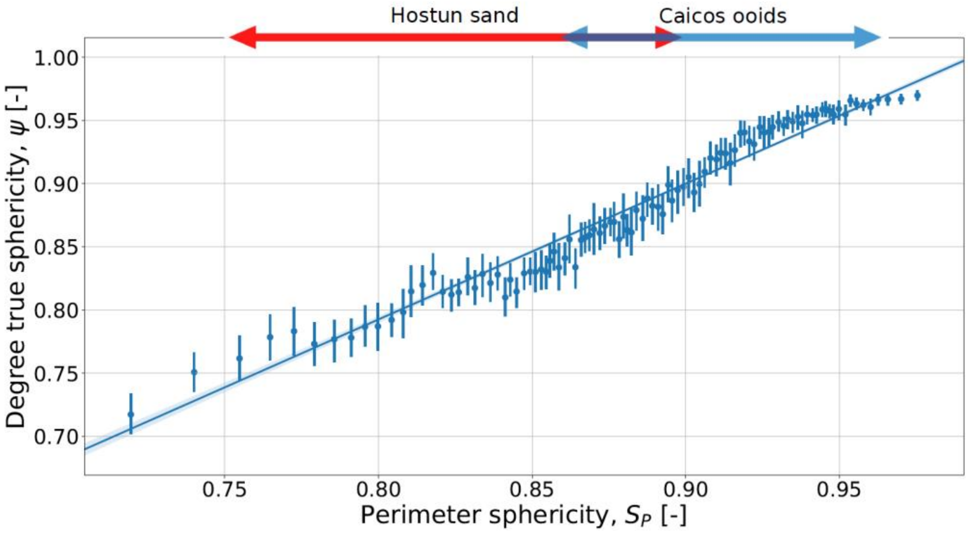

Figure 6.31: Linear regression line between true sphericity (3D) and perimeter sphericity (2D). The arrows show the ranges (5% and 95% percentiles) of the two sands.

6.7 Statistical convergence of sample size

The sand specimens studied in this work contain many thousands grains each. Shape was measured in all of them. This exhaustive procedure was necessary for other studies – not reported here – but will not have been so if the goal was simply shape characterization. Figure 6.32 shows the deviation from the whole specimen value of the three first statistical moments (*i.e., mean, standard deviation* and *skew*) of the true sphericity distribution computed in random sub-samples of varying sample size.

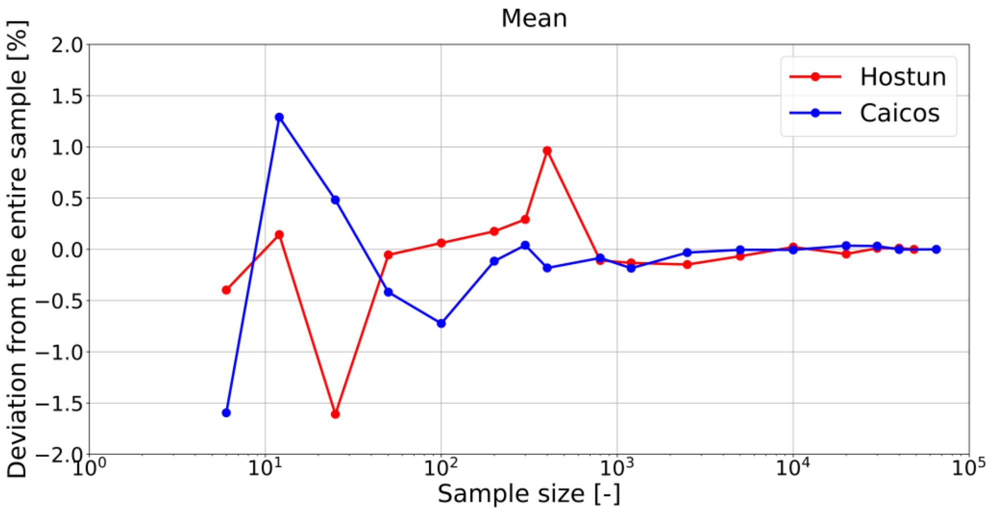

(a)

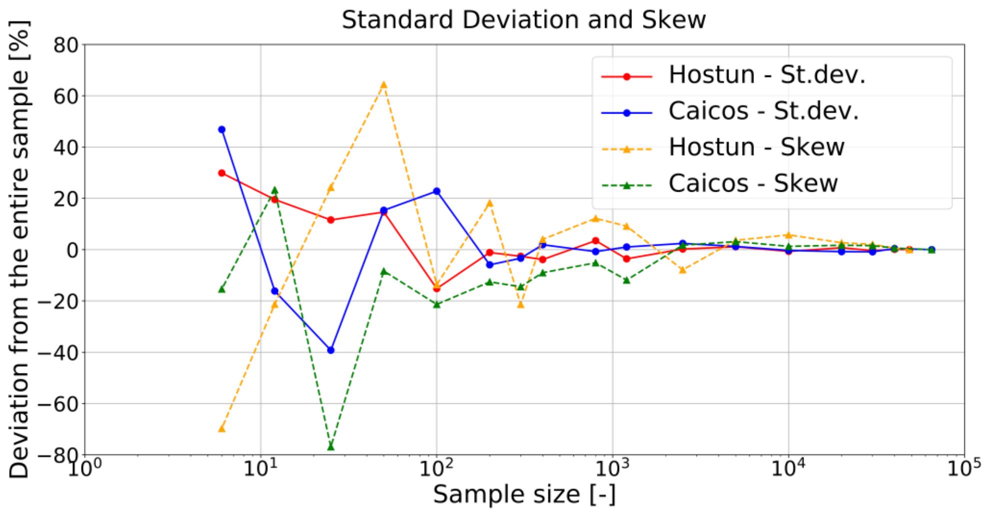

(b)

Figure 6.32: Evolution of the first three sample moments (mean, standard deviation, skew) of true sphericity with sample size

As expected, it is evident that the error decreases with sample size, and it suggests that sample sizes of at least 1000 particles should be employed to capture shape variability in sands. This number, although far smaller than that used in this study is still one order of magnitude higher of that reported in most 3D studies of sand shape to date. The effect of shape variability has been studied by (Rorato et al., 2018). Using a DEM model it was shown that the macroscopic response under triaxial loading was strongly affected by the variance of the particle shape distribution, and not just by its mean.

6.8 Sphericity evolution during triaxial shearing

The sand specimens analysed here were then tested in triaxial compression under a cell confinement of 100 kPa (Andò, 2013). The stress level applied in these tests is well below that required for breakage and indeed no breakage was visible in tomography. Using a reduced subset of grains (*i.e.,* 2000) a check was made on the evolution of shape parameters during the triaxial test. The summary statistics for some parameters at the final state are reported in Table 6.11. The averages and standard deviations remain practically unchanged when compared with the initial values (Table 6.3), particularly for the harder Hostun sand. Minor changes are noted in skew, a statistic that is highly sensitive to changes at the extremes of the distribution. A tiny decrease in particle size is detected in Caicos. These very small changes are consistent with previous work (e.g. Altuhafi and Coop 2011) where insignificant shape change was noted for tests below the onset of particle breakage.

Name	**Mean**	**St. Dev.**	**Skew**	**CV**
	Hostun	*Hostun*	*Hostun*	*Hostun*
	Caicos	*Caicos*	*Caicos*	*Caicos*
Volume (mm^3)	0.028	0.017	1.61	0.62
	0.023	0.014	2.75	0.63
True Sphericity	0.82	0.06	-0.75	0.07
	0.95	0.04	-2.14	0.05
Flatness index	0.73	0.13	-0.17	0.18
	0.84	0.09	-0.74	0.11
Elongation index	0.76	0.12	-0.24	0.16
	0.80	0.11	-0.80	0.14
Intercept sphericity	0.74	0.08	-0.20	0.11
	0.81	0.08	-0.80	0.10

	Mean	**St. Dev.**	**Skew**	**CV**
Name	*Hostun*	*Hostun*	*Hostun*	*Hostun*
	Caicos	*Caicos*	*Caicos*	*Caicos*
Operational Sphericity	0.58	0.07	-0.15	0.11
	0.72	0.08	-0.62	0.11
Convexity	0.77	0.08	-1.14	0.11
	0.93	0.05	-2.97	0.05
Alshibli Sphericity	1.96	0.91	2.04	0.47
	0.86	0.15	-0.16	0.21

Table 6.11: Statistics of the 3D shape descriptors for the two sands at the critical state on 2000 grains

6.9 Summary

In this chapter, it is shown how individual particles can be (1) extracted from a three-dimensional image representing a sand sample and (2) studied in order to quantify shape properties and descriptors. In particular, the main findings are summarised hereafter:

- The shape of more than 200.000 particles has been quantified in three-dimensions, exploiting efficient open-source algorithms;
- True sphericity is independent of particle size and well correlated with 3D Convexity;
- True sphericity (3D) is well correlated with Perimeter sphericity (2D) under maximum particle projections;
- Two thousand (2000) grains are enough to capture the statistical variability of true sphericity for a sand sample;
- Hostun and Caicos sands do not change shape (and do not crash) after triaxial shearing at 100kPa confining.

7

Study of grain kinematics during triaxial tests

7.1 Introduction

As explained in Chapter 3 particle shape has a strong effect on the mechanical response of coarse soils. This has been usually observed examining specimen-scale or engineering-scale responses, which are the result of many microscale interactions. Granular soils are made of discrete particles that interact with each other, therefore changes at the small-scale (*i.e.,* grain-scale) affect the material response at the large-scale (*i.e.,* engineering-scale) (Baudet and Bolton, 2010; Jiang et al., 2011; Soga et al., 2014).

It follows that particle shape must affect grain-scale interactions to produce those effects. This hypothesis has been repeatedly supported, from various perspectives, by the results of numerical simulation. In numerous discrete element models direct control of element shape has been shown to result in major changes in ensemble mechanical responses (e.g. (Cleary, 2008; Ferellec and Mcdowell, 2010; Jiang et al., 2016; Ng and Lin, 1997; Rothenburg and Bathurst, 1992)). It is noteworthy, however, that similar macroscopic effects are observed when particle shape effects are represented indirectly, through appropriately modified element contact interaction laws, for instance introducing some resistance against rolling at the contact (Belheine et al., 2009; Huang et al., 2017; Iwashita and Oda, 1998; Jiang et al., 2005). Both direct and indirect shape modelling strategies inevitably involve some degree of simplification, to be adjusted in applications under typically conflicting constraints of computational speed, accuracy and ease of calibration (Coetzee, 2016).

In this context, direct experimental observation of the microscale effects of particle shape appears relevant, as it may provide evidence beyond that implicit in the ensemble behaviour of the specimen. This has been a relatively unexplored avenue, because it requires relevant and accurately measured shape descriptors, as well as particle-scale resolution of internal mechanisms. There are few experimental techniques useful for that purpose (Guillard et al., 2017) and the main one is relatively recent: microfocus or μX-ray tomography (Hall et al., 2010; Hasan and Alshibli, 2010; Matsushima et al., 2006; Oda et al., 2004).

Despite significant difficulties, progress in 3-D tomographic imaging and post-processing technologies, (Alshibli et al., 2015; Fonseca et al., 2012; Kong and Fonseca, 2018; Rorato et al., 2019; Zhao and Wang, 2016), has made accurate grain shape determination feasible for most sands. Identification of particle-scale mechanisms is more difficult, as it requires imaging not just isolated particles, but particles in collective interaction, within specimens. Particles need to be separated from one another, within the imaged ensemble. Ideally, the existing contacts amongst particles need to be identified, as interactions between particles occur through contact forces in coarse soils. Single snapshots of microstructures (typically acquired "post-mortem", after dismounting the test, Oda et al. 2004, Hasan and Alshibli 2010, Fonseca et al. 2013) cannot reveal kinematics. For that purpose a sequence of images needs to be acquired during a test, and triaxial tests have been the target for most of this kind of work (Alshibli et al., 2017; Andò et al., 2012a; Cheng and Wang, 2018a; Hasan and Alshibli, 2012; Higo et al., 2013). Clearly, one added difficulty here is the need to track particles confidently across different images.

Progress in these tasks has been also very significant, but there are still some important obstacles, particularly in the area of contact detection and measurement. Indeed, the level of image resolution required to image particle contacts – and contact properties such as orientation - appears far more demanding than that required to image, identify and measure particles (Wiebicke et al., 2018, 2017). This has implicitly limited the scope (number of tracked particles and/or number of imaged test steps) of kinematic contact fabric imaging studies (Alshibli and Alramahi, 2006; Cheng and Wang, 2018b; Hasan and Alshibli, 2012; Vlahinić et al., 2017).

Current technology may be exploited to obtain more statistically sound results if the focus is restricted to particle kinematics. This is the avenue explored in this Chapter, in which it is examined in detail the relations between individual grain shape and individual kinematical history of sand grains as observed during triaxial compression of two dense sand specimens comprising more than 100.000 grains altogether. For the purposes of this study, the specimens selected for examination had the advantage of failing in sharply localized shear modes. As clearly identified in previous research (Hall et al., 2010; Hasan and Alshibli, 2010; Oda et al., 2004) the structure and kinematics of particles within a shear band are very different from those outside, as particles in a shear band approach critical state flowing conditions. As long as a criterion for belonging or not into the shear band could be clearly established, this experimental feature ensured that the influence of particle shape could be examined in two very different and separate kinematic settings (*i.e.,* within the band and outside it), thus making the study relevant for a larger set of conditions.

7.2 Digital image correlation for particle tracking

Digital Image Correlation (DIC) is the ideal tool for comparing and analysing images of deforming materials, such the ones obtained from x-ray scans. DIC is a widely used technique in experimental mechanics to deduce motion and shape features of an object by comparing its appearance in different images (Sutton et al., 2009). A first classification of DIC may be based on the dimensional support of the images employed in the comparison (Hall, 2012): surface-DIC is based on bi-dimensional images, whereas volumetric DIC (or, simply, digital volume correlation, DVC), is based on three-dimensional images. Surface-DIC is widely employed in field and laboratory experimental geotechnics (Take, 2015). DVC has seen fewer applications because of the increased difficulties associated with 3D image acquisition.

In DIC a subset F of intensity values from a reference image is systematically compared with subsets G_i of the transformed image until some optimality condition is achieved (Pan et al., 2009). This optimality condition is frequently based on a cross correlation measure, for instance searching for a maximum normalised cross correlation:

$$NCC = \frac{F * G_i}{\|F\| \|G_i\|} \tag{7.1}$$

Different algorithms are obtained depending on how the subset F is chosen, what kind of motion is assumed to relate F and G_i and how the search window (SW, the zone in which G_i is searched for) is defined.

Two broad variants of DVC have been employed in geotechnical applications: *continuum* (C-DVC) and *discrete* (D-DVC). In C-DVC, the subset F (usually referred to as correlation window, *CW*) is a cubical cell centred around some pre-established evaluation grid points. Although more complex transformations are sometimes used (Stanier et al., 2016), the motion relating F and G is usually assumed as a simple rigid translation, and cross correlation is employed to find a displacement vector, which is assigned to the grid node. From the displacement field thus obtained, strain measures are derived using different procedures (Pinyol and Alvarado, 2017). The underlying assumption is that subset F is a representative volume element RVE in a continuum; therefore, the scale of the *CW* should contain enough grains to make that assumption realistic.

C-DVC ignores the discrete nature of a granular material. If the resolution of the images is such that individual grains may be identified, other alternatives are possible. Hall (Hall et al., 2010) proposed a novel discrete *grain-based* approach (D-DVC) to track individual particles. The method has as a starting point a *segmented* labelled image, in which groups of voxels are identified as grains. In D-DVC the subset F is selected considering which voxels have been previously assigned to a certain grain and is named a grain mask. The assumed motion between F and G is a rigid body motion, including translation and rotation. With D-DVC the kinematics of each identified particle is thus directly obtained. An example output of D-DVC is shown in Figure 7.2, giving as input the greyscales images of Figure 7.1.

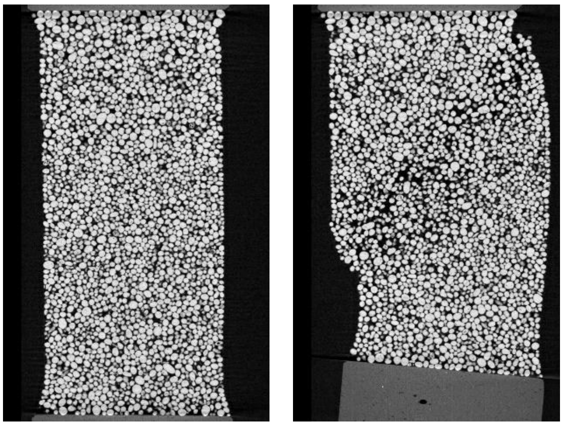

Figure 7.1: *Grey-scale images (slices) of specimen COEA04 at increments "01" (left) and "11" (right). It is clear how the bottom plates moved upwards, inducing axial shortening and failure in the specimen.*

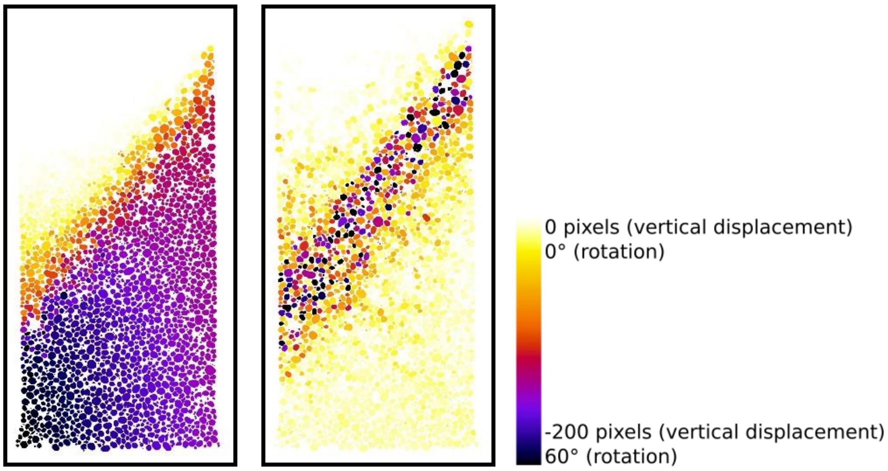

Figure 7.2: *Vertical slices of Caicos sand showing grains vertical displacement (on the left) and rotations (on the right) measured from increment "01" (start of deviatoric load) to increment "11" (end of the test). Grains are coloured by the value of their measured z-displacement and total rotation at step "11", although the image is referred to the loading step "01" (initial state).*

Hall (Hall et al., 2010) went on to illustrate the potential of D-DVC obtaining maps of incremental displacements and rotations in a triaxial specimen of Hostun sand, showing also that the kinematic history of single grains was very different if they were involved in a shear band or not.

Andò (Andò et al., 2012a) proposed an alternative method to follow grain kinematics across images, called ID-track. In this method grain match between successive images is based on listed properties of grains, such as volume, surface area, etc. obtained through single-image analysis. The method requires two segmented images as input. The grain matching operation is faster than in D-DVC, as volume cross-correlation is not needed.

With some modifications, ID-track has been later used by Alshibli *et al.* (2017), and Cheng and Wang (2018a), amongst others. However, ID-track has some difficulties to assign precise rotation values, particularly when dealing with very spherical particles (Andò et al., 2012a), and was therefore extended to include a D-DVC based technique for rotation measurement in (Andò et al., 2012b). For this reason, the work presented here was based on the more robust, if slower, D-DVC technique.

7.2.1 Single-image post-processing

Each 3D tomograph results simply in grey-scale images, in which the only variable (the greyscale of each voxel) represents the x-ray attenuation coefficient assigned to that location. Therefore, before studying individual grains, it is necessary to *binarise*, *separate* and *label* the tomographic images. This was done here following the procedures described by Andò (Andò et al., 2012a), see chapter 5.4. At this point, it is possible to extract single grains from the 3D labelled images. The 3D tomographic images representing Hostun (specimen HNEA01) and Caicos (specimen COEA04) sands contain respectively 48.612 and 65.056 particles.

Geometrical properties (e.g. volume, surface area, inertia tensor…) of the image subset assigned to each grain are obtained through the post-processing procedures described in Chapter 6. These properties may be used, in turn, to obtain different shape descriptors in 3D or 2D. The procedures applied for this purpose are also described in detail in Chapter 6; that also includes an exhaustive database of 3D shape descriptors for all the grains in these specimens, evaluating significant statistics. It was also verified in Chapter 6.8 that the shape descriptors of the sands remained statistically invariant during the triaxial tests.

7.2.2 Tracking grains kinematics with D-DVC

The triaxial tests mentioned were scanned by x-rays at several loading stages (16 for test HNEA01 and 11 for COEA04), as described in Chapter 5. The stress-volumetric-strain curves, with indication of scanning stages are shown in Figure 7.3. The macroscopic responses of both tests are typical of dense sands, with a stress peak followed by shearing to critical state. Both tests failed in a localized shear mode.

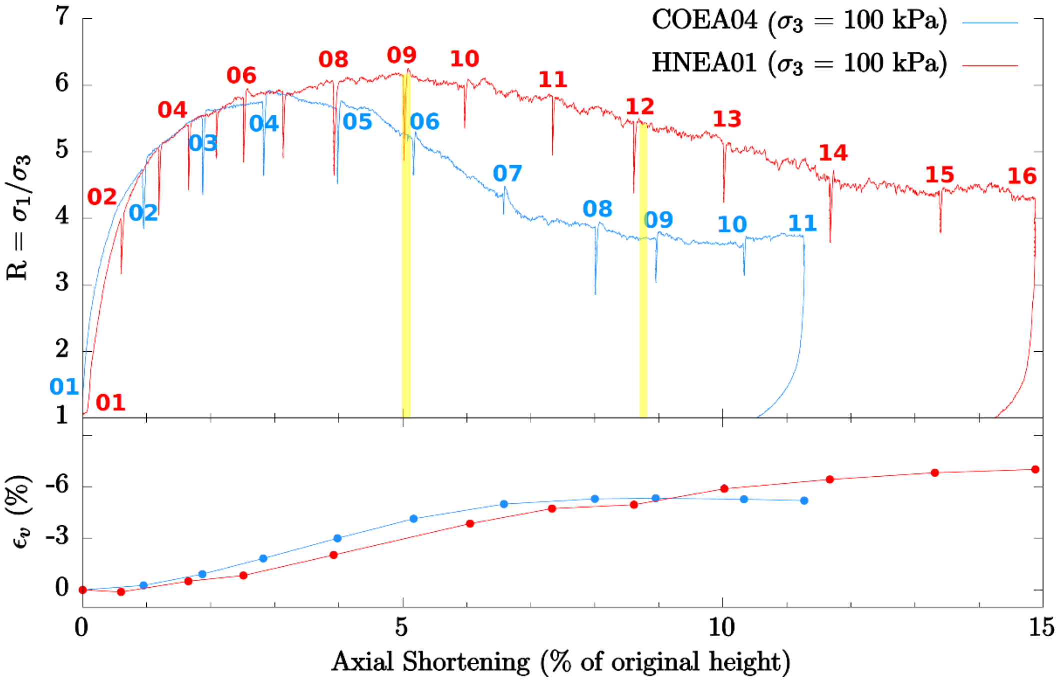

Figure 7.3: Triaxial responses of the specimens HNEA01 and COEA04 with loading stages markers. The yellow stripes indicate loading stages that are later investigated in more detail.

The D-DVC software that has been used in this work to obtain the grain kinematics (3D displacements and rotations) is an evolved version of the TomoWarp2 code (Tudisco et al., 2017). In this code, grain displacements are expressed in pixels (the pixel-size is fixed) and 3D rotations as *rotation vectors* using a Rodrigues parametrisation (Campello, 2015). In a rotation vector, the components represent the direction of the axis of rotation and the norm the magnitude of the angle of rotation around that axis. This representation system for rigid body rotations has significant practical advantages over more complex alternatives, such as those based on Euler angles or quaternions (Campello, 2015).

To visualize the 3D unit rotation vector orientation, stereographic projection is sometimes used below. The angular coordinates used in this projection are illustrated in Figure 7.4. The angle θ (inclination) goes from 0° (vertical) to 90° (horizontal), while the angle φ (azimuth) goes from 0° to 360°, being the north (φ=0°) the direction of the Cartesian x-axis of the specimen. Stereograms were created using the plotting tool *"orientationPlotter"* from the external open-source Python package SPAM (Andò et al., 2017).

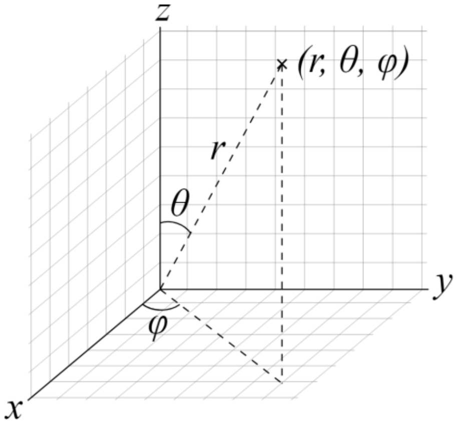

Figure 7.4: Spherical coordinates system adopted for the stereoplots (Wikipedia)

Previous applications of D-DVC had focused mostly on incremental grain kinematics (Andò et al., 2012a; Hall et al., 2010). In such approach only the incremental kinematics between two subsequent loading steps (e.g. 1-2, 2-3, 3-4, etc…) are obtained. The starting point are the two 3D greyscale images bracketing the increment (*i.e.,* initial and deformed configurations); of these two the image corresponding to the initial configuration has to be already labelled, so that grain bounding-boxes that are used as correlation windows can be extracted.

This incremental or "tangent" correlation approach cannot be applied sequentially to obtain cumulative kinematics of the grains. The reason is that grain labels assigned to the same grains by processing different scans of the same specimen will be different. To ensure consistency, a single set of grain labels, obtained from the first scan, is required. An alternative method to get the history of grain displacements and rotations, will be to use a "secant" correlation (usually referred to as "leapfrog" in C-DVC applications). In this approach, the initial labelled image is always selected for paired searches on those resulting from all the subsequent scans (*i.e.,* 1-2, 1-3, 1-4, etc…). A direct secant approach has clear limitations, being both very expensive (as the grain search window would have to increase during the process) and prone to errors.

The algorithm applied here aims to overcome those difficulties using a mixed approach, in which a secant correlation scheme (1-2, 1-3, … , 1-10) is still employed, but the search is aided by the results of the previous steps, namely the cumulative grains displacement up to the last correlation step. The initial search window is translated by a vector pointing the position of the grain in the previous correlation and can remain of a small size, saving calculation time. The inputs required in this procedure are four: two greyscale images, one labelled image and one data file with the prior grain displacements. Since previous rotations are not taken into account in setting up the search window, for large deformations where there are large rotations the possibility of losing grains still remains.

7.2.3 Validation of the D-DVC procedure

To validate the implementation of D-DIC in TomoWarp2 a simple uniform rotation check was employed (Andò et al., 2012a; Pannier et al., 2010). The rotations of all the grains contained in specimen HNEA01 were individually computed after applying a five degrees (5° deg) rigid rotation around its vertical *z*-axis. The main objectives of the validation are three: (a) to evaluate the attrition rate of the algorithm (*i.e.,* the number of grains that are lost from one image to the next); (b) to evaluate the accuracy and precision with which grain rotation was measured and (c) to explore the possible relationship between the precision of the calculation and the shape of the grains (as grains masks are used as correlation windows, there is some expectation that grains closer to spherical will present a greater deviation from the imposed motion).

The check was positive from the attrition viewpoint, with more than 99.8% of the grains correctly tracked attaining a correlation coefficient between the two image subsets greater than 0.99 for each of them. Figure 7.5a shows the histogram of the rotations measured by D-DVC. The rotation measurements follow a normal distribution with a mean value of 4.998°deg and 0.042°deg standard deviation. Rotations as obtained by this code are as accurate (*i.e.,* have similar mean error), but far more precise (*i.e.,* have much smaller error standard deviation), than those obtained with the ID-track implemented by Andò *et al*. (2012). Indeed, the coefficient of variation (standard deviation / mean) of measurement error is here below 1%, while it was above 400% for ID-track. Another way of conveying this information is by means of a stereogram of the computed grain rotations (Figure 7.5b). The radial distance from the centre of the stereoplot represents the inclination θ, whereas the angles on the external perimeter represent the azimuth φ. As expected, all the grain rotations are located at the centre of the stereoplot ($\theta = 0°$), indicating rotations around the vertical axis, with very low deviation from the vertical. Finally, Figure 7.5c illustrates the relation between measured rotation and sphericity; it is clear that the deviation from the exact solution (5° deg) increases symmetrically with the sphericity of the grains. However, the deviation remains very limited (around ±0.1° deg) and, therefore, this inbuilt bias can be safely ignored.

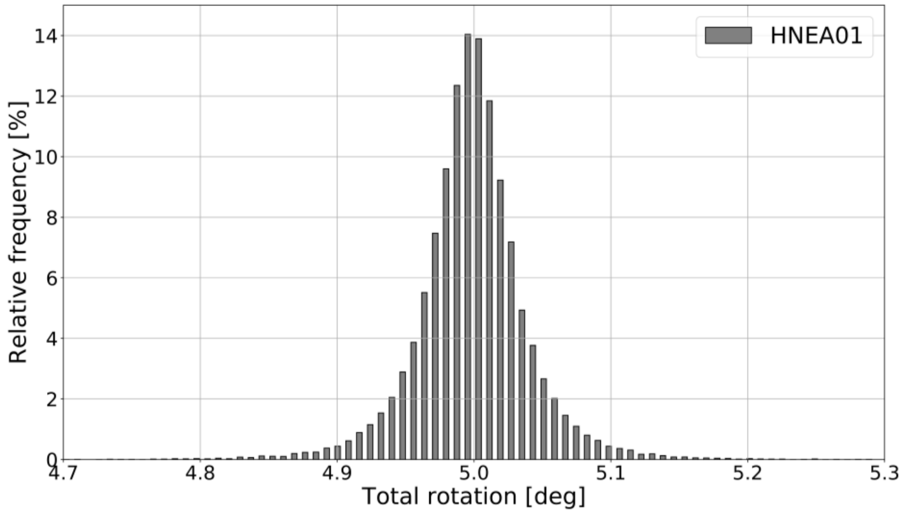

(a)

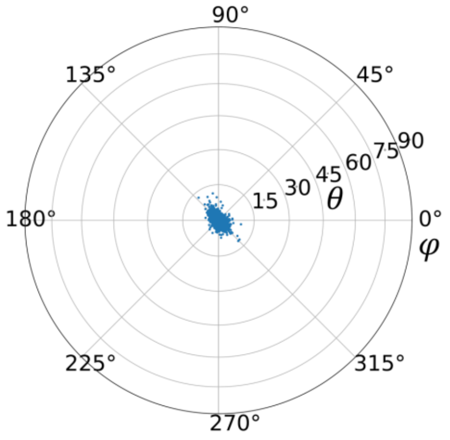

(b)

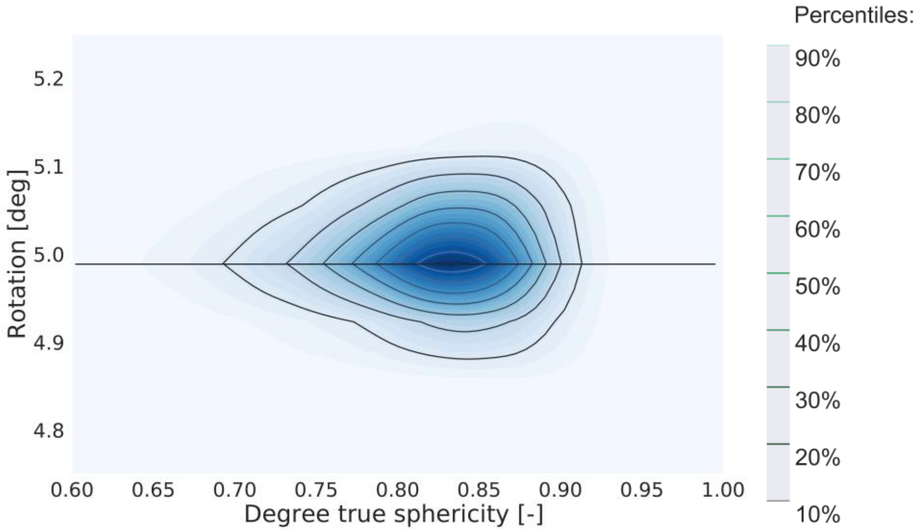

(c)

Figure 7.5a-b-c: (a) Histogram of measured rotation after rigid rotation of the specimen (b) Stereoplot showing the rotation versor of each grain (c) 2D histogram showing the correlation between grains sphericity and grains rotation.

7.2.4 Shear band identification

The two specimens analysed in this work showed localised deformation through shear banding (Andò, 2013). In shear bands void ratio increases, coordination numbers are much reduced and the microstructural constraints on kinematics are therefore very different. Before examining the relation between grain shape and grain kinematics it was therefore necessary to first classify the grains, separating those that belong to the shear band and those that do not. The criterion applied here to classify the grains as belonging to the shear band was based on shear strain.

To assign a nominal deviatoric strain to each grain we applied a procedure developed for DEM post-processing by Catalano et al. (2014). In this procedure, available within the code YADE (Šmilauer, 2015), a Voronoi cell hosting each grain is created using a regular Delaunay triangulation having as vertices the mass centres of the labelled grains. Thus, the grain positions at the last loading increments (*i.e.*, 15-16 for HNEA01, 10-11 for COEA04) were calculated by D-DVC and then introduced in YADE. Displacements of neighbouring grains were then used to compute a nominal displacement gradient tensor for the tetrahedrons whose vertices are the grains centres of mass. A nominal averaged deviatoric strain, ε_{d_g} was projected back to each grain and a threshold value of ε_{d_g} used to classify grains as belonging to the shear band.

7.3 Results from D-DVC

7.3.1 Shear band identification

The results of the shear band identification procedure are shown in Figure 7.6, in which the black grains form the "shear band": it contains 7007 grains for COEA04, and 21000 for HNEA01. The threshold value ε_{d_g} is set at 0.1; the zones identified correspond closely to those apparent in previous studies (Andò et al., 2013).

The local reference system that will be used to define the virtual plane representing the shear band is shown in Figure 7.7, in which vector $\vec{n}$ is the normal to the plane and vector $\vec{a}$ indicates the steepest slope direction in the plane. Both specimens present a shear band with an inclination angle (θ) of about 45° (see Figure 7.4 for the definition of inclination angle).

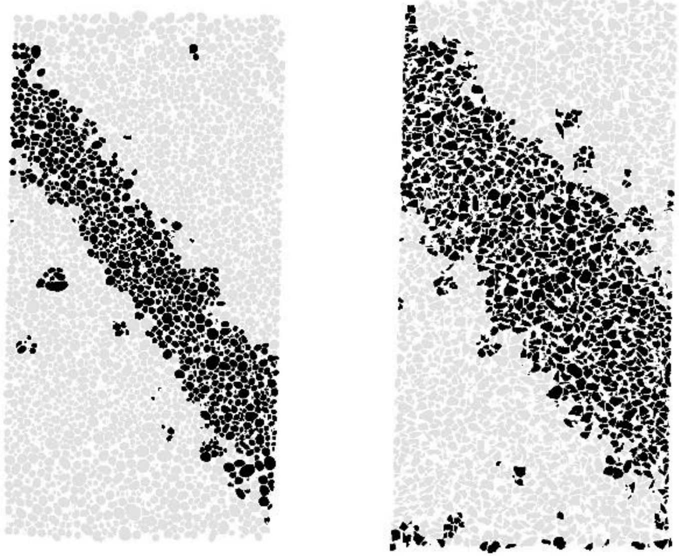

(a) (b)

Figure 7.6: Shear band identification for specimens COEA04 (a) and HNEA01 (b). Particles are coloured black if the "micro-strain" (Catalano et al., 2014) calculated on the Voronoi domain centred on the particle is greater than 0.10 (i.e., they belong to the shear band).

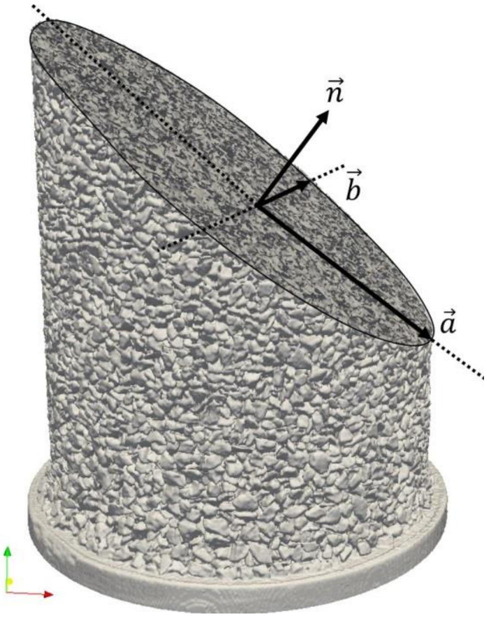

Figure 7.7: Local reference system for the shear band

Vector $\vec{b}$ is orthogonal to $\vec{n}$ and $\vec{a}$ and therefore is horizontal ($\theta = 90°$) . It can be used to characterise the azimuthal orientation of the shear band with respect to the global Cartesian coordinate system. The azimuth (φ) is different, being of about 135° for Hostun and 75° (from the global x-axis) for Caicos. The sections represented in Figure 7.6 correspond then to vertical planes orthogonal to vector $\vec{b}$.

7.3.2 Spatial distribution of grain shapes and shear localization

A check was performed to verify if particle shape was spatially homogeneously distributed in the specimens. The reason was to exclude any possibility that subsequent localisation into shear bands was prompted by non-uniformity in the initial spatial distribution of grain shapes (note that a similar check was performed by Andò (2013) with respect to local porosity). To do so, two vertical sections orthogonal to each other (defined respectively by vectors $\vec{n}$-$\vec{b}$ and $\vec{n}$-$\vec{a}$) are examined where the grains have been coloured by their value of degree of true sphericity, as shown in Figure 7.8. It is evident that grain true sphericity was initially homogeneously distributed within both specimens.

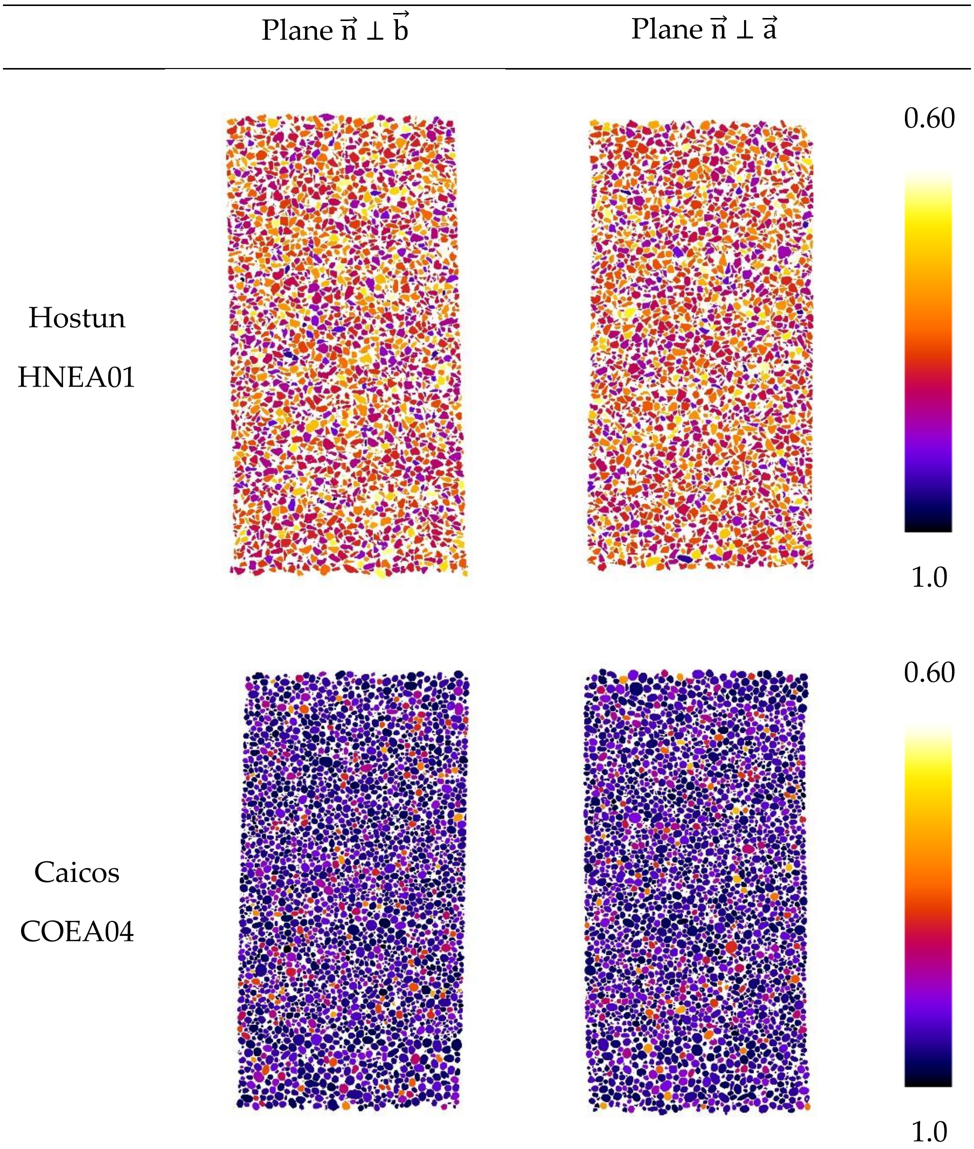

Figure 7.8: Sphericity spatial distribution for Hostun and Caicos sand in two vertical sections: parallel and perpendicular to the shear band.

Another check was performed on the possibility that shear banding would entrap or select particular grain shapes. To this end, histograms of the degree of true sphericity for the grains located both inside and outside the shear band were plotted; the results are shown in Figure 7.9. Again, it is evident that there are no significant differences of shape between the grains that were involved in the localisation process and those that remained outside the shear band.

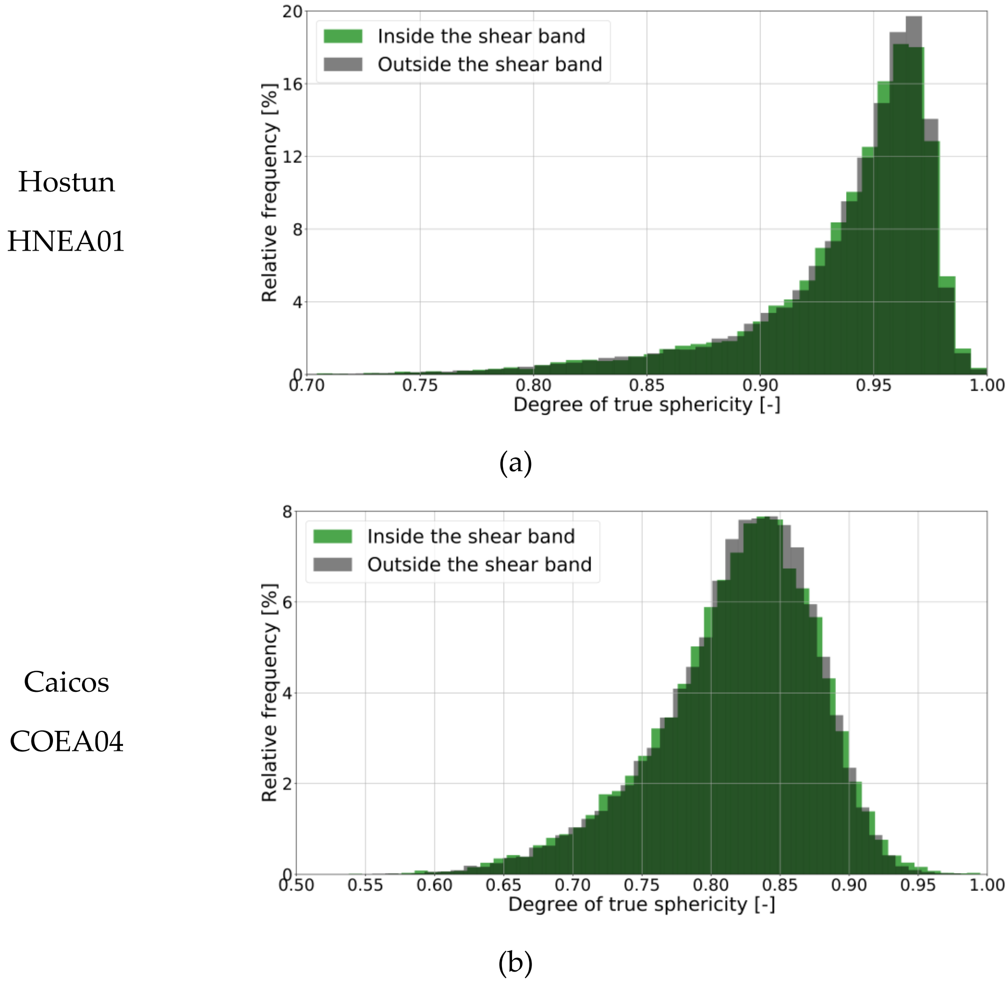

Figure 7.9: Histograms of true sphericity for Hostun (a) and Caicos (b) sands both inside and outside the shear bands.

7.3.3 Overall grain kinematics

Figure 7.10 and Figure 7.11 show the *cumulative* kinematic histories, in terms of vertical displacements and rotations, for Caicos ooids (specimen COEA04) and Hostun sand (specimen HNEA01) during several loading increments in the triaxial test (note that similar images reporting *incrementa*l values were presented by Andò *et al.*, 2012). Results for both sands are plotted at the same scale and confirm the general observation made from incremental results by Andò *et al*. (2012): within the shear band, the very rounded Caicos sand grains rotate more than the more angular grains of Hostun sand. On the other hand, it is difficult to tell the difference between the two sands outside the shear band.

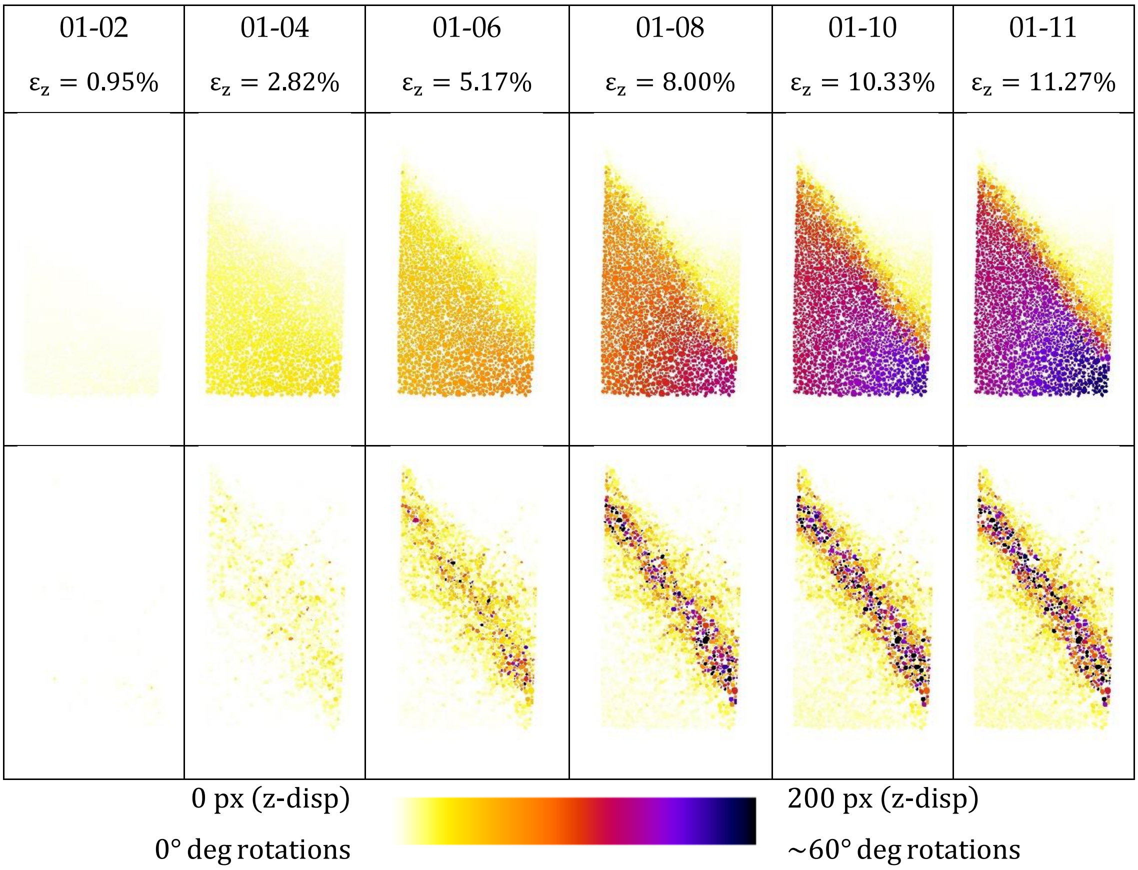

Figure 7.10: Vertical slices of Caicos sand (specimen COEA04) showing grain vertical displacement (above) and rotation (below) ***accumulated*** *during the test. Grains are coloured by the value of their measured z-displacement (above) and total rotation (below). Not all the increments are shown.*
Stage "01" = start of deviatoric loading. Stage "11" = end of the TX test.

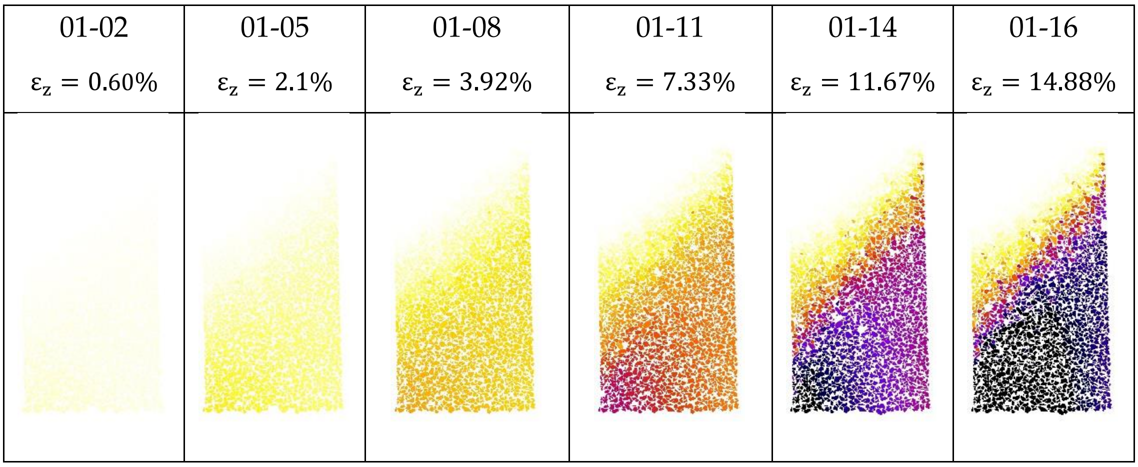

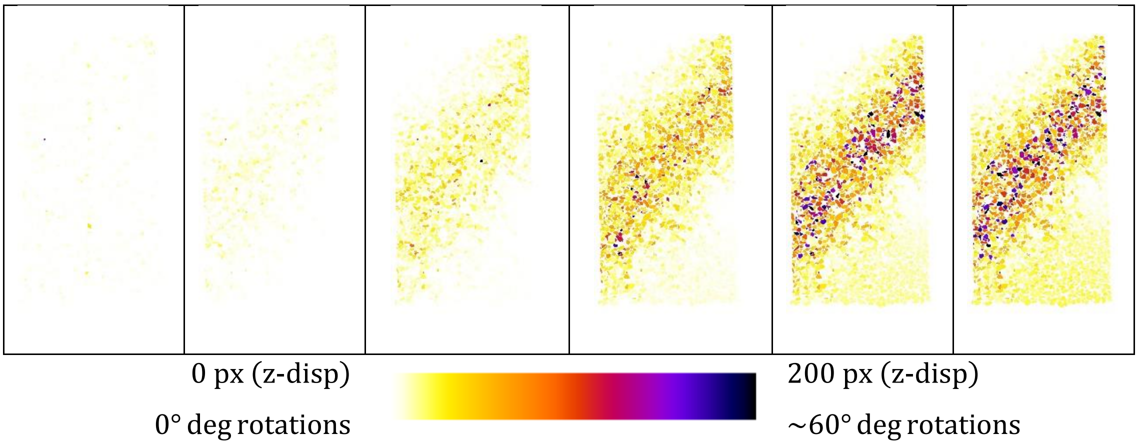

Figure 7.11: Vertical slices of Hostun sand (specimen HNEA01) showing grain vertical displacement (above) and rotation (below) ***accumulated*** *during the test. Grains are coloured by the value of their measured z-displacement (above) and total rotation (below). Not all the increments are shown.*
Stage "01" = start of deviatoric loading. Stage "16" = end of the TX test.

This observation is conveyed more precisely in Figure 7.12, showing the histories of the cumulated mean particle rotation magnitudes, both inside and outside the shear bands. Outside the shear band, the average grain rotations of both sands are very similar and appear quite flat, with a limited increase between 1% and 5% axial strain. That increase in the average rotation outside the shear band may reflect the fact that the shear bands become somewhat narrower as deformation progresses (Andò, 2013), whereas the grain classification criterion is only applied in the final test stage.

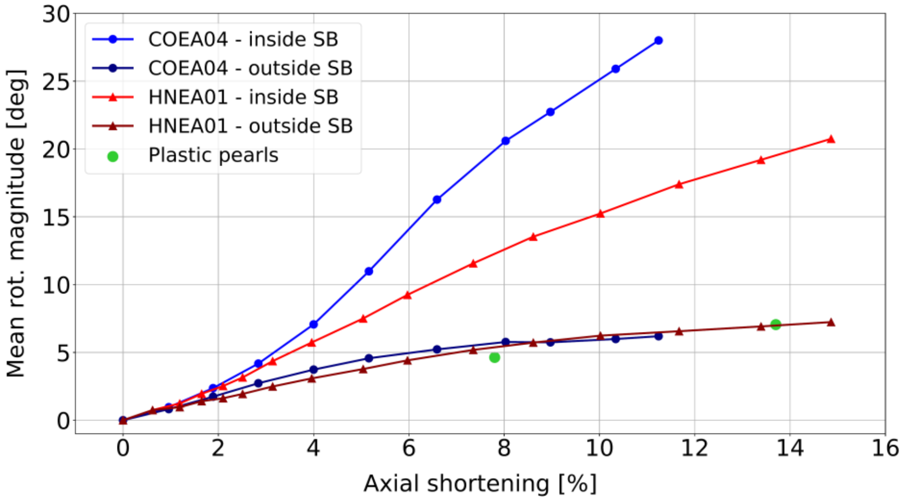

Figure 7.12: Histories of cumulated mean particle rotations inside and outside the shear bands (SB in the legend), measured by D-DVC throughout the triaxial tests. The green dots represent interpreted results from Alshibli and Alramahi (2006) for a triaxial experiment involving 400 plastic pearls.

Average rotations increase much faster within the shear band. In the Caicos specimen (COEA04) average rotation magnitude raises to about 30 degrees. The trend in the Hostun specimen (HNEA01) is somewhat slower, raising to a level of about 21degrees. The distribution of cumulative rotation magnitudes in the shear bands is rather skewed (Figure 7.13) with the mode remaining almost constant but the high end tail progressively thickening.

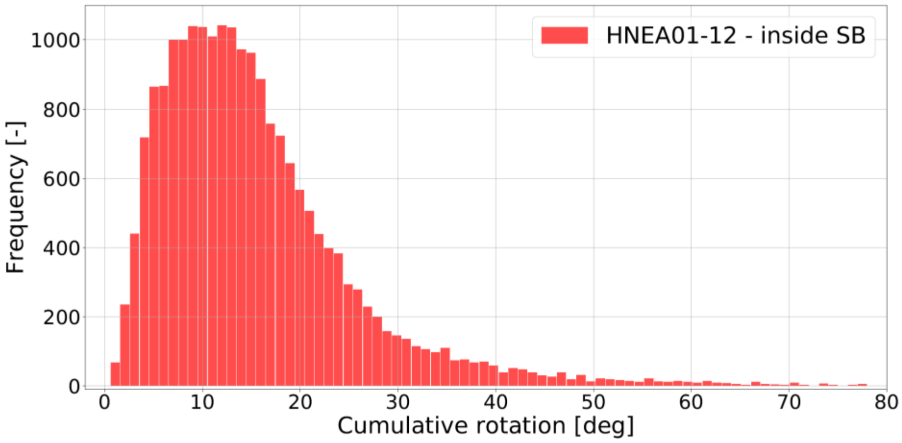

(a)

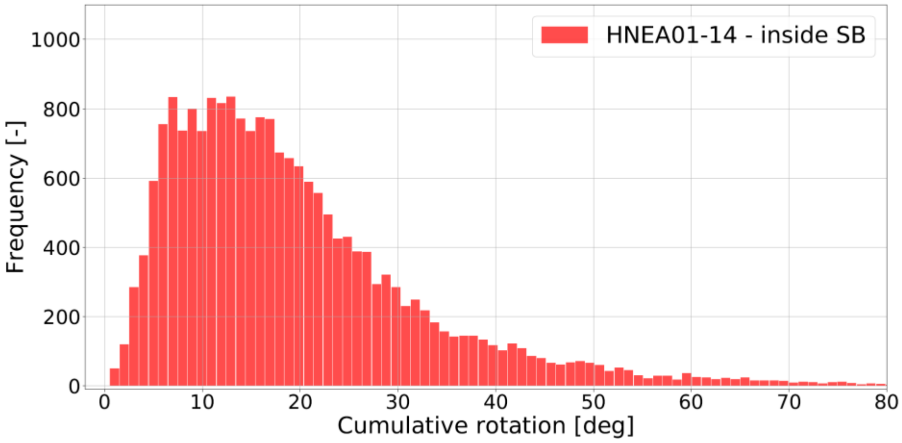

(b)

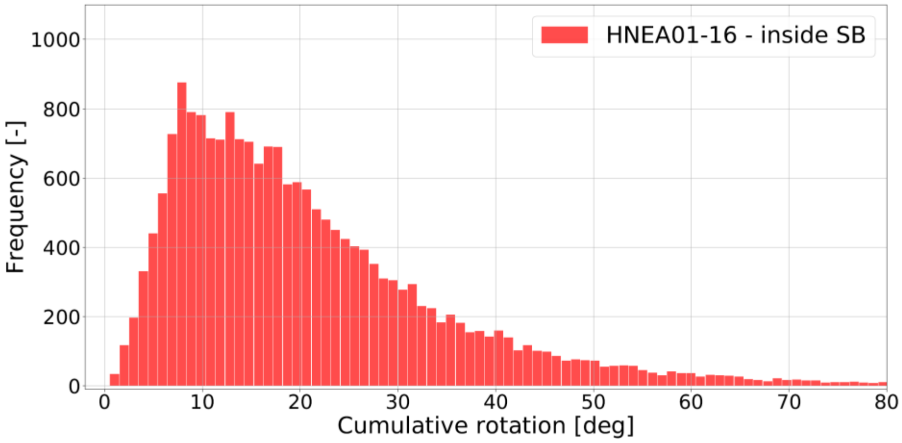

(c)

Figure 7.13: Distribution of accumulated particle rotation magnitudes at different test stages (12-14-16) for particles within the shear band of the Hostun sand HNEA01 specimen.

The attrition rate during this sequence of image correlations is shown in Figure 7.14. It is clear that in this more realistic context, the D-DVC procedure has more difficulties than in the idealized uniform rotation check discussed before. The correlation problems increase as the grains rearrange more, which is what happens in the shear band. Despite that, it should be noted that a) the correlation validity criterion was set at a very stringent limit ($\mathrm{CC} = 0.98$) and b) the procedure was able to track to the end almost 80% of the grains within the shear bands and more than 95% outside them.

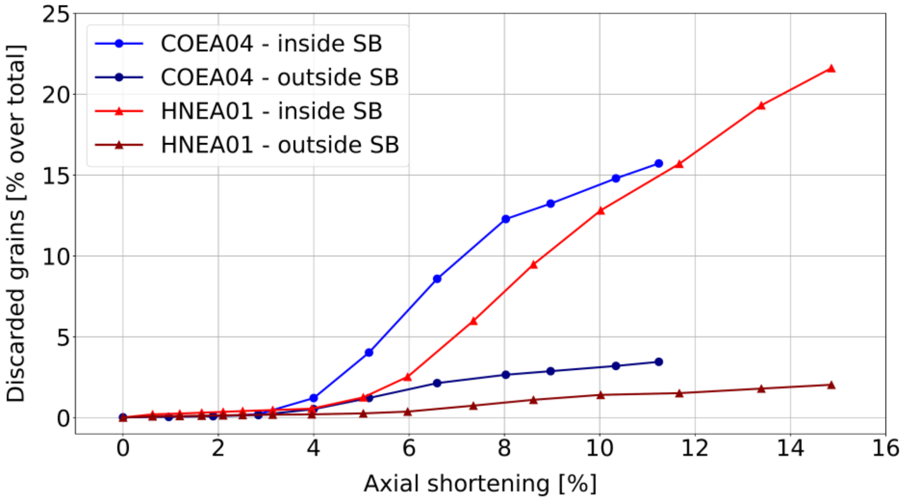

Figure 7.14: Particles with correlation maximum below 98% as a percentage of total number of particles

7.3.4 Axes of rotation

Stereoplots (see Figure 7.5b) can be used to investigate the alignment of particle rotation axes during shearing. The orientations of *cumulative* rotation versors are plotted for all grains (about 110000 in total), both inside and outside the shear bands, at two different test stages in Figure 7.15 (at approximately 5% axial strain, corresponding to steps 01-09 in Hostun and 01-06 in Caicos) and Figure 7.16 (at approximately 9% axial strain, corresponding to 01-12 for Hostun and 01-09 for Caicos). The raw stereoplots are presented alongside binned frequency diagrams.

	Inside the shear band	Outside the shear band
HNEA01 stage 01-09	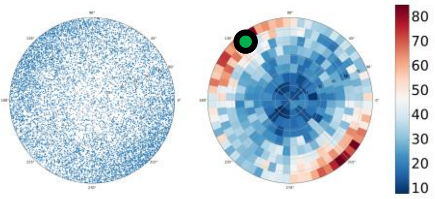	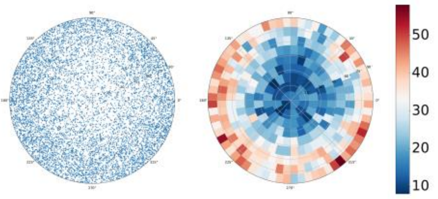
COEA04 stage 01-06	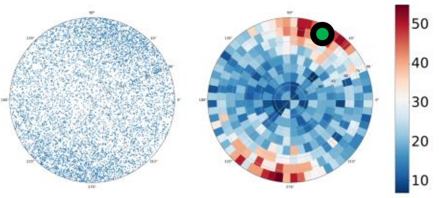	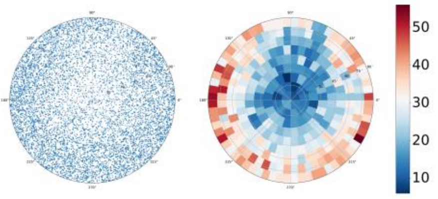

Figure 7.15: Stereoplots showing the rotation versor directions at 5% shortening. The green dots indicate the orientation of vector $\vec{b}$ (see Figure 7.7) belonging to the shear bands of Hostun and Caicos sands. The stereoplot angles markers are not shown for readability, see Figure 7.5b for reference.

	Inside the shear band	Outside the shear band
HNEA01 stage 01-12	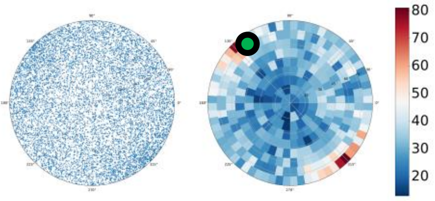	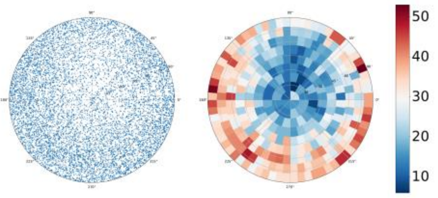

COEA04

stage

01-09

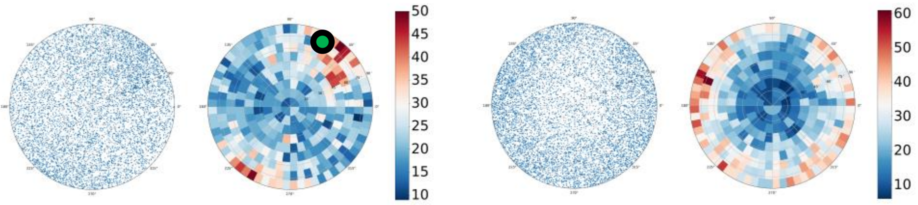

Figure 7.16: Stereoplots showing the rotation versor directions at 9% shortening. The green dots indicate the orientation of vector $\vec{b}$ (see Figure 7.7) belonging to the shear bands of Hostun and Caicos sands. Stereoplot grid not shown for readability, see Figure 7.5b for reference.

Both sands exhibit similar trends (Figure 7.15). Outside the shear bands, the rotation axes accumulate towards the periphery of the stereoplot, with inclination angles close to 90° that indicate horizontal axes of rotation. The azimuthal angle, on the other hand, is almost homogenously distributed around the stereoplot periphery, indicating no preferential alignment for the grain rotational axis within the horizontal plane.

The situation is different inside the shear band, which is already present at 5% strain (Figure 7.10; Figure 7.11). The rotation axes are still mainly horizontal ($\theta = 90°$), but now the azimuthal angles (φ) concentrate around values of about 135° (Hostun sand) and 75° (Caicos sand). As indicated in the figures these values are, precisely, the azimuths of vector $\vec{b}$ in Figure 7.7 *i.e.*, those corresponding to directions orthogonal to that of steepest descent within the shear band. This alignment means that grains are rolling downslope the plane of the shear band. Another azimuthal accumulation point is observed at the diametrically opposed direction in the stereoplot, that is at 315° for Hostun and 255° for Caicos. That position corresponds to grains rotating upslope on the plane of the shear band. These preferential orientations become sharper as localisation progresses (compare with results at 9% axial strain, shown in Figure 7.16) and appear generally sharper for Hostun sand than for Caicos ooids.

The results obtained contrast with those presented in Andò (2012) in a similar analyses for the Hostun HNEA01 specimen. There the alignment of particle rotation axis and shear band normal was far less evident. The difference is likely due to the superior precision of particle rotation measurement achieved by the D-DVC technique over the ID-track used in Andò 2012. The presence of particle with opposite spins in shear zones, previously documented in experiments with simplified granular media (such as flat disks – Veje *et al*. (1999); Pasternak *et al*. (2015) – or uniform plastic beads – Alshibli and Alramahi (2006)), is here confirmed for natural sands.

7.3.5 Relation between grain shape and magnitude of rotation

A first indication of the relationship between particle shape and rotation is already evident in Figure 7.12. Caicos ooids rotate – on average – far more than Hostun sand grains, but only if belonging to the shear band; for grains that remained outside the shear band there is almost no difference between the more rounded Caicos ooids and the angular Hostun sand. This insensitivity to particle shape outside the critical shearing zone is corroborated by data deduced from Alshibli and Alramahi (2006), also plotted in Figure 7.12. Those authors reported histograms of particle rotations for 400 perforated plastic pearls, almost uniformly spherical, in a triaxial compression test that did not present a clear shear band. The averaged rotations from that test plot very close to our data.

Although averaged values of rotation are interesting, the data collected allow a more detailed inspection of the effect of grain shape on rotation. Figure 7.17 presents bivariate frequency density plots exploring the effect of shape descriptors related to form on particle rotations (accumulated up to 5% axial strain). The histogram contours appear rather flat, indicating little sensitivity of particle rotations to form. The same approach is followed in Figure 7.18, but now using shape descriptors that measure sphericity. The histogram contours are more sensitive, particularly those at the edge, indicating larger percentiles. This is particularly evident for convexity and to true sphericity – two shape descriptors that are tightly correlated for these two sands (see Chapter 6.4, Table 6.4 and Table 6.5).

HNEA01-09	COEA04-06

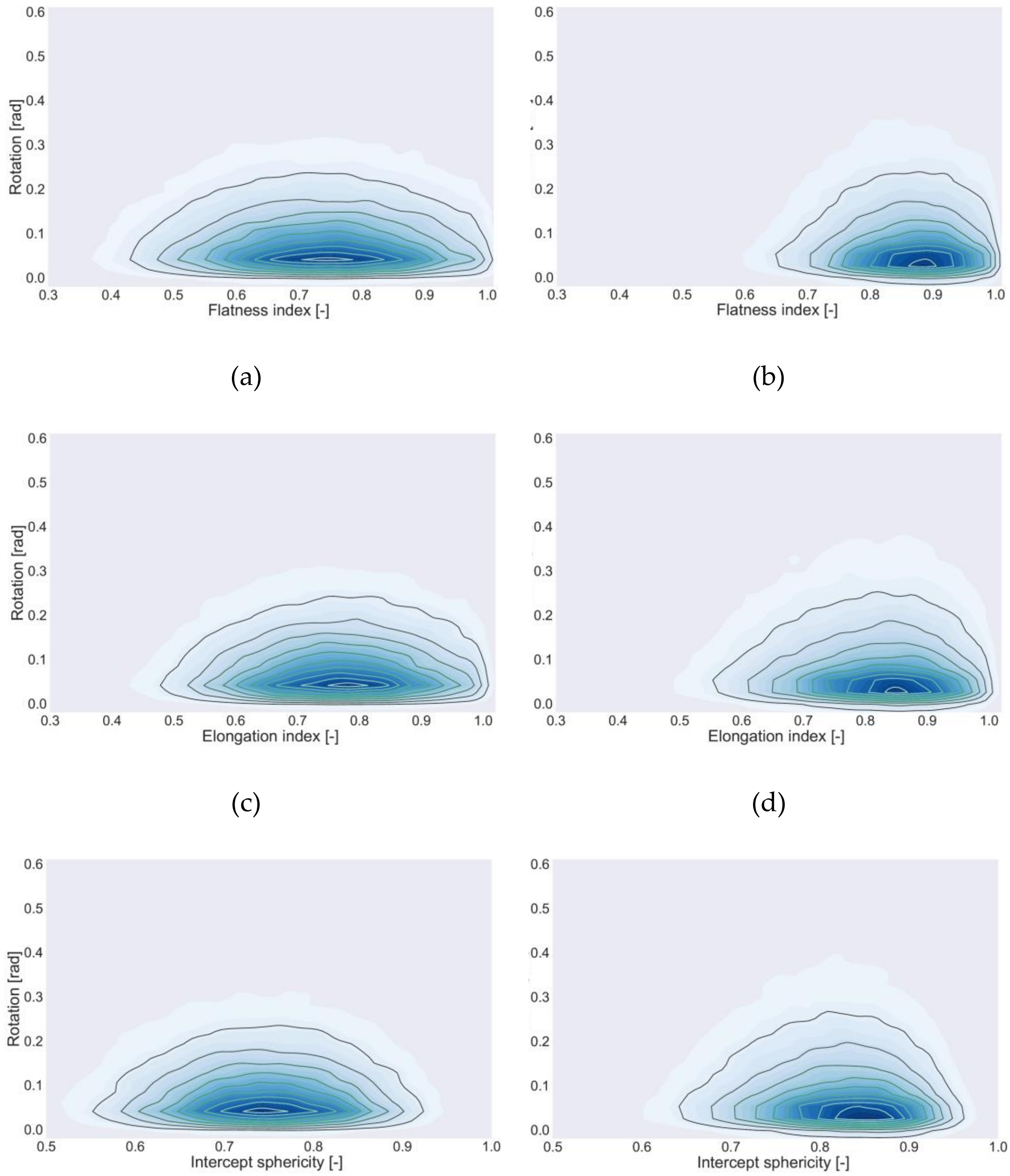

(a) (b)

(c) (d)

(e) (f)

Figure 7.17: Normalised bivariate frequency density plots of ***form*** *descriptors versus* ***cumulative*** *grain rotation magnitude at 5% shortening (loading stages HNEA01-09 and COEA04-06, respectively 48.612 and 65.056 grains). The contours colour bar is shown in Figure 7.5c.*

HNEA01-09	COEA04-06

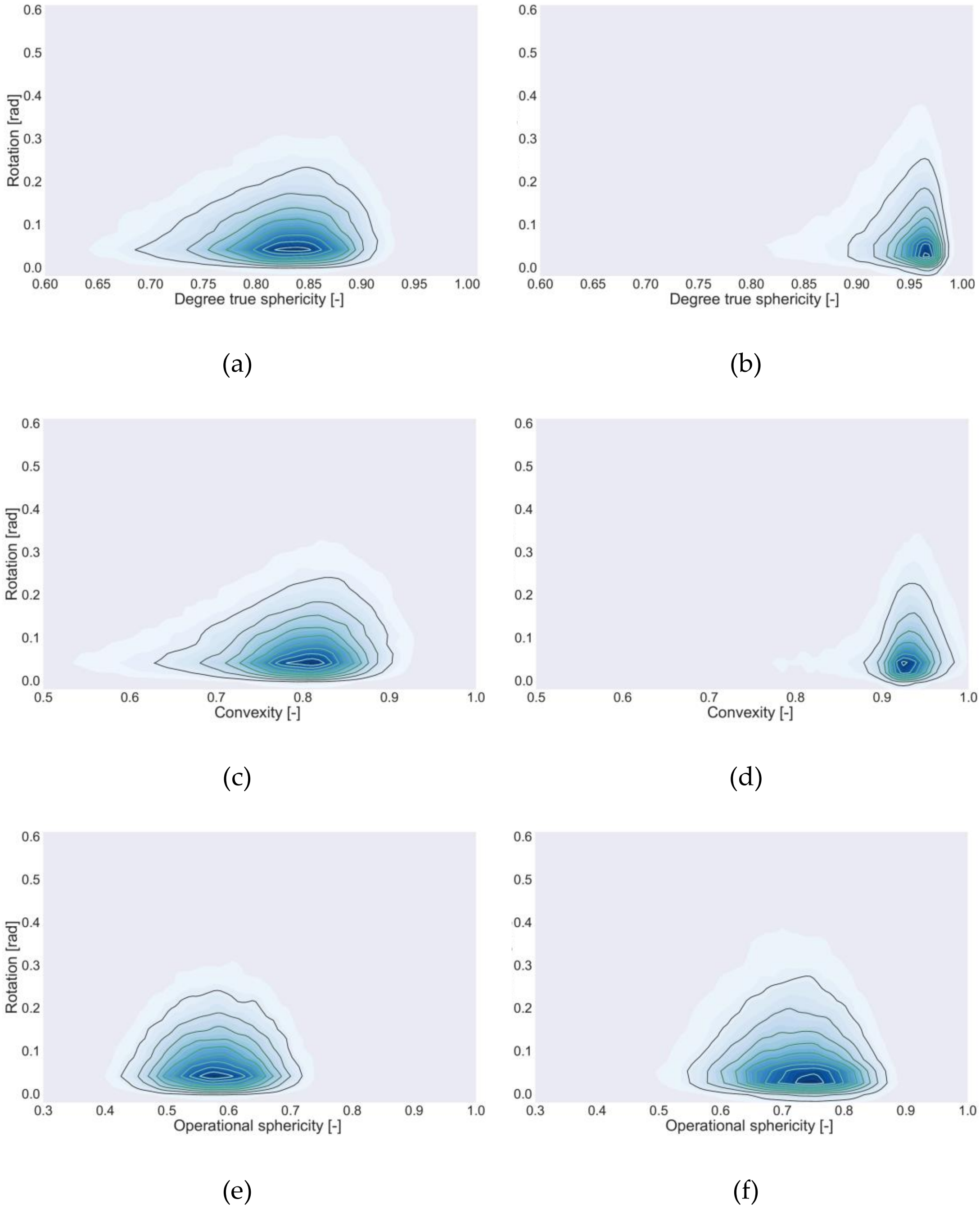

(a) (b)

(c) (d)

(e) (f)

Figure 7.18: Normalised bivariate frequency density plots of ***sphericity*** *descriptors versus the* ***cumulative*** *grain rotations measured at 5% shortening (loading stages HNEA01-09 and COEA04-06, respectively 48.612 and 65.056 grains). The contours colour bar is shown in Figure 7.5c.*

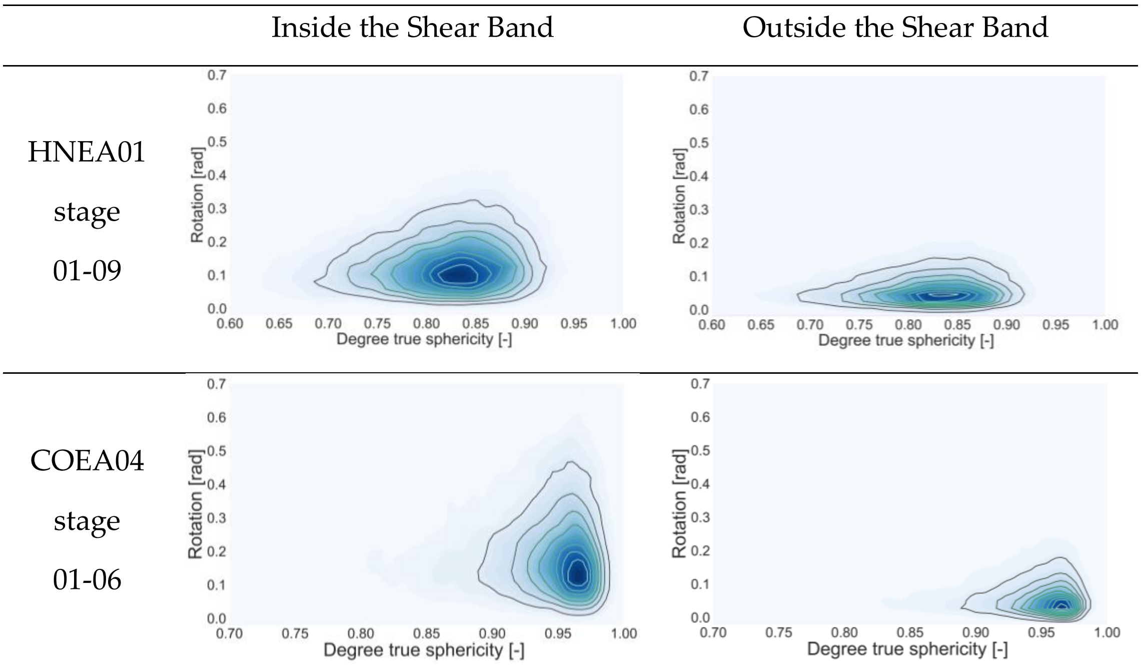

Figure 7.19: Normalised histograms showing the observed relation between the degrees of true sphericity and the total grains rotation measured at 5% sample shortening.

The histograms become more triangular if restricted to particles in the shear band. Figure 7.19 shows that the *degree of true sphericity* seems to have a significant influence on the upper limit of particle rotation, which increases as particles become more spherical. This idea is explored in more detail in Figure 7.20 and Figure 7.21, where mean and extreme values (99.5% percentiles) of rotation, measured on both Caicos sand and Hostun sand specimens, are plotted as a function of true sphericity. The values are derived from marginal distributions, obtained at fixed true sphericity intervals (width 0.025). Because the number of particles in each interval is highly variable, error bands (plus and minus one standard error) are also represented. The error bands for the 99.5% quantile are estimated using a bootstrapping technique (Efron and Tibshirani, 1994), resampling with replacement the original samples (for each interval) one thousand times. Error band thickness increases with small sample sizes (e.g. at low values of *degree of true sphericity*) and with marginal variability (high at large values of *degree of true sphericity*, as correlating very spherical grains carries more uncertainty).

It appears that the mean values of rotation, both inside and outside the shear band are insensitive to particle sphericity, whereas the extreme upper values (the 99.5 % percentile) show a clear positive dependency between rotations and particle sphericity. There is not much difference between the mean values of Caicos and Hostun, at any given true sphericity. On the other hand, the upper limit rotations of Caicos are somewhat above those of Hostun, even at the same sphericity, and particularly for those particles inside the shear band. Andò (2013) observed that porosity in the shear band was higher for Hostun than for Caicos, so it is unlikely that connectivity –which is inversely related to porosity- will explain that difference. Still, the differences between the two sands not accounted for true sphericity are less important than the common effect of sphericity on the upper bound. These trends were confirmed when other test stages were analysed, for instance at around 9% axial strain, Figure 7.22 and Figure 7.23.

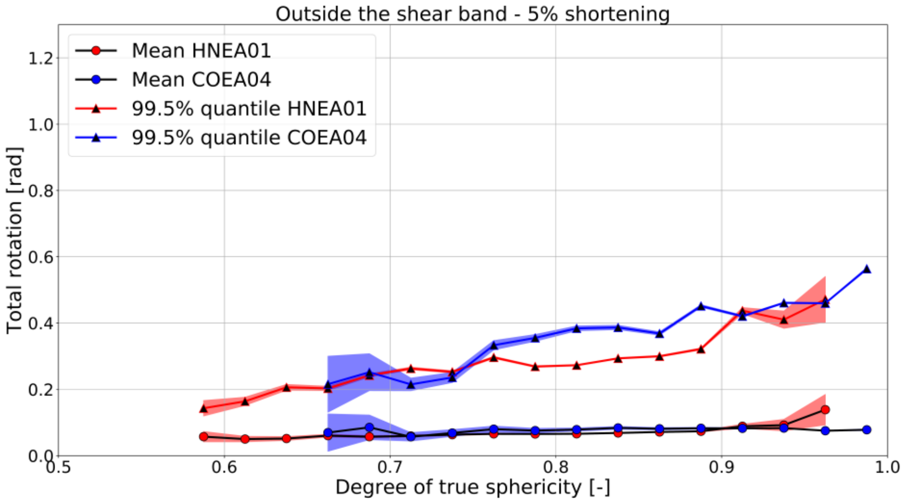

Figure 7.20: Influence of the degree of true sphericity on the total grains rotation (at 5% shortening) outside the shear band.

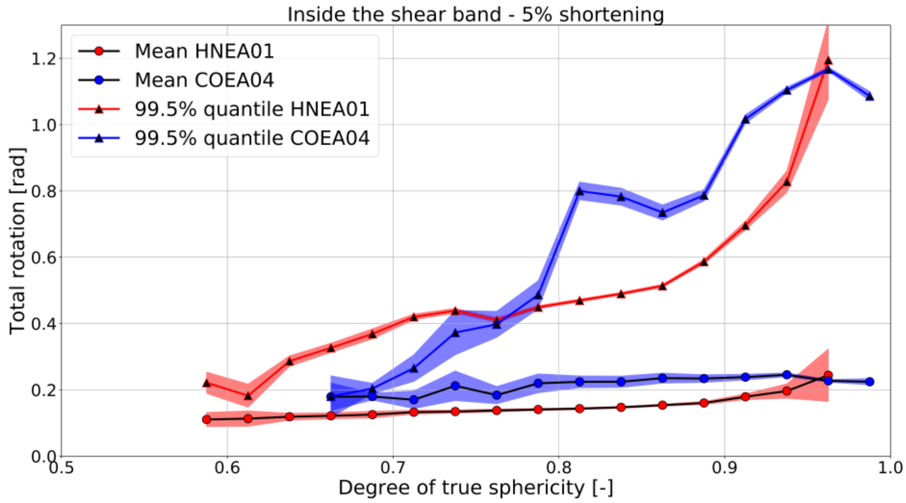

Figure 7.21: Influence of the degree of true sphericity on the total grains rotation (at 5% shortening) inside the shear band.

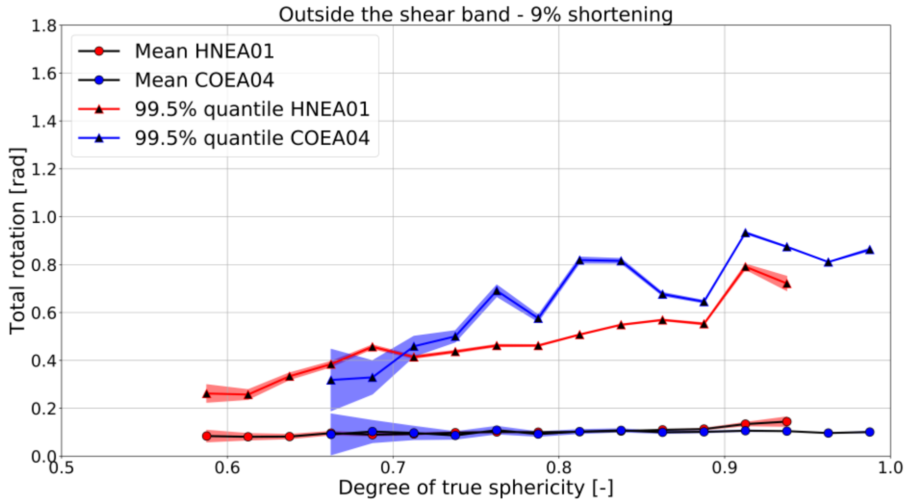

Figure 7.22: Influence of the degree of true sphericity on the total grains rotation (at 9% shortening) outside the shear band.

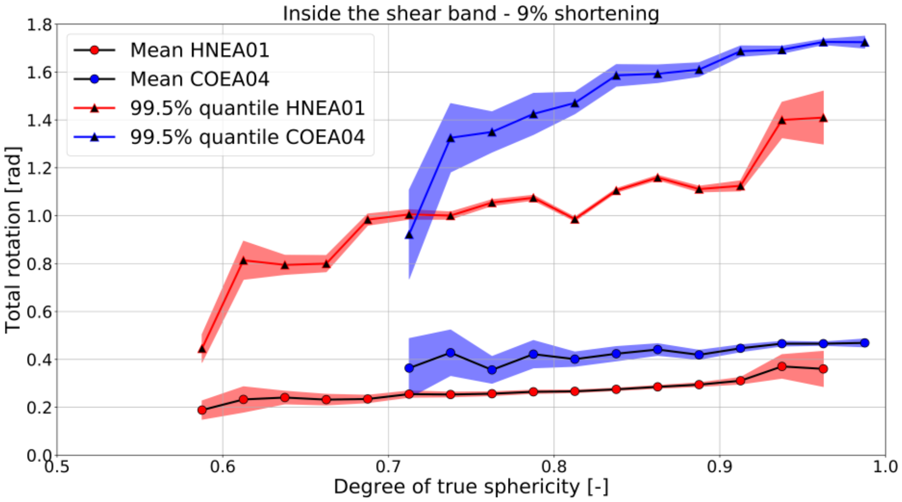

Figure 7.23: Influence of the degree of true sphericity on the total grains rotation (at 9% shortening) inside the shear band.

7.4 New definition of "local" porosity

This section describes an attempt to describe a new "local" (*i.e.*, grain based) definition of porosity and to investigate a potential relationship existing with grain shape.

An algorithm for the computation of the set-voronoi for each grain is implemented in SPAM and detailed in (Schaller et al., 2013). The entire 3D labelled images of Caicos and Hostun sands can be input in SPAM to get a new-labelled image with the voronoi set related to each grain. As a result, the original grains are "expanded" (according to the algorithm implemented in SPAM) in order to fill all the void space around them, though preserving the initial grain labels, as shown in Figure 7.24.

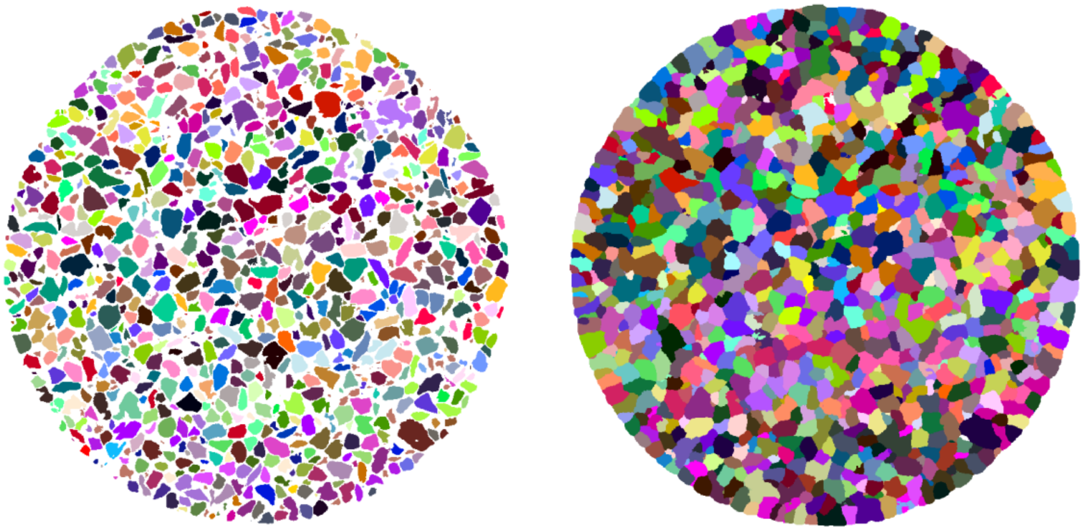

(a) (b)

Figure 7.24: Horizontal section (800 of 1750) of the labelled image of HNEA01-01 (a). Horizontal section (800 of 1750) of the labelled image with the built set voronois (b). All the voids have been filled preserving the grains labels.

It is now possible to compute the volume of the set-voronois (summing up the voxels making it up) and the volume of the pore space "attached" to each grain, as difference between the set-voronoi and the known -original- grain volume. Therefore, new local definitions of porosity (n_{local}) and void ration (e_{local}) can be defined for each grain as:

$$n_{local} = \frac{\text{void volume}}{\text{set voronoi volume}} \tag{7.2}$$

$$e_{local} = \frac{\text{void volume}}{\text{grain volume}} \tag{7.3}$$

These quantities have been obtained for each grain contained in the HNEA01 and COEA04 specimens. The values of local porosity have been plotted for each grain in Figure 7.25.

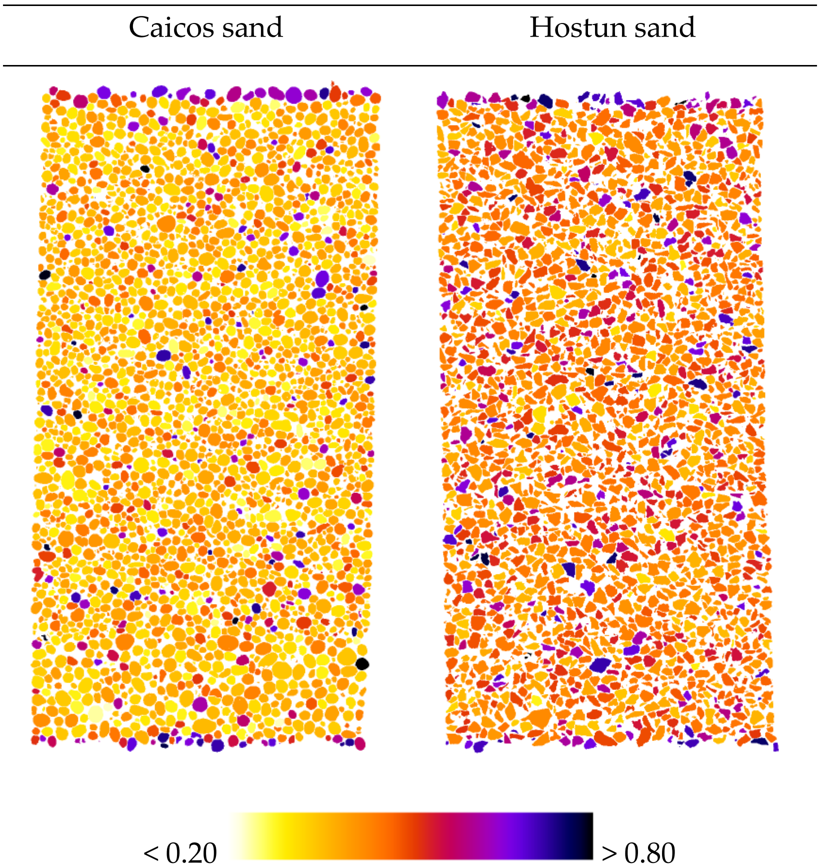

Figure 7.25: Vertical slices showing the local porosity value for each grain of Caicos and Hostun sands.

The average local porosities are respectively 0.484 and 0.411 for Hostun and Caicos sand. These values are far from the experimental measures of porosity (31.9% Caicos and 39.7% Hostun), however this approach is able to detect the higher initial porosity of Hostun compared to Caicos.

At this point, the statistical relationship between these new quantities and the shape of each grain can be investigated by plotting the Pearson's correlation coefficient in the form of a correlation matrix, as shown in Table 7.1a (Caicos) and Table 7.1b (Hostun). Note that the future particle rotations that will be measured at 9% axial strain are also included in the correlation matrix to check if the initial local porosity may affect the future grains kinematics.

CAICOS sand		
Shape descriptor	***Rot. ‘09’***	n_{local} ***‘01’***
Grain volume, V	-0.17	-0.51
True Sphericity, Ψ	0.10	-0.06
Flatness index; FI	-0.02	-0.17
Elongation index, EI	0.00	-0.13
Intercept sphericity, Ψ_{int}	-0.01	-0.23
Operation. sphericity	0.02	-0.17
Convexity, Co	0.12	0.09
Alshibli Sph., Ψ_{al}	0.03	0.22
Rot. (stage ‘09’- $\varepsilon_z = 9\%$***)***	1.00	0.06
Local porosity (stage ‘01’)	0.06	1.00

(a)

HOSTUN sand		
Shape descriptor	***Rot. ‘12’***	n_{local} ***‘01’***
Grain volume, V	-0.15	-0.37
True Sphericity, Ψ	-0.01	-0.06
Flatness index; FI	-0.05	-0.06
Elongation index, EI	-0.04	-0.09
Intercept sphericity, Ψ_{int}	-0.06	-0.12
Operation. sphericity	-0.05	-0.14
Convexity, Co	0.05	0.07
Alshibli Sph., Ψ_{al}	0.06	0.10
Rot. (stage ‘12’- $\varepsilon_z = 9\%$***)***	1.00	0.03
Local porosity (stage ‘01’)	0.03	1.00

(b)

Table 7.1: Pearson’s correlation coefficients between the measured particles rotations (9% axial shortening) and the local porosity computed at the initial state with the known shape parameters for Caicos (a) and Hostun (b) sands.

It is evident that, at the end of the consolidation (loading stage ‘01’) at least, there is no any statistical correlation between the shape of a grain and the new defined local porosity. A slight negative correlation (0.51 and 0.37 respectively for Caicos and Hostun sands) exists between local porosity and grain volume. It means smaller grains tend to have more space around them compared to larger grains.

No correlation is found between local porosity and the grain rotation measured at 9% shortening, it means the initial local porosity does not have an influence on the rotations that will develop at a later stage.

The local porosity has been then measured in the deformed configuration, at 9% axial strain, to investigate some statistical correlations at this loading stage. The localisation of failure (*i.e.,* shear band) is fully developed at this stage and therefore we divided the study in two parts: inside and outside the shear band, as reported in Table 7.2 and Table 7.3 respectively for Hostun and Caicos sands.

HOSTUN sand *- Outside shear band -*		
Shape descriptor	***Rot. '09'***	n_{local} ***'09'***
Grain volume, V	-0.11	-0.50
True Sphericity, Ψ	0.04	0.00
Flatness index; FI	-0.02	-0.14
Elongation index, EI	0.00	-0.12
Intercept sphericity, Ψ_{int}	-0.01	-0.19
Operation. sphericity	0.00	-0.14
Convexity, Co	0.07	0.09
Alshibli Sph., Ψ_{al}	0.02	0.19
Rot. (stage '09'- $\varepsilon_z = 9\%$***)***	1.00	0.19
Local porosity (stage '09')	0.19	1.00

(a)

HOSTUN sand *- Inside the shear band -*		
Shape descriptor	***Rot. '12'***	n_{local} ***'09'***
Grain volume, V	-0.09	-0.55
True Sphericity, Ψ	0.04	0.05
Flatness index; FI	-0.02	-0.14
Elongation index, EI	0.01	-0.14
Intercept sphericity, Ψ_{int}	0.00	-0.21
Operation. sphericity	0.01	-0.13
Convexity, Co	0.09	0.14
Alshibli Sph., Ψ_{al}	0.03	0.21
Rot. (stage '12'- $\varepsilon_z = 9\%$***)***	1.00	0.13
Local porosity (stage '09')	0.13	1.00

(b)

Table 7.2: Pearson's correlation coefficients between the measured particles rotations and the local porosity (both measured at 9% axial shortening) with the known shape parameters for Hostun sand both outside (a) and inside (b) the shear band.

CAICOS sand - Outside shear band -		
Shape descriptor	***Rot.* *'09'***	n_{local} ***'09'***
Grain volume, V	-0.15	-0.54
True Sphericity, Ψ	0.09	0.03
Flatness index; FI	-0.06	-0.11
Elongation index, EI	0.02	-0.15
Intercept sphericity, Ψ_{int}	-0.04	-0.21
Operation. sphericity	0.01	-0.10
Convexity, Co	0.08	0.04
Alshibli Sph., Ψ_{al}	0.08	0.14
Rot. (stage '09'- $\varepsilon_z = 9\%$)	1.00	0.21
Local porosity (stage '09')	0.21	1.00

(a)

CAICOS sand - Inside the shear band -		
Shape descriptor	***Rot.* *'12'***	n_{local} ***'09'***
Grain volume, V	-0.10	-0.58
True Sphericity, Ψ	0.08	0.09
Flatness index; FI	-0.02	-0.11
Elongation index, EI	0.00	-0.17
Intercept sphericity, Ψ_{int}	0.01	-0.22
Operation. sphericity	0.05	-0.15
Convexity, Co	0.04	0.18
Alshibli Sph., Ψ_{al}	0.06	0.17
Rot. (stage '12'- $\varepsilon_z = 9\%$)	1.00	0.26
Local porosity (stage '09')	0.21	1.00

(b)

Table 7.3: Pearson's correlation coefficients between the measured particles rotations and the local porosity (both measured at 9% axial shortening) with the known shape parameters for Hostun sand both outside (a) and inside (b) the shear band.

The only significant correlation that has been found, again, is with particle volume. Moreover, this dependency of local porosity with grain volume makes impossible any further investigation about the effect of local porosity on both particle shape and grain rotations. This is also evident from Figure 7.26b, showing that the sizes of the set voronois seem uniform through the whole sample, even for the grains with more space around them (*i.e.*, in the shear band), well evident in Figure 7.26a. It seems therefore that local porosity as defined here has limited explanatory capacity and alternatives would need to be explored in future work.

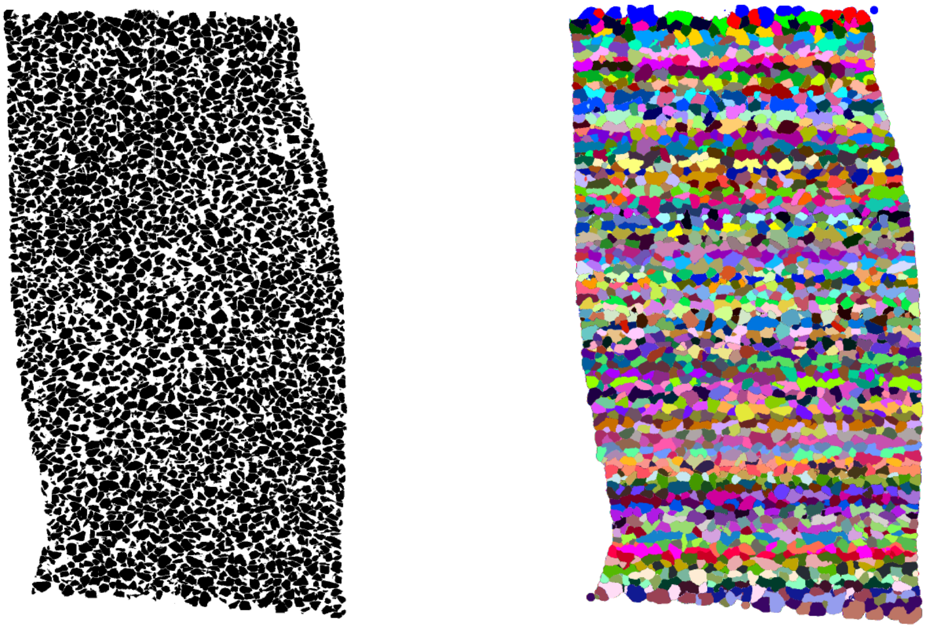
(a) (b)

Figure 7.26: Vertical slice perpendicular to the shear band of HNEA01 at 9% axial strain (a). Representation of the set-voronois for the same slice (b).

7.5 Summary

This Chapter sets out to explore the relationship between particle shape and particle rotation at the grain scale, for all the sand grains within triaxial specimens that failed in a localized shear mode. The main findings can be summarized as follows:

- The systematic use of Discrete-Digital Volume Correlation allowed successful tracking of rotational kinematics in the large majority of grains; those measurements were far more precise than previous attempts using 1D-track
- Kinematics within the shear bands are very different from those outside the shear band. Particle rotation magnitudes increase much faster in the bands. Rotational axes align themselves preferentially, perpendicular to the steepest descent direction of the band.
- Sand grains in the shear plane show both positive and negative spins (upwards and downwards the plane), revealing commonalities in the shear flow mechanisms of sands with those of simpler granular materials.

- Shape descriptors related to particle form, such as elongation or flatness indexes appear to be poorly correlated with observed particle rotation.
- Shape descriptors related to particle sphericity have a significant effect on particle rotation. This effect is far less important on the average value than on the upper limit of rotation.

It may be concluded that the link between particle shape and particle kinematics is only effective at the margin. This was to be expected, as it is a link necessarily mediated by particle connectivity. Despite this limitation, and until particle connectivity can be imaged with equal precision in experiments, the microscale results here presented should facilitate the calibration of advanced DEM contact models to represent shape effects, as it will be detailed in Chapter 8.

References Part II

Alshibli, K.A., Alramahi, B.A., 2006. Microscopic Evaluation of Strain Distribution in Granular Materials during Shear. J. Geotech. Geoenvironmental Eng. 132, 80–91. https://doi.org/10.1061/(asce)1090-0241(2006)132:1(80)

Alshibli, K.A., Druckrey, A.M., Al-Raoush, R.I., Weiskittel, T., Lavrik, N. V., 2015. Quantifying Morphology of Sands Using 3D Imaging. J. Mater. Civ. Eng. 27. https://doi.org/10.1061/(ASCE)MT.1943-5533.0001246

Alshibli, K.A., Jarrar, M.F., Druckrey, A.M., Al-Raoush, R.I., 2017. Influence of Particle Morphology on 3D Kinematic Behavior and Strain Localization of Sheared Sand. J. Geotech. Geoenvironmental Eng. 143, 04016097. https://doi.org/10.1061/(ASCE)GT.1943-5606.0001601

Altuhafi, F.N., Coop, M.R., 2011. Changes to particle characteristics associated with the compression of sands. Géotechnique 61, 459–471. https://doi.org/10.1680/geot.9.P.114

Andò, E., 2013. Experimental investigation of microstructural changes in deforming granular media using x-ray tomography. PhD Thesis. Université de Grenoble.

Andò, E., Cailletaud, R., Roubin, E., Stamati, O., the spam contributors, 2017. SPAM: The Software for the Practical Analysis of Materials [WWW Document]. https://ttk.gricad-pages.univ-grenoble-alpes.fr/spam/.

Andò, E., Hall, S.A., Viggiani, G., Desrues, J., Bésuelle, P., 2012a. Grain-scale experimental investigation of localised deformation in sand: A discrete particle tracking approach. Acta Geotech. 7, 1–13. https://doi.org/10.1007/s11440-011-0151-6

Andò, E., Hall, S.A., Viggiani, G., Desrues, J., Bésuelle, P., 2012b. Experimental micromechanics: grain-scale observation of sand deformation. Géotechnique Lett. 2, 107–112. https://doi.org/10.1680/geolett.12.00027

Baudet, B., Bolton, M., 2010. Editorial Soil mechanics at the grain scale: issue 1 and 2. Géotechnique 60, 313–314. https://doi.org/10.1680/geot.2010.60.5.313

Belheine, N., Plassiard, J.P., Donzé, F. V., Darve, F., Seridi, A., 2009. Numerical simulation of drained triaxial test using 3D discrete element modeling. Comput. Geotech. 36, 320–331. https://doi.org/10.1016/j.compgeo.2008.02.003

Bernard, L., Fave, S., Noirfalise, E., Saragaglia, A., 2011. Visilog 7 Reference Guide, Manual. ed. Noesis S.A., Espace technologique, Route de l'orme, Batiment Mercury 2, 91190 Saint Aubin, France: Noesis S.A.

Blott, S.J., Pye, K., 2008. Particle shape: A review and new methods of characterization and classification. Sedimentology 55, 31–63. https://doi.org/10.1111/j.1365-3091.2007.00892.x

Calvetti, F., Prisco, C., Nova, R., 2004. Experimental and Numerical Analysis of Soil – Pipe Interaction. J. Geotech. Geoenvironmental Eng. 130, 1292–1299. https://doi.org/10.1061/(ASCE)1090-0241(2004)130

Campello, E.M.B., 2015. A description of rotations for DEM models of particle systems. Comp. Part. Mech 2, 109–125. https://doi.org/10.1007/s40571-015-0041-z

Catalano, E., Chareyre, B., Barthélémy, E., 2014. Pore-scale modeling of fluid-particles interaction and emerging poromechanical effects. Int. J. Numer. Anal. Methods Geomech. 38, 51–71. https://doi.org/10.1002/nag.2198

Cheng, Z., Wang, J., 2018a. A particle-tracking method for experimental investigation of kinematics of sand particles under triaxial compression. Powder Technol. 328, 436–451. https://doi.org/10.1016/j.powtec.2017.12.071

Cheng, Z., Wang, J., 2018b. Experimental investigation of inter-particle contact evolution of sheared granular materials using X-ray micro-tomography. Soils Found. 58, 1492–1510. https://doi.org/10.1016/j.sandf.2018.08.008

Cleary, P.W., 2008. The effect of particle shape on simple shear flows. Powder Technol. 179, 144–163. https://doi.org/10.1016/j.powtec.2007.06.018

Coetzee, C.J., 2016. Calibration of the discrete element method and the effect of particle shape. Powder Technol. 297, 50–70. https://doi.org/10.1016/j.powtec.2016.04.003

Combe, A.-L., 1998. Comportement du sable d'Hostun S28 au triaxial axisymétrique.

Comparaison avec le sable d'Hostun RF. Diss. MA thesis, Université Joseph Fourier.

Coop, M.R., 1990. The mechanics of uncemented carbonate sands. Géotechnique 40, 607–626. https://doi.org/10.1680/geot.1990.40.4.607

Desrues, J., Chambon, R., Mokni, M., Mazerolle, F., 1996. Void ratio evolution inside shear bands in triaxial sand specimens studied by computed tomography. Géotechnique 46, 529–546. https://doi.org/10.1680/geot.1996.46.3.529

Druckrey, A.M., Alshibli, K.A., Al-Raoush, R.I., 2016. 3D characterization of sand particle-to-particle contact and morphology. Comput. Geotech. 74, 26–35. https://doi.org/10.1016/j.compgeo.2015.12.014

Efron, B., Tibshirani, R., 1994. An introduction to the bootstrap. Chapman & Hall.

Ferellec, J.-F., Mcdowell, G.R., 2010. A method to model realistic particle shape and inertia in DEM. Granul. Matter 12, 459–467. https://doi.org/10.1007/s10035-010-0205-8

Fonseca, J., O'Sullivan, C., Coop, M.R., Lee, P.D., 2013. Quantifying the evolution of soil fabric during shearing using directional parameters. Géotechnique 63, 818–829. https://doi.org/10.1680/geot.11.P.150

Fonseca, J., O'Sullivan, C., Coop, M.R., Lee, P.D., 2012. Non-invasive characterization of particle morphology of natural sands. Soils Found. 52, 712–722. https://doi.org/10.1016/j.sandf.2012.07.011

Guillard, F., Marks, B., Einav, I., 2017. Dynamic X-ray radiography reveals particle size and shape orientation fields during granular flow. Sci. Rep. 7, 1–11. https://doi.org/10.1038/s41598-017-08573-y

Hall, S.A., 2012. Digital Image Correlation in Experimental Geomechanics, in: Gioacchino Viggiani, Stephen A. Hall, Enrique Romero (Eds.), ALERT Doctoral School 2012 Advanced Experimental Techniques in Geomechanics. Aussois (France), pp. 69–102.

Hall, S.A., Bornert, M., Desrues, J., Pannier, Y., Lenoir, N., Viggiani, G., Bésuelle, P., 2010. Discrete and continuum analysis of localised deformation in sand using X-ray μCT and volumetric digital image correlation. Géotechnique 60, 315–322. https://doi.org/10.1680/geot.2010.60.5.315

Hasan, A., Alshibli, K., 2012. Three dimensional fabric evolution of sheared sand. Granul. Matter 14, 469–482. https://doi.org/10.1007/s10035-012-0353-0

Hasan, A., Alshibli, K.A., 2010. Experimental assessment of 3D particle-to-particle interaction within sheared sand using synchrotron microtomography. Géotechnique 60, 369–379. https://doi.org/10.1680/geot.2010.60.5.369

Higo, Y., Oka, F., Sato, T., Matsushima, Y., Kimoto, S., 2013. Investigation of localized deformation in partially saturated sand under triaxial compression using microfocus X-ray CT with digital image correlation. Soils Found. 53, 181–198. https://doi.org/10.1016/j.sandf.2013.02.001

Huang, X., Hanley, K.J., O'Sullivan, C., Kwok, C.Y., 2017. Implementation of rotational resistance models: A critical appraisal. Particuology 34, 14–23. https://doi.org/10.1016/j.partic.2016.08.007

Iwashita, K., Oda, M., 1998. Rolling resistance at contacts in simulation of shear band development by DEM. J. Eng. Mech. 124, 285–292. https://doi.org/10.1061/(ASCE)0733-9399(1998)124:3(285)

Jiang, M., Liu, F., Bolton, M., 2011. Proceedings of the International Symposium on Geomechanics and Geotechnics: from Micro to Macro (IS-Shanghai 2010). CRC Press/Balkema, Shanghai.

Jiang, M.J., Liu, J.D., Arroyo, M., 2016. Numerical evaluation of three non-coaxial kinematic models using the distinct element method for elliptical granular materials. Int. J. Numer. Anal. Methods Geomech. 40, 2468–2488. https://doi.org/10.1002/nag.2540

Jiang, M.J.J., Yu, H.-S., Harris, D., 2005. A novel discrete model for granular material incorporating rolling resistance. Comput. Geotech. 32, 340–357. https://doi.org/10.1016/j.compgeo.2005.05.001

Jones, E., Oliphant, T., Peterson, P., 2001. SciPy: Open source scientific tools for Python.

Kawamoto, R., Andò, E., Viggiani, G., Andrade, J.E., 2018. All you need is shape: Predicting shear banding in sand with LS-DEM. J. Mech. Phys. Solids 111, 375–392. https://doi.org/10.1016/j.jmps.2017.10.003

Kong, D., Fonseca, J., 2018. Quantification of the morphology of shelly carbonate sands using 3D images. Géotechnique 68, 249–261. https://doi.org/10.1680/jgeot.16.P.278

Lorensen, W.E., Cline, H.E., 1987. Marching cubes: A high resolution 3D surface construction algorithm. ACM siggraph Comput. Graph. 21, 163–169. https://doi.org/10.1145/37402.37422

Matsushima, T., Uesugi, K., Nakano, T., Tsuchiyama, A., 2006. Visualization of Grain Motion inside a Triaxial Specimen by Micro X-ray CT at SPring-8, in: Desrues, J., Besuelle, P., Viggiani, G. (Eds.), Advances in X-Ray Tomography for Geomaterials. London, pp. 35–52. https://doi.org/10.1002/9780470612187.ch24

Ng, T.-T., Lin, X., 1997. A three-dimensional discrete element model using arrays of ellipsoids. Géotechnique 47, 319–329. https://doi.org/10.1680/geot.1997.47.2.319

Oda, M., Takemura, T., Takahashi, M., 2004. Microstructure in shear band observed by microfocus X-ray computed tomography. Géotechnique 54, 539–542.

Oliphant, T.E., 2006. Guide to NumPy.

Pan, B., Qian, K., Xie, H., Asundi, A., 2009. Two-dimensional digital image correlation for in-plane displacement and strain measurement: a review. Meas. Sci. Technol. 20. https://doi.org/10.1088/0957-0233/20/6/062001

Pannier, Y., Lenoir, N., Bornert, M., 2010. Discrete volumetric digital image correlation for the investigation of granular type media at microscale: accuracy assessment. EPJ Web Conf. 6. https://doi.org/10.1051/epjconf/20100635003

Pasternak, E., Dyskin, A. V., Esin, M., Hassan, G.M., MacNish, C., 2015. Rotations and pattern formation in granular materials under loading. Philos. Mag. 95, 3122–3145. https://doi.org/10.1080/14786435.2015.1059517

Pinyol, N.M., Alvarado, M., 2017. Novel analysis for large strains based on particle image velocimetry. Can. Geotech. J. 54, 933–944.

Ritter, J., 1990. An efficient bounding sphere, Graphics Gems. Academic Press Professional, Inc., San Diego (California).

Rorato, R., Arroyo, M., Andò, E., Gens, A., 2019. Sphericity measures of sand grains. Eng. Geol. 254, 43–53. https://doi.org/10.1016/j.enggeo.2019.04.006

Rorato, R., Arroyo, M., Gens, A., Andò, E., Viggiani, G., 2018. Particle Shape Distribution Effects on the Triaxial Response of Sands: A DEM Study, in: Giovine, P., et al. (Eds.), Micro to MACRO Mathematical Modelling in Soil Mechanics, Trends in Mathematics. Reggio Calabria (Italy), pp. 277–286. https://doi.org/10.1007/978-3-319-99474-1_28

Rothenburg, L., Bathurst, R.J., 1992. Micromechanical features of granular assemblies with planar elliptical particles. Géotechnique 42, 79–95. https://doi.org/10.1680/geot.1992.42.1.79

Schaller, F.M., Kapfer, S.C., Evans, M.E., Hoffmann, M.J.F., Aste, T., Saadatfar, M., Mecke, K., Delaney, G.W., Schröder-Turk, G.E., 2013. Set Voronoi diagrams of 3D assemblies of aspherical particles. Philos. Mag. 93, 3993–4017. https://doi.org/10.1080/14786435.2013.834389

Schanz, T., Vermeer, P.A., 1996. Angles of friction and dilatancy of sand. Géotechnique 46, 145–151. https://doi.org/10.1680/geot.1996.46.1.145

Šmilauer, V. et al., 2015. Yade Documentation 2nd ed. The Yade Project. https://doi.org/DOI 10.5281/zenodo.34073

Soga, K., Kumar, K., Biscontin, G., Kuo, M., 2014. Geomechanics from micro to macro : Proceedings of the TC105 ISSMGE International Symposium on Geomechanics from Micro to Macro, Cambridge, UK, 1-3 September 2014.

Stanier, S.A., Blaber, J., Take, W.A., White, D.J., 2016. Improved image-based deformation measurement for geotechnical applications. Can. Geotech. J. 53, 727–739. https://doi.org/10.1139/cgj-2015-0253

Suh, H.S., Kim, K.Y., Lee, J., Yun, T.S., 2017. Quantification of bulk form and angularity of particle with correlation of shear strength and packing density in sands. Eng. Geol. 220, 256–265. https://doi.org/10.1016/j.enggeo.2017.02.015

Sutton, M.A., Schreier, H.W., Orteu, J.-J., 2009. Image correlation for shape, motion and deformation measurements : basic concepts, theory and applications. Springer.

Take, W.A., 2015. Thirty-Sixth Canadian Geotechnical Colloquium: Advances in visualization of geotechnical processes through digital image correlation. Can. Geotech. J. 52, 1199–1220. https://doi.org/10.1139/cgj-2014-0080

Tudisco, E., Andò, E., Cailletaud, R., Hall, S.A., 2017. TomoWarp2: A local digital volume correlation code. SoftwareX 6, 267–270. https://doi.org/10.1016/J.SOFTX.2017.10.002

Veje, C.T., Howell, D.W., Behringer, R.P., 1999. Kinematics of a two-dimensional granular Couette experiment at the transition to shearing. Phys. Rev. E - Stat. Physics, Plasmas, Fluids, Relat. Interdiscip. Top. 59, 739–745. https://doi.org/10.1103/PhysRevE.59.739

Vlahinić, I., Kawamoto, R., Andò, E., Viggiani, G., Andrade, J.E., 2017. From computed tomography to mechanics of granular materials via level set bridge. Acta Geotech. 12, 85–95. https://doi.org/10.1007/s11440-016-0491-3

Wiebicke, M., Andò, E., Herle, I., Viggiani, G., 2018. On the metrology of interparticle contacts in sand from x-ray tomography images. Meas. Sci. Technol. 28, 124007.

Wiebicke, M., Andò, E., Salvatore, E., Viggiani, G., Herle, I., 2017. Experimental measurement of granular fabric and its evolution under shearing, in: Radjai, F., Nezamabadi, S., Luding, S., Delenne, J.Y. (Eds.), European Physical Journal Web of Conferences. EDP Sciences, p. 02020. https://doi.org/10.1051/epjconf/201714002020

Zhao, B., Wang, J., 2016. 3D quantitative shape analysis on form, roundness, and compactness with micro-CT. Powder Technol. 291, 262–275. https://doi.org/10.1016/j.powtec.2015.12.029

Zingg, T., 1935. Beitrag zur Schotteranalyse. Schweizerische Mineral. Petrogr. Mitteilungen. https://doi.org/10.3929/ethz-a-000103455

Part III: Numerical Simulations

8

A rolling resistance contact model accounting for Particle Shape

8.1 Introduction

Rolling resistance elasto-plastic contact models are frequently used to approximate particle shape effects in simulations using the Discrete Element Method (DEM). These models offers substantial computational benefits at the price of increased calibration complexity. Usually a calibration of several micro-parameters is required, most importantly a rolling resistance coefficient. A different approach is taken in this work, where the value of rolling resistance has been directly linked to true sphericity (Equation 2.5), a basic measure of grain shape. When shape measurements are performed (Chapter 6), this link enables independent assignment of the rolling resistance coefficient for each particle in a manner that is statistically compatible with shape characteristics. It does also allow the shape variability of natural soils to be easily taken into account.

The link between rolling resistance and shape is here formulated and then calibrated to reproduce the triaxial tests – in terms of mechanical (see Chapter 5) and kinematic (see Chapter 7) responses – of two different sands: Hostun and Caicos sands. It is then validated by simulating other triaxial tests (1) with the same sands, but in different conditions (2) with Ottawa sand, for which 3D grain images were also available for examination, and (3) with Ticino sand, for which only 2D grain images were available.
The Itasca DEM software PFC5 (Itasca Consulting Group Inc., 2014) has been used for all the numerical simulations.

8.2 Contact rolling resistance model

In this work, a simplified version of the Iwashita-Oda contact model (Iwashita and Oda, 1998) has been used under the following assumptions:

(1) The *rolling stiffness* (k_r) is defined as Iwashita's original contact model:

$$k_r = k_s R^2 \tag{8.1}$$

where k_s is the contact *shear stiffness* and R the *effective radius* defined as

$$R = \frac{1}{R_1} + \frac{1}{R_2} \tag{8.2}$$

being R_1 and R_2 the radii of the two particles in contact.

(2) The moment-rotational contact law is implemented as an elastic-perfectly plastic model with the yielding moment (M^*) defined as:

$$M^* = \mu_r F_n R \tag{8.3}$$

where μ_r is defined as *rolling friction coefficient* and F_n is the normal contact force. The rolling resistance part of the contact model used in this study is illustrated in Figure 8.1.

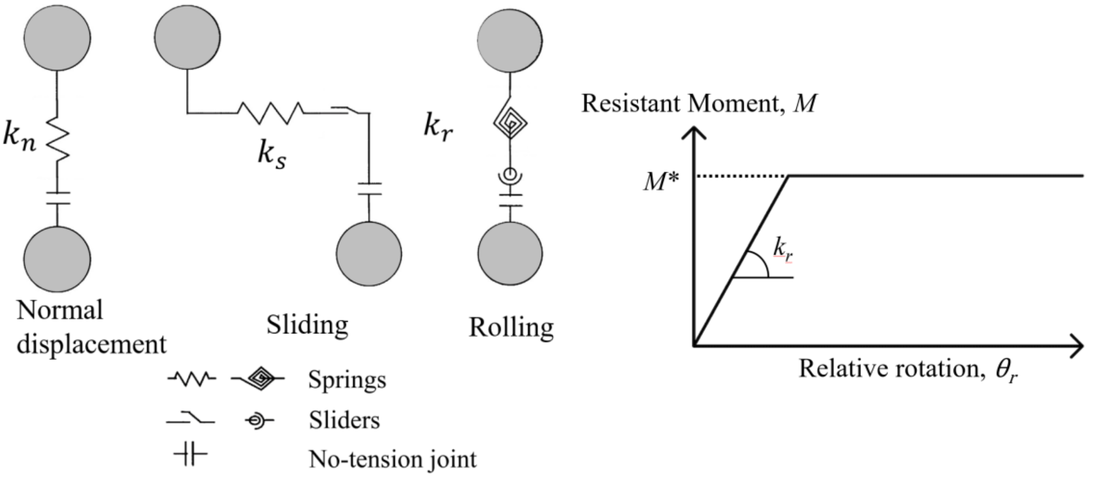

(a) *(b)*

Figure 8.1: Rolling resistance contact model (Iwashita and Oda, 1998) (a) and elastic-perfectly plastic model accounting for rolling resistance at contact (b)

Additional viscous dissipation parameters are not added to the model because not needed for the quasi-static condition (low inertial numbers) under the previous assumptions, as pointed out by (Wensrich and Katterfeld, 2012). Therefore, the rolling dashpot of Figure 8.1a is not included in the contact model.

8.3 Relating rolling resistance and particle shape

This Chapter exploits a novel approach to relate the particle shape with the rolling resistance applied at the contacts, extending the model that was originally proposed in (Rorato et al., 2018). In particular, it is hypothesized that the *degree of true sphericity* (ψ) of one particle is univocally related with a *coefficient of rolling friction* (μ_r), through a relation

$$\mu_r = F(\psi) \tag{8.4}$$

valid for all the spherical particles participating in the DEM simulation. Therefore, if the statistical distribution of sphericity is known for one particular sand (see Figure 6.21), it is possible to extract infinite values so that one measure of ψ can be assigned to each sphere of the numerical specimen, and therefore the *rolling friction coefficients* can distributed through all the discrete elements.

Note that when two spheres overlap, a contact is formed and two different values of μ_r participate to the contact law. The solution to avoid this ambiguity is to select the minimum, as

$$\mu_r = min\ (\mu_{r,1}, \mu_{r,2}) \tag{8.5}$$

where $\mu_{r,1}$ and $\mu_{r,2}$ are the rolling friction coefficients of the two contacting spheres. A similar consideration is usually made with the *sliding friction coefficient* when two bodies of different materials contact. Thus, the rolling resisting yielding moment (M^*) varies at each contact depending on (1) the radii of the contacting spheres, that is the *effective radius*, *R*, (2) the normal contact force F_n and (3) the *coefficient of rolling friction*, different for each contact (from Eq. 8.4 and 8.5).

8.4 Model calibration

The question then is what shape function $F(\psi)$ might take. Chapter 7.3 showed that rounded sands tend to rotate more in average than angular sands, especially inside the shear band, and it is known that the rolling friction coefficient is the contact parameter that controls the magnitude of relative rotation in the DEM. Therefore, a first reasonable hint come from the fact that $F(\psi)$ should provide low values of rolling friction when the grain sphericity is high, and vice-versa. Theoretically, it should be zero for a sphere ($\psi=1$), however many researchers agree that the experimental responses of real soils cannot be fitted numerically when freely rotating spheres are used (Ng, 1994; Rothenburg and Bathurst, 1992; Zhou et al., 1999). Experimentally, Skinner (Skinner, 1969) noted that the macroscopic friction angle of an assembly of glass ballotini does not change significantly if the inter-particle friction is varied by a factor of 5. Therefore, it is crucial to assign some rotational resistance to DEM spherical elements if the goal is to reproduce experimental results. To the extreme, some researchers inhibited the particles relative rotation in order to mimic the effect of angular sand grains, achieving successful results (Arroyo et al., 2011; Calvetti et al., 2003; Ciantia et al., 2015), however this approach is far from physical. Bardet (Bardet and Huang, 1992) claimed that both choices (freely and fixed balls rotations in DEM) provide macroscopic friction angles that are different from those observed experimentally.

8.4.1 Target experimental data

In this work, the goal is to find the equation of $F(\psi)$ that could best match the experimental triaxial tests performed on Hostun sand (specimen "HNEA01") and Caicos ooids (specimen "COEA04"). The calibration procedure here proposed aims to fit the conventional macro-mechanical responses (shown in Figure 6.1) together with kinematic micro measures. In particular, the histories of the cumulated grain rotations are known for each grain from the experiments (Chapter 7.3) and the particles rolling frictions - that is Eq. (8.4) - can be adjusted trying to reproduce similar kinematic responses inside the shear bands of the numerical specimens (Figure 7.12). It is indeed well known from past DEM studies (Cheng et al., 2017; Estrada et al., 2008; Wensrich et al., 2014; Wensrich and Katterfeld, 2012) that the same macroscopic friction angle can be obtained from several couples of *sliding friction coefficient* (μ) and *rolling friction coefficient* (μ_r) (see Chapter 4.3.5 for some example results). Both parameters contribute to the shear resistance of the numerical specimen, and their influence is coupled. In other words, the effect of increasing rolling friction saturates if the sliding friction is not increased together, and vice-versa. The coupling between these parameters does not affect only the overall shear resistance, but also how the particles rearrange, slide and rotate under shearing. Fixing the rolling friction (μ_r) to a value, the average rotation of the balls will be high if the sliding friction is high. This is because a low sliding friction eases sliding at contact between two particles, thus hindering their relative rotation. However, the rotational information available from Chapter 7.3 (see Figure 7.12) provides a unique solution, able to respect either the mechanics either the kinematics at failure.

In order to fit the average grains rotations inside the shear bands, it is necessary first to individuate the grains belonging to the shear band for both the physical and numerical specimens. Regarding the experimental samples, this task is already accomplished in Chapter 7.3.1 (see Figure 7.6). The same procedure is exploited here for the numerical samples. As explained in section 7.2.4, it computes a local strain at the particle-level (called "*micro-strain*" by Catalano et al. 2014) on each Voronoi domain centred at each particle. A threshold is then set to separate the discrete elements that belong to the shear band with those which are outside of it. Once the labels of the particles belonging to the shear band are known, the average rotations can be obtained and plotted in function of the axial strain, so that the evolution of the mean rotations inside the shear band can be followed as the test proceeds, as it will be shown later in Figure 8.5 and Figure 8.7.

8.4.2 Mapping function

The equation of $F(\psi)$ is finally chosen, after an iterative procedure, according to a power law written as

$$\mu_r = 0.1963(\psi)^{-8.982} \tag{8.6}$$

and plotted in Figure 8.2.

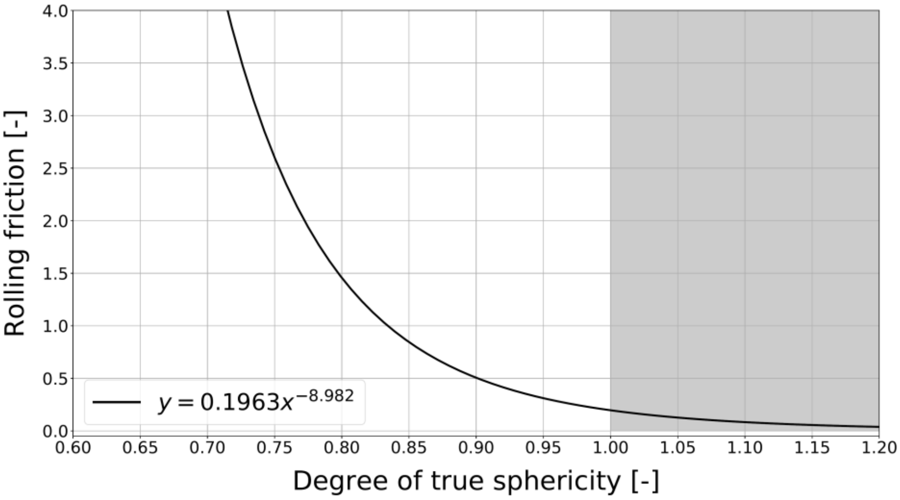

Figure 8.2: Power law relating the degree of true sphericity of a grain (known) with the rolling friction coefficient to apply to its spherical counterpart in the DEM simulation. The shaded area indicates the maximum

The proposed equation presents an inversely proportional relationship between ψ and μ_r, in which a minimum limiting rolling friction coefficient of about 0.2 is assigned to spherical particles (ψ=1), for the reasons previously explained. Since the maximum admissible value of true sphericity is one, the plot is shaded area above this limit.

8.4.3 Calibration procedure

The triaxial test on Hostun and Caicos sands at 100kPa confining pressure are used to calibrate the contact model. The initial DEM samples are prepared matching the void ratio and Particle Size Distribution (PSD) of the physical specimens before performing the triaxial test, the target porosities are achieved by using different initial friction coefficients (μ_0). The small size of the samples (10mm diameter and 20mm height) allows preparing the numerical specimens at the same scale of the experiments, so that a scaling factor is not applied to the balls radii. Doing so, the initial models contain about 60.000 particles, comparable to the number of grains inside specimens HNEA01 and COEA04.

The contact normal and shear stiffness are defined as

$$k_n = \frac{AE_{mod}}{L} \; ; \; k_s = \frac{k_n}{k_{ratio}} \tag{8.7}$$

where E_{mod} and k_{ratio} have been set respectively equal to 0.2GPa and 2.0, being A the diameter of the smallest contacting sphere and L the distance between grain centres. This method assures that the normal and shear contact forces are independent of the element diameter, thus allowing scaling of the particles without affecting the deformability (Feng and Owen, 2014). The specimens are then isotropically compressed by a servo-controlled mechanism that applies 100kPa confining pressure.

Afterwards, the sliding friction and the rolling friction coefficients equation (Eq. 8.4) are adjusted independently for the two sands to fit the experimental results, according to the described calibration procedure. After several iterations, the sliding friction coefficients is finally set to 0.575 for both sands, and Eq. 8.4 is finally set equal to Eq. 8.6 to fit the rotations of both experiments. Under all these assumptions, the stress-strain responses comparisons of the two sand samples are showed in Figure 8.3 and Figure 8.4, together with other two experimental curves of Hostun (HNEA03) and Caicos (COEA03) sands at same confining pressure.

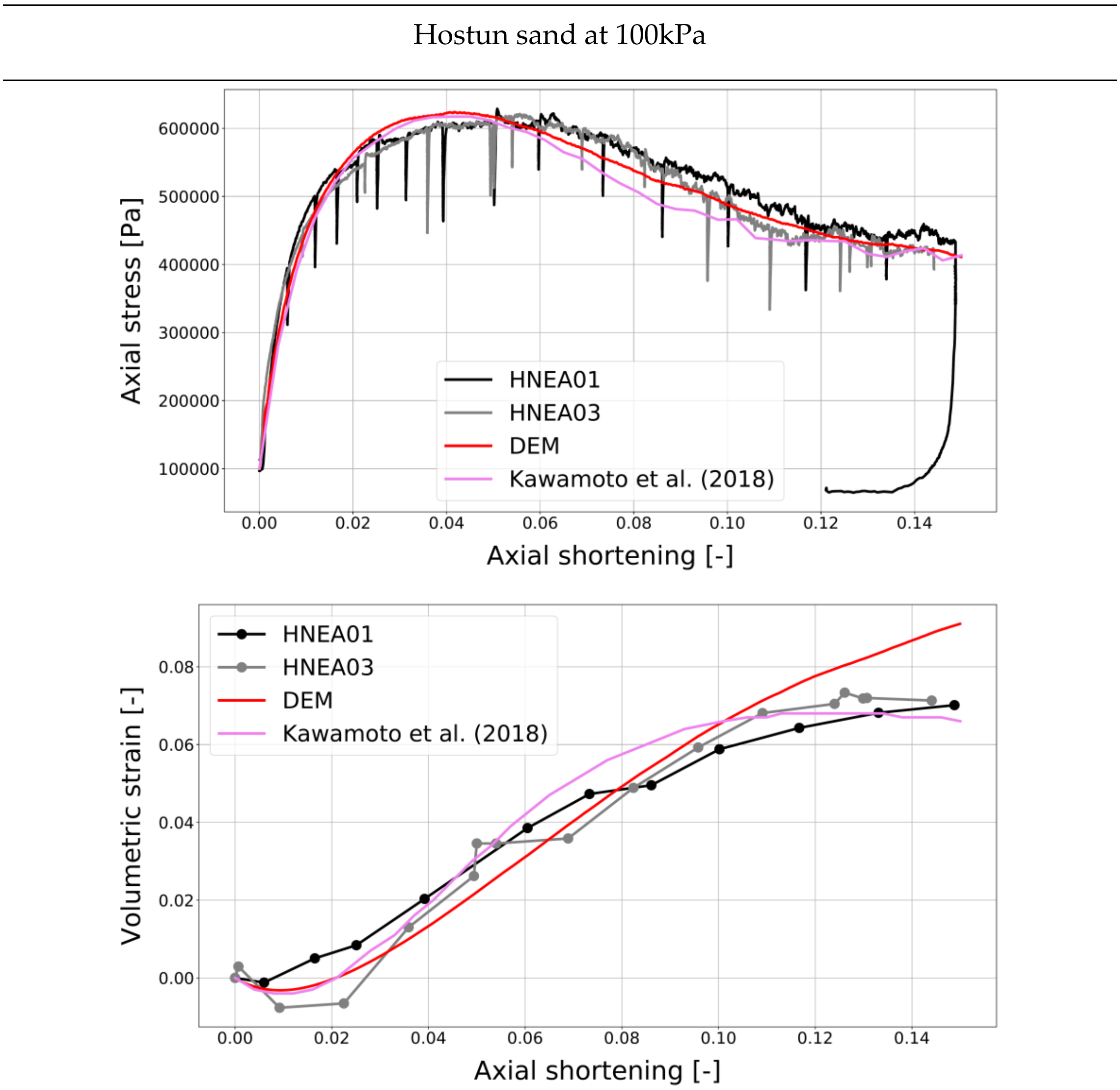
Hostun sand at 100kPa

Figure 8.3: Comparison between the triaxial responses (100kPa confining pressure) of the experiments (specimens HNEA01 and HNEA03) and the numerical model (DEM) replicating Hostun sand. The mechanical responses from Kawamoto et al. (2018) are also reported for comparison.

Caicos sand at 100kPa

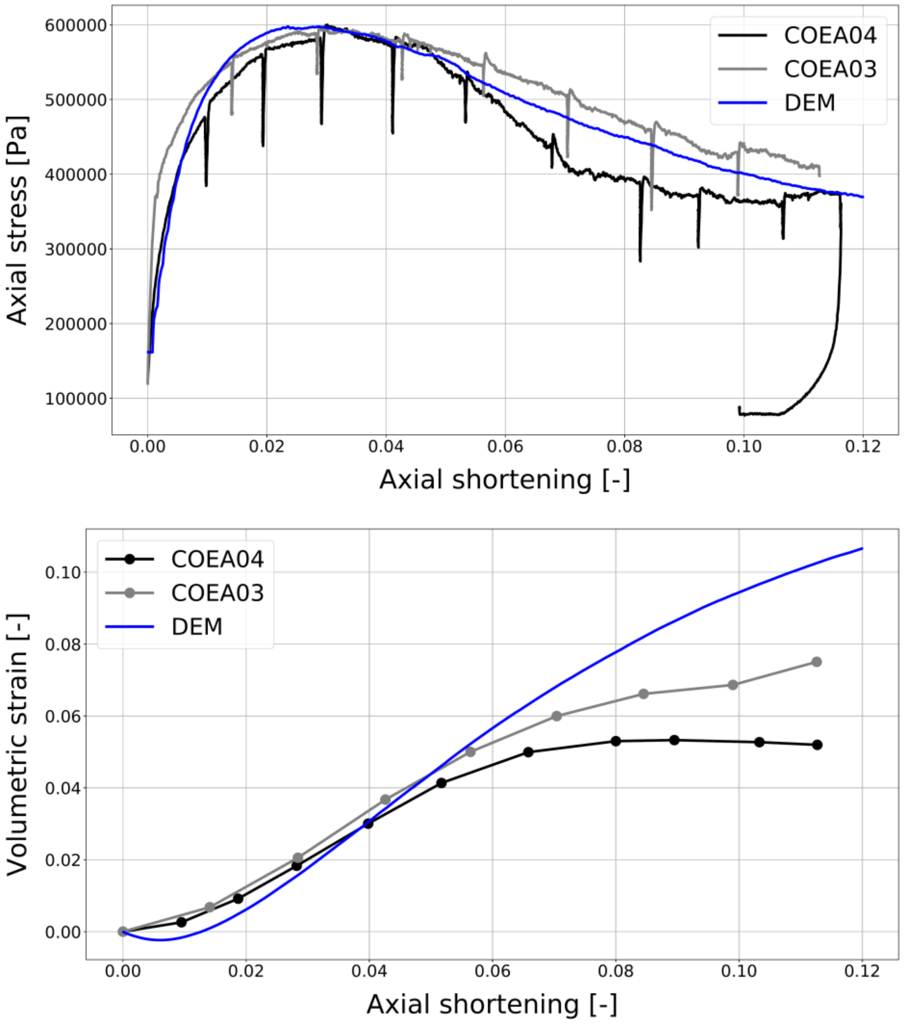

Figure 8.4: Comparison between the triaxial responses (100kPa confining pressure) of the experiments (specimens COEA03 and COEA04) and the numerical model (DEM) replicating Caicos sand.

The macro-mechanical responses can be well reproduced using the proposed approach. A slight diversion can be noted for the volumetric strain of Caicos sand, however this is due to lateral boundary conditions that are different for the physical (flexible membrane) and numerical samples (rigid cylindrical wall).

The other element our approach aims to fit is the mean particles rotations histories inside the shear bands. Figure 8.5 shows the results of the shear band identification procedure, described in the previous section, for both the experiment and the DEM simulation.

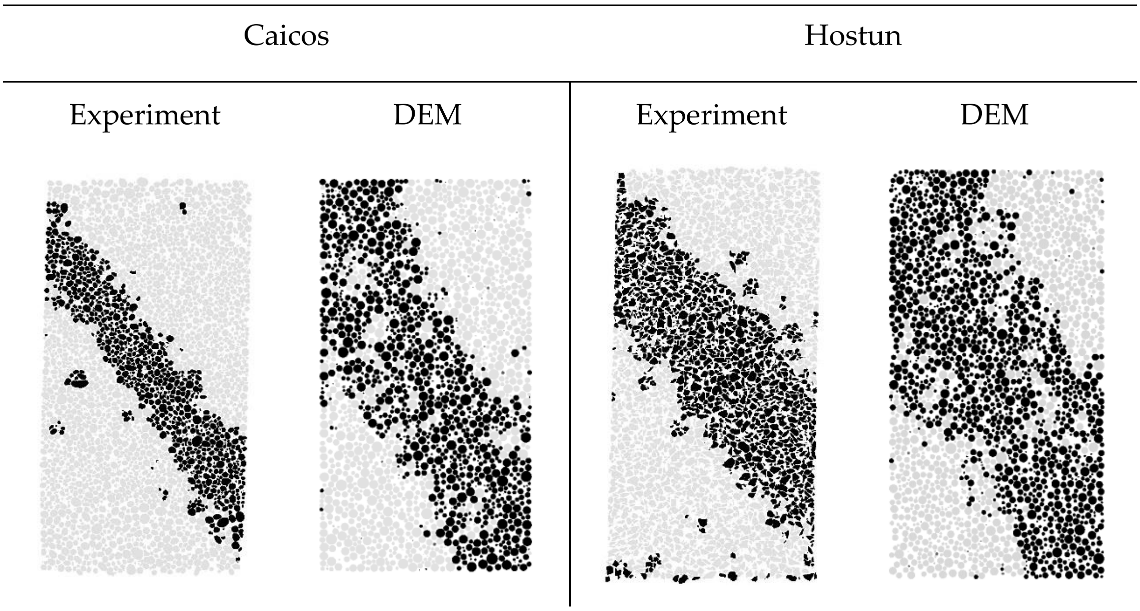

(a) (b) (c) (d)

Figure 8.5: Shear band identification for the experiments and the DEM simulation for both sands (specimens HNEA01 and COEA04). Physical (a-c) and numerical (b-d) particles are coloured black if the "micro-strain" (Catalano et al., 2014) *calculated on the Voronoi domain centred on the particle is greater than 0.10 (i.e. they belong to the shear band). The same threshold separates the grains from both sands and both physical and numerical samples.*

The first important observation is that the numerical sample is clearly able to localise failure, whereas the extreme cases of freely and fixed rotating spheres cannot (Iwashita and Oda, 1998). This effect is here made visible in Figure 8.6 showing the vertical (*i.e.,* "Z") balls displacements at the end of the triaxial tests (*i.e.,* 15% shortening) in three different situations (i.e. fixed rotations, free rotations, and exploiting rolling resistance).

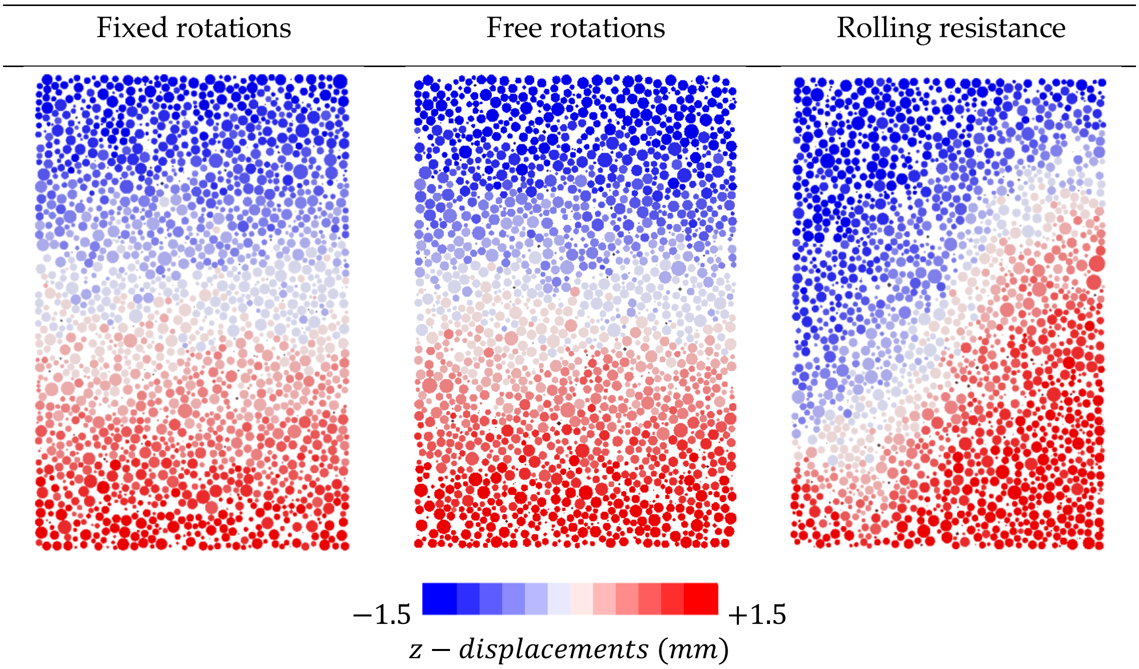

Figure 8.6: Z-displacements in a vertical section of the DEM sample representing Hostun sand compressed at 100kPa confining at 15% axial strain.

It is evident that the shear bands geometries of Figure 8.5 compares well, although the band thicknesses are larger in the numerical samples because of the absence of a deformable lateral constrain. However, the experimental observation that the shear band of Hostun is thicker than that of Caicos sand (due to interlocking effects) is also visible in the DEM samples, proving that the DEM materials behave physically.

Once the balls labels belonging to the shear band are known (black grains of Figure 8.4b-d), as well as their cumulated rotations (obtained in Chapter 7), it is possible to adjust Eq. 8.4 to fit these experimental histories. The comparisons between these histories measured inside the shear band are shown in Figure 8.7, and it is evident they compare well. Therefore, it can be concluded that the set of DEM parameters used is well calibrated to reproduce the macroscopic triaxial responses as well as the particles kinematics where the material failure occurs. In other words, the rolling resistance contact model here proposed induces rotations of the spheres that are comparable to those of the physical grains throughout the whole execution of the test.

Caicos (COEA04)	Hostun (HNEA01)
Mean rotations inside the shear band	Mean rotations inside the shear band
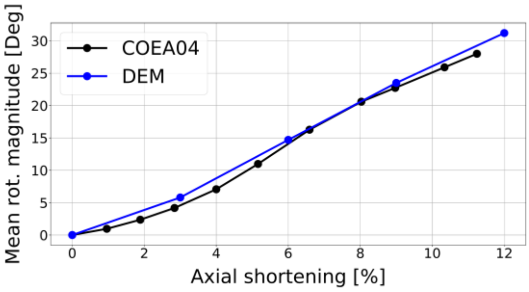	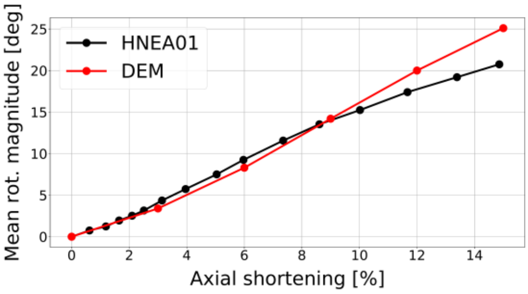

Figure 8.7: Mean particle rotations for the grains located inside the shear bands (the black grains of Figure 8.5) for both the experimental and numerical samples, throughout the execution of the triaxial test. The good fit ensures the kinematics at failure is respected.

Table 8.1 and Table 8.2 summarises respectively the initial conditions and DEM parameters used for the DEM calibration on Hostun and Caicos sands and the drained triaxial tests performed. The properties and tests of Ottawa and Ticino sands, which will be later used for validation, are also reported.

Parameter	**Symbol**	**Hostun**	**Caicos**	**Ottawa**	**Ticino**
Specimen sizes *(height, diameter)*	$H_C(mm)$ $D_c(mm)$	20 10	20 10	20 10	20 10
Effective normal contact stiffness	E_{mod} $(10^8 Pa)$	2.0	2.0	1.5	4.0
Normal-to-shear stiffness ratio	k_{ratio}	2.0	2.0	2.0	2.0
Inter-particle friction coefficient	μ	0.575	0.575	0.450	0.600
Degree of true sphericity	ψ	(Fig. 6.21)	(Fig. 6.21)	(Fig. 6.21)	(Eq. 6.6)
Rolling friction coefficients	μ_r	(Eq. 8.6)	(Eq. 8.6)	(Eq. 8.6)	(Eq. 8.6)

Parameter	**Symbol**	**Hostun**	**Caicos**	**Ottawa**	**Ticino**
Rolling stiffness	k_r	(Eq. 8.1)	(Eq. 8.1)	(Eq. 8.1)	(Eq. 8.1)
Local damping	*(-)*	0.7	0.7	0.7	0.7
Ball density	$\rho\ (\frac{kg}{m^3})$	2500	2500	2500	2500
Ball scaling factor	*(-)*	1	1	1	1
Confining pressures	$P\ (kPa)$	100 300	100 300	100 300	100 200 300
Inertial number	$I\ (10^{-4})$	4.00	4.74	3.67	6.28

Table 8.1: Parameters and input variables employed in the DEM simulations on Hostun, Caicos and Ottawa sands.

Sand	**Specimen**	**Purpose**	**Relative density (EXP)**	**Confining pressure**	**Initial porosity (EXP)**	**Initial porosity (DEM)**
-	-	-	$D_R(\%)$	(KPa)	$n_{0,exp}(\%)$	$n_{0,DEM}(\%)$
Hostun	HNEA01	Calibration	83	100	39.7	39.0
Hostun	HNEA02	Validation	95	300	38.2	38.6
Caicos	COEA04	Calibration	-	100	31.9	33.2 (*)
Caicos	COEA02	Validation	-	300	33.2	34.3 (*)
Ottawa	OUEA04	Validation	112	100	31.4	34.1 (*)
Ottawa	OUEA02	Validation	84.9	300	35.6	35.8

Table 8.2: Drained triaxial compression tests performed in this chapter. The relative density and porosity of each experimental/numerical test are reported. The symbol (*) means that a denser specimen could not be generated for the DEM simulation.

8.5 Validation of the contact model

A first hint that the proposed model can represent properly the effect of shape comes from the original work of Kawamoto et al. (Kawamoto et al., 2018). They used a level-set approach to build an avatar specimen of HNEA01 and simulated real shaped particles with DEM. The 480 cores of the San Diego Supercomputer provided the triaxial response of specimen HNEA01 that was found to be very close to the experiment. The fact that the results here obtained (using spheres with rolling resistance and very similar sliding friction coefficients, 0.55 vs 0.575) are comparable, suggests that the effect of particle shape can be well imitated by our contact model. In other words, the effect of particle shape in Hostun sand is adequately simulated by the proposed – more practical – approach exploiting rolling resistance.

Apart for that, the proposed equation (Eq. 8.6) to relate univocally the degree of true sphericity of a particle and the coefficient of rolling friction to assign is tested for validation in three different situations: (1) higher confining pressures, (2) testing a third type of sand (Ottawa sand) for which the statistical distribution of 3D sphericity was known and (3) testing a fourth type of sand (Ticino sand) for which the distribution of 3D sphericity was not known (presented in Chapter 9).

8.5.1 Validation 1: Triaxial test on Hostun and Caicos sands at 300kPa confining pressure

The proposed approach is tested for validation at higher confining pressures, for which the experimental data is available from (Andò, 2013). Firstly, the initial porosities (before shearing) of the Caicos and Hostun samples are matched using initial friction angles (μ_0) greater than zero, secondly the 300kPa confining pressure is applied by a servo-controlled mechanism, and finally the specimens are compressed in triaxial condition until failure is reached. The model properties for balls and contacts are same as the 100kPa confining case, since the sand types are the same.

Figure 8.8 and Figure 8.9 show the stress-strain-volumetric response of the numerical and experimental tests. The numerical curves compare well with the experiments except for the volumetric dilatation of Caicos sand. A similar trend was observed at 100kPa confining case, this is due to boundary effects created by the rigid lateral wall. Further work will implement an elastic membrane in order to ease the material failure localisation along a narrow shear band that would induce a lower global volumetric dilatation of the soil sample.

Hostun sand at 300kPa

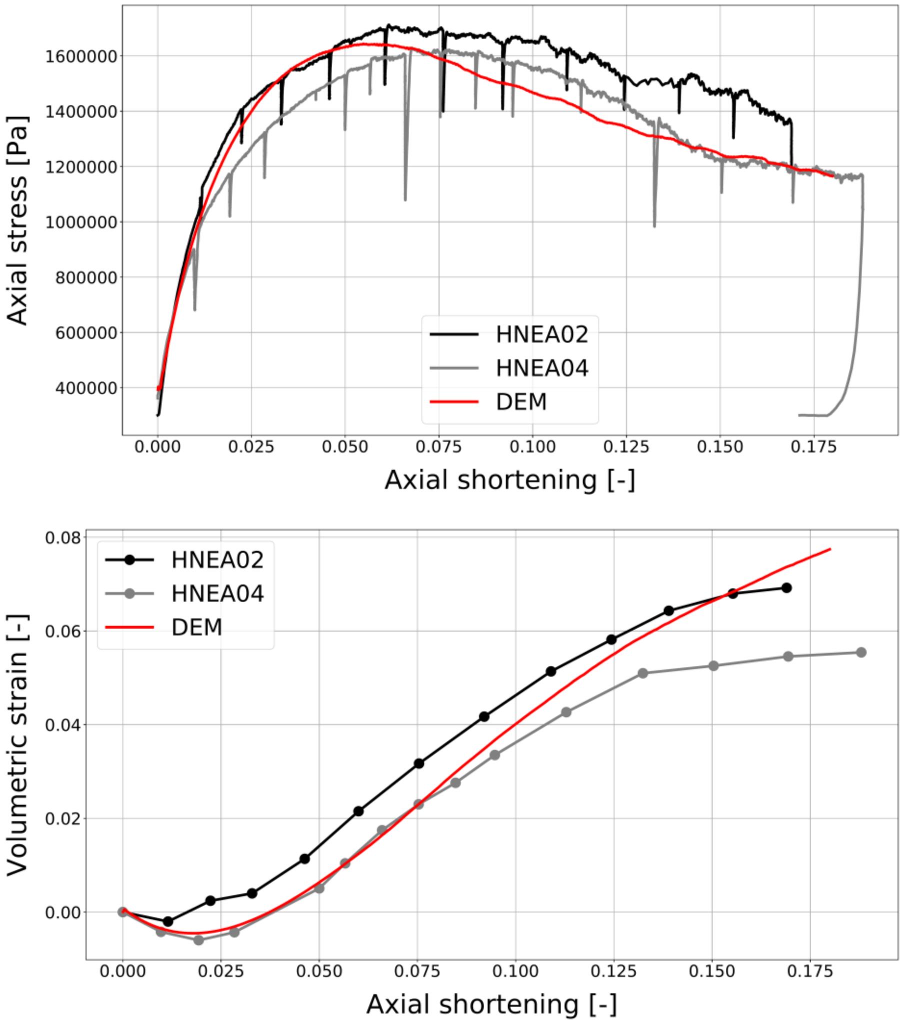

Figure 8.8: Comparison between the triaxial responses (300kPa confining pressure) of the experiments (specimens HNEA02 and HNEA04) and the numerical model (DEM) replicating Hostun sand.

Caicos sand at 300kPa

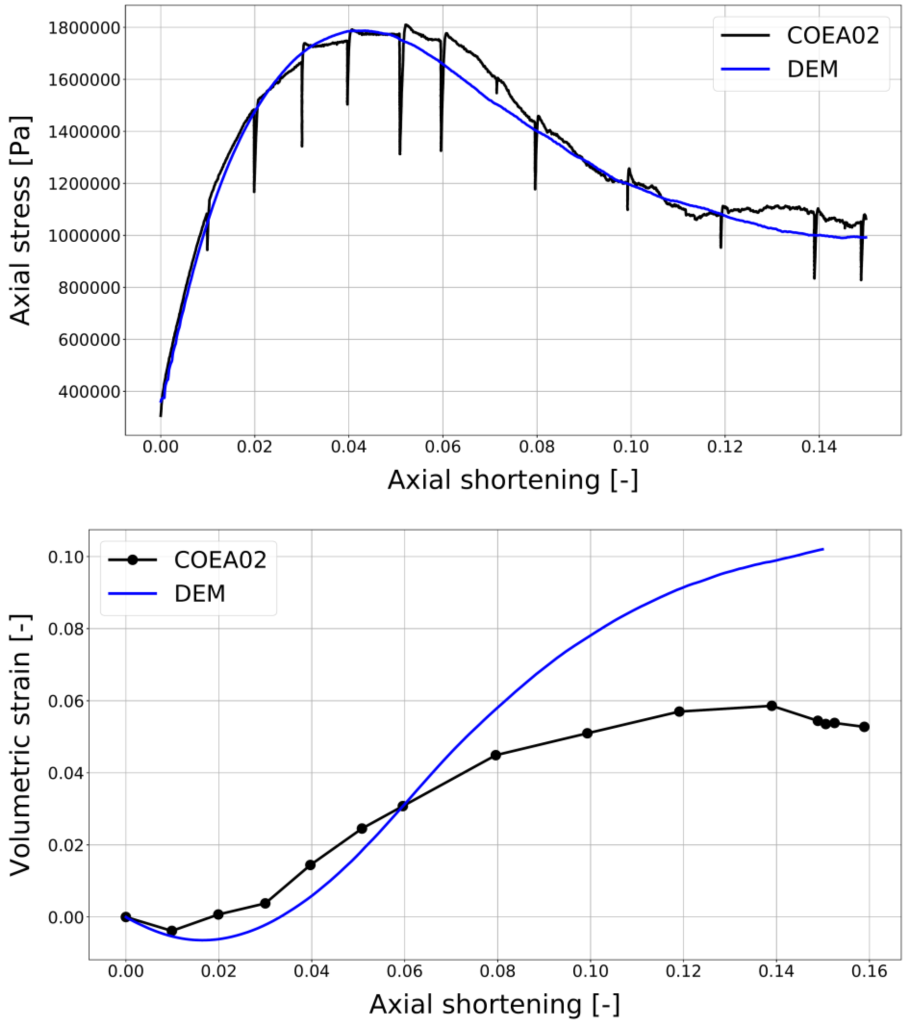

Figure 8.9: Comparison between the triaxial responses (300kPa confining pressure) of the experiment (specimen COEA02) and the numerical model (DEM) replicating Caicos sand.

8.5.2 Validation 2: Triaxial test on Ottawa sand at 100kPa and 300kPa

First, the shape properties of one labelled 3D tomographic image of Ottawa sand (scanned by Edward Andò at 3SR Laboratory, Grenoble) have been measured, so that the *degree of true sphericity* can be easily calculated, as shown in Chapter 6.3 (Figure 6.21). Secondly, the initial DEM specimen is prepared matching the experimental PSD and porosity (31.4% for OUEA04 and 35.6% for OUEA02). Doing so, about 102.000 balls are generated, that approximate well the grains contained in the physical sample, 110.000.

The contact stiffness properties E_{mod} and k_{ratio} (i.e. k_n and k_s) are set respectively $1.5 \cdot 10^8$ Pa and 2.0 in order to fit the initial elastic part of the stress-strain mechanical curve.

Subsequently, the relationship proposed (Eq. 8.6) is used to relate shape with rolling friction, so that finally the coefficient of sliding friction (μ) remains the only important free parameter to be adjusted in order to fit the macro-mechanical response of Ottawa sand, and it is set 0.45.

Figure 8.10 and Figure 8.11 shows the comparison between the experimental and numerical results respectively at 100kPa and 300kPa confinements, after shearing in triaxial conditions at the same shear rate of the previous simulations. Additional details about the physical experiments can be found in Chapter 5.3.3. The simulations provide similar results compared to the experiments, indeed both the stress-strain and volumetric curves are well reproduced.

Ottawa sand at 100kPa

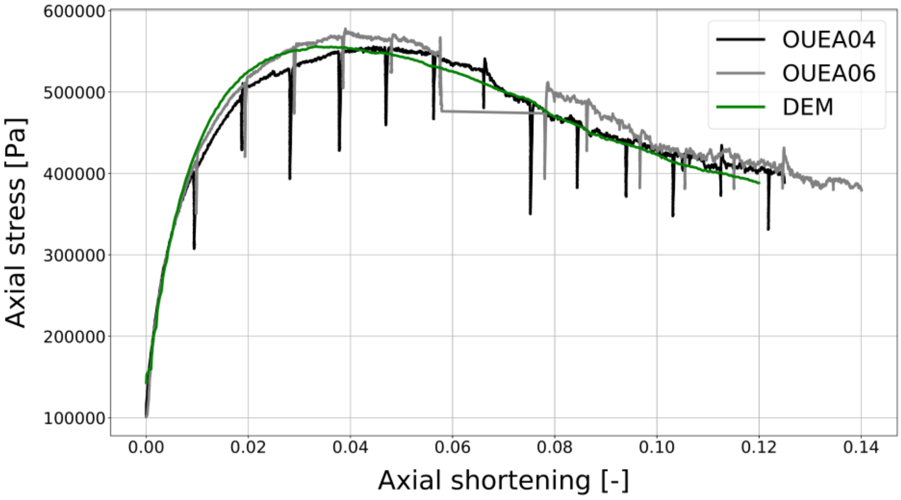

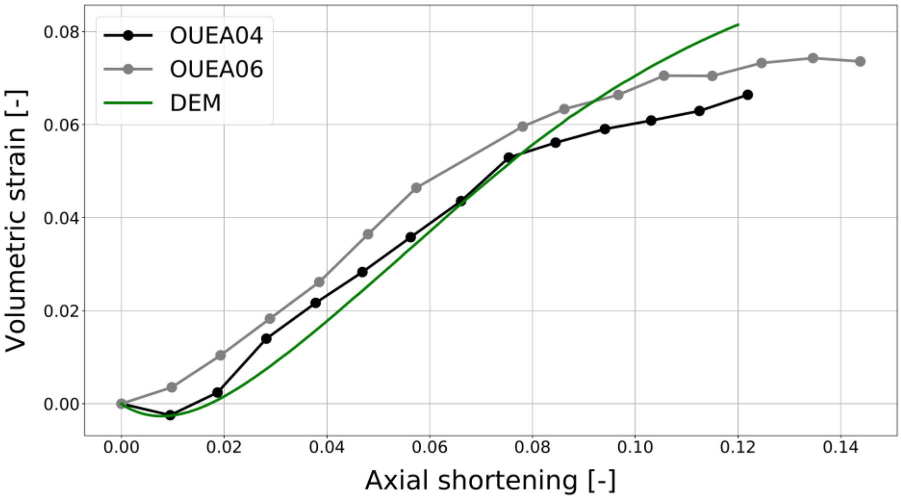

Figure 8.10: Comparison between the triaxial responses (100kPa confining pressure) of the experiments (specimens OUEA04 and OUEA06) and the numerical model (DEM) replicating Ottawa sand.

Ottawa sand at 300kPa

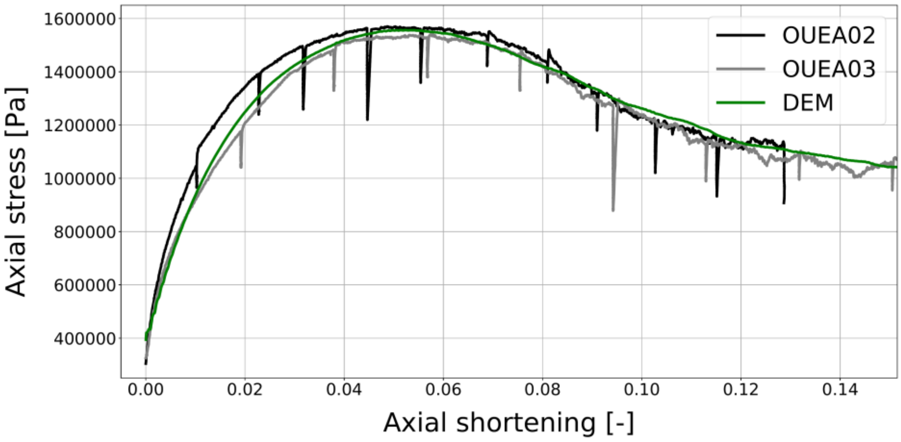

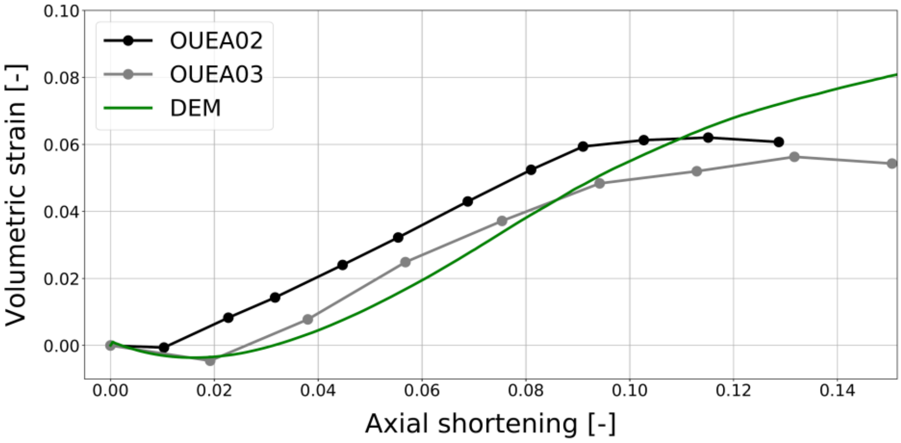

Figure 8.11: Comparison between the triaxial responses (300kPa confining pressure) of the experiments (specimens OUEA02 and OUEA03) and the numerical model (DEM) replicating Ottawa sand.

8.5.3 Validation 3: Triaxial tests on dense, medium and loose Ticino sand at 100-200-300 kPa

An additional validation of the proposed approach will be shown in Chapter 9.3 for Ticino sand, for which the 3D distribution of true sphericity is not known.

8.6 Comparison with rolling frictions from particles eccentricity

In this section, the values of rolling frictions obtained from Eq. (8.6) are compared to the ones computed using a completely different -geometrical- approach originally proposed by Wensrich & Katterfeld (2012) (Wensrich and Katterfeld, 2012) and then improved in (Wensrich et al., 2014). In particular, they claimed that rolling resistance is originated at the micro-scale level by the eccentricity of the contact, as shown in Figure 8.12.

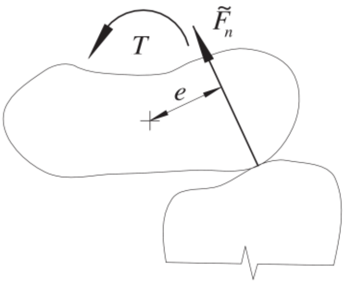

Figure 8.12: Contact of un-spherical particles producing a torque (T) due to the eccentricity (e) of the normal contact force (F_n) (Wensrich and Katterfeld, 2012)

Assuming the magnitude of the torque T at the contact equal to

$$|T| = e|F_n| \tag{8.8}$$

and being M^* the limiting value of from the contact model (Eq. 8.3), Wensrich & Katterfeld supposed that a good estimation of the rolling friction is obtained imposing $|T| = M^*$, that leads to

$$\mu_r = \frac{\langle e \rangle}{R_r} \tag{8.9}$$

where $\langle e \rangle$ is the average eccentricity of contact over all possible contacts and R_r is the rolling radius.

In this work, the values of μ_r are first computed using this approach for all the grains of HNEA01 and COEA04, and then compared with the values obtained from Eq. (8.6). The average eccentricity and the rolling radius of each grain are computed numerically exploiting the vertices of the surface mesh created by the Marching Cubes algorithm implemented in the Scikit-image python library (van der Walt et al., 2014). The comparison between the two approaches is shown in Figure 8.13.

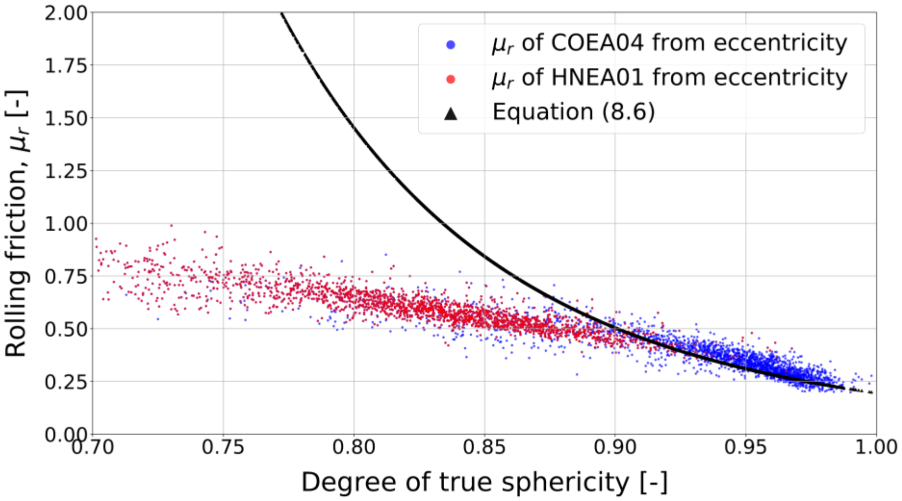

Figure 8.13: Rolling frictions of all particles involved in the simulation obtained from both eccentricity calculation and Equation 8.6. For high values of particle sphericity (i.e., ψ>0.90) the two approaches provide similar values.

It is evident from Figure 8.13 that both approaches provide values of rolling frictions that decrease with particle sphericity, as expected. It is somehow surprising that the two approaches, although conceptually completely different, provide similar rolling frictions values, especially at higher values of particle sphericity (*i.e.*, ψ>0.90). Both approaches suggest that even for very spherical grains, a coefficient of rolling friction of about 0.20 should be assigned. However, the results start diverging when the grains become more angular. It worth reminding that Eq. (8.6) has been design to match the experimental material responses. Therefore, if the rolling frictions from the eccentricity calculations are assigned in the DEM simulation, the numerical response is weaker than the experiments, especially for specimen HNEA01 as shown in Figure 8.14.

Hostun sand at 100kPa

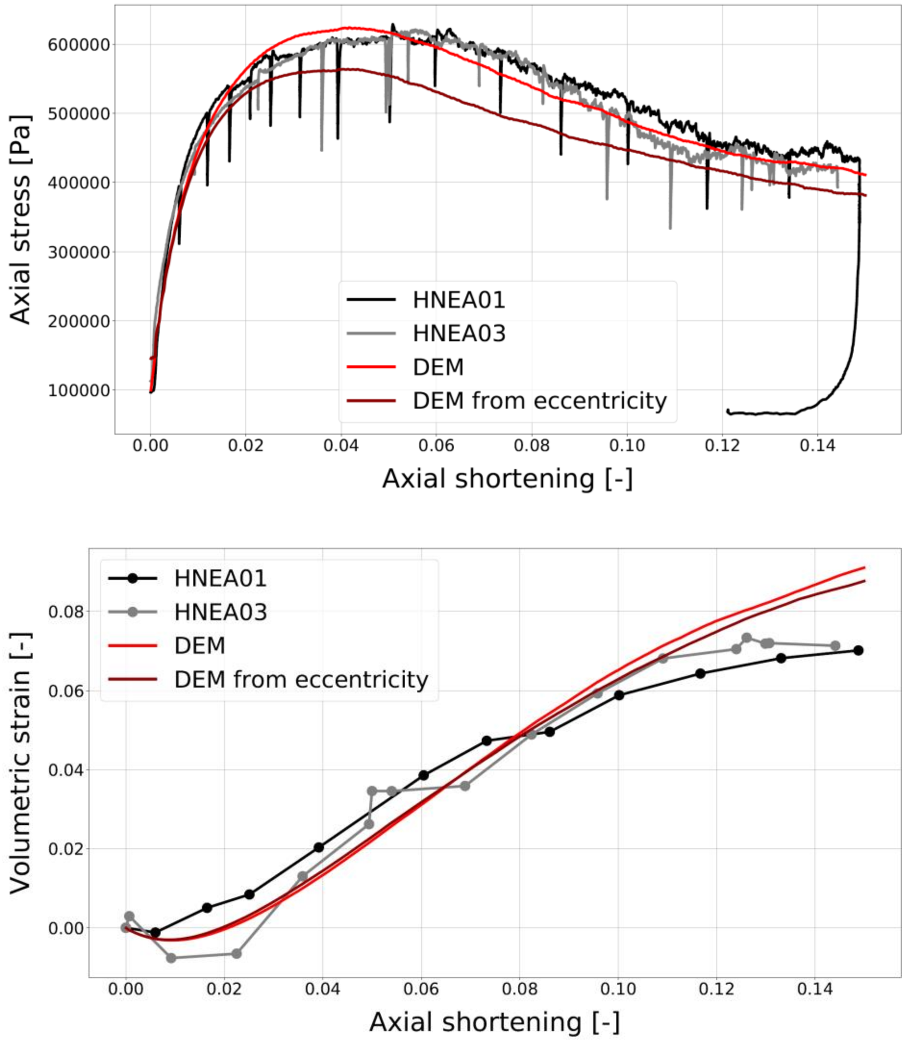

Figure 8.14: Comparison between the triaxial responses (100kPa confining pressure) of the experiments (specimens HNEA01 and HNEA03) and the numerical DEM models exploiting rolling resistance obtained from Eq. 8.6 (red curves) and from the eccentricity calculation (Eq. 8.9, dark red curves).

It means that the geometrical description of particle shape is not sufficient to capture all of the contributions provided by shape to the shearing material resistance. However, some other contributions (*e.g.*, grain interlocking, adhesion), which are not directly related to shape as a geometric property of one single particle, are somehow included in the proposed relationship described by Eq. (8.6).

8.7 Summary

A new DEM contact model exploiting rolling resistance to mimic the effects of particle shape has been described in this Chapter. The main concepts and findings are summarised hereafter:

- An innovative technique to relate univocally the *degree of true sphericity* of each grain with the *rolling friction* of its numerical counterpart is proposed;
- This approach has been calibrated to respect either the triaxial macro-mechanical responses (*i.e.,* stress-volumetric-strain) of Hostun and Caicos sands (at 100kPa) either the kinematics at failure (*i.e.,* the cumulated rotations in the shear bands);
- An extensive validation for different sands and different confining pressures has been made;
- If the statistical distribution of sphericity is known, either from experiments either from the literature, the resisting rolling moment is entirely determined since all the parameters involved in the contact model are known or predictable;
- Natural shape variability is automatically incorporated in the numerical samples;
- The contact detection remains economical and advanced algorithms are not required, maintaining low the computational time;
- If the initial numerical sample reproduces the experimental void ratio and PSD, the only crucial free parameter that must be determined by trial-and-error procedures is the inter-particle sliding friction coefficient.

9

Cone Penetration Test on a Virtual Calibration Chamber (VCC) using DEM

9.1 Introduction

The Cone Penetration Test (CPT) is the most popular type of *in-situ* test performed around the world, because it is fast, economical, and provide a continuous reading of soil parameters with stratigraphy. It consists in pushing a cylindrical steel rod (with a diameter of 35.6 mm) equipped with a cone probe into the ground at constant rate (2 cm/s). Electric sensors transmit the readings of the cone tip and shaft resistances that can be input in empirical relationships (calibrated in Calibration Chambers) to assess soil properties and parameters. Additional sensors can be used to measure pore water pressure (*i.e.,* piezocone), resistivity, and shear wave velocity among others.

Calibration Chambers (CC) are laboratory equipments capable of representing large-scale environmental conditions to run in situ geotechnical tests in the laboratory. The soil sample size is large enough and the boundary conditions are set so that the experimental laboratory results can be interpreted as if they were applied in-situ, as shown in Figure 9.1.

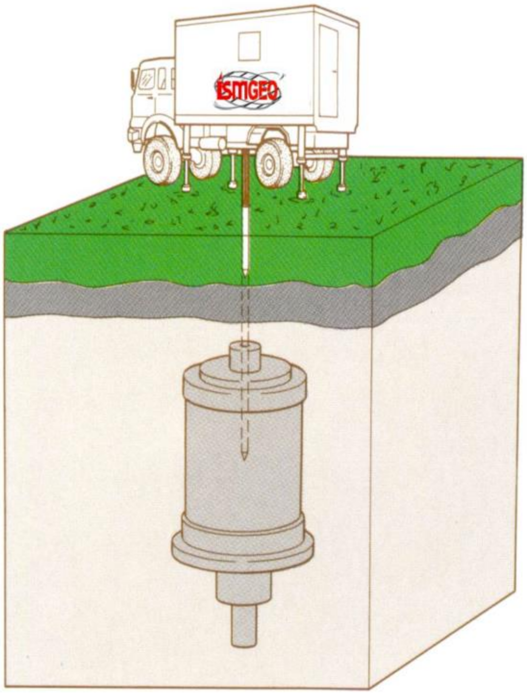

Figure 9.1: Purpose of calibration chambers (from ISMGEO website)

Calibration chambers are historically used to establish correlations between geotechnical parameters for CPT, for example to relate the penetration resistance with the relative density of the material tested (Ghionna and Jamiolkowski, 1991; Jamiolkowski et al., 1988), to develop new geotechnical instrumental tools, to test model piles, tie roads, and for many other applications.

The major disadvantage of testing soil in calibration chambers is that it is extremely expensive and time consuming. Not many calibration chambers have been built around the world, and each test requires the preparation of several tons of soil materials.

This Chapter describes how a Virtual Calibration Chamber (VCC) can be built using DEM to investigate efficiently the effect of chamber geometry, soil parameters and boundary conditions on the penetration resistance of CPT tests.

9.2 Previous work

A major contribution to the investigation of CPT tests performed in a virtual calibration chamber with DEM is given by Arroyo & Butlanska (Arroyo et al., 2011; Butlanska, 2014; Butlanska et al., 2014).

Butlanska (Butlanska, 2014) simulated a discrete material representing Ticino sand under different initial conditions (i.e. stress history, relative density, consolidation method) and different boundary conditions to (a) reproduce some experimental results, (b) investigate the effect of cone and chamber geometry, (c) explore the possibility of exploiting chamber radial symmetries.

The numerical results were compared to the experimental tests performed in the calibration chamber of ENEL-CRIS (Milan, Italy) and ISMES (Bergamo, Italy) by Jamiolkowski (Jamiolkowski et al., 2003, 1988), that is one of the largest testing campaigns ever performed on a calibration chamber. The ISMES calibration chamber is shown in Figure 9.2, as well as its cross-section geometry.

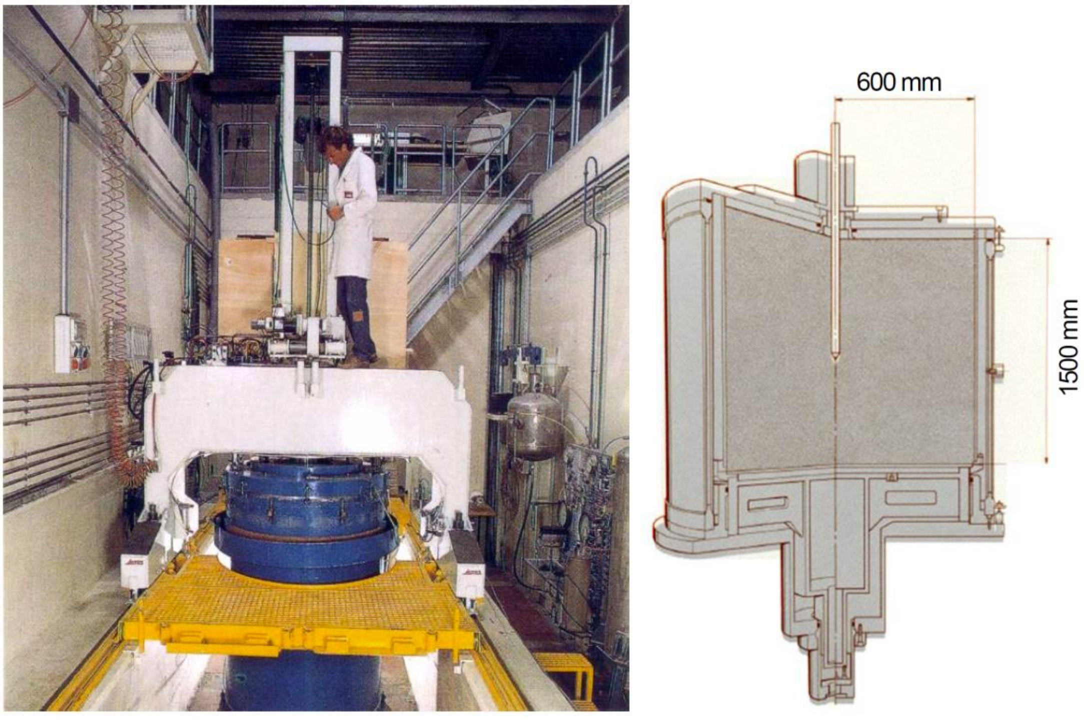

Figure 9.2: ISMES calibration chamber located in Bergamo (Italy) and its cross-section geometry.

The chamber height is 150cm and the diameter is 120cm. It can apply four types of boundary conditions (BC1, BC2, BC3, BC4) as schematically shown in Table 9.1 and Figure 9.3. The vertical stress is applied by a piston on the bottom boundary, whereas the top is fixed because of the presence of the cone. The lateral stress is applied by water pressure acting on the lateral membrane surrounding the soil specimen.

	Top and bottom boundary		**Lateral boundary**	
BC Name	Stress	Strain	Stress	Strain
BC1	const.	-	const.	-
BC2	-	0	-	0
BC3	const.	-	-	0
BC4	-	0	const.	-

Table 9.1: Boundary conditions that can be applied by the ISMES calibration chamber

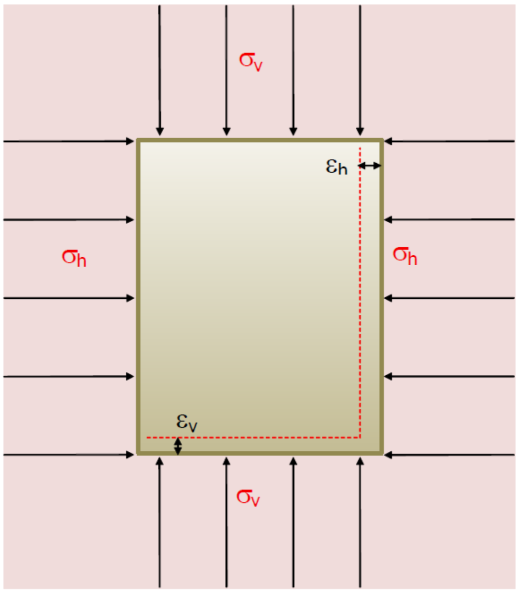

Figure 9.3: Representation of stresses and strains applied by the ISMES calibration chamber

The soil sample is prepared by pluvial deposition until the chamber is entirely filled, then it is left for 30 minutes at the target boundary conditions before starting penetrating. The Virtual CC build by Butlanska was shortened by a factor two compared to the ENEL chamber, while the diameter was kept of real size. The lateral walls were modelled as rigid and frictionless, while in the physical chamber was flexible, the stress boundary conditions were applied by a servo-controlled mechanism applied on the lateral cylindrical wall and on the top wall only, with the bottom wall fixed. This is in contrast with what was performed in the physical tests, where the top wall was fixed and the bottom one was moved by the piston.

The balls for the DEM simulations were generated with the radius expansion method inducing slightly denser specimens compared to the experiments, and the ball were scaled-up 50 times to have a reasonable number of spheres (about 60 thousands). The particles properties were calibrated by fitting the macroscopic triaxial responses of Ticino sand at 100kPa at medium relative density ($D_R = 75\%$) and then validated at 100-200-300kPa for three different relative densities ($D_R = 45\%, D_R = 75\%,\ D_R = 90\%$). Table 9.2 lists all the parameters of their VCC DEM simulations. In all the simulations, the ball rotations were inhibited to consider the angularity of the Ticino sand grains.

Parameter	Symbol	Value or relationship
Chamber sizes (height, diameter)	H_{VCC}, D_{VCC}	70cm, 120cm
Normal contact stiffness	k_n	$300MN/m \cdot 2.0\frac{D1\,D2}{D1+D2}$
Shear contact stiffness	k_s	$0.25\ k_n$
Inter-particle friction coefficient	μ_b	0.35 (19.3º)
Ball rotation		Inhibited
Local damping		0.1
Ball density	ρ	2500 kg/m^3
Ball size		$GSD \times 50$
Boundary conditions	BC	BC1 - BC3
Confining pressures	σ_v, σ_h	• $\sigma_v = 122kPa - \ \sigma_h = 54kPa$ • $\sigma_v = 212kPa - \ \sigma_h = 88kPa$ • $\sigma_v = 313kPa - \ \sigma_h = 133kPa$
Cone size	d_c	$d_{c,EXP} \times 2 = 71.2mm$
Penetration velocity	v_c	$v_{c,EXP} \times 5 = 10cm/s$
Cone tip	$\mu_{c,t}$	$\mu_{c,t} = \mu_b = 0.35$
Frictional cone sleeves (<100cm) *Frictionless cone sleeves (>100cm)*	$\mu_{c,s}$ $\mu_{c,s}$	$\mu_{c,s} = \mu_b = 0.35$ $\mu_{c,s} = 0$

Table 9.2: List of DEM properties and parameters used by Butlanska (Butlanska, 2014)

The cone size has been doubled compared to the physical test in order to guarantee a minimum number of contacts between the particles and the con tip of ten. Below this number, the penetration curves presented large oscillations that make impossible any comparison with physical curves. However, this changes the ratio $R_d = {}^{D_{VCC}}/_{d_c}$ (doubling it) which strongly affected the results, and required the application of difficult to calibrate size effect correction factors (Butlanska, 2014).

The results of the CPT DEM simulations are reported in Figure 9.4, Figure 9.5 and Figure 9.6 for different confining pressures and boundary conditions.

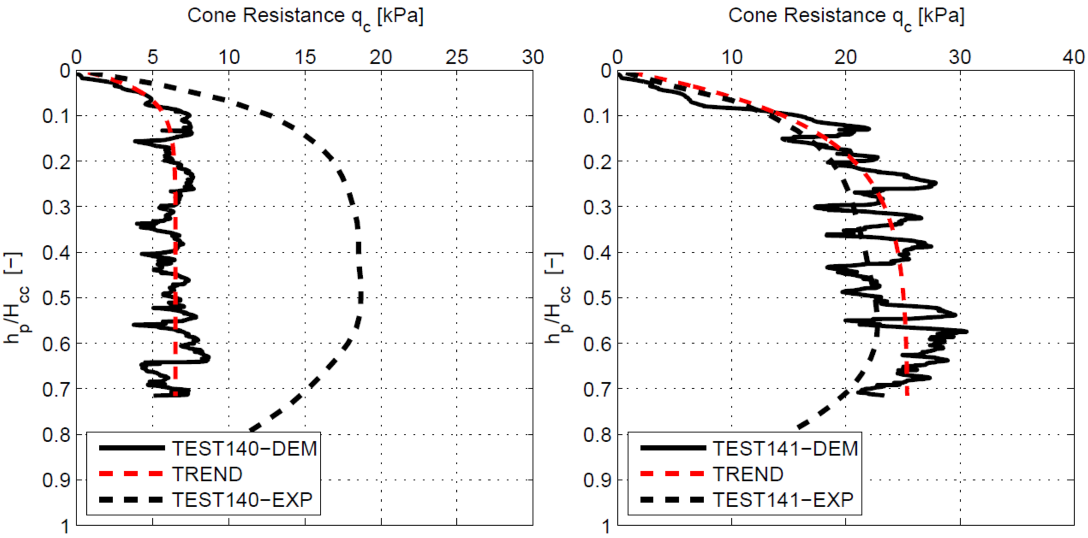

(a) T140, BC1 (b) T141, BC3

Figure 9.4: Comparison of raw experimental and numerical tip resistances for both BC1-BC3 boundary conditions at $\sigma_v = 122kPa,\ \sigma_h = 54kPa$ (Butlanska, 2014)

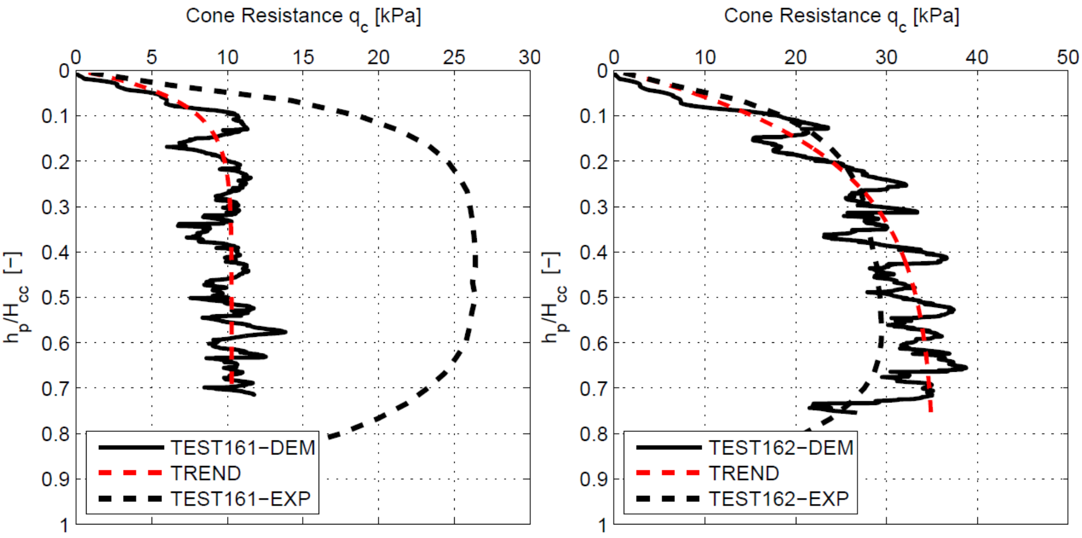

(a) T161, BC1 (b) T162, BC3

Figure 9.5: Comparison of raw experimental and numerical tip resistances for both BC1-BC3 boundary conditions at $\sigma_v = 212kPa,\ \sigma_h = 88kPa$ *(Butlanska, 2014)*

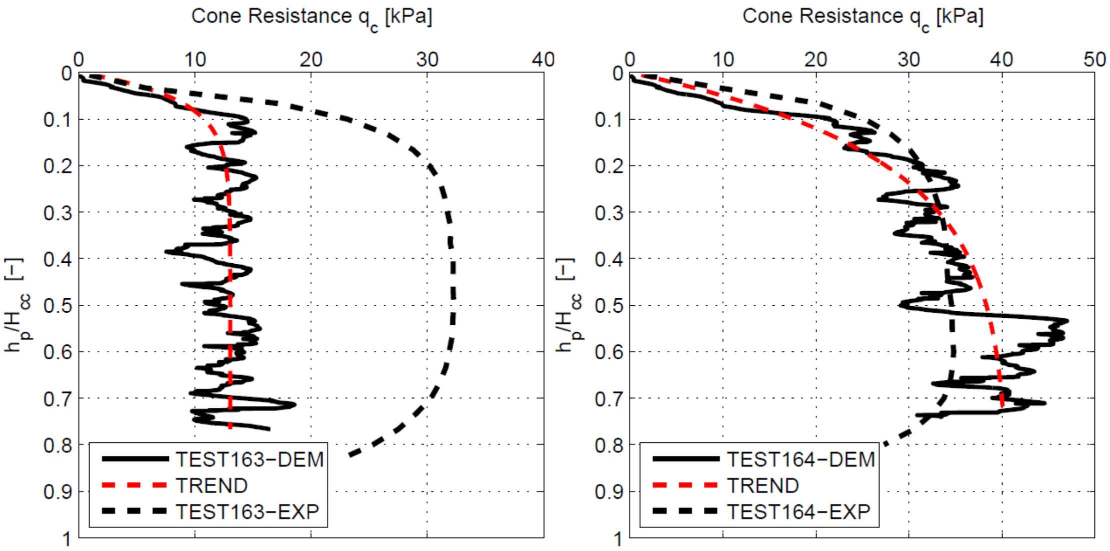

Figure 9.6: Comparison of raw experimental and numerical tip resistances for both BC1-BC3 boundary conditions at $\sigma_v = 313kPa,\ \sigma_h = 133kPa$ (Butlanska, 2014)

It is evident BC3 was well reproduced by Butlanska under all (anisotropic) confining pressures. However, for BC1, the numerical curves were found to be far below the experimental ones. This was due to the different ratio chamber to cone diameters (R_d) that strongly influences the results under BC1 conditions, and therefore a chamber size correction would need to be applied.

In the current work, the proposed rolling resistance approach is tested by recalibrating Ticino sand and simulating anew the calibration chamber tests. Moreover, a multi-scaling technique for particle sizes is proposed to avoid any change in the R_d ratio.

Falagush et al. (Falagush et al., 2015) studied with DEM the effect of particle shape and crushing on the penetration resistance of the CPT test, although they did not intend to reproduce experimental tests, but only to reproduce qualitatively the behaviour. They considered only 1/4 and 1/12 (*i.e.*, respectively 90° and 30°) of the entire calibration chamber to save computational time, exploiting the cylindrical symmetry of the problem. A similar approach was also tested by Butlanska (Butlanska, 2014) who however claimed the cylindrical symmetry is hard to be maintained. Several particle shapes were tested by Falagush et al. (2015) using clumps, who also tested freely and fixed rotating spheres. In addition, they created the initial chamber using different particle scales (dividing the chamber from 3 to 5 zones), in order to have finer particles near the cone tip but avoiding the migration of smaller particles into larger voids, as shown in Figure 9.7. They named this technique the particle refinement method.

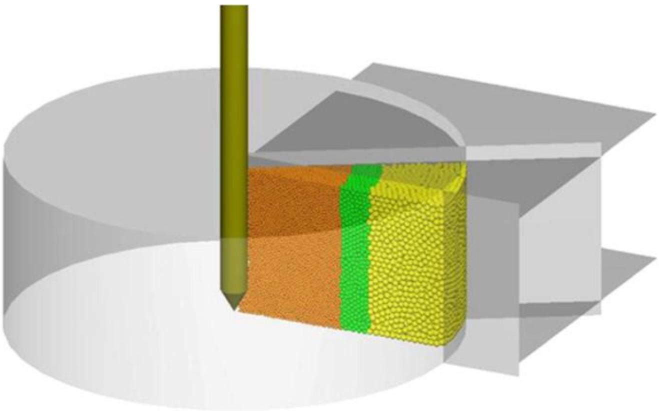

Figure 9.7: Virtual Calibration Chamber segment (30°) with three zones with different particle sizes (McDowell et al., 2012).

This multi-scaling approach was previously presented by the same research group in (McDowell et al., 2012). Prohibiting particle rotation was found to be the most influential factor on the tip resistance.

The particle refining method is still used nowadays by other researchers (e.g. (Sharif et al., 2019)) to achieve a fast generation of DEM samples, together with other methods as the Periodic Cell Replication Method (PCRM), proposed by Ciantia (Ciantia et al., 2018). An example of cell built using both methods together is shown in Figure 9.8.

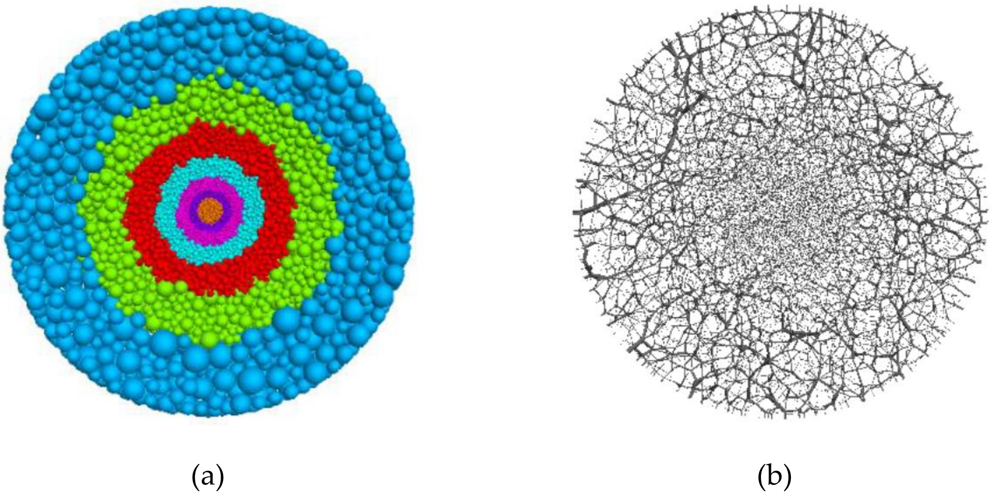

(a) (b)

Figure 9.8: Top view of the VCC built by Sharif et al., (2019) exploiting multiple particle scales (7 zones) and the PCRM method showing ball sizes (a) and contact forces (b). Images from (Sharif et al., 2019).

9.3 Microscopic calibration of DEM parameters: Drained triaxial test on Ticino sand

Ticino sand is a poorly graded medium-sized sand, with grains of medium angularity. The macroscopic responses of Ticino sand have been well reproduced with DEM by several researchers using unspherical particles (Gotteland et al., 2009) and with the assumption of fixed ball rotations (Arroyo et al., 2011; Butlanska et al., 2014; Calvetti, 2008). In this work Ticino sand is modelled using rolling resistance to mimic grain shape, exploiting the proposed relationship (Eq. 8.6). However, there are no tomographic images of this sand in the literature nowadays. Therefore, the statistical distribution of the 3D degree of true sphericity to be input in Eq. (8.6) was not available. Nevertheless, it is shown by (Rorato et al., 2019) that the 3D true sphericity present a high correlation coefficient with a 2D sphericity measure, *perimeter sphericity* (S_P), under the hypothesis of "oriented" particle projection, that means if the particle outline is obtained from a projection of the grain laying on their plane of greatest stability (i.e. perpendicularly to its minor length).

9.3.1 Acquisition of 2D perimeter sphericity from a table scanner (oriented projection) and determination of rolling friction from 2D sphericity

The simplest way to get a collection of perimeter sphericities under such "oriented" projection is to scan about four thousands of grains with a table scanner. Rorato et al. (2019) demonstrated that one thousand grains is the minimum sample size able to represent the population of sphericities of one sand specimen. The table scanner allows high-resolution parallel projection of each grain without parallax errors that can be made by a photograph. The table scanner used here has 1200 dpi, or equivalently about 20μm/pixel, which is only slightly above the 15μm voxel side used in the 3D μ-CT image acquisition for the other sands

After the scan is performed, the image is binarised, segmented and labelled using the open-source python package SPAM (Andò et al., 2017), as shown in Figure 9.9, and the 2D perimeter sphericity can be calculated for each grain label.

Original image (from scanner)	Labelled image

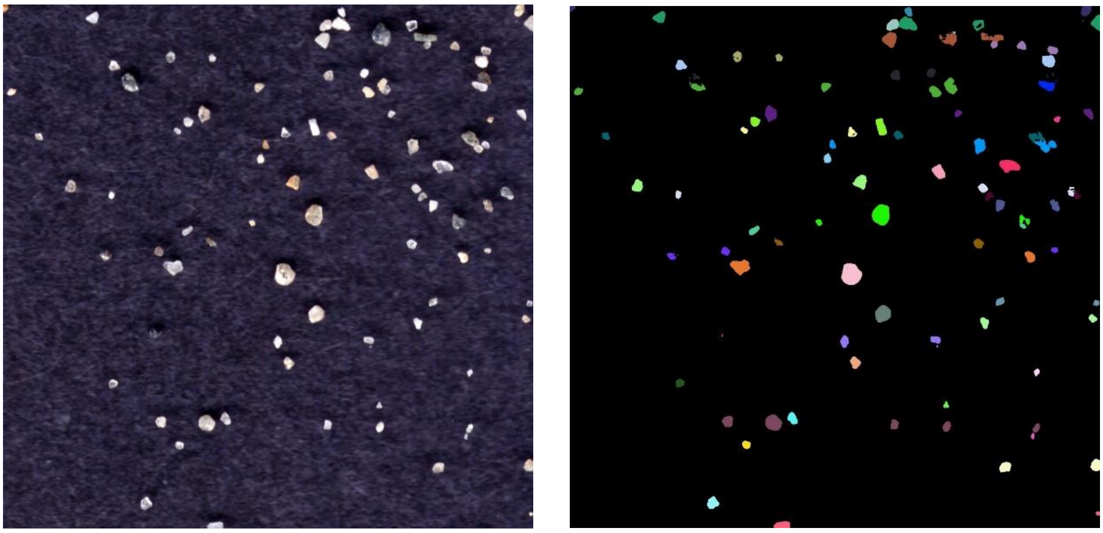

(a) (b)

Figure 9.9: Zoom on (a) the original scan and (b) the labelled image of Ticino sand.

Then, the Equation 6.6 (reported again below, for ease of reference) that relates the known 2D perimeter sphericity (S_P) and the 3D true sphericity (ψ) can be applied for each grain

$$\psi = 1.075(S_P) - 0.067 \tag{6.6}$$

and the statistical distribution of 3D true sphericity can be plotted as in Figure 9.10, together with the Hostun, Caicos and Ottawa ones for comparison.

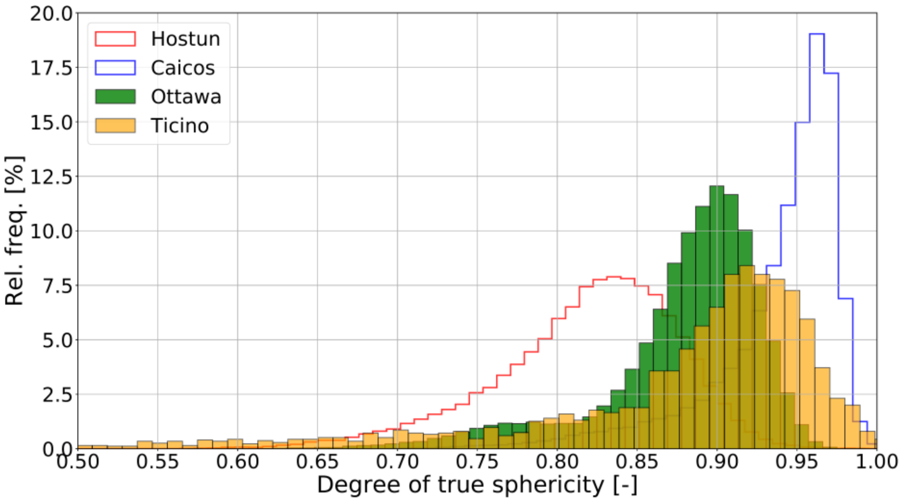

Figure 9.10: Statistical distributions of 3D true sphericity for Hostun, Caicos and Ticino sands.

As expected, the mean sphericity of Ticino sand is located between Hostun and Caicos sands, and it can be noted that the sample deviation is higher than the other sands, especially in the left-tail of sphericities.

9.3.2 Results at 100-200-300kPa confining pressures

It is now possible to run the DEM simulations, a total of nine triaxial tests are carried out and compared to the triaxial experiments performed on Ticino sand selected for the GEODIS project (2004-2005, involving 3SR Grenoble, LIRIGM Grenoble, Ecole Centrale de Lyon, LMGC Université de Montpellier, DIS Politecnico di Milano), as reported in (Calvetti, 2008). Again, the PSD and initial porosities are matched for all the dense ($D_R \cong 90\%$), medium ($D_R \cong 75\%$) and loose ($D_R \cong 45\%$) states, slightly different for each confining pressures (100, 200 and 300kPa).

The triaxial specimen used for the DEM simulations has the same geometry as the ones used for Caicos, Hostun and Ottawa sands, as indicated in Table 8.1, together with the properties and parameters employed in the DEM simulations. Particle sizes are kept equal to the real grains, so that about 16.000 balls are generated. The contact stiffness properties E_{mod} and k_{ratio} (i.e. k_n and k_s) are set respectively $4 \cdot 10^8$ Pa and 2.0 in order to fit the initial elastic part of the stress-strain mechanical curve.

Since the distribution of 3D true sphericity is now known, the rolling frictions are assigned to each sphere applying first Eq. (6.6) and then Eq. (8.6). The sliding friction coefficient (μ) is calibrated by trial-and-error using the case (100kPa confining, $D_R \cong 75\%$) and finally fixed to 0.60.

The mechanical responses (stress-strain-volumetric) of the nine DEM simulations (1 calibration, 8 predictions) and relative experiments (three relative densities tested at three confining pressures) are showed in Figure 9.11 ($D_R \cong 50\%$), Figure 9.12 ($D_R \cong 75\%$) and Figure 9.13 ($D_R \cong 90\%$).

The complete list of triaxial tests that are performed on Ticino sand is showed in Table 9.3.

Sand	**Specimen**	**Relative density (EXP)**	**Confining pressure**	**Initial porosity (EXP)**	**Initial porosity (DEM)**
-	-	$D_R(\%)$	(KPa)	$n_{0,exp}(\%)$	$n_{0,DEM}(\%)$
Ticino	TC1	47	109	43.5	44.1
Ticino	TC2	46	200	43.7	43.0
Ticino	TC3	41	300	44.1	43.8
Ticino	TC4	72	100	40.5	39.8
Ticino	TC5	74	200	40.3	39.7
Ticino	TC6	75	300	40.1	40.2
Ticino	TC7	90	100	38.2	38.2
Ticino	TC8	93	200	37.8	38.4
Ticino	TC9	93	300	37.8	37.6

Table 9.3: Drained triaxial compression tests performed on Ticino sand. The relative density and porosity of each experimental/numerical test are reported.

Loose state ($D_R \cong 50\%$)

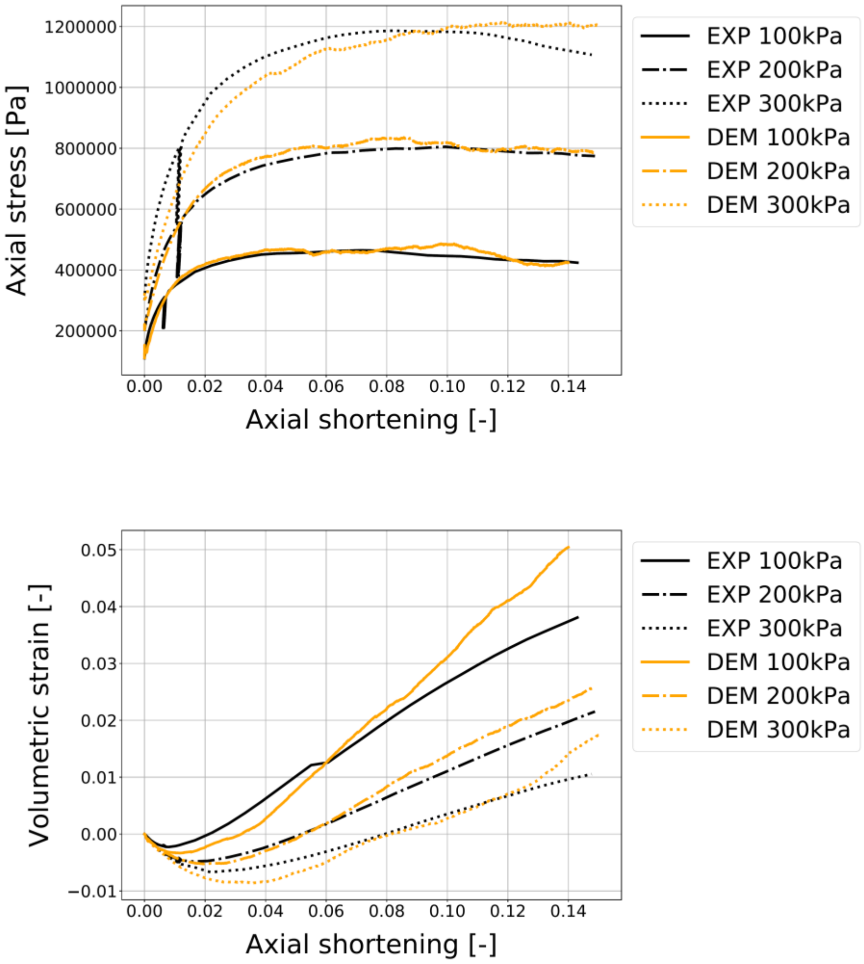

Figure 9.11: Triaxial responses of loose Ticino sand at 100-200-300kPa

Medium state ($D_R \cong 75\%$)

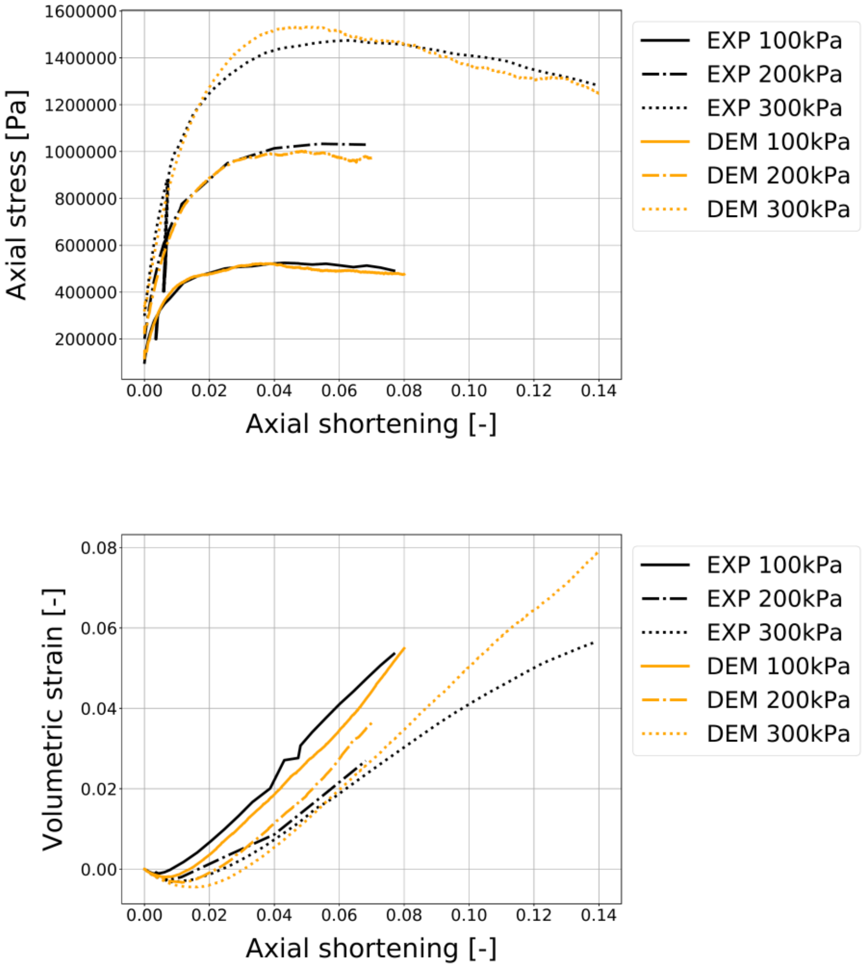

Figure 9.12: Triaxial responses of medium Ticino sand at 100-200-300kPa

Dense state ($D_R \cong 90\%$)

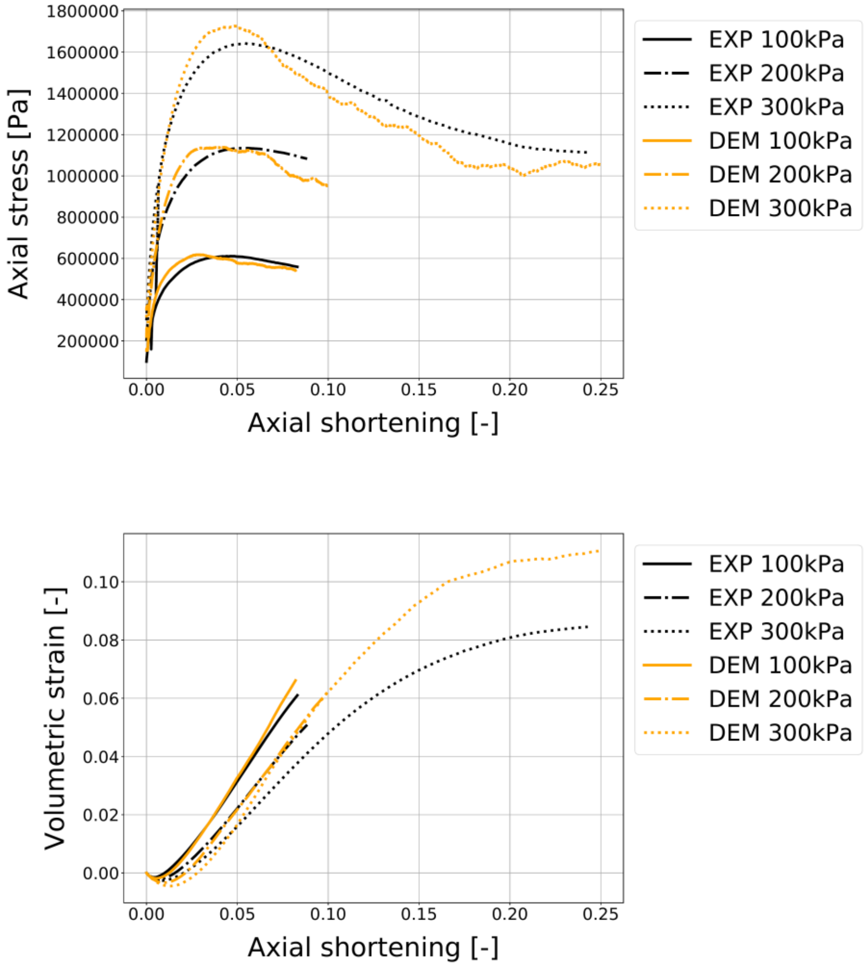

Figure 9.13: Triaxial responses of dense Ticino sand at 100-200-300kPa

It is evident that the triaxial response are well reproduced under all the stress and state conditions, confirming the reliability of the proposed approach exploiting rolling resistance to take into account the shape of particles (from 2D scans) efficiently. Very slight diversions can be seen for the DEM simulations at 300kPa but it must be mentioned that some particle crushing was found in the physical samples at the end of the tests, and crushing has not been modelled here.

9.4 DEM simulations of CPT tests in the ENEL-ISMES calibration chamber

This section describes a series of simulations aimed to reproduce several experimental CPT experiments performed at the geotechnical laboratories of ENEL-ISMES mentioned in Chapter 9.2. In particular, the aim here is to fit the macroscopic penetration curves obtained under low ($\sigma_v = 122kPa$, $\sigma_h = 54kPa$) and medium ($\sigma_v = 212kPa, \sigma_h = 88kPa$) confining pressure, under BC1 and BC3 boundary conditions. The high confinement case ($\sigma_v = 313kPa, \sigma_h = 133kPa$) is ignored because of particle crushing, that was present in the experiments but it is not modelled in the current DEM contact model. Including crushing in the model is feasible, as demonstrated in the work of Ciantia and co-workers (Ciantia et al., 2019a, 2015), but is out of the scope of this work.

9.4.1 Chamber & cone geometry and properties

The VCC chamber used here in shown in Figure 9.14. It consists in a rigid frictionless cylindrical wall with diameter equal to the physical chamber (*i.e.,* 120 cm) applying the target radial stresses by a servo-controlled mechanism. The top and bottom walls are flat and frictionless, placed at a distance of 100 cm. That means 50 cm shorter than the physical chamber, to limit computational expense. As in the experimental tests the top platen is fixed and is penetrated by the cone, whereas the bottom platen is servo-controlled.
The cone is designed to have the same size of the experiment, so that the ratio $R_d = {}^{D_{VCC}}/_{d_c}$, that strongly affects the results as evidenced by Butlanska, can be maintained equal to that of the physical chamber.
As in the experimental tests, the cone diameter is set to 35.6mm, the cone tip and the first 150cm of cone shaft are frictional ($\mu_{c,t} = \mu_{c,s} = 0.60$), and the rest of the shaft is frictionless ($\mu_{c,s} = 0$). The cone is pushed from the top at a constant vertical speed of 10cm/s, which is five times higher than in the physical test. This penetration velocity is equivalent to that used by Butlanska (Butlanska, 2014) and below the value chosen by other

researchers (Ciantia et al., 2019b; Falagush et al., 2015; Tran et al., 2016), who claimed that dynamic effects are only relevant for penetration velocities above 100cm/s.

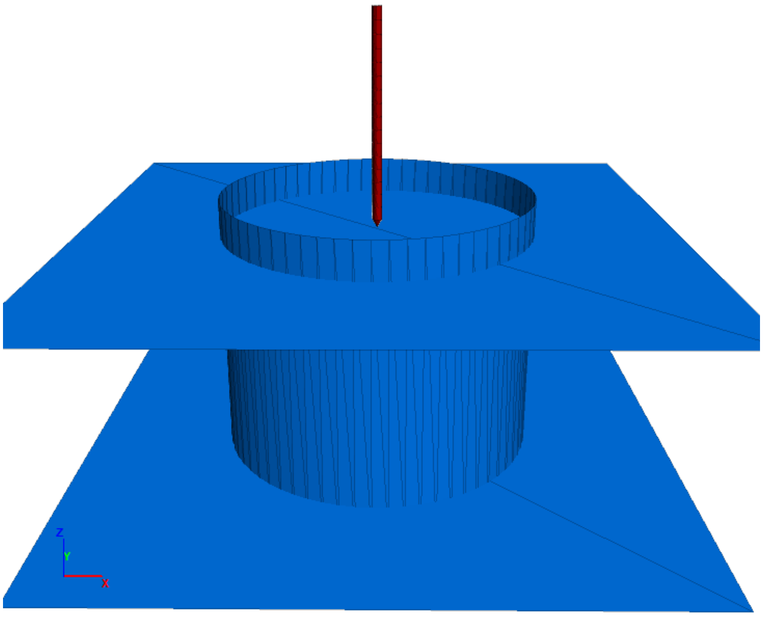

Figure 9.14: DEM-VCC model reconstruction

9.4.2 Multiscaling approach for particle size of Ticino sand

The number of contacts between the cone tip and the particles has a paramount importance. Indeed, as reported by Butlanska (Butlanska, 2014), a minimum number of ten (>10) is needed to avoid large oscillations in the penetration curve. On the other hand, it is known that the number of elements in DEM simulations strongly affects the computational time, and that it is impossible to reproduce the real PSD of a soil without scaling-up the particles. Arroyo (Arroyo et al., 2011) scaled up the Ticino sand granulometry by 50 to have a reasonable number of balls but also doubled the cone diameter to guarantee a minimum number of contacts of 10. However, this changed the ratio $R_d = {}^{D_{VCC}}/_{d_c}$, thus affecting the results.

In this work, this problem is tackled with a different approach. In order to (a) maintain the ratio chamber to cone diameters (R_d) equal to the physical specimen (b) guarantee a minimum number of contacts between cone and particles of ten, and (c) have a reasonable number of particles, it is necessary to adopt a multi-scaling technique (see Chapter 9.2) for the ball sizes. In particular, the Ticino PSD of the particles located near the cone tip have been multiplied by a scaling factor of 25. This is half of the scaling factor used by Butlanska.

One uniform scaling factor of 25 throughout all the VCC would generates about 1.74×10^6 of particles, as obtained (see detail in Appendix C) by exploiting the equation proposed by Arroyo et al. (Arroyo et al., 2011). Simulation with such a large number of particles is possible but slow and unpractical –without access to large-scale computing facilities.

Therefore, two other scaling factors (50 and 90) are introduced moving away from the cone axis (respectively at the radial distances of 0.075m and 0.20m from the cone axis). The scaling factor of 90 is chosen to generate a reasonable number of particles (about 40.000) and the factor of 50 is set to avoid inter-particle penetrations between the fine/coarse zones. Figure 9.15 shows the results of this multi-scaling approach.

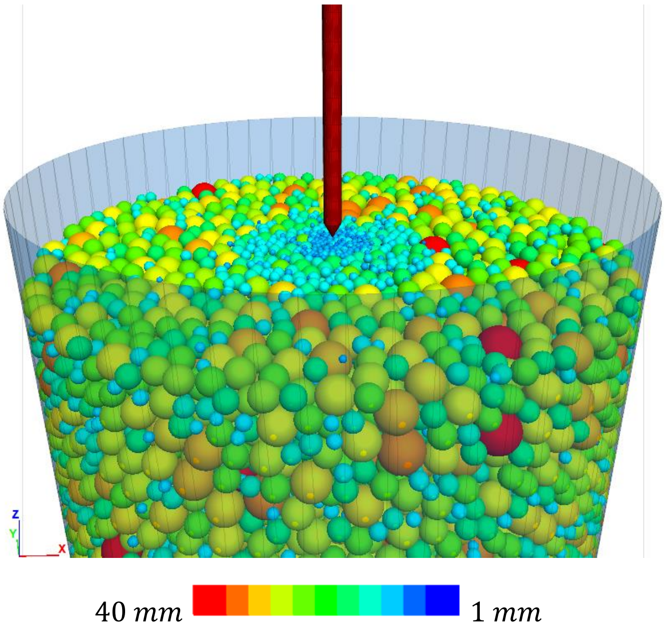

(a)

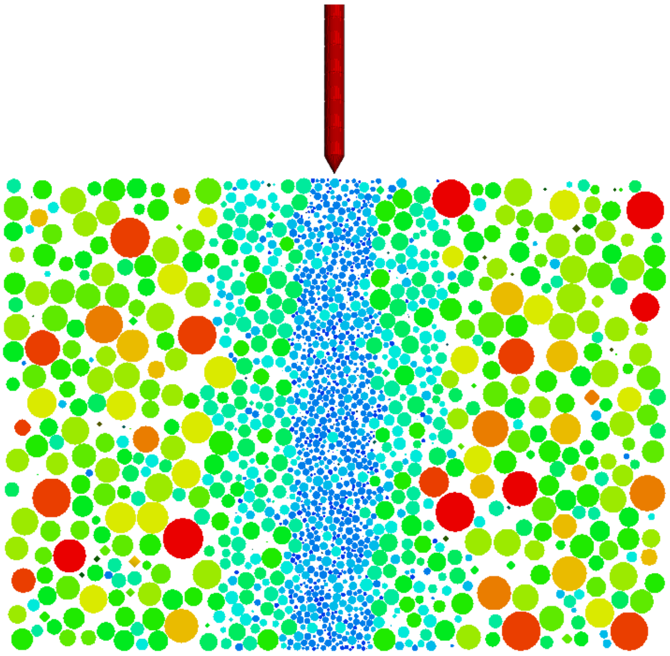

(b)

Figure 9.15: Visualisations of the multi-scaling technique for particle sizes in 3D (a) and 2D, from a vertical slice (b). The particles located closer to the VCC vertical axis are smaller compared to the others. The balls are coloured by the value of their radii.

The properties and parameters regarding the balls used in the DEM simulations were calibrated for Ticino sand in Chapter 9.3.

Figure 9.16 shows the contact distribution at the end of the anisotropic compression at $\sigma_v = 122kPa,\ \sigma_h = 54kPa$. It is evident that contact forces are homogenously distributed and the specimen can be considered well equilibrated. Obviously, the zone near the cone present many weaker forces because of the smaller scale factor applied to ball sizes. This can be also observed from Figure 9.17 showing the cumulative density function of normal contact forces for the tree zones with different ball scaling factors. The forces are normalised by the mean value (for each zone). About 62% of the normal forces are below the mean, therefore the majority of contact forces can be considered weak. Similar considerations were found in (Radjai et al., 1999). The probability density distributions (after normalisation) are very similar for the three zones, confirming the homogenous forces distribution within the entire numerical sample.

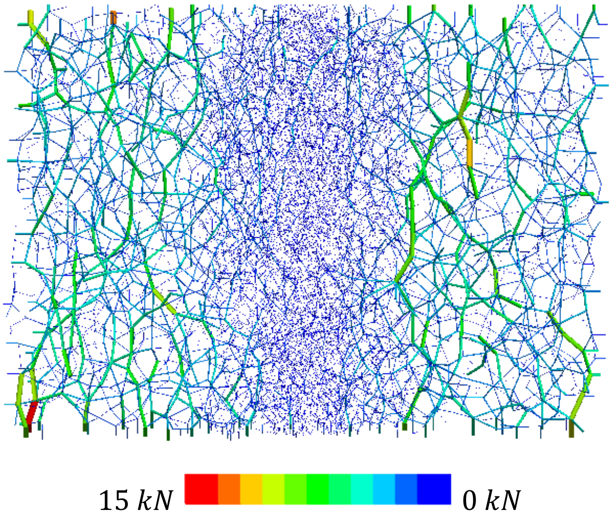

Figure 9.16: Contact network at the initial anisotropic state ($\sigma_v = 122kPa,\ \sigma_h = 54kPa$)

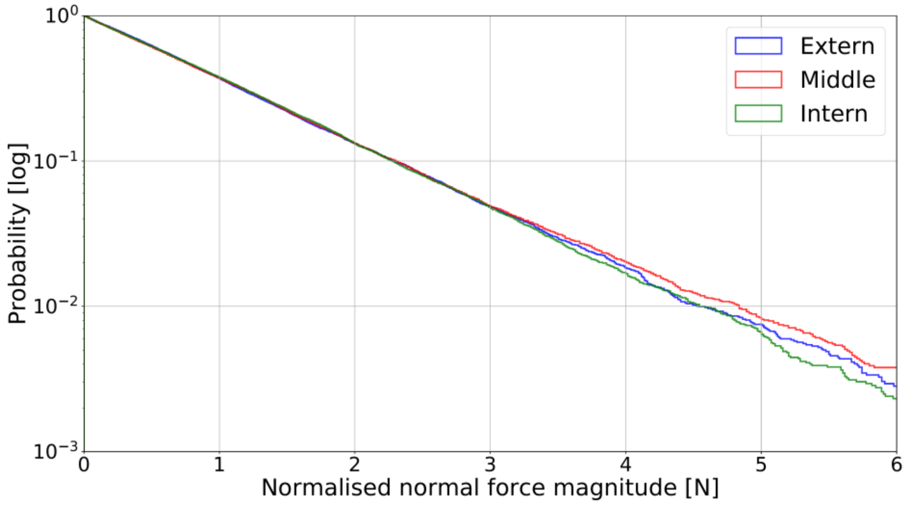

Figure 9.17: Cumulative density functions (in log scale) of the normal contact forces in the three zones with different ball scaling factors. Normal forces are normalised with respect to the mean force.

9.4.3 Comparison of macro-responses with physical dataset of Ticino sand

Table 9.4 summarises all the properties and parameters used in the CPTs performed in this VCC.

Parameter	**Symbol**	**Value or relationship**
Chamber sizes (height, diameter)	H_{VCC}, D_{VCC}	100cm, 120cm
Effective normal contact stiffness	E_{mod}	$4.0\ \cdot 10^{8}$ Pa
Normal-to-shear stiffness ratio	k_{ratio}	2.0
Inter-particle friction coefficient	μ_b	0.60 (calibrated)
Wall friction	μ_w	0.0 (frictionless)
Degree of true sphericity	ψ	Distributions know from 2D scans
Rolling friction coefficients	μ_r	$\mu_r = 0.1963(\psi)^{-8.982}$ (Eq. 8.6)
Rolling stiffness	k_r	$k_s R$ (Eq. 8.1)
Local damping		0.7
Ball density	ρ	2500 kg/m3
Ball size (GSD of Ticino sand)	GSD	$GSD \times 90$ (coarse, far from the cone) $GSD \times 50$ (in between coarse/fine) $GSD \times 25$ (fine, near the cone)
Boundary conditions	BC	BC1 - BC3
Confining pressures	σ_v, σ_h	• $\sigma_v = 122kPa - \ \sigma_h = 54kPa$ • $\sigma_v = 212kPa - \ \sigma_h = 88kPa$
Initial relative density (initial porosity, DEM)	D_R (n_0)	$D_R \cong 90\%$ $(n_0 = 0.375)$
Cone size	d_c	$d_{c,EXP} \times 1 = 35.6mm$
Cone stiffness	k_n, k_s	$k_n = k_s = 3 \cdot 10^{6} N/m$
Penetration velocity	v_c	$v_{c,EXP} \times 5 = 10cm/s$
Cone tip friction coefficient	$\mu_{c,t}$	$\mu_{c,t} = \mu_b = 0.60$

Frictional cone sleeves (<150cm) Frictionless cone sleeves (>150cm)	$\mu_{c,s}$ $\mu_{c,s}$	$\mu_{c,s} = \mu_b = 0.60$ $\mu_{c,s} = 0$

Table 9.4: List of DEM properties and parameters used for the DEM-VCC CPT tests in this work

The comparisons between the experimental and numerical penetration curves are shown in Figure 9.18 for both confinements ($\sigma_v = 122kPa - \sigma_h = 54kPa$ and $\sigma_v = 213kPa - \sigma_h = 88kPa$) and both boundary conditions (BC1 and BC3).

A steady-state cone resistance is also reported together with the numerical responses in order to filter out the oscillations. It has been obtained by applying the following expression:

$$q_{c,fit}(x) = a(1 - e^{-b \cdot x}) \tag{9.1}$$

in which a, b are fitting parameters (that need be computed by an optimization procedure) governing the shape of the fitting curve, x is the independent variable (the penetration depth in our case) and $q_{c,fit}(x)$ is the dependent variable (*i.e.,* the value of tip resistance). The best fitting parameters are reported in Table 9.5, for the four cases.

Case	$\boldsymbol{a}$ $[\boldsymbol{MPa}]$	$\boldsymbol{b}$ $[-]$	$\boldsymbol{R^2}$	$\boldsymbol{q_{c,exp}}$ $[\boldsymbol{MPa}]$
BC1 ($\sigma_v = 122kPa - \sigma_h = 54kPa$)	18.36	29.71	0.35	18.68
BC3 ($\sigma_v = 122kPa - \sigma_h = 54kPa$)	19.50	23.27	0.21	22.42
BC1 ($\sigma_v = 213kPa - \sigma_h = 88kPa$)	22.84	34.32	0.49	25.11
BC3 ($\sigma_v = 213kPa - \sigma_h = 88kPa$)	27.32	21.69	0.47	29.04

Table 9.5: Best fitting parameters for the numerical penetration curves. The representative values of $q_{c,exp}$ were selected at 50% of the total penetration depths.

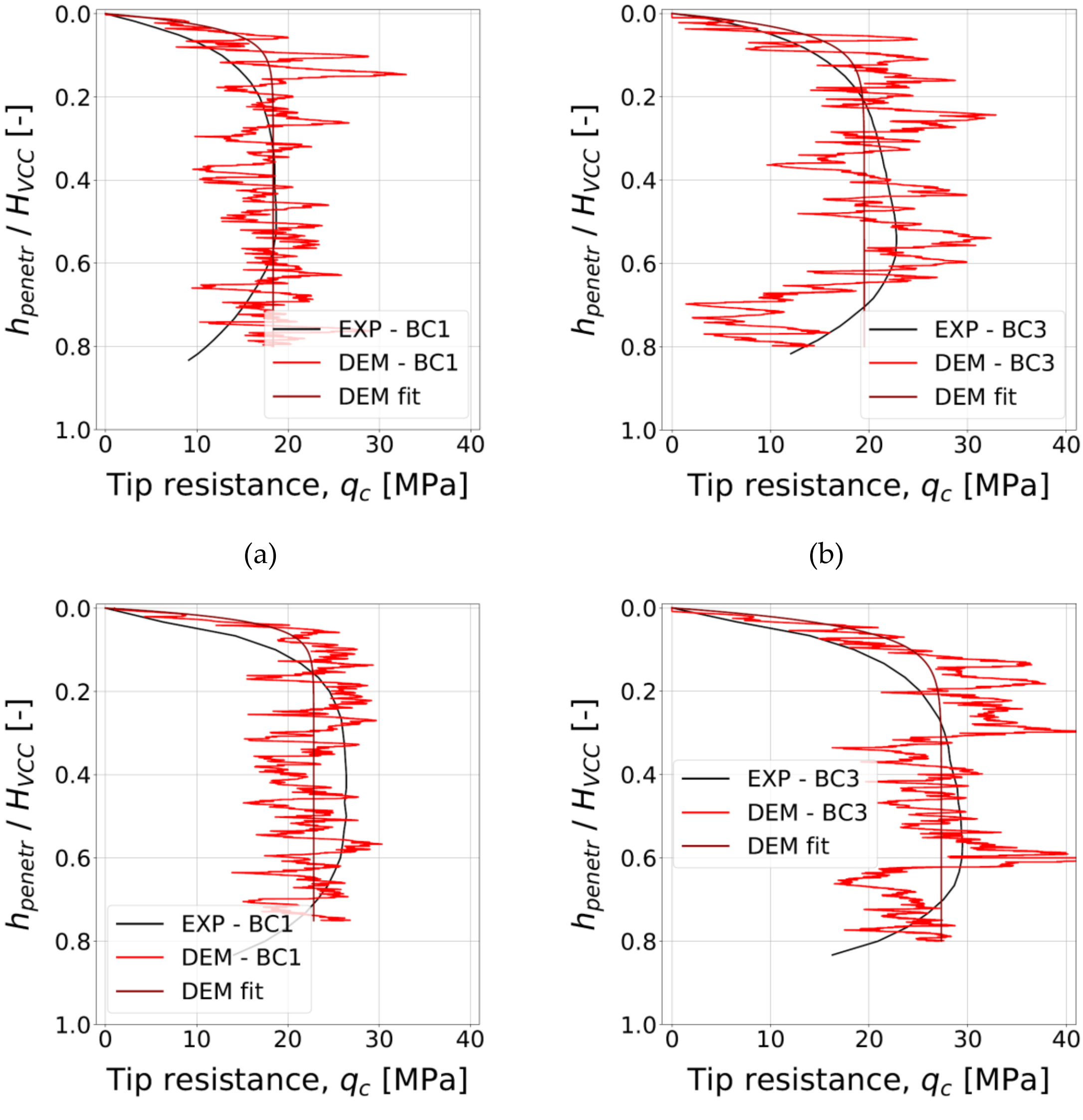

(a) (b)

(c) (d)

Figure 9.18: Comparison of raw experimental and numerical tip resistances (with fitting curves) respectively at 121-54kPa confinement for BC1 (a) and BC3 (b) and at 212-88kPa for BC1 (c) and BC3 (d)

The DEM tip penetration curves compares well with the experimental counterparts, as showed in Figure 9.18. A slight discrepancy can be seen in the first 20 centimetres of penetration, in which the numerical curves tend to reach earlier a steady-state value (*i.e.,* the fitting parameter a of Eq. 9.1).

Figure 9.19a-b show respectively the cumulated ball rotations and the contact forces measured at a penetration depth of 40 cm.

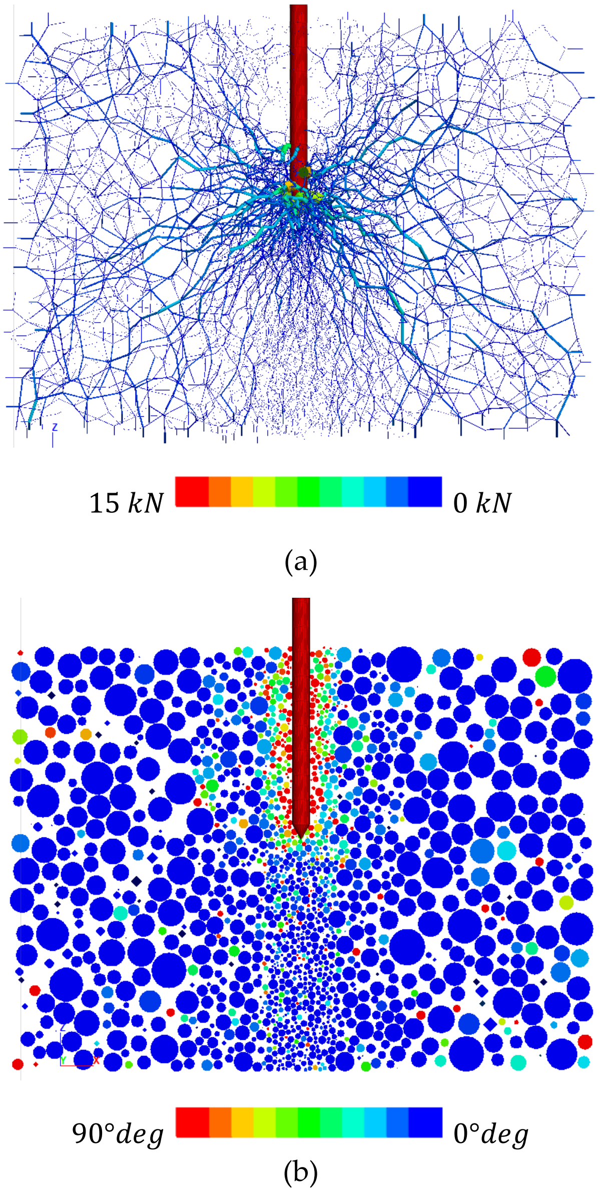

Figure 9.19: Contact force network (a) and ball rotations (b) during cone penetration ($h_{penet} = 40cm$)

9.5 Effect of particle shape on penetration resistance: parametric study

This chapter investigates the influence of particle shape (i.e., rolling resistance) on the penetration resistance during cone penetration testing. The combined effect of the inter-particle sliding friction coefficient (μ_b), the rolling friction coefficient (μ_r) and the coefficients of friction at the interface between the frictional cone ($\mu_{c,t}$ and $\mu_{c,s}$) and the particles, is examined through a parametric study.

9.5.1 Model properties

The granular material simulated in this parametric study is similar to the one used to simulate the Ticino sand experiments, reported in the previous section. In particular, the experimental PSD of Ticino sand is reproduced making use of three different scaling factors for particle size (90 – 50 – 25), with finer particles near the cone tip. The target relative density achieved in the numerical sample is 90%, therefore it can be classified as dense. The balls properties are the same as listed in Table 9.4 above.

The calibration chamber is slightly shorter than the one created in Chapter 9.4 to save computational time. In particular, the diameter is 120cm and the height is 70cm, as the one used by Arroyo & Butlanska (Arroyo et al., 2011; Butlanska, 2014). The cone is of standard size, with a diameter of 35.6mm. The penetration velocity is set to 10cm/s. The boundary conditions is BC1 type (isotropic) with a confining pressure of 100kPa, applied on both radial and top/bottom walls.

Three different situations are considered regarding the coefficient of sliding friction, as reported in Table 9.6 below.

Friction coefficient	**Case A**	**Case B**	**Case C**
μ_b (ball-ball)	0.60	0.30	0.60
$\mu_{c,t}$ (ball-cone tip)	0.60	0.30	0.30
$\mu_{c,s}$ (ball-shaft)	0.60	0.30	0.30

Table 9.6: Cases of study. Three different situations of frictions ball-ball, ball-tip, ball-shaft are considered in the parametric study.

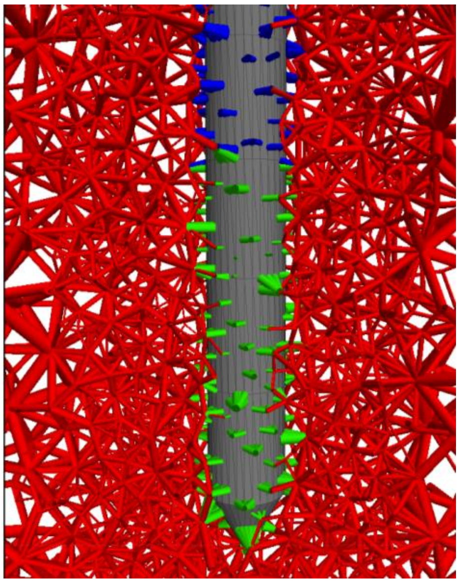

Figure 9.20: Contact visualisation near the cone tip for case **C**. *Contacts are coloured by the value of their friction coefficient (red=0.60, blue=0.0, green=0.30).*

Two inter-particle friction coefficients are considered, 0.60 and 0.30. The potential friction existing between particles and cone is assumed equal to the inter-particle friction in cases **A** ($\mu_b = \mu_{c,t} = \mu_{c,s} = 0.60$) and **B** ($\mu_b = \mu_{c,t} = \mu_{c,s} = 0.30$), whereas in case **C** they differ ($\mu_b = 0.60 - \mu_{c,t} = \mu_{c,s} = 0.30$), to consider the potential lower friction existing between the soil grains and the metallic cone, as shown in Figure 9.20.

For each of the three cases, different values of rolling frictions are applied to mimic the effect of particle shape. In particular, six different situations are investigated, according to Table 9.7.

In Series 1, particles are left completely free to rotate, as to simulate perfect smooth spheres, this scenario can be obtained in our contact model simply setting $\mu_r = 0.0$. Series 2 is conceptually opposite to Series 1, the rotations of particles is completely inhibited, this approach is used by several researches to approximately take into account the shape effects of very angular sand types.

Series 3 exploits the proposed Equation (8.6) to determine the coefficient of rolling friction for each contact based on grain sphericity. For a uniform shaped specimen, comprised of perfect spheres ($\psi = 1.0$), it assumes a single value of $\mu_r = 0.1963$, valid for all the contacts. Similarly, Series 4 exploits Eq. (8.6) to obtain the rolling frictions to apply at each contact formed between cubic shaped ($\psi = 0.806$) particles, leading to a single very high value of $\mu_r = 1.3621$ for all contacts.

Series 5 and 6 introduce the concept of shape variability within the soil sample. In particular, a coefficient of variation (ratio between the sample standard deviation and mean) of 0.07, that is a realistic value for physical sands (see Chapter 6.3) is introduced in both shape distributions.

Regarding Series 5, a Normal ($\mathbb{N}$) distribution of sphericities is artificially generated as $\mathbb{N}(\psi, \sigma) = \mathbb{N}(1.0, 0.07)$, being σ the standard deviation obtained as $\sigma = CV \cdot mean = 0.07 \cdot 1.00 = 0.07$. However, this shape distribution would assume values greater than one that is the upper limit of ψ, therefore the whole right tail is truncated and the final shape distribution is half Gaussian.

Similar considerations can be done for Series 6, the artificial shape distribution is Normal and is defined as $\mathbb{N}(\psi, \sigma) = \mathbb{N}(0.806, 0.056)$, being the standard deviation obtained as $\sigma = CV \cdot mean = 0.07 \cdot 0.806 = 0.056$. Again, truncation is applied to avoid values above 1, although in this case only few extreme right-tail values are affected.

Series	**Friction case**	**Particle shape**	**Rolling condition at contacts**
1	**A – B – C**	Perfect smooth spheres	Free rotations, $\mu_r = 0.0$
2	**A – B – C**	Iper-angular	Fixed rotations, $\mu_r = \infty$
3	**A – B – C**	$\psi = 1.0$ (sphere)	$\mu_r = 0.1963$
4	**A – B – C**	$\psi = 0.806$ (cube)	$\mu_r = 1.3621$
5	**A – B – C**	$\psi = 1.0 - \sigma$ (half gaussian, truncated at 1.0)	μ_r = distribution below 0.1963
6	**A – B – C**	$\psi = 0.806 \pm \sigma$ (gaussian, truncated at 1.0)	μ_r = distribution around 1.3621

Table 9.7: Scenarios that are considered for the parametric study of particle shape effects

The histograms of the assigned distributions of sphericities for Series 5 and Series 6 are respectively shown in Figure 9.21a and Figure 9.21b. The histograms of the rolling frictions distributed for each particle, after applying Eq. (8.6), are reported in Figure 9.21c (Series 5) and Figure 9.21d (Series 6).

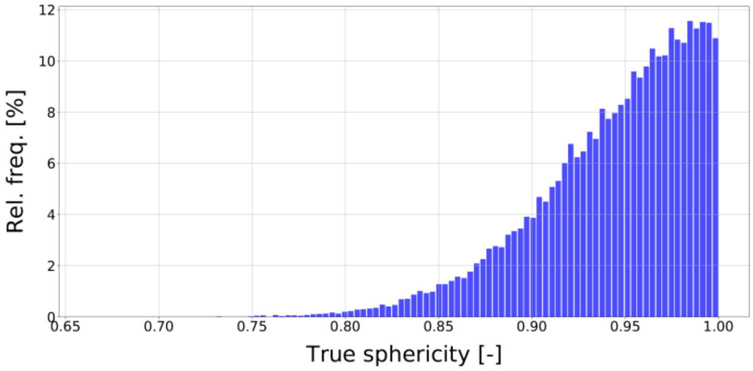

(a)

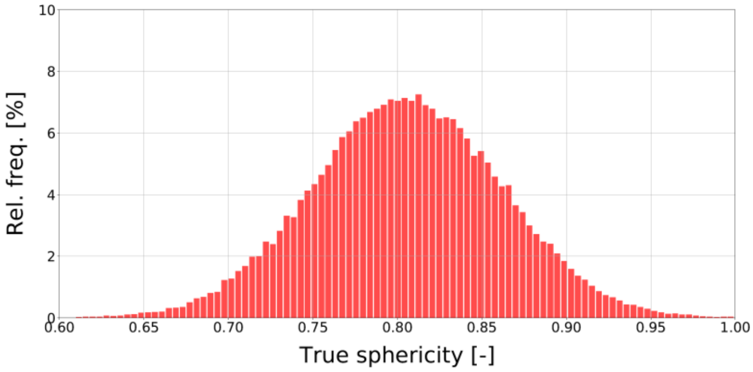

(b)

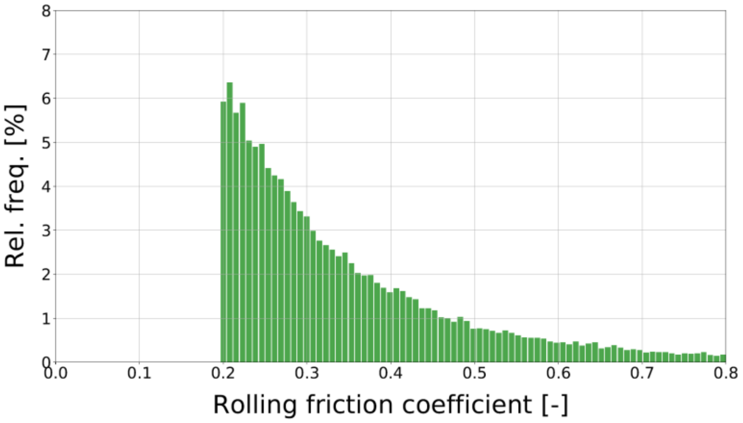

(c)

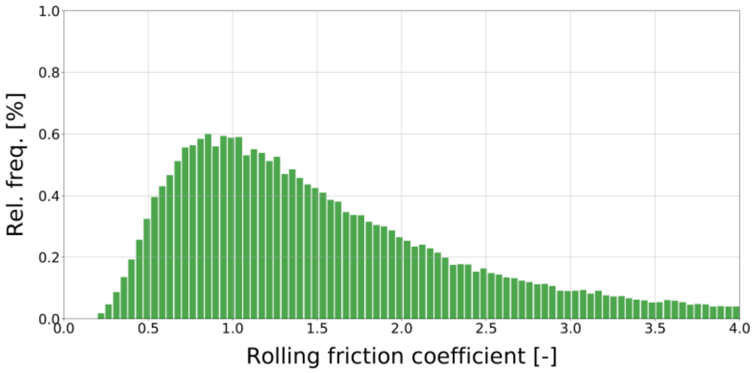

(d)

Figure 9.21: Assigned values of true sphericity for Series 5 (a) and Series 6 (b) and resulting rolling frictions for Series 5 (c) and Series 6 (d)

9.5.2 Results

The results of cases **A, B, C** for all Series 1 – 6, for both tip and shaft resistance, are shown in Figure 9.22a-f. It is reminded (Table 9.6) that the inter-particle friction is set 0.60 for both cases **A** and **C.** They differ from each other in the “roughness” of the cone-particles contacts. In the first case (case **A**) it is set equal to the particles (*i.e.*, 0.60) in the latter (case **C**) it is set 0.30, to imitate the smoother contact between the steel cone tip and the granular material. Regarding case **B**, both particle-particle and cone-particle frictions are set equal to 0.30.

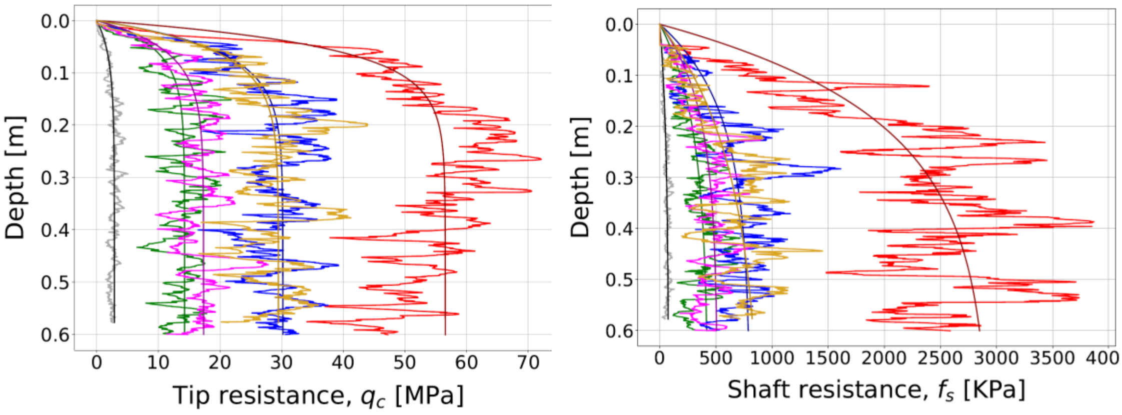

(a) (b)

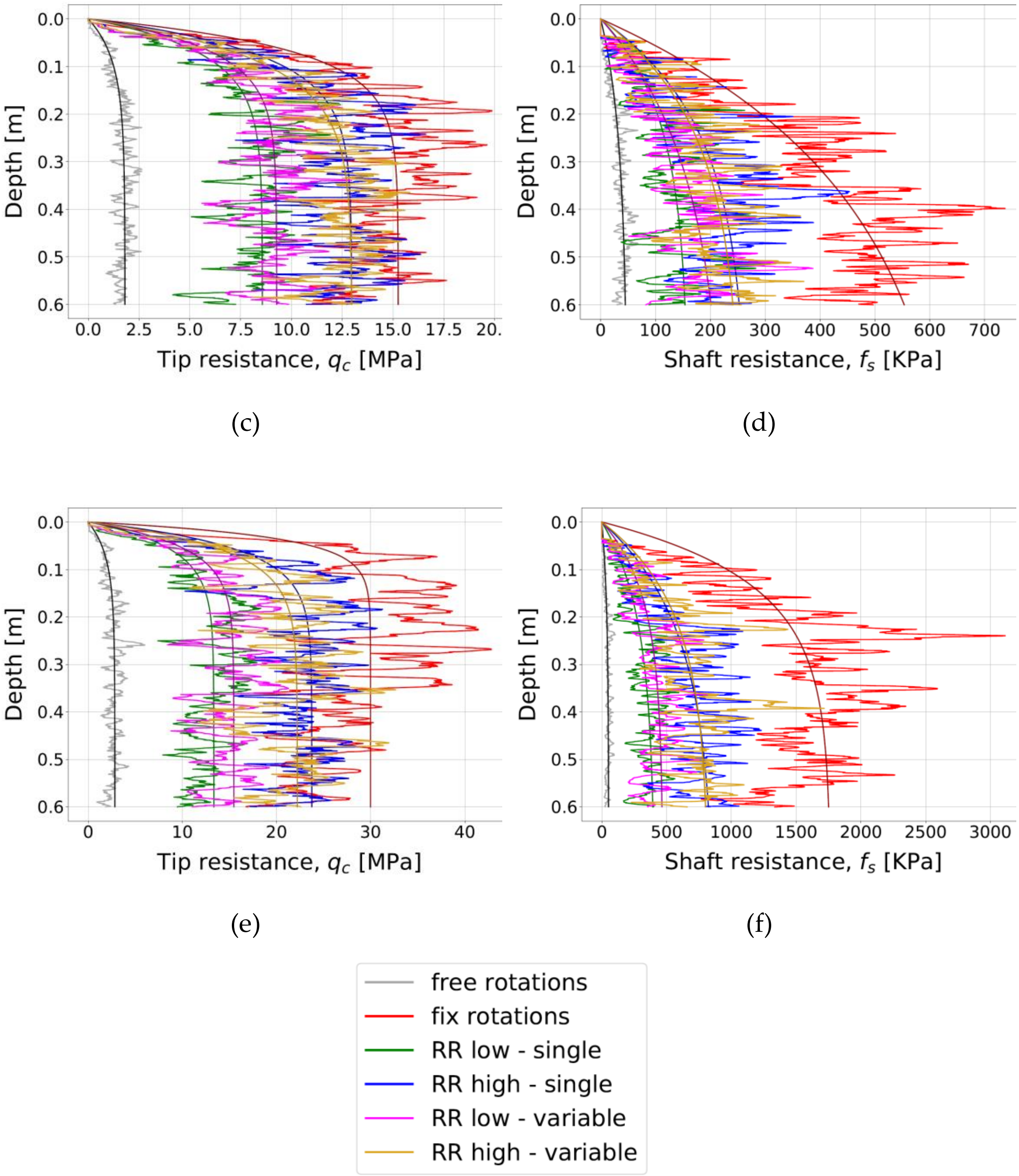

(c)

(d)

(e)

(f)

Figure 9.22: Tip and shaft resistance of the CPT tests performed for the parametric study of particle shape effects under Cases A (a-b), B (c-d) and C (e-f)

It is evident the results change significantly with the coupled variations of friction and rolling friction coefficients. In particular, both the penetration and shaft resistances increase with an increase of both sliding and rolling friction coefficients.

It worth pointing out that introducing some rotational constraints at the contacts strongly affects the results, increasing the tip resistance up to ten times, moving from

Series 1 (free rolling tests) to Series 2 (fixed rotations), particularly pronounced for case A. The use of rolling resistance (Series 3-4-5-6) does affect the results but in a relatively narrow range, compared to the unphysical extreme cases mentioned above.

The results are also reported in the Robertson & Campanella chart (Robertson, 1990; Robertson et al., 1986) to assess the soil classification, as shown in Figure 9.23, Figure 9.24 and Figure 9.25, respectively for Cases A, B and C.

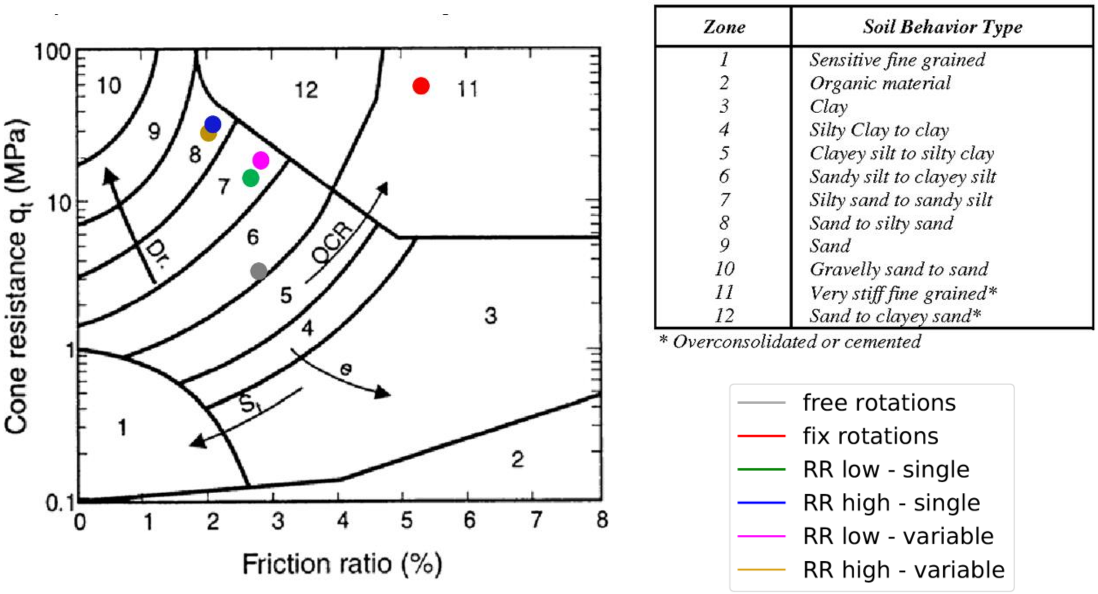

Zone	Soil Behavior Type
1	Sensitive fine grained
2	Organic material
3	Clay
4	Silty Clay to clay
5	Clayey silt to silty clay
6	Sandy silt to clayey silt
7	Silty sand to sandy silt
8	Sand to silty sand
9	Sand
10	Gravelly sand to sand
11	Very stiff fine grained*
12	Sand to clayey sand*

* Overconsolidated or cemented

Figure 9.23: Soil classification from Robertson & Campanella chart (Robertson et al., 1986) for Case A. The dots colours represent the Series from 1 to 6 and respect the colours of the legend in Figure 9.22, also reported here.

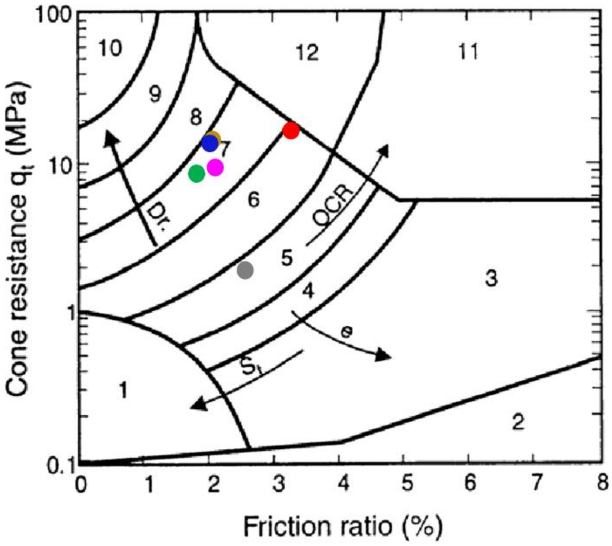

Figure 9.24: Soil classification from Robertson & Campanella chart (Robertson et al., 1986) for Case B. The dots colours represent the Series from 1 to 6 and respect the colours of the legend in Figure 9.22.

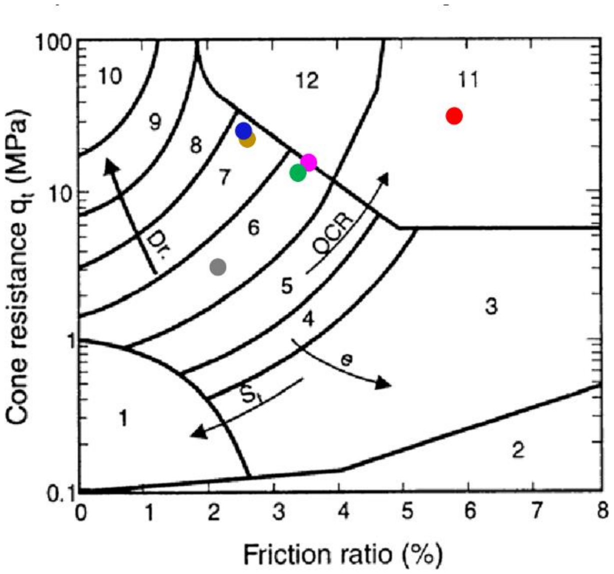

Figure 9.25: Soil classification from Robertson & Campanella chart (Robertson et al., 1986) for Case C. The dots colours represent the Series from 1 to 6 and respect the colours of the legend in Figure 9.22.

According to the Robertson charts reported, the majority of the numerical samples tested in this parametric study can be identified as *sandy silt/silty sand/sand*, depending on the DEM input parameters. The only cases that fall under other domains are the extremes of freely and fixed rotations spheres, which are identified respectively as *silty clay* and *very stiff overconsolidated fine grained,* with the only exception of fixed rotations for Case B (red dot in Figure 9.24 that will be examined later. As expected, it is not possible to simulate stiffer granular soils using freely rotating spheres, as stated in Chapter 8.4.

To better understand the effect of rolling resistance on the macroscopic results, it is useful to investigate the stresses in the soil induced by the cone penetration. In order to do this, a MATLAB script has been created by Ciantia (Ciantia et al., 2019b) to plot the vertical and radial stresses developed through the numerical samples, as shown in Figure 9.26 and Figure 9.27 respectively for cases **A** (Series 1-2-3-4) and **B** (Series 1-2-3-4).

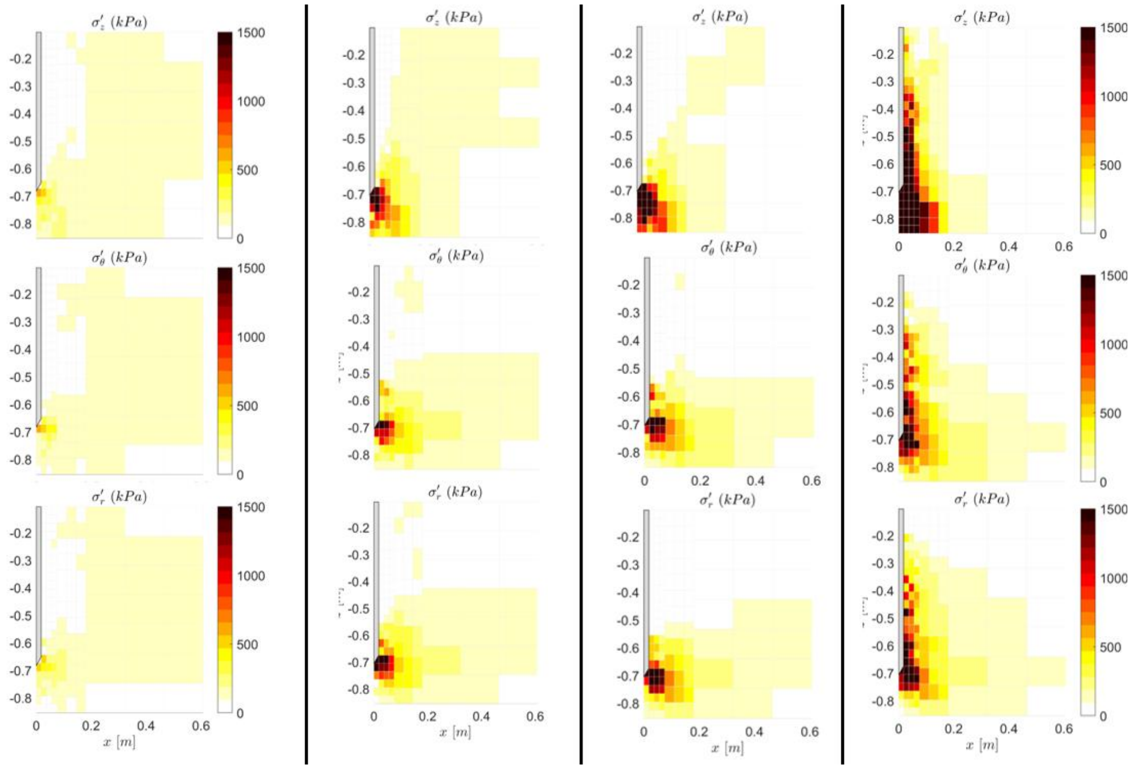

(a) (b) (c) (d)

Figure 9.26: Vertical (top figures) and radials stress distributions induced by the cone penetration for simulation Case A for Series 1 (a), Series 3 (b), Series 4 (c) and Series 2 (d)

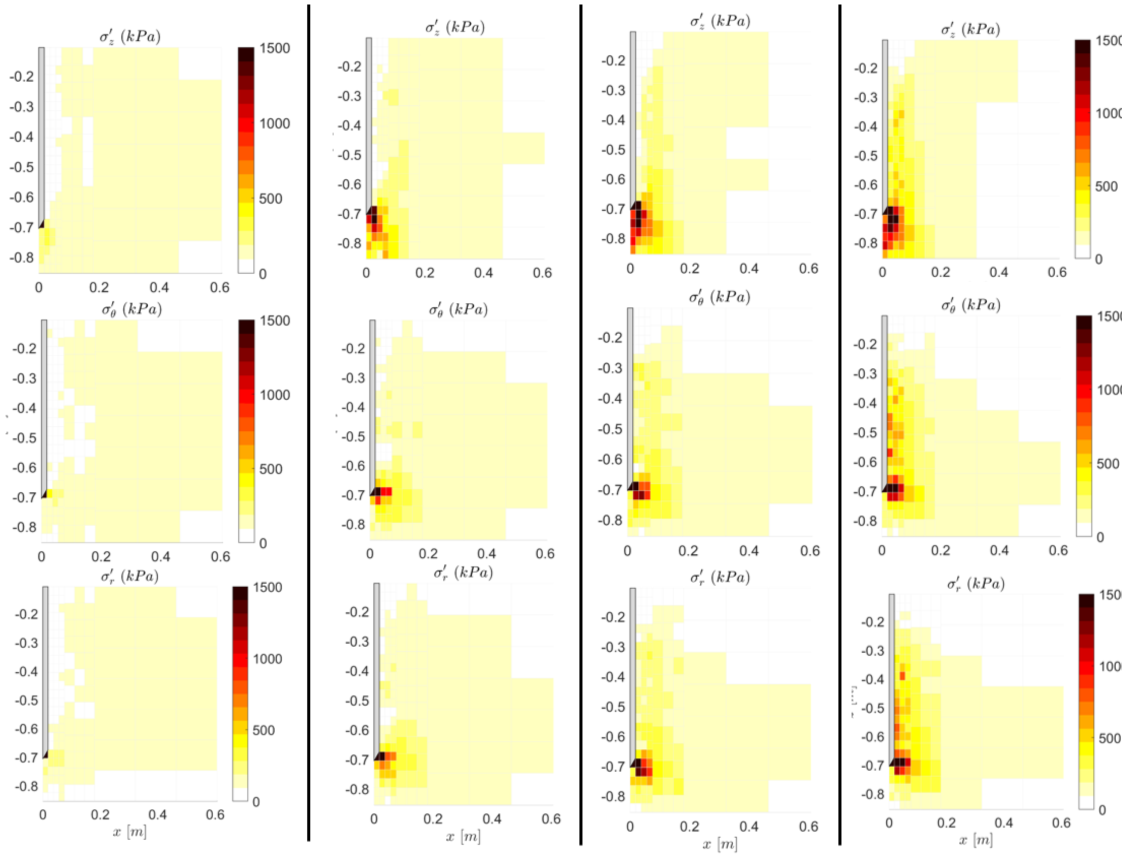

(a) (b) (c) (d)

Figure 9.27: Vertical (top figures) and radials stress distributions induced by the cone penetration for simulation Case B for Series 1 (a), Series 3 (b), Series 4 (c) and Series 2 (d).

The stress distributions around the cone differs significantly depending on the contact friction coefficients. It can be noted that when freely rotating spheres are used (Figure 9.26a and Figure 9.27a), the stresses remain low. On the other hand, if particles rotations are inhibited, the stresses may become very high, especially for the vertical stress (σ_{zz}) aligned with the direction of penetration (Figure 9.26d and Figure 9.27d).

It is interesting to point out that the simulations performed by Arroyo & Butlanska (Arroyo et al., 2011; Butlanska, 2014) on Ticino sand, with fixed rotations and a friction coefficient of 0.35 (similar to the here called Series 2 Case B), provide similar responses (both macroscopically – red curves of Figure 9.22c-d – and microscopically from Figure 9.27d) to the ones obtained with the calibrated friction coefficient of Ticino sand (0.60, from triaxial tests) and the rolling resistance approach used to mimic the grain shape of Ticino sand, represented in Figure 9.18b, at similar confinements, and Figure 9.26b-c.

This fact can be confirmed observing the Robertson & Campanella charts of Figure 9.23, Figure 9.24 and Figure 9.25. Indeed, observing the red dot of Figure 9.24, it is evident it is located in the same soil classification area of the other cases exploiting rolling resistance and higher coefficient of friction. Therefore, these approaches can be considered almost equivalent, from the physical (*i.e.,* soil classification), macroscopic (*i.e.,* penetration curves) and microscopic (*i.e.,* stress distributions) points of view.

Finally, it can be concluded that particle shape and shape variability do affect the results in terms of penetration resistance (*i.e.,* tip-shaft resistances) at both the macro-scale and the micro-scale (*i.e.,* stress distribution near the cone) levels. Moreover, the proposed rolling resistance contact model and model approach can be used to mimic successfully particle shape effects in the DEM-VCC-CPT tests.

9.6 Summary

Numerical simulations using the proposed rolling resistance contact model have been carried out in this Chapter. The major findings are summarised hereafter:

- An innovative technique to get the 3D *degree of true sphericity* of each grain from a 2D image (obtained from a table scanner) is proposed;
- Several triaxial tests performed on Ticino sand at different confinements and relative densities are successfully reproduced using the proposed rolling resistance contact model approach, giving as input the particle shape obtained using the table scanner;
- A multi-scaling technique for ball sizes is exploited in the Virtual Calibration Chamber (VCC) construction to have finer particles near the cone tip. This approach allows maintaining the ratio chamber to cone ($R_d = {}^{D_{VCC}}/_{d_c}$) equal to the physical experiment;

- The experimental penetration curves from Jamiolkowski (Jamiolkowski et al., 2003, 1988) are well reproduced by the DEM model, for different boundary conditions and confining pressures.
- The effect of particle shape on the penetration resistance is investigated. Constraining the rotation of particles dramatically affects both tip and shaft resistances. The effect of particle shape (*i.e.,* rolling friction coefficient) is strongly coupled with the choice of the sliding friction coefficient.
- A low coefficient of friction (*e.g.,* 0.30) combined with fixed balls rotations, provide results comparable to the calibrated rolling resistance approach proposed, at both the macro (*i.e.,* penetration responses) and micro (*i.e.,* stress distribution near the cone tip) levels.

References Part III

Andò, E., 2013. Experimental investigation of microstructural changes in deforming granular media using x-ray tomography. PhD Thesis. Université de Grenoble.

Andò, E., Cailletaud, R., Roubin, E., Stamati, O., the spam contributors, 2017. SPAM: The Software for the Practical Analysis of Materials [WWW Document]. https://ttk.gricad-pages.univ-grenoble-alpes.fr/spam/.

Arroyo, M., Butlanska, J., Gens, A., Calvetti, F., Jamiolkowski, M., 2011. Cone penetration tests in a virtual calibration chamber. Geotechnique 61, 525–531. https://doi.org/10.1680/geot.9.P.067

Bardet, J.P., Huang, Q., 1992. Numerical modeling of micropolar effects in idealized granular materials. Mech. Granul. Mater. powder Syst. 37, 85–92.

Butlanska, J., 2014. Cone penetration tests in a virtual calibration chamber. PhD Thesis. Universitat Politecnica de Catalunya (UPC). https://doi.org/10.1680/geot.9.p.067

Butlanska, J., Arroyo, M., Gens, A., O'Sullivan, C., 2014. Multi-scale analysis of cone penetration test (CPT) in a virtual calibration chamber. Can. Geotech. J. 51, 51–66. https://doi.org/10.1139/cgj-2012-0476

Calvetti, F., 2008. Discrete modelling of granular materials and geotechnical problems. Eur. J. Environ. Civ. Eng. 12, 951–965. https://doi.org/10.3166/EJECE.12.951-965

Calvetti, F., Viggiani, G., Tamagnini, C., 2003. A numerical investigation of the incremental behavior of granular soils. Riv. Ital. di Geotec. 37, 11–29.

Catalano, E., Chareyre, B., Barthélémy, E., 2014. Pore-scale modeling of fluid-particles interaction and emerging poromechanical effects. Int. J. Numer. Anal. Methods Geomech. 38, 51–71. https://doi.org/10.1002/nag.2198

Cheng, K., Wang, Y., Yang, Q., Mo, Y., Guo, Y., 2017. Determination of microscopic parameters of quartz sand through tri-axial test using the discrete element method. Comput. Geotech. 92, 22–40. https://doi.org/10.1016/j.compgeo.2017.07.017

Ciantia, M.O., Arroyo, M., Calvetti, F., Gens, A., 2015. An approach to enhance efficiency of DEM modelling of soils with crushable grains. Géotechnique 65, 91–110. https://doi.org/10.1680/geot.13.P.218

Ciantia, M.O., Arroyo, M., O'Sullivan, C., Gens, A., Liu, T., 2019a. Grading evolution and critical state in a discrete numerical model of Fontainebleau sand. Géotechnique 69, 1–15. https://doi.org/10.1680/jgeot.17.P.023

Ciantia, M.O., Boschi, K., Shire, T., Emam, S., 2018. Numerical techniques for fast generation of large discrete-element models, in: Proceedings of the Institution of Civil Engineers: Engineering and Computational Mechanics. pp. 147–161. https://doi.org/10.1680/jencm.18.00025

Ciantia, M.O., O'Sullivan, C., Jardine, R.J., 2019b. Pile penetration in crushable soils : Insights from micromechanical modelling, in: Proceedings of the XVII ECSMGE. Reykjavik. https://doi.org/10.32075/17ECSMGE-2019-1111

Estrada, N., Taboada, A., Radjaï, F., 2008. Shear strength and force transmission in granular media with rolling resistance. Phys. Rev. E 78, 1–11. https://doi.org/10.1103/PhysRevE.78.021301

Falagush, O., McDowell, G.R., Yu, H.S., 2015. Discrete element modeling of cone penetration tests incorporating particle shape and crushing. Int. J. Geomech. 15, 1–14. https://doi.org/10.1061/(ASCE)GM.1943-5622.0000463

Feng, Y.T., Owen, D.R.J., 2014. Discrete element modelling of large scale particle systems-I: exact scaling laws. Comp. Part. Mech 1, 159–168. https://doi.org/10.1007/s40571-014-0010-y

Ghionna, V.N., Jamiolkowski, M., 1991. A critical appraisal of calibration chamber testing on sands, in: FIRST INT. SYMPOSIUM ON CC TESTING. CLARKSON UNIVERSITY, POTSDAM (USA), pp. 13–40.

Gotteland, P., Villard, P., Salot, C., Nakagawa, M., Luding, S., 2009. Using Nonconvex Discrete Elements to Predict Experimental Behaviour of Granular Materials, in: Proceedings of the 6th International Conference on Micromechanics of Granular Media. AIP, pp. 361–364. https://doi.org/10.1063/1.3179934

Itasca Consulting Group Inc., 2014. PFC — Particle Flow Code, Ver. 5.0. Minneapolis:

Itasca.

Iwashita, K., Oda, M., 1998. Rolling resistance at contacts in simulation of shear band development by DEM. J. Eng. Mech. 124, 285–292. https://doi.org/10.1061/(ASCE)0733-9399(1998)124:3(285)

Jamiolkowski, M., Ghionna, V.N., Lancellotta, R., Pasqualini, E., 1988. New correlations of penetration tests for design practice, in: De Ruiter, J. (Ed.), Proc., Penetration Testing 1988, ISOPT 1. Orlando, Florida, pp. 263–296.

Jamiolkowski, M., Lo Presti, D.C.F., Manassero, M., 2003. Evaluation of Relative Density and Shear Strength of Sands from CPT and DMT, in: Symposium on Soil Behavior and Soft Ground Construction Honoring Charles C. "Chuck" Ladd. Cambridge, USA. https://doi.org/10.1061/40659(2003)7

Kawamoto, R., Andò, E., Viggiani, G., Andrade, J.E., 2018. All you need is shape: Predicting shear banding in sand with LS-DEM. J. Mech. Phys. Solids 111, 375–392. https://doi.org/10.1016/j.jmps.2017.10.003

McDowell, G.R., Falagush, O., Yu, H.S., 2012. A particle refinement method for simulating DEM of cone penetration testing in granular materials. Geotech. Lett. 2, 141–147. https://doi.org/10.1680/geolett.12.00036

Ng, T.T., 1994. Numerical simulations of granular soil using elliptical particles. Comput. Geotech. 16, 153–169. https://doi.org/10.1016/0266-352X(94)90019-1

Radjai, F., Roux, S., Moreau, J.J., 1999. Contact forces in a granular packing. Chaos 9, 544–550. https://doi.org/10.1063/1.166428

Robertson, P.K., 1990. Soil classification using the cone penetration test. Can. Geotech. J. 27, 151–158. https://doi.org/10.1139/t90-014

Robertson, P.K., Campanella, R.G., Gillespie, D., Greig, J., 1986. Use of Piezometer Cone Data, in: IN-SITU '86 Use of In-Situ Testing in Geotechnical Engineering. ASCE Speciality Conference, pp. 1263–1280.

Rorato, R., Arroyo, M., Andò, E., Gens, A., 2019. Sphericity measures of sand grains. Eng. Geol. 254, 43–53. https://doi.org/10.1016/j.enggeo.2019.04.006

Rorato, R., Arroyo, M., Gens, A., Andò, E., Viggiani, G., 2018. Particle shape distribution effects on the triaxial response of sands: a DEM study, in: Giovine, P., et al. (Eds.), Micro to MACRO Mathematical Modelling in Soil Mechanics, Trends in Mathematics. Reggio Calabria (Italy), pp. 277–286. https://doi.org/10.1007/978-3-319-99474-1_28

Rothenburg, L., Bathurst, R.J., 1992. Micromechanical features of granular assemblies with planar elliptical particles. Géotechnique 42, 79–95. https://doi.org/10.1680/geot.1992.42.1.79

Sharif, Y., Ciantia, M., Brown, M.J., Knappett, J.A., Ball, Jonathan, D., 2019. Numerical Techniques For the Fast Generation of Samples Using the Particle Refinement Method, in: Proceedings of the 8th International Conference on Discrete Element Methods (DEM8). p. 181.

Skinner, A.E., 1969. A note on the influence of interparticle friction on the shearing strength of a random assembly of spherical particles. Géotechnique 19, 150–157.

Tran, Q.A., Chevalier, B., Breul, P., 2016. Discrete modeling of penetration tests in constant velocity and impact conditions. Comput. Geotech. 71, 12–18. https://doi.org/10.1016/j.compgeo.2015.08.010

van der Walt, S., Schönberger, J.L., Nunez-Iglesias, J., Boulogne, F., Warner, J.D., Yager, N., Gouillart, E., Yu, T., 2014. scikit-image: image processing in Python. PeerJ 2:e453. https://doi.org/10.7717/peerj.453

Wensrich, C.M., Katterfeld, A., 2012. Rolling friction as a technique for modelling particle shape in DEM. Powder Technol. 217, 409–417. https://doi.org/10.1016/j.powtec.2011.10.057

Wensrich, C.M., Katterfeld, A., Sugo, D., 2014. Characterisation of the effects of particle shape using a normalised contact eccentricity. Granul. Matter 16, 327–337. https://doi.org/10.1007/s10035-013-0465-1

Zhou, Y.C., Wright, B.D., Yang, R.Y., Xu, B.H., Yu, A.B., 1999. Rolling friction in the dynamic simulation of sandpile formation". Phys. A Stat. Mech. its Appl. 269, 536–553. https://doi.org/10.1016/j.physa.2005.01.019

Part IV: Conclusions

10 Conclusions

10.1 Summary results

This thesis presented a multidisciplinary work aimed at improving the current DEM simulations to reproduce standard experimental tests widely used in soil mechanics and geotechnical engineering. In particular, a novel rolling resistance contact model able to include the effects of particle shape in the simulations has been developed, calibrated and validated. In order to calibrate the proposed contact model, it has been necessary first how to measure and quantify the shape of sand grains, and then to understand the influence of particle shape on the kinematics of shearing granular materials.

Regarding the first task (presented in *Chapter 6*), reliable replicable algorithms have been developed to quantify some geometrical properties of sand grains (*e.g.,* volume, surface area, lengths, etc.) that have been later combined together to origin shape descriptors in two and three dimensions. An extensive statistical study showed the correlations existing between the computed shape parameters. After that, it was necessary to measure the kinematics (*i.e.,* displacements and rotations in three-dimensions) of single grains during triaxial tests (scanned by x-rays with time) in order to investigate the influence of particle shape on their motion (*Chapter 7*). A direct comparison between the shape and kinematic datasets showed that particle shape is related to observed kinematics. In particular, true sphericity is a good predictor of upper bound rotational restraint.

Chapter 8 described in detailed the central part of this doctoral project: the DEM rolling resistance contact model. It has been calibrated to reproduce the triaxial tests of Hostun and Caicos sands, respecting the particles kinematics at failure. The value of rolling resistance is directly linked to true sphericity. When shape measurements are performed, this link enables independent evaluation of the rolling resistance coefficient for each particle. It does also allow the characteristic shape variability of natural soils to be easily taken into account. It has been then validated by simulating other triaxial tests (1) with the same sands, but in different conditions (2) with Ottawa sand, for which 3D grain images were also available for examination, and (3) with Ticino sand (in *Chapter 9*), for which only 2D grain images were available.

Finally, *Chapter 9* presented results on the Cone Penetration Test (CPT) performed in a Virtual Calibration Chamber (VCC). Experimental penetration curves have been well reproduces exploiting the proposed rolling resistance model calibrated for Ticino sand. Then, a numerical study about the influence of particle shape on the tip and shaft resistances has been carried out. It was shown that the combined effect of rolling friction and sliding friction is determinant, and therefore an accurate parameters calibration is crucial.

10.2 Recommendations for future work

Some aspects that have not been considered in this doctoral work are listed in this section. They can eventually open future lines of research to improve or complete the results of the current project. They have been divided in two categories regarding (1) the analysis of particle shape and (2) the numerical simulations.

10.2.1 Particle shape

It is evident that the shape study carried out in this project was focused on the measure of particle shape at the largest scale (*i.e.,* the grains-scale): sphericity. This choice was made because of the high number of particles that has been studied (more than one hundred thousand) and because of the resolution of the images available ($15.56\mu m/px$). However, it was presented in Chapter 6.7 that about one thousand grains are enough to capture a sufficient amount of shape variability in a sand sample. In addition, 3D high-resolution images of grains (about 1-2 $\mu m/px$) have been recently made (Amirrahmat et al., 2019; Wiebicke et al., 2017), allowing an accurate measure of particle roundness and (perhaps) roughness (see Figure 10.1). Moreover, new image-analysis algorithms to compute 3D Roundness have been recently proposed (Kong and Fonseca, 2018; Nadimi and Fonseca, 2017; Zhao and Wang, 2016), extending the original idea of roundness proposed by Wadell (Wadell, 1932). Therefore, it worth exploring systematically eventual statistical correlations existing between (a) particle sphericity and roundness (b), particle roundness and grains kinematics.

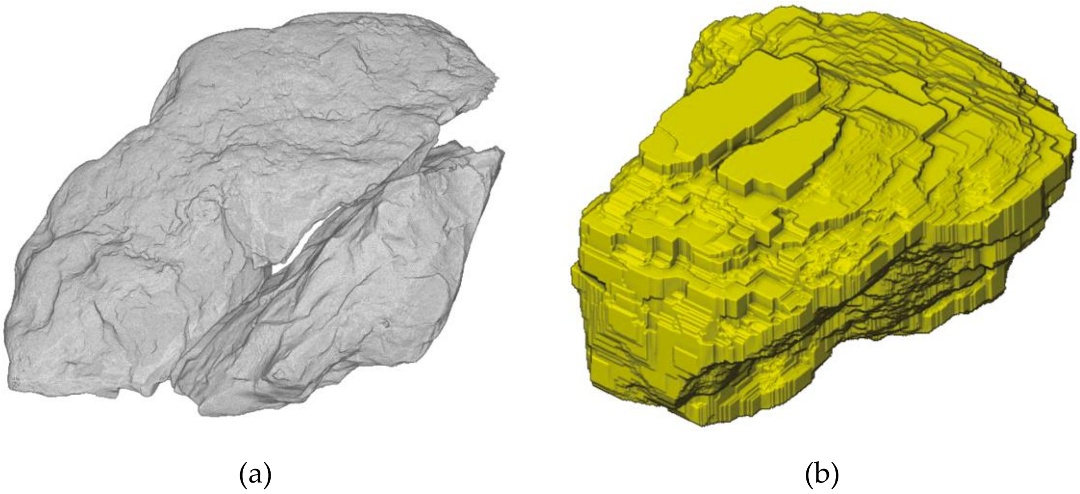
(a) (b)

Figure 10.1: Rendering of (a) two high-resolutions (1 $\mu m/px$) Hostun sand grain in contact (Wiebicke et al., 2017) (b) a single particle of Mason sand scanned at a resolution of 2 $\mu m/px$ (Amirrahmat et al., 2019).

10.2.2 Numerical simulations

Some improvements can be envisaged regarding the numerical simulations performed in this doctoral work, which may constitute future lines of investigation.

- Particle crushing has not been considered in the DEM simulations here performed. It has been clearly indicated in this dissertation that particle crushing was not relevant for the materials tested in the triaxial experiments (Hostun, Ottawa, Caicos, Ticino sands) at the pressure levels involved. However, it is an important aspect that must be taken into account at higher stress levels (*e.g.*, in the

Cone Penetration Test) or for other –more crushable- sand types. The implementation of an efficient crushing model for DEM (PFC5 in particular) has been proposed by Ciantia (Ciantia et al., 2015, 2014) and successfully tested and validated for CPT simulations (Ciantia et al., 2019, 2016), even though particles rotations were inhibited in all of his numerical tests. Therefore, the natural outgrowth for both research projects will be to combine together the two model approaches in order to create a single advanced DEM contact model capable of considering both particle shape effects (with the here proposed rolling resistance contact model) and the crushing of particles.

- The rolling resistance contact model proposed in Chapter 8.4 has been calibrated by reproducing the experimental triaxial tests of Hostun and Caicos sands, in terms of macroscopic responses and kinematics at failure. However, in contrast to the experiments, the lateral cylindrical wall used in the DEM simulations was built as a rigid wall with a servo-controlled mechanism to apply the target confining pressure. The numerical sample was able to localise failure in a shear band but including an elastic deformable membrane may result in more realistic simulations of the material deformation occurring in the experiments, especially post-localization (Cheung and O'Sullivan, 2008; Khoubani et al., 2018). This has been tested in a later stage of this doctoral work, simulating the membrane with the finite differences Itasca software FLAC6 (PFC5-FLAC6 coupling is now available) with little success. However, other methodologies exist to build a deformable lateral wall in DEM (Cheung and O'Sullivan, 2008; de Bono et al., 2012; Khoubani et al., 2018; Tang et al., 2017) that are worth investigating further.

- In this work, we validated the proposed DEM rolling resistance contact model by testing in triaxial conditions four different sands (Hostun, Caicos, Ottawa and Ticino sands) at different confining pressures (between 100kPa and 300kPa). However, it would be interesting to simulate different laboratory experimental tests for the sands studied in this work (*e.g.,* repose angle test, oedometer test, undrained triaxial tests, cyclic triaxial tests, direct shear tests) that can be easily found in the literature.

10.3 Final remarks

The last chapter of this doctoral thesis is dedicated to a reflection about the role that this 45-months work may have on the future of geotechnics. It is indeed known that a PhD thesis represent a new drop in the ocean of knowledge but it is important to be aware of where this drop may be valuable.

The behaviour of geomaterials is complex because of their diverse nature in size, mineralogy and shapes. Moreover, the addition of fluids as air and water makes the behaviour time-dependent and even more complex to understand and predict. The deformation of granular materials has been historically studied at the macro-scale level, which is the scale of interest for most geotechnical engineering problems, developing constitutive equations to predict the strains from the stresses, generally exploiting finite elements softwares. This approach relied on empirical observation of the soil overall response at the large-scale (laboratory or field tests). However, the mechanics occurring at the particle-scale was ignored, although it allows explaining complex situations that cannot be fully understandable or predictable focusing at larger scales (*e.g.,* insertion problems, liquefaction triggering, internal erosion, sand production, etc.).

The micro-mechanical inspection of granular soils is now an easily realisable task, thanks to the new technologies and the increase of computer power. The Discrete Element Method takes advantage of these recent developments carving out a space in this respect.

We believe this doctoral work constitute a further step in the direction of using the micro-response to first understand and then predict the macro-response of granular soils, which is the main goal of geotechnical engineers.

References Part IV

Amirrahmat, S., Alshibli, K.A., Melton, J.L., 2019. 3D Finite Element Modelling of Fracture of Sand Particles Subjected to High Strain Loading Rate. J. Dyn. Behav. Mater. 1–19. https://doi.org/10.1007/s40870-019-00211-0

Cheung, G., O'Sullivan, C., 2008. Effective simulation of flexible lateral boundaries in two- and three-dimensional DEM simulations. Particuology 6, 483–500. https://doi.org/10.1016/j.partic.2008.07.018

Ciantia, M.O., Arroyo, M., Butlanska, J., Gens, A., 2016. DEM modelling of cone penetration tests in a double-porosity crushable granular material. Comput. Geotech. 73, 109–127. https://doi.org/10.1016/j.compgeo.2015.12.001

Ciantia, M.O., Arroyo, M., Butlanska, J., Gens, A., 2014. DEM modelling of a double-porosity crushable granular material, in: Soga, K. (Ed.), International Symposium on Geomechanics from Micro to Macro. pp. 269–274. https://doi.org/10.1016/j.compgeo.2015.12.001

Ciantia, M.O., Arroyo, M., Calvetti, F., Gens, A., 2015. An approach to enhance efficiency of DEM modelling of soils with crushable grains. Géotechnique 65, 91–110. https://doi.org/10.1680/geot.13.P.218

Ciantia, M.O., O'Sullivan, C., Jardine, R.J., 2019. Pile penetration in crushable soils : Insights from micromechanical modelling, in: Proceedings of the XVII ECSMGE. Reykjavik. https://doi.org/10.32075/17ECSMGE-2019-1111

de Bono, J., Mcdowell, G., Wanatowski, D., 2012. Discrete element modelling of a flexible membrane for triaxial testing of granular material at high pressures. Géotechnique Lett. 2, 199–203. https://doi.org/10.1680/geolett.12.00040

Khoubani, A., Evans, T.M., Evans, M., 2018. An efficient flexible membrane boundary condition for DEM simulation of axisymmetric element tests. Numer. Anal. Methods Geomech. 42, 694–715. https://doi.org/10.1002/nag.2762

Kong, D., Fonseca, J., 2018. Quantification of the morphology of shelly carbonate sands using 3D images. Géotechnique 68, 249–261. https://doi.org/10.1680/jgeot.16.P.278

Nadimi, S., Fonseca, J., 2017. Single-Grain Virtualization for Contact Behavior Analysis on Sand. J. Geotech. Geoenvironmental Eng. 143, 06017010. https://doi.org/10.1061/(ASCE)GT.1943-5606.0001740

Tang, H., Zhang, X., Ji, S., 2017. Discrete element analysis for shear band modes of granular materials in triaxial tests. Part. Sci. Technol. 35, 277–290. https://doi.org/10.1080/02726351.2016.1153547

Wadell, H., 1932. Volume, Shape, and Roundness of Rock Particles. J. Geol. 40, 443–451.

Wiebicke, M., Andò, E., Herle, I., Viggiani, G., 2017. On the metrology of interparticle contacts in sand from x-ray tomography images. Meas. Sci. Technol. 28. https://doi.org/10.1088/1361-6501/aa8dbf

Zhao, B., Wang, J., 2016. 3D quantitative shape analysis on form, roundness, and compactness with micro-CT. Powder Technol. 291, 262–275. https://doi.org/10.1016/j.powtec.2015.12.029

Part V: Appendices

Appendix A: Scripts

Appendix A.1 Python script “GetAllGrains_MPI.py”

This python script (1) takes a 3D labelled image as input, (2) loops through all the grains, (3) computes and saves the geometric properties of the grains. It is designed to work in MPI. Professor Edward Andò is strongly acknowledged for his help.

```
import numpy as np
import scipy.ndimage
import tifffile
import skimage
import tracking_functions
import random_orientation
from scipy.spatial import ConvexHull
import matplotlib.pyplot as plt
# from mpl_toolkits.mplot3d.art3d import Poly3DCollection
# from mpl_toolkits.mplot3d import Axes3D
# from matplotlib.patches import FancyArrowPatch
# from mpl_toolkits.mplot3d import proj3d
import time
initialtime = time.time()

import multiprocessing
NUMBER_OF_THREADS = 8
DEBUG=False

voxelVolumeMM3 = ( 15.56/1000 )**3
pixelAreaMM2 = ( 15.56/1000 )**2
print 'Start loading the image...'

#if CAICOS
# labImageShape = ( 1600, 950, 950 )
# labImageFile = "/home/riccardo/Desktop/COEA01-01-0950x0950x1600-lab.tif"

#if HOSTUN
#labImageShape = ( 1750, 960, 960 )
#labImageFile = "/home/riccardo/Desktop/HNEA01-01-0960x0960x1750-lab.tif"

print "\nStarting to load labelled image file {}".format( labImageFile )

lab = tifffile.imread( "labImageFile" )
lab = lab.reshape( labImageShape )

print "\nDone.\n"
print "\tMinimum Value in labelled matrix: ", lab.min()
print "\tMaximum Value in labelled matrix: ", lab.max(), '\n'

if DEBUG: print "Master: Setting up queues"
q_jobs     = multiprocessing.Queue()
```

```python
q_results = multiprocessing.Queue()

if DEBUG: print "Master: Adding jobs to queues"
for grainNumber in range( 1, lab.max() ):
    if grainNumber > 0:
        q_jobs.put( grainNumber )
for i in range( NUMBER_OF_THREADS ):  q_jobs.put( "STOP" )

def processOneGrainJob( worker_number, q_jobs, q_results ):
    print "Worker Number {}".format( worker_number )
    while True:
        grainNumber = q_jobs.get()

        if grainNumber == "STOP":
            q_results.put("STOP")
            break

        else:
            print "\n\tWorking on Grain #", grainNumber

            grainCoordinates = 0
            grainCoordinates_array = 0
            grainCoordinates_arrayTR = 0
            grainVolume = 0
            grainCOM = 0
            xlist=0
            ylist=0
            zlist=0
            ###########################################################
            #########  1. Find our grain in space
            ###########################################################
            # Get a list of coordinates where the pixels of the big labelled volume are = to the grain
            grainCoordinates = np.where( lab == grainNumber )
            grainCoordinates_array = np.array (grainCoordinates)
            grainCoordinates_arrayTR = np.transpose (grainCoordinates_array)

            # Count the number of coordinates to get a voxel volume for this grain
            grainVolume      = np.array(grainCoordinates).shape[1]

            if DEBUG: print "\n\tGrain {} has {} voxels".format( grainNumber, grainVolume )

            # Get the bounding box for this grain from the labelled volume
            #grainBoundingBox  = scipy.ndimage.measurements.find_objects( lab == grainNumber )[0]

            min_array = np.amin(grainCoordinates_array,axis=1)
            max_array = np.amax(grainCoordinates_array,axis=1)

            # Get a minimum parallepiped subvolume continaing our grain
            #grainSubvolume   = lab[ grainBoundingBox ]
            grainSubvolume  = np.copy(lab[ min_array[0]:max_array[0]+1,
                                           min_array[1]:max_array[1]+1,
                                           min_array[2]:max_array[2]+1 ])

            # Erase all voxels which are not our grain
            grainSubvolume[ np.where( grainSubvolume != grainNumber ) ] = 0
            grainCOM = scipy.ndimage.measurements.center_of_mass( grainSubvolume )
            X_glob = grainCOM[0] + min_array[0]+1
                  Y_glob = grainCOM[1] + min_array[1]+1
```

```
                Z_glob = grainCOM[2] + min_array[2]+1

                if grainVolume < 50:
                    print 'Skip this grain!'
                    continue

                ###########################################################

                ######  2. Copy grain into cubic subvolume for analysis
                ###########################################################


                # define size of cube to hold all data with 2 pixel border
                cubeDimension  = max( grainSubvolume.shape ) + 4
                grainSubvolumeCube = np.zeros( ( cubeDimension, cubeDimension, cubeDimension ), '<f4' )

                # offest to this from our non-cube data
                grainSubvolumeCubeOffset = ( np.array( grainSubvolumeCube.shape ) - np.array( grainSubvolume.shape ) ) / 2

                # copy non-cube data into the vube with the offset we calculated above
                grainSubvolumeCube[ grainSubvolumeCubeOffset[0]:grainSubvolumeCubeOffset[0]+grainSubvolume.shape[0],\
                                    grainSubvolumeCubeOffset[1]:grainSubvolumeCubeOffset[1]+grainSubvolume.shape[1],\
                                    grainSubvolumeCubeOffset[2]:grainSubvolumeCubeOffset[2]+grainSubvolume.shape[2]   ] = grainSubvolume
                grainCubeCOM = np.array(scipy.ndimage.measurements.center_of_mass( grainSubvolumeCube ) )
                if DEBUG: print "\nThe Center of Mass of my grain into the cube (local coordinates, box) is:\n\n\t", grainCubeCOM
                if DEBUG: print "\nThe Center of Mass of my grain in global coordinates, is:\n\n\t", X_glob, Y_glob, Z_glob
                ##########################################################
                ###########   INERTIA TENSOR     #########################
                ##########################################################

                momentOfInertia = random_orientation.inertia_tensor( grainSubvolumeCube, grainSubvolumeCube.shape )
                eigenValVec = random_orientation.eigenvalvec(  momentOfInertia )
                if DEBUG: print '\nThe inertia tensor is:\n\n', momentOfInertia
                if DEBUG: print '\nThe inertia tensor eigenvalues are: \n\t', eigenValVec[0],'\n\t', eigenValVec[1],'\n\t', eigenValVec[2]
                if DEBUG: print '\nThe inertia tensor eigenvectors are: \n\t', eigenValVec[3],'\n\t', eigenValVec[4],'\n\t', eigenValVec[5]

                #########################################################
                ########   ROTATE REFERENCE FRAME and GET GRAIN LENGTHS
                #########################################################

                grain_local_Coordinates = np.where( grainSubvolumeCube == grainNumber )
                grain_local_Coordinates = np.array (grain_local_Coordinates)
```

```
                    CambioBaseMatrix = np.array([ [eigenValVec[3][0],eigenValVec[4][0],eigenValVec[5][0]] , [eigenValVec[3][1],eigenValVec[4][1],eigenValVec[5][1]] , [eigenValVec[3][2],eigenValVec[4][2],eigenValVec[5][2]]] , dtype=float)
                    CambioBaseMatrix_INV = np.linalg.inv(CambioBaseMatrix)
                    grain_NEW_local_Coordinates = np.dot(CambioBaseMatrix_INV , grain_local_Coordinates)
                    AX1_max = np.amax( grain_NEW_local_Coordinates[0,:] )
                    AX1_min = np.amin( grain_NEW_local_Coordinates[0,:] )
                    AX2_max = np.amax( grain_NEW_local_Coordinates[1,:] )
                    AX2_min = np.amin( grain_NEW_local_Coordinates[1,:] )
                    AX3_min = np.amin( grain_NEW_local_Coordinates[2,:] )
                    AX3_max = np.amax( grain_NEW_local_Coordinates[2,:] )
                    AX1_length = AX1_max - AX1_min
                    AX2_length = AX2_max - AX2_min
                    AX3_length = AX3_max - AX3_min
                    grain_length = np.sort([AX1_length,AX2_length,AX3_length])
                    if DEBUG: print '\nThe lengths of my grain (after reference frame rotation) are:\n'
                    if DEBUG: print grain_length[0] , '=', AX1_max , '-' , AX1_min ,'\n', grain_length[1] , '=', AX2_max , '-' , AX2_min ,'\n', grain_length[2] , '=', AX3_max , '-' , AX3_min

                    ########################################################
                    ###########    MARCHING CUBES    #######################
                    ########################################################
                    grainSubvolumeCube_filtered = scipy.ndimage.filters.gaussian_filter(grainSubvolumeCube,sigma=0.75)
                    verts, faces = skimage.measure.marching_cubes_classic( grainSubvolumeCube_filtered, grainNumber/2.0 )
                    surface_area = skimage.measure.mesh_surface_area(verts, faces)
                    if DEBUG: print '\nThe surface area from MarchingCubes algorithm (smoothed) is:\n', surface_area,' pixels^2 which corresponds to', surface_area*pixelAreaMM2, 'mm2'

                    #########################################################
                    ###########      CONVEX HULL     ########################
                    #########################################################

                    hull = ConvexHull(grainCoordinates_arrayTR)
                    if DEBUG: print "\nThe volume of the convex hull is {} voxels".format(hull.volume)
                    #print "The surface area of the convex hull is {} pixels2".format(hull.area)

                    #########################################################
                    ###########   MAXIMUM INSCRIBED SPHERE    ###############
                    #########################################################

                    distance_euclidean_tensor = scipy.ndimage.morphology.distance_transform_edt( grainSubvolumeCube )
                    max_inscribedSphere_radius = np.amax (distance_euclidean_tensor)

                    for index, value in np.ndenumerate( distance_euclidean_tensor ):
                        if value == max_inscribedSphere_radius:
                            sphere_center = index
                    if DEBUG: print '\nThe maximum inscribed sphere is centered at: ', sphere_center, ' and its RADIUS is: ', max_inscribedSphere_radius
```

```

                ##########################################################
                ###########   MINIMUM CIRCUMSCRIBED SPHERE    ###########
                ##########################################################

                min_cicr_sph = random_orientation.bounding_sphere (grainCoordinates_arrayTR)
                if DEBUG: print '\nThe minimum circumscribed sphere radius is: ', min_cicr_sph[1]
                #########################################################
                ###########   Save all properties in a vector    #######
                #########################################################

                if DEBUG: print 'Save all the properties in a numpy array. '
                geometry_properties = np.array ([ grainNumber, grainVolume, Z_glob, Y_glob, X_glob, surface_area, eigenValVec[0],eigenValVec[1],eigenValVec[2], grain_length[2], grain_length[1], grain_length[0], hull.volume, hull.area, 2.0*max_inscribedSphere_radius, 2.0*min_cicr_sph[1]]  )
                if DEBUG: print '\nVoila:\n', geometry_properties

                q_results.put( [ worker_number, grainNumber, geometry_properties ] )

    if DEBUG: print "Master: Launching workers"
    for i in range(NUMBER_OF_THREADS):
        p = multiprocessing.Process( target=processOneGrainJob, args=( i, q_jobs, q_results, ) )
        p.start()

    finished_threads  = 0
    nodes_processed   = 0
    if DEBUG: print "Master: Waiting for results"

    fileHandle = open( "grain_analysis-"+time.strftime( "%Y%m%d%H%M", time.localtime( initialtime ))+".tsv", "a" )
    fileHandle.write( "Grain Number\tVolume (vx)\tBarX\tBarY\tBarZ\tSurface_Area (px2)\tEigenvalue1\tEigenvalue2\tEigenvalue3\tLength1\tLength2\tLength3\tVolume_convexHull\tSurfaceArea_convexHull\tDiam_MaxInscSph\tDiam_MinCircSph\n" )

    while finished_threads < NUMBER_OF_THREADS:
        result = q_results.get()

        if result == "STOP":
            finished_threads += 1
            print "\nNumber of finished threads = ", finished_threads

        else:
            #print "Master: got {}".format( result )
            for item in result[2]:
                fileHandle.write( "{}\t".format( item ) )
            fileHandle.write( "\n" )

    finaltime = time.time()

    fileHandle.close()
    print "Calculation time = ", finaltime-initialtime, " seconds"
```

Appendix A.2 Python script “GetAllGrains_2Dprojection.py”

This python script (1) takes as input a 2D labelled image, (2) loops through all the grains, (3) computes the 2D geometric properties of the grains, (4) saves the 2D sphericities.

```python
import numpy as np
import scipy.ndimage
import tifffile
import skimage.measure
import skimage.morphology
import tracking_functions
import random_orientation
from scipy.spatial import ConvexHull
import matplotlib.pyplot as plt
#import trimesh
#import mayavi
#import seaborn as sns
import time
import math

DEBUG = 0
initialtime = time.time()
voxelVolumeMM3 = ( 15.56/1000 )**3
pixelAreaMM2 = ( 15.56/1000 )**2
labImageShape = ( 4500, 4500 )
labImageFile = "/home/riccardo/labelled_2Dscan_Ticino-4500x4500.tif"

print "\nStarting to load labelled image file {}".format( labImageFile )
lab = plt.imread(labImageFile)
lab = lab.reshape( labImageShape )
print "\nDone.\n"

print "\tMinimum Value in labelled matrix, excluding zero: ", np.amin(lab[lab != 0])
print "\tMaximum Value in labelled matrix: ", lab.max(), '\n'

t1 = time.time()
fileHandle = open( "grain_analysis-"+time.strftime( "%Y%m%d%H%M", time.localtime( initialtime ))+".tsv", "a" )
fileHandle.write( "Grain Number\tProjArea (px)\tBarX\tBarY\tEigenvalue1\tEigenvalue2\tLength1\tLength2\tDiam_MaxInscSph\tDiam_MinCircSph\tSphericity1\tSphericity2\tSphericity3\tSphericity4\tSphericity5\n" )

for grainNumber in range( 1,lab.max() ):
    if grainNumber == 0: continue
    print "\nWorking on grain", grainNumber
    #################################################################
    ##  1. Find our grain in space
    #################################################################
    # Get a list of coordinates where the pixels of the big labelled volume are = to the grain
    grainCoordinates = np.where( lab == grainNumber )
    grainCoordinates_array = np.array (grainCoordinates)
    grainCoordinates_arrayTR = np.transpose (grainCoordinates_array)
    t2 = time.time()

    # Count the number of coordinates to get a voxel volume for this grain
    grainVolume      = np.array(grainCoordinates).shape[1]

    if DEBUG: print "\nGrain {} has {} pixels".format( grainNumber, grainVolume )
    if DEBUG: print "This means {:0.3f} mm3".format( grainVolume*pixelAreaMM2 )
    if grainVolume < 12 or grainVolume > 50000: continue #skip very small and big labels (not grains)

    min_array = np.amin(grainCoordinates_array,axis=1)
    max_array = np.amax(grainCoordinates_array,axis=1)
    xlist = np.arange(min_array[0],max_array[0])
    ylist = np.arange(min_array[1],max_array[1])

    # Get a minimum parallepiped subvolume continaing our grain
    grainSubvolume  = np.copy(lab[ min_array[0]:max_array[0]+1,
                           min_array[1]:max_array[1]+1 ])
    # Erase all voxels which are not our grain
    grainSubvolume[ np.where( grainSubvolume != grainNumber ) ] = 0
    grainCOM = scipy.ndimage.measurements.center_of_mass( grainSubvolume )
    X_glob = grainCOM[0] + min_array[0]+1
    Y_glob = grainCOM[1] + min_array[1]+1

    ###########################################################
    ##  2. Copy grain into cubic subvolume for analysis
    ###########################################################

    # define size of cube to hold all data with 2 pixel border
    cubeDimension  = max( grainSubvolume.shape ) + 4
    grainSubvolumeCube = np.zeros( ( cubeDimension, cubeDimension ), '<f4' )

    # offest to this from our non-cube data
    grainSubvolumeCubeOffset = ( np.array( grainSubvolumeCube.shape ) - np.array( grainSubvolume.shape ) ) / 2

    # copy non-cube data into the cube with the offset we calculated above
    grainSubvolumeCube[ grainSubvolumeCubeOffset[0]:grainSubvolumeCubeOffset[0]+grainSubvolume.shape[0],grainSubvolumeCubeOffset[1]:grainSubvolumeCubeOffset[1]+grainSubvolume.shape[1] ] = grainSubvolume
    grainCubeCOM = np.array(scipy.ndimage.measurements.center_of_mass( grainSubvolumeCube ) )
    if DEBUG: print "\nThe Center of Mass of my grain into the cube (local coordinates, box) is:\n\n\t", grainCubeCOM
    if DEBUG: print "\nThe Center of Mass of my grain in global coordinates (Fiji), is:\n", Y_glob, X_glob

    ########################################################################
    ###########   INERTIA TENSOR     #######################################
    ########################################################################
    t3 = time.time()
    momentOfInertia = random_orientation.inertia_tensor2d( grainSubvolumeCube, grainSubvolumeCube.shape )
    eigenValVec = random_orientation.eigenvalvec2d(  momentOfInertia )
    if DEBUG: print '\nThe inertia tensor is:\n', momentOfInertia
    if DEBUG: print '\nThe inertia tensor eigenvalues are: \n\t', eigenValVec[0],'\n\t', eigenValVec[1]
    if DEBUG: print '\nThe inertia tensor eigenvectors are: \n\t', eigenValVec[2],'\n\t', eigenValVec[3]

    #######################################################################
    ###########   ROTATE REFERENCE FRAME and GET GRAIN LENGTH     #########
    #######################################################################
    t4 = time.time()

```

```python
        grain_local_Coordinates = np.where( grainSubvolumeCube == grainNumber )
        grain_local_Coordinates = np.array (grain_local_Coordinates)
        CambioBaseMatrix = np.array([ [eigenValVec[2][0],eigenValVec[3][0]] , [eigenValVec[2][1],eigenValVec[3][1]]] , dtype=float)
        CambioBaseMatrix_INV = np.linalg.inv(CambioBaseMatrix)
        grain_NEW_local_Coordinates = np.dot(CambioBaseMatrix_INV , grain_local_Coordinates)
        AX1_max = np.amax( grain_NEW_local_Coordinates[0,:] )
        AX1_min = np.amin( grain_NEW_local_Coordinates[0,:] )
        AX2_max = np.amax( grain_NEW_local_Coordinates[1,:] )
        AX2_min = np.amin( grain_NEW_local_Coordinates[1,:] )
        AX1_length = AX1_max - AX1_min
        AX2_length = AX2_max - AX2_min
        grain_length = np.sort([AX1_length,AX2_length])
        if DEBUG: print '\nThe lengths of my grain (after reference frame rotation) are:\n'
        if DEBUG: print grain_length[0] , '=', AX1_max , '-' , AX1_min ,'\n', grain_length[1] , '=', AX2_max , '-' , AX2_min ,'\n'

        ##################################################################
        ###########   MAXIMUM INSCRIBED SPHERE    ########################
        ##################################################################
        t7 = time.time()

        distance_euclidean_tensor = scipy.ndimage.morphology.distance_transform_edt( grainSubvolumeCube )
        max_inscribedSphere_radius = np.amax (distance_euclidean_tensor)

        for index, value in np.ndenumerate( distance_euclidean_tensor ):
            if value == max_inscribedSphere_radius:
                sphere_center = index

        if DEBUG: print '\nThe maximum inscribed sphere is centered at: ', sphere_center, ' and its RADIUS is: ', max_inscribedSphere_radius

        ##################################################################
        ###########   MINIMUM CIRCUMSCRIBED SPHERE    ####################
        ##################################################################
        t8 = time.time()

        # Ritter algorithm --> https://gist.github.com/paulswtang/074b612d4e5980a18a94
        min_cicr_sph = random_orientation.bounding_sphere2d (grainCoordinates_arrayTR)
        if DEBUG: print '\nThe minimum circumscribed sphere center and radius are: ', min_cicr_sph[0], min_cicr_sph[1],min_cicr_sph[2]
        #################################################################
        ###########   SPHERICITY CALCULATION      ######################
        #################################################################

        grainSubvolumeCube = scipy.ndimage.morphology.binary_fill_holes(grainSubvolumeCube).astype(int)

        sphericity1 = grainVolume/(math.pi*min_cicr_sph[2]*min_cicr_sph[2])
        sphericity2 = (2*(grainVolume/math.pi)**0.5)/(2*min_cicr_sph[2])
        sphericity3 = max_inscribedSphere_radius/min_cicr_sph[2]
        sphericity4 = (2*math.pi*(grainVolume/math.pi)**0.5)/(skimage.measure.perimeter(grainSubvolumeCube, neighbourhood=4))
        sphericity5 = grain_length[0]/grain_length[1]
        t9 = time.time()
```

```
            if DEBUG: print '\nSave all the properties in a numpy array.\n'
            geometry_properties = np.array ([ grainNumber, grainVolume, X_glob, Y_glob, eigenValVec[0],eigenValVec[1], grain_length[1], grain_length[0], 2.0*max_inscribedSphere_radius, 2.0*min_cicr_sph[2], sphericity1, sphericity2, sphericity3, sphericity4, sphericity5 ])
            if DEBUG: print geometry_properties
            if DEBUG: print '********************************************************************************'

            finaltime = time.time()

            for item in geometry_properties:
                fileHandle.write( "{}\t".format( item ) )
            fileHandle.write( "\n" )

        fileHandle.close()
        exit()
```

Appendix A.3 Python script “GetLabels_2Dimage.py”

This python script (1) takes a (coloured) scan of grains as input, (2) binarises the image, (4) segments it and assigns labels to all grains.

```
import tifffile
import matplotlib.pyplot as plt
import spam.plotting.greyLevelHistogram as glh
#import spam.label.ITKwatershed as ws
import spam.label
import scipy.ndimage.morphology
import numpy

# if coloured image (table scanner), first binarise it:
grey = tifffile.imread( "/home/riccardo/Ticino_scan_color_4500x4500.tiff" )
plt.imshow( grey[:,:,grey.shape[2]/2], cmap="Greys_r"); plt.show()
glh.plotGreyvalueHistogram( grey )
# following from above
binary = grey >= 120 # i.e., binary is where "grey" is bigger than or equal to 120 (set it from Fiji)
binary = scipy.ndimage.morphology.binary_fill_holes(binary)
print binary.sum() # let's count the number of "True" voxels:
plt.imshow( binary[:,:,binary.shape[2]/2], cmap="Greys_r"); plt.show()
######## If binarised start from here:
print 'Now start labelling:'
#labelled = ws.run( binary )
labelled = spam.label.watershed( binary )
labelled = numpy.uint16(labelled)
print labelled.max()
plt.imshow( labelled[:,:,labelled.shape[2]/2], cmap=ltk.randomCmap); plt.show()
tifffile.imsave("labelled_2Dimage.tif",labelled)
exit()
labelled = ltk
```

Appendix A.4 PFC5 script “Make_initial.p3dat”

This script runs on PFC5. It creates the initial cylindrical sample with target model dimensions, PSD and porosity and equilibrates it. The output is the “initial.p3sav” model. Some of the functions/scripts which are called but not reported in the *Appendices* can be easily download from the PFC material-modelling support (*FISHTank*) available (open-source) at: https://www.itascainternational.com/software/support/utilities/fishtank).

```
new
set random 10002
; STEP 1: Build initial state
fish create domain_extent = 20e-3
domain extent [-domain_extent] [domain_extent]

[scale_factor = 1.0]
[target_porosity = 0.38]
[sand_type = 0] ;0=Hostun, 1=Caicos ; 2=Ottawa ;3=Ticino
[fric=0.20]
cmat default type ball-facet model rrlinear method deformability emod 2.0e8 kratio 2.0 prop fric [fric] rr_fric 0.0
cmat default type ball-ball  model rrlinear method deformability emod 2.0e8 kratio 2.0 prop fric [fric] rr_fric 0.0
wall generate name 'VesselLateral' cylinder axis 0 0 1 base 0 0 [-domain_extent*0.75] ...
                                      radius [domain_extent*0.25] height [domain_extent*1.5] cap False resol 0.1
wall generate name 'VesselTop' plane position 0 0 [domain_extent*0.5]
wall generate name 'VesselBottom' plane position 0 0 [-domain_extent*0.5]
[mvWpCyl = wall.find(1)]
[mvWp0z  = wall.find(3)]
[mvWp1z  = wall.find(2)]

;Get vessel initial height (the width will be set the half)

define wlz
    wlz = math.abs(wall.pos.z(mvWp0z) - wall.pos.z(mvWp1z))
end
@wlz
call granulometry.p3dat
define delete_fines
  loop foreach local ball ball.list
    if ball.radius(ball) <= dmin_scaled then
      ball.delete(ball)
    endif
  endloop
end
@delete_fines
ball attribute density 2500.0 damp 0.7
ball property fric [fric]
hist mech solve aratio
cycle 2000 calm 5
set timestep scale
solve aratio 1e-5
calm
set timestep auto
```

```
cycle 1000 calm 20
calm

define identify_floaters
  loop foreach local ball ball.list
    ball.group.remove(ball,'floaters')
    local contactmap = ball.contactmap(ball)
    local size = map.size(contactmap)
    if size <= 1 then
      ball.group(ball) = 'floaters'
    endif
  endloop
end
@identify_floaters

define delete_balls ;delete balls that jumped out of the initial cylinder (if any)
  loop foreach local ball ball.list
    local dist_radial = math.sqrt((ball.pos.x(ball))^2+(ball.pos.y(ball))^2)
    local dist_z2 = (ball.pos.z(ball))^2
    if dist_radial > wlz/4
        ball.delete(ball)
    endif
    if dist_z2 > (wlz/2)^2
        ball.delete(ball)
    endif
  endloop
end
@delete_balls

save initial.p3sav
call isotropic_compression.p3dat
```

Appendix A.5 PFC5 script “Isotropic_compression.p3dat”

This script runs on PFC5. It (1) restores the initial model, (2) applies the target boundary conditions and confining pressure, (3) equilibrates it. The output is the “isotropic.p3sav” model.

```
restore initial.p3sav

call utilities.p3dat
call ct.fis suppress
call ft_my.fis

ball attribute density 2500.0 damp 0.7 ; [kg/m3]

def ctSetParams
  mv_type = 0 ; Physical vessel type (no periodic)
  mv_shape = 1 ; Cylindrical shape
  mv_H = wlz ; Set initial dimensions
  mv_W = wlz / 2.0

; Set Compression-Test Parameters.
  ct_testType = 0 ;Confined Test
  ct_Pc = 100e3 ;Confining Pressure
  ct_eRate = 0.50; Axial strain rate
  ct_loadCode = 0 ;Single stage
  ;servo-control group:
  ct_ARatLimit = 1e-5 ;Equilibrium ratio limit
  pk_PTol = 1e-5 ; Pressure tollerance
  pk_stepLimit = 20000000 ; 2 million
end
@ctSetParams

@_ctCheckParams ;Check validity of given parameters
@ctListProps ;Print things on screen
@mv_wInit ;Initialise some strain-stress and force their calculation during cycling (callbacks)

[mvs_vLimit = ct_vLimit]
@mvs_on ;Function for keeping updated some values through callbacks (Radial diameter and velocity of walls)
@mv_mStrainZero
@mv_wStrainZero

hist hist_rep 100
hist @mv_wPz
hist @mv_wPr
hist @poros
hist @mv_wn

;Set my case (mvs_BCz=1, mvs_BCr=1, etc.) and perform cycles
@mvs_applyConfinement( @ct_Pc, @ct_PTol, @ct_ARatLimit, @ct_stepLimit )
;Monitor volumetric strain
[mv_wn0 = mv_wn] ;initial porosity after isotropic compression
hist @eps_vol

[topforce = wall.force.contact(mvWp0z)]
[botforce = wall.force.contact(3)]
list @topforce ;check if top/bottom forces are correct
list @botforce

save isotropic.p3sav
call triaxial_compression_RR_OTTAWA.p3dat
return
```

Appendix A.6 PFC5 script “Triaxial_compression.p3dat”

This script runs on PFC5. It (1) restores the isotropic model, (2) assigns the rolling friction to the grains, (3) executes a triaxial test.

```
restore isotropic.p3sav
set random 10010
calm
set orientation on
wall tolerance etol 0.0 ctol [0.1*dmax_scaled/2]
clean all

[emod=2e8]
[kratio=2.0]
[fric=0.575]

```

```
[file_name = 'hostun_sphericity.csv']
[trend='power']
[coeff1 = 0.1963] ;y=Ax+B (A) -or- y=Cx^n (C)
[coeff2 = -8.982] ;y=Ax+B (B) -or- y=Cx^n (n)

;ball fix spin
[StrainIncrement_SaveModel = 0.03] ;save every 3% (5 times) = 15%
[NameByUser='Hostun_DEM']
[save_flag=1] ;1=Save models every increment, 0=do not

cmat default type ball-ball model rrlin method deformability emod [emod] kratio [kratio] ...
                        property fric [fric] rr_fric 0.0
cmat apply
;initialise some values for the deviatoric load. Real quantities!
ball property fric [fric]
wall property fric 0.0

@mv_wPoros ;call once to get the initial porosity
[mv_wn0 = mv_wn] ;set initial porosity
define volumetric_strain_from_porosity
    eps_vol = (mv_wn-mv_wn0)/(1-mv_wn)
end
set fishcallback -5.0 @volumetric_strain_from_porosity
hist @eps_vol n 100

call rolling_utilities.p3dat
@apply_rolling_friction_from_StaTrasform([sphericity])

;New parameters for the deviatoric phase
def ctSetParams
  mvs_vLimit = 0.10
  ct_eRate = 1.0 ;1.0=axial velocity 0.01 for each platen
  ct_loadCode = 1
end

def ctPerformStages ; Set here the target axial strains
  _ctPerformStage( 1, [-StrainIncrement_SaveModel] )
  _ctPerformStage( 2, [-StrainIncrement_SaveModel] )
  _ctPerformStage( 3, [-StrainIncrement_SaveModel] )
  _ctPerformStage( 4, [-StrainIncrement_SaveModel] )
  _ctPerformStage( 5, [-StrainIncrement_SaveModel] )
  ;_ctPerformStage( 6, [-StrainIncrement_SaveModel] )
end
@ctSetParams

hist purge
hist hist_rep 100
hist @mv_wsd
hist @mv_wsa
hist @mv_wea
hist @mv_wer
hist @mv_wev
hist @mv_wn
hist @CN_mean
hist @mean_rot

@ctLoadingPhase

save triaxial_final.p3sav
return
```

Appendix A.7 PFC5 script “Prepare_Cone.p3dat”

This PFC5 script executes a CPT test in a virtual calibration chamber (previously built using two scripts similar to what reported in Appendix A.4 and Appendix A.5).

```
restore isotropic_VCC.p3sav

set orientation on
[_mvCylRes=0.1]
[wadd_cyl = wall.find(1)]
[wadd_bot = wall.find(2)]
[wadd_top = wall.find(3)]

@mvs_off
def _mvsActive
; Control velocities of wall pairs with pressure BCs.
  local wGain, wVel
  if mv_shape == 1
    if mvs_BCz == 1 then
      wGain = _mvsGain(3)
      if wGain == -1.0 then
        wVel = -mvs_vLimit  ; closing at velocity limit
      else
        wVel = wGain * ( mv_wPz - mvs_BCzVal )
      end_if
      wall.vel( mvWp0z, 3 ) = -wVel ;stress control on the bottom wall (as in the exp)
      wall.vel( mvWp1z, 3 ) = 0 ;set to zero the top (as in the exp)
    end_if
    if mvs_BCr == 1 then
      wGain = _mvsGain(4)
      if wGain == -1.0 then
        wVel = mvs_vLimit  ; set=0 for BC3 (no lateral strain)
      else
        wVel = wGain * ( mv_wPr - mvs_BCrVal ) ; set=0 for BC3 (no lateral strain)
      end_if
      _mvsSetRadVel( wVel )
    end_if
  end_if
  _mvsEnforceVlimit
end
@mvs_on

hist purge
;ball fix spin
[penetration_vel = -0.1]
[b_fric = 0.60]
[rr_fric = 0.0] ;set to zero now
[emod = 4e8]
[kratio = 2.0]
[kn_pile = 3e6] ; for linear model
[c_fri_Pile = 0.00] ; frictionless sleeve
[c_fri_fricPile = 0.60] ;frictional sleeve
[c_fri_cone = 0.60]; set = ball fric

[file_name = 'ticino_sphericity_from2DScan.csv']
[trend='power']
```

```
[coeff1 = 0.1963] ;y=Ax+B (A) -or- y=Cx^n (C)
[coeff2 = -8.982] ;y=Ax+B (B) -or- y=Cx^n (n)
call rolling_utilities.p3dat

cmat default type ball-ball model rrlin method deformability emod [emod] kratio [kratio] ...
                        property fric [b_fric] rr_fric [rr_fric]
cmat apply
ball property fric [b_fric]
wall property fric 0.0

@apply_rolling_friction_from_StaTrasform([sphericity])

def _out_rad_cur  ; fish to determine the current radius of cylinder
local radx
local rady
      loop foreach vp wall.vertexlist( wadd_cyl )
      radx = comp.x( wall.vertex.pos(vp))
      rady = comp.y( wall.vertex.pos(vp) )
    end_loop
    _out_rad_cur=math.sqrt(radx^2+rady^2)
    _height_cur= _wdz
end
@_out_rad_cur

define cone_geometry
    ks_pile = kn_pile   ; for linear model
    Theta = 60          ; cone angle
    d_c = 1.0 * 0.0356  ; cone diameter
    h_c = (d_c/2)*math.tan(Theta*math.pi/180)
    h_fr = 0.130        ; length of friction sleeve
end
@cone_geometry

[tip_pos0 = wall.pos.y(wadd_top) ]
[cone_pos_z = wall.rotation.center.z(wadd_cone)]
[h_penet =  - cone_pos_z]
[tip_pos= tip_pos0 + cone_pos_z]

wall generate id 4 group CONE facet cone axis 0 0 -1 base (0.0,0.0,[tip_pos0+h_c]) height @h_c radius [d_c*0.5] cap false false onewall ...
     resolution [_mvCylRes]

cmat add 1 model linear property kn @kn_pile ...
                      ks @ks_pile ...
                      fric @c_fri_cone ...
                      range group CONE

[wadd_cone = wall.find(4)]

      def vel_pile ; set pile velocity
          wall.vel.z(wadd_cone) = penetration_vel
         shaft_for_z=0
         shaft_for_r=0
          loop i(1,pieces)
              wall.vel.z(wadd_shaft(1,i)) = penetration_vel
          endloop
      end
      @vel_pile

      call monitor_cone.fis
      set timestep auto
set nstep 500

define stop_me
  if h_penet < 0.80
    exit
  endif
  stop_me = 1
end
solve fishhalt @stop_me

save CPT_final.p3sav
return
```

Appendix B: Dataset

The most relevant data that has been used in this doctoral work, together with the instructions to open and manage the files, is available in open-access on the "Zenodo" open-source storage platform (www.zenodo.org).

The archives can be found with a simple research from the search box by typing the thesis author's name (Riccardo Rorato) and are citable with the following DOI: 10.5281/zenodo.3407138.

The full contents will be available from November 2019.

Appendix C: Number of particles estimation in a cylindrical DEM sample

Arroyo et al. (2011) proposed an equation to estimate the number of particles (N) involved in CPT-DEM simulations performed in a cylindrical Virtual Calibration Chamber (VCC). This estimation allows a straightforward pre-setting of the chamber and cone diameters, in order to get a reasonable number of particles. It is defined as follow:

$$N = f_G \, \frac{3}{2} \, n_p^3 \, R_d^2 \, n_h (1 - n)$$

in which n represent the porosity, f_G is an empirical factor accounting for the grain size distribution (roughly 1.3 for the fine-truncated Ticino sand they used) and the three a-dimensional ratios are:

$$n_p = \frac{d_c}{D_{50}} \; ; \; R_d = \frac{D_C}{d_c} \; ; \; n_h = \frac{H}{d_c}$$

where H and D_C are respectively the VCC height and diameter, D_{50} is the characteristic grain diameter and d_c is the cone diameter. It is evident this equation is valid if the VCC is filled with particles generated from a single scaling factor. However, it may be useful to extend this equation in case multiple scaling factors are applied to different zones within the VCC (as the ones used in Chapter 9).

The extended equation has been developed in this work and it is reported below. It is valid for a VCC filled with particles originated from three different scaling factor applied to three cylindrical zones (see Figure C.1). It assumes the form

$$N = f_G \, \frac{3}{2} \, H \, (1 - n) \left\{ \left(D_{50,1}^{-3} \cdot D_{C,1}^2 \right) + \left[D_{50,2}^{-3} \cdot \left(D_{C,2}^2 - D_{C,1}^2 \right) \right] + \left[D_{50,3}^{-3} \cdot \left(D_{C,3}^2 - D_{C,2}^2 \right) \right] \right\}$$

where $D_{50,1-2-3}$ are the characteristic grains diameters for the three particle scaling factors and $D_{C,1-2-3}$ are the diameters of the three cylinders defining the different zones of the VCC (see Figure C.1).

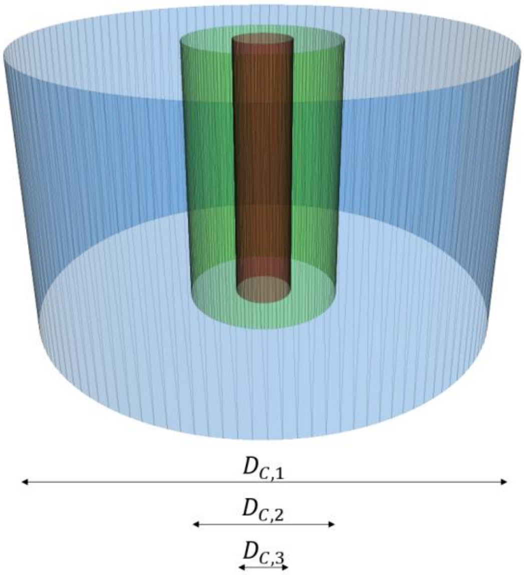

Figure C.1: Representation of a VCC built with three cylindrical zones with three different scaling factors

Arroyo, M., Butlanska, J., Gens, A., Calvetti, F., Jamiolkowski, M., 2011. Cone penetration tests in a virtual calibration chamber. Geotechnique 61, 525–531. https://doi.org/10.1680/geot.9.P.067